

ORIGIN OF PLAGIOCLASE-OLIVINE INCLUSIONS

Thesis by

Yuntai Jack Sheng

In Partial Fulfillment of the Requirements

for the Degree of

Doctor of Philosophy

California Institute of Technology

Pasadena, California

1992

(Defended November 1, 1991)

To my loving family.

© 1992

Yuntai Jack Sheng

All rights Reserved

To my loving family.

ACKNOWLEDGEMENT

I thank Professor G. J. Wasserburg for his guidance and support. His instinct to grasp the major issues in the scientific frontiers, his ability to distill a problem into its most fundamental components and his relentless pursuit of scientific truth will continue to grow with me.

I thank Ian Hutcheon for his encouragement, support and advice. He generously shared his time and great knowledge, not to mention his patience in teaching me how to use the ion microprobe.

John Beckett taught me the basic knowledge and skills for conducting high temperature experiments. I thank him for generously allocating his time to review my work and to share his stimulating ideas.

Professor E. M. Stolper and Professor D. S. Burnett kindly allowed me to use their laboratories. Their enthusiasm and advice to my study are sincerely appreciated. Professor G. R. Rossman generously provided samples for my experimental studies. I am grateful to Professor Y. Yung's concern about my study and other matters.

I am thankful to John Armstrong for teaching me how to use the electron probe, to Allen Kennedy for his help with my ion microprobe analysis. I appreciate Mary Johnson and Tom LaTourette for their good spirited aid and support in the use of the furnace. Special thanks are due to Lindsey Hedges for her expert help in sample preparation and photography, and to Priscilla Piano and Kathie Venturelli for taking care of the many things over the period of my stay in the asylum.

..... all physical objects contain within themselves some representation of their integrated history. This representation lies in the physical, chemical and isotopic constitution of a piece of matter which can reveal some of the major processes and schedule of events that led to the formation of that object over the history of the universe. We must expect that a unique interpretation is not possible, particularly as the complex of events which leads up to the present time will tend to smear or partially erase the detailed memory in a single object. However, it is my claim that in any case, some inference of major significance can be obtained.

Gerry Wasserburg

Crafoord Lectures

ABSTRACT

Plagioclase-Olivine Inclusions (POIs) are an abundant group of chondrule-like objects found in carbonaceous chondrites. Despite textural evidence of a molten or partially molten origin, approximately half of the POIs studied exhibited variations in Mg isotope composition of up to 11‰/amu between spinel and coexisting silicates. Equilibrium crystallization experiments performed to study the crystallization behavior of melts of POI compositions showed that the phase assemblages predicted on the basis of phase equilibria are generally consistent with those observed in POIs. Spinel is the liquidus phase for most of the inclusions that contain spinel with fractionated Mg isotopes, and therefore these spinels could be preserved if melting was below the liquidus temperature for the bulk composition of the inclusion. The presence of resorbed spinels in some inclusions whose bulk composition does not permit spinel in its phase assemblage requires that these spinels were relict. The petrographic and chemical properties of POIs indicate that they are not condensates or evaporative residues, but formed by melting or partial melting of pre-existing solids that had originated from isotopically distinct reservoirs. The presence of isotopically heterogeneous spinel in the POIs requires that the maximum temperature experienced by these objects was low enough, the duration of heating short enough, and the subsequent cooling rate fast enough to prevent homogenization of Mg isotopes by diffusive transport. The self-diffusion rate of Mg was measured in spinel and coexisting melt using isotope tracers. For spinel, the activation energy of 384 ± 7 kJ for Mg and pre-exponential factor of 7791.9 ± 1.3 cm²/s is obtained.

The temperatures of melting of POIs is estimated to be in the range of 1350-1500°C, the duration of the heating events were < 2 hr, and the initial cooling rate was $> 25^\circ/\text{hr}$. The melting occurred after most ^{26}Al had decayed and possibly subsequent to the extensive oxygen isotopic exchange between solids and nebula gas. The melting of POIs is probably by flash heating or impact melting in a hot parcel or region of the nebula. These refractory objects (including CAIs) are believed to be the result of repetitive heating events that had frequently generated or reprocessed refractory residues over a prolonged timescale of very early solar system history.

TABLE OF CONTENTS

Acknowledgements	iii
Abstract	vi
Table of Contents	viii
Table of Figuresxii
Table of Tablesxv
CHAPTER 1 INTRODUCTION	1
1.1. Thesis Background	3
1.2. Thesis Approach and Scope	8
CHAPTER 2 ANALYTICAL TECHNIQUES AND EXPERIMENTAL METHODS	13
2.1. Petrographic Analysis	13
2.2. Electron Microscope Analysis	14
2.2.1. Wavelength dispersive spectrometer	15
2.2.2. Energy dispersive spectrometer	15
2.2.3. Quantitative analysis	16
a. Analysis of individual phases	18
b. Analysis of bulk inclusions	18
2.3. Ion Microprobe Analysis	20
2.3.1. Instrumentation	21
a. Primary ion source and primary optics	21
b. Secondary ion optics	24
c. Mass analyzer	24
d. Detection system	25
2.3.2. Analytical conditions	26
a. Mg isotope analysis	27
b. Rare earth elements analysis	30
2.4. Experimental Method	32
2.4.1. Sample preparation	32
2.4.2. Furnace setup and temperature calibration	32
2.4.3. Experimental procedure	33
CHAPTER 3 PETROGRAPHICAL AND CHEMICAL CHARACTERISTICS OF PLAGIOCLASE-OLIVINE INCLUSIONS	38
3.1. Petrography	38

3.2. Bulk Chemistry	43
3.3. Mineral Chemistry	48
3.3.1. Plagioclase	48
3.3.2. Olivine	50
3.3.3. Spinel	52
3.3.4. Pyroxene	52
3.3.5. Accessory Phases	59
a. Armalcolite	59
b. Zirconolite	61
c. Sapphirine	61
3.3.6. Glass and mesostasis	63
3.4. REE Data	65
3.5. Comparison of Plagioclase-Olivine Inclusions with CAIs and CA Chondrules	75
CHAPTER 4 Mg ISOTOPE COMPOSITION	77
4.1. Mg Isotope Fractionation	77
4.1.1. Mg isotope fractionation in silicates	77
4.1.2. Mg isotope fractionation in spinel	81
4.2. Summary of Mg Isotope Fractionation in POIs	81
4.3. Excess $^{26}\text{Mg}^*$	85
CHAPTER 5 PHASE EQUILIBRIA STUDY	90
5.1. Bulk Compositions of Starting Material	94
5.2. Experimental Results	95
5.2.1. Crystallization experiments	95
5.2.2. Cooling rate experiments	107
5.3. Construction of Phase Diagrams	108
5.4. Phase Diagrams for Determining Crystallization Sequences	111
5.4.1. Effect of Na_2O and FeO on the phase boundaries	127
5.4.2. Crystallization Sequences of POIs	128
a. Crystallization sequences of melt compositions in the spinel projection	132
b. Crystallization sequences of melt compositions in the forsterite projection	135
c. Crystallization sequences of melt compositions in the anorthite projection	138
5.5. Implications for Petrographic Classification	141
5.6. Evaluation of POIs with Higher Fe and/or Na	143
CHAPTER 6 Mg SELF-DIFFUSION EXPERIMENTS	145
6.1. Analytical Technique	146
6.2. Experimental Method	148

6.3.	Mathematical Treatment	153
6.4.	Evaluation of the Diffusion Couple	161
6.4.1.	Treatment of the diffusion couple	161
6.4.2.	Importance of chemical equilibrium during diffusion experiment	162
6.5.	Results	166
6.6.	Activation Energy of Mg in Spinel and Melt	184
6.7.	Effects of the Boundary Condition	187
6.8.	Extracting Diffusion Coefficient from a Coexisting Phase	195
CHAPTER 7 ORIGIN OF PLAGIOCLASE-OLIVINE INCLUSIONS		196
7.1.	Interpretation of Textural and Chemical Features	197
7.2.	Implication of Igneous Textures versus Mg Isotope Heterogeneity	199
7.3.	Model for POI Formation	203
7.4.	²⁶ Al as a Relative Chronometer	210
7.5.	Comparison of Isotopic Heterogeneity in POIs and CAIs	212
7.6.	Experimental Constraints on the Thermal History of POIs	214
7.6.1.	Maximum melting temperature of POIs	214
7.6.2.	Cooling rates of POIs	218
7.6.3.	Possible heat source	226
7.7.	Conclusions	227
REFERENCES		231
APPENDIX		
Sheng Y.J., Hutcheon I.D. and Wasserburg G.J. (1991)	Origin of Plagioclase-Olivine Inclusions in carbonaceous chondrites. <u>Geochim. Cosmochim. Acta</u> 55 , 58 1-599.	244
Sheng Y.J., Hutcheon I.D. and Wasserburg G.J. (1988)	Plagioclase-Olivine Inclusions in Allende- a link between CAI and ferro-magnesian chondrules. <u>Lunar Planet.Sci. Conf. XIX</u> , 1075-1076.	263
Sheng Y.J., Hutcheon I.D. and Wasserburg G.J. (1990)	Magnesium isotope heterogeneity in Plagioclase Olivine Inclusions. <u>Lunar Planet.Sci. Conf. XXI</u> , 1138-1139.	265
Sheng Y.J., Beckett J.R., Hutcheon I.D. and Wasserburg G.J. (1991)	Experimental constraints on the origin of Plagioclase-Olivine Inclusions and CA chondrules. <u>Lunar Planet. Sci. Conf. XXII</u> , 1231-1232.	267
Sheng Y.J., Hutcheon I.D. and Wasserburg G.J. (1991)	Mg self-diffusion in spinel: constraints on the thermal history of Plagioclase-	

Olivine Inclusions. <u>Lunar Planet. Sci. Conf. XXII</u> , 1233-1234.	269
Sheng Y.J., Hutcheon I.D. and Wasserburg G.J. (1991) An experimental study of Mg self-diffusion in spinel. <u>Meteoritics 54</u>	271

LIST OF FIGURES

Fig.2.1	Schematic Drawing of the PANURGE Ion Microprobe	23
Fig.2.2	Schematic Drawing of Deltech DT-31 Vertical Furnace	35
Fig.2.3	Schematic Drawing of Sample Configuration	36
Fig.3.1	Compositions of POIs	45
Fig.3.2	Comparison of POI Compositions with Other Refractory Inclusions and Chondrules	46
Fig.3.3	POI Spinel Compositions	54
Fig.3.4	Al and Ti Contents in POI Pyroxenes	57
Fig.3.5	Compositions of Ti-poor POI Pyroxenes	58
Fig.3.6	Chondrite-normalized REE Abundances of POI Plagioclase	70
Fig.3.7	Chondrite-normalized REE Abundances of POI Pyroxene	71
Fig.3.8	Chondrite-normalized REE Abundances of POI Mesostasis	73
Fig.3.9	Chondrite-normalized REE Abundances of Bulk POI	74
Fig.4.1	Mg Isotopic Fractionation in POI Silicates	83
Fig.4.2	Mg Isotopic Fractionation in POI Spinel	84
Fig.4.3	Mg Isotopes of POI 3510	87
Fig.4.4	Mg Isotopes of POI 5ALLB6	88
Fig.4.5	Mg Isotopes of Other POIs	89
Fig.5.1	Spinel Saturated Liquidus Phase Diagram from Stolper	93
Fig.5.2	Experimentally Determined Crystallization Sequences	99
Fig.5.3	Calculated Modes for Experiments on POI-2	102
Fig.5.4	Comparison of Sappirine Compositions	106
Fig.5.5	Schematic Drawing of the Three Projection Schemes	110
Fig.5.6	Isotherms and Contours on Spinel Saturation Surface	120
Fig.5.7	Isotherms and Contours on Forsterite Saturation Surface	122
Fig.5.8	Isotherms and Contours on Anorthite Saturation Surface	124
Fig.5.9	Effect of Na on Phase Boundaries	130
Fig.5.10	Effect of Fe on Phase Boundaries	131
Fig.5.11	Bulk Compositions of POIs Projected on the Spinel Saturated Liquidus Phase Diagram	134
Fig.5.12	Bulk Compositions of POIs and CACs Projected on the Forsterite Saturated Liquidus Phase Diagram	137

Fig.5.13	Bulk Compositions of POIs and CACs Projected on the Anorthite Saturated Liquidus Phase Diagram	140
Fig.6.1	Schematic Drawing showing the Preparation of the Diffusion Couple	150
Fig.6.2	SEM Image of Spinel That Settled to Bottom of Pt Crucible	151
Fig.6.3	SEM Image of Experimental Run Product	152
Fig.6.4	SEM Image of Boundary of Diffusion Couple	152
Fig.6.5	Schematic Drawing Illustrating the Chemical and Isotopic Compositions of the Diffusion Couple	154
Fig.6.6	SEM Image Showing Serrated Contact of a Diffusion Couple in Chemical Disequilibrium	164
Fig.6.7	Chemical Profiles in Spinel and Melt after Diffusion Experiment	168
Fig.6.8	Concentration Variation of Mg Isotopes in Spinel and Melt following Run at 1495°C	169
Fig.6.9	Concentration Profile of ^{25}Mg in Spinel for 1495°C	170
Fig.6.10	Best Fit of Measured Data to determine D_{sp}	171
Fig.6.11	Concentration Profile of ^{25}Mg in Melt for 1495°C	172
Fig.6.12	Concentration Profile of ^{25}Mg in Spinel for 1553°C	174
Fig.6.13	Concentration Profile of ^{25}Mg in Melt for 1553°C	175
Fig.6.14	Concentration Profile of ^{25}Mg in Spinel for 1415°C	176
Fig.6.15	Concentration Profile of ^{25}Mg in Melt for 1415°C	177
Fig.6.16	Concentration Profile of ^{25}Mg in Spinel for 1261°C	178
Fig.6.17	Concentration Profile of ^{25}Mg in Melt for 1261°C	179
Fig.6.18	Concentration Profile of ^{25}Mg in Spinel for 1497°C	181
Fig.6.19	Concentration Profile of ^{25}Mg in Spinel for 1354°C	182
Fig.6.20	Concentration Profile of ^{25}Mg in Spinel for 1302°C	183
Fig.6.21	Temperature Dependence of Mg Diffusion Coefficients in Spinel	185
Fig.6.22	Temperature Dependence of Mg Diffusion Coefficients in Melt	186
Fig.6.23	Effect of Boundary Values on Fitted Curves of Measured Data for 1497°C	190
Fig.6.24	Effect of Boundary Values on Fitted Curves of Measured Data for 1354°C	191
Fig.6.25	Effect of Boundary Values on Fitted Curves of Measured Data for 1302°C	192
Fig.6.26	Comparison of Diffusion Coefficients for Melts using Different Boundary Values	193
Fig.6.27	Comparison of Diffusion Coefficients for Spinel using Different Boundary Values	194
Fig.7.1	Proposed Model for POI Formation	209
Fig.7.2	Relation between Mg Fractionation and Liquidus Temperatures of POIs	216

Fig.7.3	Maximum Duration of Heating at 1500°C allowed for Preservation of Mg Isotopic Heterogeneity in POIs	219
Fig.7.4	Initial Cooling Rates	222

LIST OF TABLES

Table 1.1	Chondritic Classes and Mean Properties	4
Table 2.1	Comparison of EDS and WDS Analysis of POI Bulk Composition	19
Table 2.2	Ion Microprobe Operating Conditions	29
Table 3.1	Petrographic Features of POIs	40
Table 3.2	POI BULK Compositions	44
Table 3.3	Plagioclase Compositions	49
Table 3.4	Olivine Compositions	51
Table 3.5	Spinel Compositions	53
Table 3.6	Pyroxene Compositions	56
Table 3.7	Armalcolite Compositions	60
Table 3.8	Sapphirine Compositions	62
Table 3.9	Glass and Mesostasis Compositions	64
Table 3.10	Clinopyroxene REE Data	66
Table 3.11	Pyroxene REE Data	66
Table 3.12	Plagioclase REE Data	67
Table 3.13	Mesostasis REE Data	67
Table 3.14	Comparison of POI with Type B, Type C CAI and CA Chondrule	76
Table 4.1	Mg Isotopic Compositions of POI Plagioclase	78
Table 4.2	Mg Isotopic Compositions of Other Phases	79
Table 5.1	Compositions of Starting Material	94
Table 5.2	Experimental Results	96
Table 5.3	Representative Analyses of Experimental Products	103
Table 5.4	Data Used in Constructing Phase Diagrams	113
Table 6.1	Compositions of Starting Material	163
Table 6.2	Experimental Results	180

CHAPTER ONE

INTRODUCTION

Most of the meteorites that fall on the Earth are chondrites. The insights that these meteorites can provide about conditions and processes in the early solar system, became apparent when it was realized that these chondritic meteorites were very old, and for nonvolatile elements, closer in composition to the sun than any other known material on earth. It was also realized that most of the relatively small differences in compositions between major chondritic groups apparently were caused by the fractionation of various solid components and gas that existed in the nebula prior to the final accretion of the parent bodies. Thus chondrites are the logical places to search for surviving examples of solids that were present in the early stages of the solar nebular history.

Carbonaceous chondrites are generally considered to be the most primitive surviving materials from the early solar system. Refractory inclusions, more commonly referred to as calcium- and aluminum-rich inclusions (CAIs), were known to exist in carbonaceous chondrites (see, e.g., Christophe Michel-Lévy, 1968), but it was only after the fall of the very large Allende meteorite in 1969 that the attention of the meteoritic community was drawn to these unusual objects. In the ensuing years since the fall of the Allende, it was recognized that these refractory inclusions constitute a diverse group of

complex objects. The relationship between the bulk chemistries of CAIs and high temperature condensates from a solar composition suggests that these inclusions constitute primitive materials condensed from the solar nebula. After their formation, many refractory inclusions experienced complex histories involving a variety of processes which, to different degrees, obscured the evidence concerning their formation process(es). It has been their primitive and intriguing features that challenged many scientists to devote extensive studies to these objects in an attempt to unveil the mysteries of the history of our solar system.

In this thesis, I present the study of a distinct class of refractory objects which are distinct from the usual CAIs and that will be referred to as Plagioclase-Olivine Inclusions (POIs). POIs are an abundant group of chondrule-like objects with igneous textures found in carbonaceous chondrites. The petrographic and chemical properties of POIs indicate that they are formed by melting or partial melting of pre-existing solids. Despite their igneous textures, I have found that many POIs are heterogeneous in Mg isotopic composition within individual inclusions. It was this observation that motivated me to conduct a series of experimental studies. The experimental study consists of two parts. The first part is a study of phase relations to develop a framework to assist in the interpretation of petrographic and isotopic data. The second part is a study of the self diffusion of Mg in spinel, which is used to provide constraints on the thermal history of POIs. It is based on these observations and experimental studies that a model of the formation of POIs is proposed. The processes involved in the formation of POIs suggest that many refractory objects were the result of multiple stages of processing over a time scale of several million years during the earliest stages of solar history.

1.1. Thesis Background

The study of meteorites represents one aspect of the continuing human inquiry into the origin of our Earth and solar system. Meteorites comprise a highly diverse group of objects that includes the results of melting and chemical-mechanical segregation on small planets and those materials (the chondrites) which appear to be aggregates of more primitive material. Chondrites apparently have been only partially affected by post formational physical or chemical planetary processes. The relative abundances of the chemical elements in the chondrites have long been used as a basis for estimating the solar abundances (Urey, 1952; Goldschmidt, 1954, Suess and Urey, 1956). It has been established that the isotopic composition of many elements (O, Ne, Mg, Si, Ca, Kr, Xe, Ba, Nd, Sm) in some meteoritic materials is distinctly different from that in terrestrial samples (reviews by Begemann, 1980; Wasserburg *et al.*, 1980). In addition, evidence has been found in these primitive materials that indicate that very-short-lived radioactive nuclides (^{26}Al , ^{107}Pd , ^{129}I , ^{244}Pu) were present in the early solar system (see Podosek, 1978; Lee, 1979; Begemann, 1980; Grossman, 1980; Wasserburg and Papanastassiou, 1982; D. Clayton, 1982; Niederer and Papanastassiou, 1984; Niederer *et al.*, 1985; Wasserburg, 1985; R. Clayton *et al.*, 1985).

Chondrites are composed of a coarse-grained fraction generally called chondrules and a fine-grained fraction referred to as matrix. Chondrules are irregular to spherical in shape, ranging from a few tenths mm to over one cm in diameter. They are commonly composed of olivine, pyroxene, glass and feldspar. In the more primitive chondrites (with the exception of CI chondrites), the matrix consists of micron-sized

particles of the same minerals as appear in the chondrules.

Chondrites are classified, by their chemistry, into several groups. These groups include carbonaceous chondrites (CI, CM, CO, and CV), ordinary chondrites (H, L, and LL), and enstatite chondrites (EH and EL). Table 1.1 shows the major chemical criteria that define the difference between the different chondrites. Carbonaceous chondrites can be distinguished from other chondrites by their Mg/Si atomic ratio (>1), Ca/Si ratio (>0.6), low iron metal versus total iron ratio, and their characteristic oxygen isotopic composition.

Table 1.1
Chondrite Classes and Mean Properties^a

Group	Mg/Si	Ca/Si	Fe/Si	$\text{Fe}_{\text{met}}^{\text{b}} / \text{Fe}_{\text{tot}}^{\text{b}}$	$\delta^{18}\text{O}$ (‰) ^c	$\delta^{17}\text{O}$ (‰) ^c
CI	1.05	0.064	0.86	0	~16.4	~8.8
CM	1.05	0.068	0.80	0	~12.2	~4.0
CO	1.05	0.067	0.77	0-0.2	~-1.1	~-5.1
CV	1.07	0.084	0.76	0-0.3	~0	~-4.0
H	0.96	0.050	0.81	0.58	4.1	2.9
L	0.93	0.046	0.57	0.29	4.6	3.5
LL	0.94	0.049	0.52	0.11	4.9	3.9
EH	0.77	0.035	0.95	0.76	5.6	3.0
EL	0.83	0.038	0.62	0.83	5.3	2.7

^a Data from Sears and Dodd (1988) and references therein.

^b Metal iron to total iron ratio.

^c Relative to SMOW.

The carbonaceous chondrites are characterized by relatively high C contents. On the basis of subtle differences in the proportion of major, nonvolatile elements, and

differences in mineralogy and mineral composition, the carbonaceous chondrites are divided into four classes: the CI (C1), CM (C2), CO (CO3), and CV (CV3) chondrites (Van Schmus and Wood, 1967; Wasson, 1974). CI chondrites consist primarily of hydrated phyllosilicate matrix and lack any chondrules or inclusions. CM chondrites contain numerous inclusions and fragments in addition to dark phyllosilicate matrix. CO chondrites are characterized by abundant small (0.2- to 0.5-mm diameter) sized inclusions, chondrules and lithic fragments embedded in a dark matrix of fine grained olivine. CV chondrites have the large inclusions (commonly > 1cm) and also have the greatest variety of inclusion types. The petrography and mineralogy of these different classes of carbonaceous chondrites have been summarized by McSween (1979) and MacPherson *et al.* (1988).

Irregular shaped inclusions occur as a major component in some carbonaceous chondrites and occasionally in ordinary chondrites. The calcium-aluminum-rich inclusions (CAIs), which occur in both coarse-grained and fine-grained varieties, have been the focus of many studies. These CAIs are often spheroidal and may be considered as chondrules. The coarse-grained CAIs commonly consist of melilite, spinel, perovskite, pyroxene (fassaite or diopside), and anorthite (Grossman, 1975). These inclusions often contain nepheline and sodalite, and may contain hibonite (Grossman, 1975), grossular, olivine (Blander and Fuchs, 1975), wollastonite, rhönite, andradite (Fuchs, 1971), molybdenite (Fuchs and Blander, 1977), and rarely cordierite (Fuchs, 1969). Pt group metal alloys have been found in many of these inclusions (see e.g., Palme and Wlotzka, 1976; Wark and Lovering, 1976; El Goresy *et al.*, 1978). Fine-grained CAIs are composed mainly of feldspathoid minerals, grossular, spinel, and

pyroxene (Grossman and Ganapathy, 1975) or of spinel and hibonite rimmed by diopside (Macdougall, 1979). A concentric structure formed from encircling layers of the mineral assemblages as found in fine-grained inclusions are often found as rims (Wark-Lovering rims) around coarse-grained CAIs (Wark and Lovering, 1977).

The CV chondrites (such as Allende) are especially known for the presence of CAIs. Relative to average chondritic material and to ferromagnesian chondrules, CAIs are enriched in Al, Ca, and Ti and in refractory lithophile and siderophile trace elements. Early workers were impressed by the remarkable similarity of CAI bulk compositions and mineralogy to those of high-temperature condensates predicted to form in a cooling gas of solar composition (Lord, 1965; Larimer, 1967; Grossman, 1972; Blander and Fuchs, 1975). With the additional recognition of the extreme ages of these inclusions (see, e.g., Gray *et al.*, 1973; Chen and Tilton, 1976), evidence of extinct short-lived isotope ^{26}Al (Lee *et al.*, 1976, 1977; Wasserburg *et al.*, 1982), and of trace element abundance patterns that resemble those predicted by gas-solid partitioning (Grossman, 1973; Boynton, 1975), CAIs were initially interpreted by many workers to be samples of primary, high-temperature condensate material formed during the earliest history of the solar nebula and then aggregated. However, the igneous textures were not compatible with this model. Later studies have demonstrated that CAIs are not simply vapor-to-solid or vapor-to-liquid condensates and underscore the complexity of this diverse group of objects. Texturally, most coarse-grained CAIs appear to have experienced a molten or partially molten origin but the variety and complexity of the chemical, mineralogical and isotopic signatures of CAIs attest to multi-stage formation involving a number of processes including evaporation (Chou *et al.*, 1975; Hashimoto

et al., 1979), condensation (MacPherson and Grossman, 1984; Allen *et al.*, 1978), melting (MacPherson and Grossman, 1981; Stolper, 1982; Stolper and Paque, 1986), and metamorphism (Meeker *et al.*, 1983; Clayton *et al.*, 1977; Armstrong *et al.*, 1984). Refractory inclusions are often treated as distinct from normal chondrules but observations of anorthite-rich Type C CAIs (Grossman, 1975; Wark, 1987; Beckett and Grossman, 1988) and forsterite-rich CAIs (Wark *et al.*, 1987), which are significantly less refractory than melilite-rich Type A CAIs and fassaite-rich Type B CAIs, and of ferromagnesian chondrules enriched in refractory lithophile trace elements (Misawa and Nakamura, 1987; Rubin and Wasson, 1988), and of Ca- and Al- rich objects that appear transitional between CAIs and ferromagnesian chondrules observed in carbonaceous (Sheng *et al.*, 1991a), ordinary (Nagahara and Kushiro, 1982; Bischoff and Keil, 1983), and enstatite (Bischoff *et al.*, 1985) chondrites, suggest the existence of precursor materials common to all these objects. It is plausible to consider the possibility that these are a wide variety of chondrules with distinctive chemical compositions, but are enriched to varying degrees in "refractory elements", and which are genetically related. CAIs are widely believed to preserve a record of conditions and processes that prevailed early in the solar nebula. The possibility that remnants of this record are also contained in less refractory objects is a central theme of my thesis. The identification of the major processes leading to the formation, not only of the relatively rare CAIs, but also of objects with much closer affinities to normal chondrules should provide important information on early nebular and planetary processes, environments, and the time scale over which the processes operated.

1.2. Thesis Approach and Scope

This thesis attempts to address the following problems: 1) The identification of remnants of early solar system records in less refractory objects; 2) The nature of multistage reprocessing as a major factor in preserving/destroying the differences in isotopic composition of early solar system material; 3) Thermal conditions and time scale of the reprocessing events.

The methods used to address these problems are as follows: 1) Identification of inclusions that appear to be intermediate in mineralogy and chemistry between CAIs and ferromagnesian chondrules. This was done by means of optical and scanning electron microscopy to establish textures and general mineralogy; 2) Characterization of the bulk chemistry, mineral chemistry and isotopic chemistry of the inclusions and their constituent phases. The analytical techniques include electron microscope energy dispersive (EDS) and wavelength dispersive (WDS) microanalysis and ion microprobe analysis. In the course of the analysis, it was found that a large number of these intermediate objects are heterogeneous in Mg isotopes, despite the fact that they possess igneous characteristics; 3) Experimental study of the phase equilibria and phase relations on compositions similar to those of the different inclusions; 4) Experimental study on Mg self diffusion in spinel and coexisting silicate melt to provide constraints on the thermal history of these objects; 5) Integration of the analyses and experimental results to provide a firm database, to propose a model on the origin of these inclusions, and also to provide tools to test the validity of the proposed model.

The thesis is a study of a distinct group of objects in carbonaceous chondrites that

consist of plagioclase, olivine, enstatite, clinopyroxene and spinel in various proportions and cover a wide range of bulk compositions intermediate between those of ferromagnesian chondrules and CAIs. They are much lower in Fe than ferromagnesian chondrules but substantially higher in Fe than CAIs. These inclusions differ from normal chondrules and CAIs in that they contain abundant plagioclase and olivine but no melilite. I have identified them in three CV chondrites (Allende, Leoville and Vigarano) and one ungrouped chondrite (Adelaide). These inclusions are not rare. I refer to these objects as **Plagioclase-Olivine Inclusions (POIs)**. Rare mineral phases, some of which have not been reported in CAIs, or in meteorites in general, were also found in this group of inclusions. The variation in POI mineralogy is reflected in their bulk chemistries which range from Ca-Al-rich objects similar to Type C CAIs, to more Mg-, Si-rich objects grading into CA chondrules (Christophe Michel-Lévy, 1968; McSween, 1977; Bischoff and Keil, 1984) and Mg-rich porphyritic chondrules.

Since the textures of POIs indicate an igneous origin, I have attempted to characterize the crystallization behavior through experimental studies and phase equilibria analysis. Integration of my experimental results with available phase equilibrium data from the literature provides a framework for the interpretation of mineral assemblages observed in POIs and other objects with similar bulk compositions.

A prominent feature of POIs, which distinguishes them from most coarse-grained CAIs and chondrules, is the Mg isotope heterogeneity both between coexisting spinel and silicates and among spinels. While isotopic fractionation of Mg and Si have been noted in coarse-grained CAIs (Wasserburg *et al.*, 1977; Esat *et al.*, 1978; Clayton *et al.*, 1984; MacPherson *et al.*, 1988; Brigham, 1990), they are typically homogeneous within

individual inclusions (with the exception of oxygen). The first occurrence of Mg isotope heterogeneity between spinel and silicates in a CAI was recently reported by Goswami *et al.* (1991) and Srinivasan *et al.* (1991). The common occurrence of isotopically heterogeneous phases within individual inclusions which cannot be explained by differential reaction with a nebular gas is a distinct feature of POIs. An important part of my study on these inclusions is centered on these observations. The preservation of isotopic heterogeneity indicates that the thermal event which partially melted the precursor and produced an igneous texture either had too low a temperature or was too brief to allow complete Mg isotope homogenization.

Chapter 2 provides the analytical and experimental methods used in this study. The instrumentation and analytical conditions for operation of the PANURGE ion microprobe for isotopic and REE analysis is briefly summarized. Chemical analysis of bulk inclusions and their constituent phases were performed by energy dispersive and wavelength dispersive X-ray analysis. The characteristics of electron microprobe and scanning electron microscope used in this study and data reduction methods are also documented. The procedures used for the high temperature experiments and the preparation of starting compositions used for the phase equilibria studies and diffusion experiments are described.

In Chapter 3, a comprehensive description of the petrographic, mineralogic and chemical features of POIs is presented. Analysis of the bulk compositions, mineral chemistry of major phases as well as rare phases that have not been reported previously in carbonaceous chondrites are given. Differences and similarities of POIs with other objects described in carbonaceous and ordinary chondrites is also discussed.

Chapter 4 provides ion microprobe analyses of Mg isotopes and REE analyses on various phases in POIs. An important aspect of the data is the heterogeneity of Mg isotopes among different phases within individual POI. This feature provided the motivation for experimental studies designed to place constraints on the thermal history of POIs.

Chapter 5 presents phase equilibria studies on synthetic mixtures that are similar to the bulk compositions of POIs. The results of this study integrated with literature data provided the database for construction of phase diagrams used to interpret the crystallization sequences and equilibrium phase assemblages to be expected from such bulk compositions.

The temperature history required to prevent homogenization of Mg isotopes in POIs is related to the diffusion rate of Mg in spinel. In order to establish this critical rate, experiments were designed to extract the self-diffusion coefficients of Mg in spinel and melt using an isotope tracer method. In Chapter 5, the techniques of Mg-self diffusion experiments is described in detail. The maximum melting temperature, limitations on the duration at which POIs could have been subjected to this maximum temperature, and the initial cooling rate can be deduced from the experimental and observational results.

In Chapter 7, petrographical observations and analytical data on POIs, results from phase equilibria study and Mg diffusion experiments are integrated to provide the basis for proposing a model for the origin of POIs. The proposed model is demonstrated to be consistent with the petrographical features of POIs and are tested by the constraints required by phase equilibria and diffusion studies.

In conclusion, a testable model on the origin of POIs and possibly for many other similar objects is presented. A comparison of the essential characteristics of POIs and CAIs suggest that the major processes leading to the formation of POIs are common to most CAIs and chondrules, and were repeated over a several million year period in the early solar system. The papers and extended abstracts published during the evolution of this thesis are compiled in the appendix.

CHAPTER TWO

ANALYTICAL TECHNIQUES AND EXPERIMENTAL METHODS

This chapter provides a description of the analytical techniques used to identify and characterize POIs. The preparation of starting materials, the experimental setup and general procedures for studies of phase equilibria and tracer diffusion are described.

2.1. PETROGRAPHIC ANALYSIS

Petrographic observations were first made on doubly polished thin sections using an optical microscope. Samples were selected based on their mineralogy. The basic criterion for the original selection of samples was the presence of abundant plagioclase and olivine in the inclusion. It was found that Mg-spinel was often associated with these objects. None of them were found to contain melilite. Careful observations on the mineralogical and textural features and an estimate of the modal abundance were made on each selected inclusion. The criteria were later extended to be simply the presence of plagioclase and olivine.

The thin sections were then carbon-coated for observation under the scanning electron microscope (SEM). Mosaic maps from backscattered electron images were constructed for most of the inclusions.

Plagioclase and olivine-bearing inclusions were identified by petrographic observations on doubly polished thin sections on an optical microscope. The 21 inclusions studied were from 16 thin sections of Allende and one each from the Adelaide, Leoville and Vigarano carbonaceous chondrites. Modal abundances of major phases in each inclusion were estimated from point counting on an enlarged mosaic of backscattered electron images of each inclusion. Phases that were not identified from optical microscopy due to their small sizes were analyzed with an energy dispersive spectrometer on an SEM and identified from their chemical compositions.

2.2. ELECTRON MICROSCOPE ANALYSIS

Quantitative analysis of major and minor elements of each mineral phase including variation of mineral chemistry within individual grains was performed. Chemical analysis in the scanning electron microscope (SEM) and electron microprobe was performed by measuring the energy and intensity distribution of the x-ray signals generated by a focused electron beam. In this study, quantitative analysis of major and minor elements was performed with a Tracor TN 5500 energy dispersive x-ray analyzer (EDS) on a JEOL JSM-35 CF SEM using the Bence-Albee (Bence and Albee, 1968) procedures for data correction and on the JEOL 733 electron microprobe using the ZAF correction (Love and Scott, 1978) as modified by Armstrong (1984). The instrumentation and correction procedures for x-ray microanalysis have been well documented (cf., Goldstein *et al.*, 1981; Scott and Love, 1983). Quantitative analysis

of the mineral phases in the POIs and of the phases produced in experimental studies are described in the following sections.

2.2.1. Wavelength-dispersive Spectrometer

In a wavelength-dispersive spectrometer (WDS), a small portion of the x-ray signal generated from the specimen passes out of the electron optical chamber and impinges on an analyzing crystal. If Bragg's law is satisfied, the x-rays will be diffracted and detected by a proportional counter. X-rays having a wavelength which does not satisfy the Bragg equation are absorbed by the crystal or pass through it into the crystal holder. The signal from the detector is amplified and converted to a standard pulse size by a single-channel analyzer and counted with a scaler (see Goldstein *et al.*, 1981).

The JEOL JXA-733 electron microprobe used in this study is a high performance x-ray microanalyzer capable of handling up to five spectrometers, and also functioning as a high resolution scanning electron microscope. It can be computer-controlled, providing high speed precision analysis under automatic operation.

2.3.2. Energy Dispersive Spectrometer

The energy-dispersive spectrometer (EDS) system is currently the most common x-ray measurement system to be found in a scanning electron microscope (SEM). The

EDS system offers rapid qualitative and accurate quantitative measurement of the elemental constituents of a sample. These advantages are, however, tempered by the relatively poor energy resolution of the EDS (150 eV at Mn $K\alpha$ compared with 5-10 eV for a wavelength spectrometer) (Goldstein *et al.*, 1981) which leads to frequent unresolved spectral interferences, poor peak-to-background values, resulting in poor detection limit (typically ~ 0.5 wt.% compared to ~ 0.1 wt.% for a wavelength spectrometer).

In an energy-dispersive x-ray spectrometer (EDS), the x-ray signal passes through a thin beryllium window into a cooled, reverse-biased lithium-drifted silicon detector. Absorption of each individual x-ray photon leads to the ejection of a photoelectron which gives up most of its energy to the formation of electron-hole pairs. They in turn are swept away by the applied bias to form a charge pulse which is then converted to a voltage pulse by a charge-sensitive preamplifier. The signal is further amplified and shaped by a main amplifier and finally passed to a multichannel analyzer, where the pulses are sorted by voltage. The signals are then transmitted to a computer for further processing including peak identification and quantification (see Goldstein *et al.*, 1981).

2.2.3. Quantitative Analysis

Quantitative x-ray microanalysis is based on determining the x-ray flux emitted by a sample region relative to that of a suitable standard. Data correction procedures can then be applied to reduce the measured intensity ratio to composition. X-ray data are

corrected for a variety of second-order "matrix" effects. Matrix effects have been traditionally grouped as the atomic number effect (Z), the absorption effect (A), and the fluorescence effect (F). The "ZAF" factors compensate for matrix differences between standards and unknowns. The most easily obtainable standards are those of pure elements. However, input parameters for correction, such as mass absorption coefficients and fluorescent yield values, are sometimes only poorly known. For these reasons, intermediate compositional standards are often used. These compound standards were checked for homogeneity and for stoichiometry. These standards may then be used for analysis of mineral specimens of similar composition. The standards used in my analyses include simple and complex oxides and silicates. They are periclase, corundum, quartz, rutile, Cr_2O_3 , V_2O_5 , ZrO_2 , spinel, wollastonite, kyanite, anorthite, albite, microcline, forsterite, fayalite, Mn olivine, Ni olivine, garnet, grossular, and pyrope. Before each analytical run, the instrument was tuned and checked to assure that: (1) the spectrometer system was properly calibrated, (2) the operating conditions are adequate to give sufficient x-ray counts so that a given peak can be easily distinguished from the corresponding background level, and (3) for each phase, no serious peak overlaps are present. The intensity of spectral lines corresponding to preselected elements for both samples and standards were measured under identical operating conditions. Secondary standards of similar composition as the sample were routinely analyzed as a check on the accuracy of measured results and for systematic errors. Analysis were performed at 15 keV. Beam currents of 15 to 50 nanoamps were used in WDS analysis on the electron probe compared to 60 to 75 picoamps used in EDS analysis on the SEM. The precision

in the quantitative analysis is determined by the counting statistics. An acquisition time can be chosen such that the desired precision is achieved. In all my analyses, acquisition time was set to achieve $\pm 2\%$ precision or better for major elements and $\pm 5\%$ for minor and trace elements.

a) Analysis of individual phases

Individual phases in POIs and experimental products were analyzed by EDS and WDS analysis. At least two grains of each constituent phase in each inclusion were analyzed. In the analysis of experimental products, a total of at least 5 analyses were made on each starting glass compositions and on each resulting phase. These analyses were used to check the homogeneity of each phase and the mean composition of each phase. Analysis of chemical variation within a phase was made by measuring along a traverse across the phase either by manually moving the stage, or by using an automated stepping stage.

b) Analysis of bulk inclusions

Bulk compositions of the inclusions were obtained by averaging the EDS analyses made by rastering the electron beam over several regions of each inclusion. The regions are selected so that they either cover most area of the inclusion in the thin section or that they would reasonably represent the whole area of the inclusion. Rastering was done

under 200 to 500 times magnification. Accuracy of bulk compositions of POIs obtained from EDS rastering analyses was checked by electron probe analyses on two POIs. Five hundred points evenly distributed on ten profiles were analyzed on each inclusion. Each analyzed point includes a five second count on each of the major oxides. The results are shown in Table 2.1. The two independent EDS rastering analyses of inclusion 3510 are in good agreement with each other and the WDS point analysis results. Larger deviation between the two types of analysis are observed for inclusion BG82DH2. Possible reasons for the difference are that the distribution of the profiles in the inclusion for WDS point analysis were not adequate to represent the relative proportion of the phases in the inclusion, or that the rastered area in the EDS analysis was not representative of the whole inclusion. Assuming that the cross section in the thin section approximates the volume composition of the POI, the compositions of the POI obtained from the rastering method are used to provide an estimate of the actual bulk compositions.

Table 2.1
Comparison of EDS and WDS analysis of POI Bulk Composition

	Na ₂ O	MgO	Al ₂ O ₃	SiO ₂	CaO	TiO ₂	Cr ₂ O ₃	MnO	FeO
BG82DH2									
WDS	2.14	14.02	27.69	39.91	12.07	0.77	0.25	0.03	2.73
EDS	1.49	14.92	30.91	38.08	11.25	0.67	0.34	0	1.71
3510									
WDS	2.03	12.36	29.55	41.63	12.29	0.55	0.17	0.02	1.13
EDS	1.90	11.87	29.96	41.63	12.30	0.46	0.12	0.05	1.18
EDS	2.01	11.52	29.64	41.55	12.36	0.39	0.27	0.05	1.46

2.3. ION MICROPROBE ANALYSIS

The technique of mass selective secondary ion microscopy was introduced in the sixties and seventies (Castaing and Slodzian, 1960, 1962; Liebl and Herzog, 1963; Slodzian, 1964; Liebl, 1967; Andersen and Hinthorne, 1972). The development of this technique allowed measurements of trace elements and isotopic ratios on a small spatial scale. Reviews of ion microprobe applications to geochemistry have been given by Shimizu and Hart (1982), Williams (1985) and Zinner (1989).

In Secondary Ion Mass Spectrometry (SIMS), a beam of energetic ions erodes away the surface of the specimen under study and the secondary ions produced during the sputtering process are mass analyzed. The focussing of the bombarding ions into a fine beam allows the in situ chemical and isotopic analysis of individual mineral phases of a few microns size. The main advantages of the technique are:

1. High sensitivity (detection limit can be as low as 1 ppb) for many elements (e.g., Mg, Al, Ca, Ti).
2. Small sample size (meaningful analyses can be obtained from $< 10^{-12}$ g of sample).
3. Measurements of elements that are difficult to analyze by other techniques.

The problems inherent in this technique that need to be dealt with in specific analyses are:

1. The production of molecular secondary ions along with atomic ions during sputtering. These molecular species may interfere with the atomic ions of

interest.

2. The ionization efficiency of different elements varies by many orders of magnitude.

3. The ionization efficiency of a given element depends strongly on the chemical composition of the sample from which the element is sputtered (matrix effect).

In this study, isotopic and chemical compositions were measured using PANURGE, a modified CAMECA IMS-3F ion microprobe (Huneke et al., 1983).

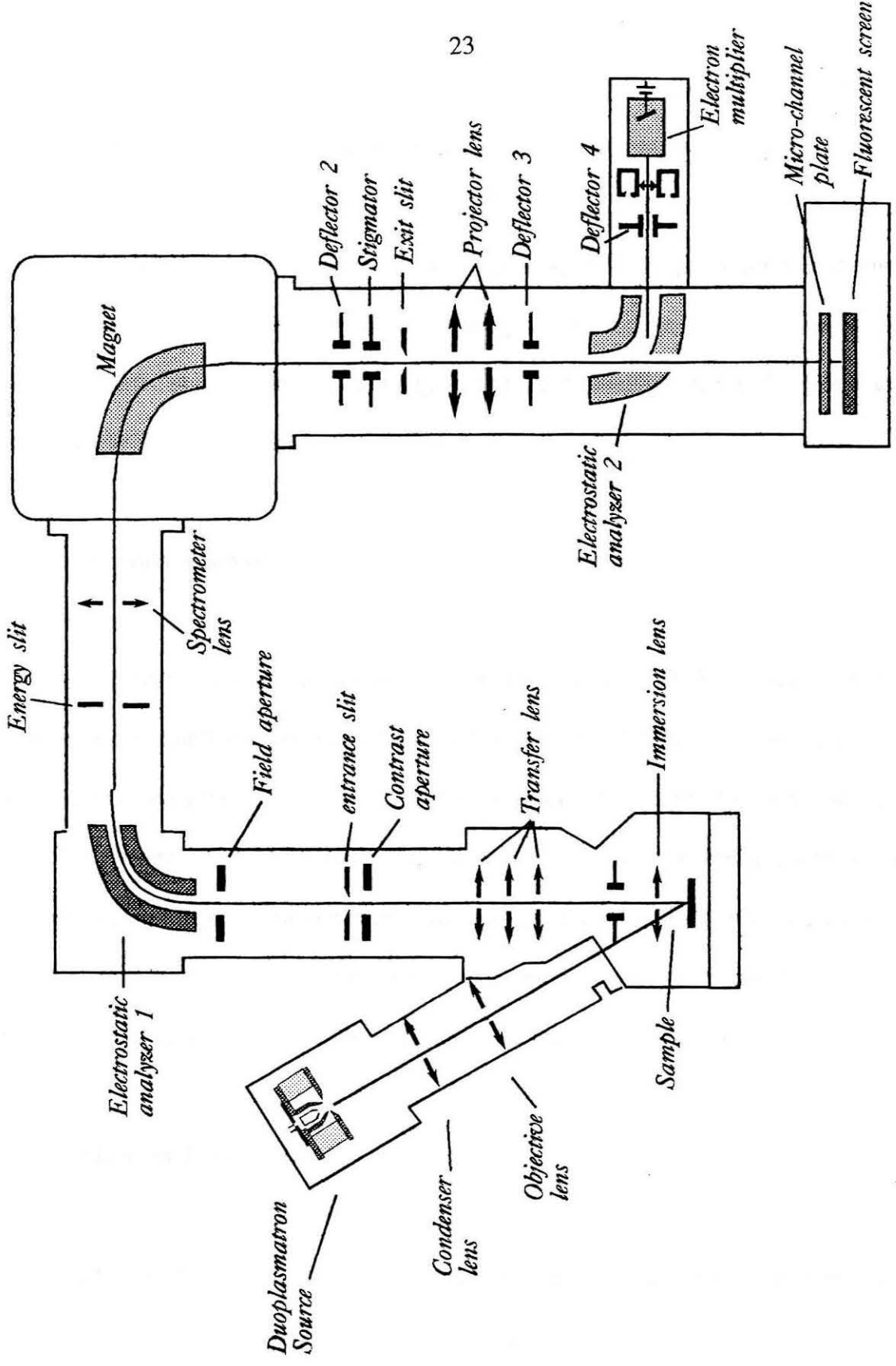
2.3.1. Instrumentation

The main elements of a SIMS apparatus are: primary ion source; primary optics comprising ion extraction and acceleration; sample stage; secondary optics consisting of secondary ion acceleration, energy selector and mass spectrometer; detector; and associated electronics. The following is a brief discussion of the instrumentation used in this work. The components of the ion microprobe referred to in the discussion is schematically shown in Figure 2.1.

a. Primary ion source and primary optics

The PANURGE uses a duoplasmatron ion source capable of producing beams of oxygen or argon ions. Negative oxygen ions are used for the analysis of positive secondary ions because oxygen enhances the yield of positive secondary ions. The

Fig.2.1 Schematic drawing of the PANURGE ion microprobe.



duoplasmatron can generate O^- and O_2^+ ions by switching the polarity of the anode. In this work negative beam was selected because it minimizes sample charging.

The primary O^- beam is accelerated to 12.5 KV and focussed by three electrostatic lenses. Scattered ions are eliminated by controlling the voltage on condenser lens to adjust the primary current density passing through a limiting aperture. The beam is then focussed by the objective lens. Beam alignment is controlled by three X-Y deflectors and a stigmator.

b. Secondary ion optics

Secondary ions are accelerated through a voltage of 4500 V and focussed by an immersion lens and a set of three transfer lens (25 μm , 150 μm , and 400 μm image fields) onto the entrance slit of the mass spectrometer. The plane of the entrance slit is an image plane of the crossover and contains a series of contrast apertures and interchangeable field apertures which allows ions sputtered only from the central 8, 60 or 150 μm diameter to enter the mass spectrometer. Small offsets (a few volts) are applied to the accelerating voltage to compensate for sample charging.

c. Mass analyzer

Mass analysis of the secondary ions is performed with a magnetic sector field. An electrostatic analyzer precedes the actual mass analyzer because the initial energy

distribution of the secondary ions is too broad to allow adequate mass resolution. The energy dispersion of the energy analyzer is matched to cancel that of the magnetic field. This combination forms a double-focussing mass spectrometer.

The magnet separates the ions according to the mass to charge ratio. The mass resolving power is defined as $m/\Delta m$, where Δm is the width of peak at 10% of maximum intensity. This resolution is determined by the widths of the entrance and exit slits of the mass spectrometer and can be adjusted between 400 and 10000. A resolution of about 3000 is typically used in this work for Mg isotope analysis, whereas the slits are fully opened for REE analysis which results in a mass resolving power of 400-500. The magnet is operated in an automated peak jumping mode, by cycling through a preselected series of magnetic field settings corresponding to the centers of the peaks of interest in order of increasing mass. These settings can be located reliably as long as the magnetic field is cycled through the same sequence of values and the peaks are centered periodically.

d. Detection system

Mass-analyzed secondary ions are deflected by an electrostatic analyzer to an electron multiplier. The electron multiplier is operated in a pulse-counting mode at a gain of $\sim 10^7$ electrons/ion and a voltage of 3000 V. The determination of the counting system dead time is achieved by isotopic measurements of a Ti metal standard.

2.3.2. Analytical Conditions

The secondary ion spectrum includes not only monatomic species but also molecular ions consisting of more than one atom and multiple charged ions. Common molecular species include hydrocarbons, oxides and hydrides. Any combination of matrix elements may also be found in the mass spectrum. Two approaches have been taken to eliminate molecular interferences: high mass resolution and energy filtering. The PANURGE ion microscope is capable of a mass resolution of 10,000. This resolution is sufficient to resolve oxides, dimers and hydrides from atomic ions for atomic masses below about 75 atomic mass units. In this work, high mass resolution ($m/dm \sim 3000$) has been used for isotopic analysis of Mg, which is sufficient to resolve all molecular interferences in the region of interest, such as Mg hydrides (Hutcheon, 1982).

Energy filtering takes the advantage of the feature that the kinetic energy distribution of secondary ions shows a maximum at a few electron volts and thereafter decreases monotonically with increasing energy. The rate of decrease is greater for molecular than for monatomic ions and falls off even more sharply for molecules of increasing complexity. Therefore, it is possible to discriminate in favor of the monatomic ions, especially against molecules consisting of several atoms. The disadvantages of this technique are the substantial loss of signal and the ineffectiveness to suppress hydrides and monoxides of heavy elements. Because of its limitation, energy filtering has been mainly applied to the analysis of rare earth elements. In this work, this

method has been used for the analysis of REE concentration in individual mineral phases of the POIs.

a. Mg isotope analysis

The PANURGE ion microprobe was used to analyze the Mg isotopic composition of various phases in POIs. The Mg isotopic compositions were determined under conditions described by Huneke *et al.* (1983) and Hutcheon *et al.* (1987). The samples to be analyzed were either carbon or gold coated. The primary ion beam was tuned to produce a beam diameter of $\sim 5 \mu\text{m}$. Prior to the analysis, high resolution scans were obtained to check the instrument tuning, and to check that the mass resolution were sufficient to exclude interferences.

Isotopic data were collected by step scanning the spectrometer magnet through mass ranges 24 to 27 for spinel, olivine, and pyroxene, and 24 to 44 for plagioclase, using a computer controlled peak switching system. The secondary ion current was measured at the peak center, and at the half intensity position on the low and high mass sides of each peak with each scan to monitor shift in the magnetic field. The magnet control program will compensate for any drift in the magnetic field during analysis. Isotope ratios were calculated after each scan from the secondary ion intensities integrated over the center of each peak. In samples with low Mg concentrations (plagioclase), 80-160 scans were averaged in a typical analysis, while in samples with high Mg content 60 scans were averaged. $^{27}\text{Al}^+$ was also measured for Mg-rich phases,

while $^{40}\text{Ca}^{++}$ and $^{44}\text{Ca}^+$ were measured for Mg-poor plagioclase in order to determine Al/Mg ratios. Count rates for $^{24}\text{Mg}^+$ ranged from 4×10^5 counts per second for Mg-rich phases such as spinel, pyroxene, and olivine, to 8×10^3 counts per second for plagioclase. Typical operating parameters of the ion microprobe are shown in Table 2.2.

The measured isotopic fractionation of an element has been demonstrated to depend upon substrate mineralogy and chemical composition (Slodzian, 1980; Hutcheon, 1982; Huneke *et al.*, 1983). For example, ion probe instrumental fractionation for Mg (ΔMg : see definition below) typically ranges from -2‰ to -16‰ for silicate and oxide phases. To minimize matrix effects, terrestrial samples of similar compositions to the phases in the inclusions were chosen as standards. They include plagioclase (An_{96}), spinel, Ti-pyroxene glass, aluminous enstatite and forsteritic olivine (Fo_{90}). Since a major objective of this study was the measurement of intrinsic Mg fractionation, standards were run daily prior to and after sample analysis to monitor shifts in the $^{25}\text{Mg}/^{24}\text{Mg}$ ratio due to different tuning conditions in the instrument.

Table 2.2 Ion Microprobe Operating Conditions

PRIMARY SYSTEM	SECONDARY SYSTEM
<u>Duoplasmatron</u> Species: O ⁻ Arc: 59 mA <u>Accelerating voltage</u> : 12.5 kV <u>Maximum Current</u> : 600 nA <u>Lens Voltage (dial settings)</u> L1: 270 L2: 360 L3: 425 <u>Beam current</u> : 2 nA <u>Beam diameter</u> : 5-10 μm <u>Vacuum system</u> Sample chamber: 2×10 ⁻⁸ torr Primary column: 3×10 ⁻⁷ torr	<u>Polarity</u> : + <u>Accelerating voltage</u> : 4500 V <u>Electron multiplier voltage</u> : 2950 V <u>Image field</u> : 150 μm <u>Contrast aperture</u> : 300 μm <u>Field aperture</u> : 60 μm <u>Lens voltage</u> [*] Transfer lens: 6507 Spectrometer lens: 4536 Immersion lens: 4704 Projector lens 1: 6925 Projector lens 2: 5157

* Only numbers proportional to voltage. The actual voltage is <4500 V.

Isotopic fractionation of Mg intrinsic to a POI was determined from the difference in the ²⁵Mg/²⁴Mg ratio of the sample relative to the ratio in a standard of appropriate mineralogy: $F_{Mg} = \Delta^{25}Mg - \Delta_{std}^{25}Mg$, where $\Delta^{25}Mg$ expresses the deviation in permil of the ²⁵Mg/²⁴Mg ratio relative to 0.12663 (Catanzaro *et al.*, 1966). The precision of F_{Mg} value is limited by the counting statistics of individual analysis, for both sample and standard. Typical errors in F_{Mg} , based on the reproducibility of analysis of standards, are ±1 ‰ for olivine, spinel and pyroxene, and ±2 ‰ for plagioclase. To search for evidence of radiogenic ²⁶Mg*, the Mg isotopic data were also corrected for fractionation by normalizing to ²⁵Mg/²⁴Mg = 0.12663 using a power law, and the corrected ratios

$(^{26}\text{Mg}/^{24}\text{Mg})_c$ used to calculate $\delta^{26}\text{Mg}$, expressed as:

$$\delta^{26}\text{Mg} = \left[\frac{(^{26}\text{Mg}/^{24}\text{Mg})_c}{0.13955} - 1 \right] \times 1000$$

This represents the permil deviation from the normal reference value, $^{26}\text{Mg}/^{24}\text{Mg} = 0.13955$ (Brigham, 1990) and is used to identify non-linear isotopic shifts in ^{26}Mg abundance. This value was obtained from the mean isotopic composition, measured with the PANURGE ion probe, from standards of Mg-rich phases (normalized to $^{25}\text{Mg}/^{24}\text{Mg} = 0.12663$) over a period six months. This normal value differs from the value 0.139805 obtained for standards by thermal ionization (Schramm *et al.*, 1970; Lee and Papanastassiou, 1974). This discrepancy between values used for normalization for the two techniques is not well understood.

b. Rare earth elements analysis

Rare earth elements (REE) were measured using energy filtering technique, (Shimizu *et al.*, 1978; Zinner and Crozaz, 1986), analytical conditions using the PANURGE is described by Kennedy *et al.* (1991). In collecting REE data, the sample voltage was offset by -75 V from the voltage at which the energy distribution of ^{42}Ca , the reference mass, dropped to 10% of its maximum value on the low energy side of the peak. The width of the energy slit was set to accept ions within a 40 V window and a 400 μm contrast image aperture was used. A 750 μm field aperture was used to obtain

a 60 μm image field for all analyses. The entrance and exit slits were fully opened, resulting in a mass resolving power of 400-500. The resulting mass spectrum, measured on masses 131 to 180, was then separated into the atomic (M^+) and monoxide (MO^+) ion intensities by solving a set of simultaneous equations.

Mineral standards with compositions similar to the phases analyzed were used to calculate sensitivity factors, which are the ratio of the concentration normalized secondary ion intensity of the element in question to the concentration normalized secondary ion intensity of the reference element (Beckett *et al.*, 1990). Measurements of standards were performed at the start and end of each ion microprobe session to account for any minor variation of ionization efficiencies produced by differences in operating conditions.

2.4. EXPERIMENTAL METHOD

All crystallization experiments were conducted at 1 atmosphere total pressure in a vertical Del-Tech VT-31 quench furnace using a Eurotherm model 90 temperature controller. Experiments were conducted in the temperature range of 1200-1615°C. The furnace setup and experimental procedures are described in the following section.

2.4.1 Sample Preparation

Starting materials were prepared by weighing out appropriate amounts of CaCO_3 , MgO , Al_2O_3 , SiO_2 , TiO_2 and Na_2CO_3 (all Johnson Matthey Puratronic), and grinding the mixtures under ethanol within an automated agate mortar for 5 hours. The mixtures were decarbonated by gradually heating to 1000°C over 24 hours, and then melted in Pt crucibles in a Del-Tech VT-31 furnace at 1600°C in air for 12 hours to produce homogeneous glasses. The glasses were verified by WDS analysis to be homogeneous to within the precision of counting statistics. Starting materials for experiments consisted either of re-ground glasses or run products from previous experiments.

2.4.2. Furnace Setup and Temperature Calibration

The configuration of the furnace is schematically drawn in Fig.2.2. Basically,

the system consists of a mullite reaction tube set inside the furnace. Moly di-silicide heating elements are uniformly spaced in a full circle and hang vertically around the reaction tube. The furnace chamber is filled by Zircar fiber refractories contained in a steel shell. The mounted samples were attached by thin Pt wires (0.005" diameter) to thick Pt wires (0.02" diameter) which extend up through different holes of a two or four hole alumina tube (Fig.2.3). The alumina tube sample holder was placed into the reaction tube and held by a brass fitting at the top of the tube. A quench port is attached to the bottom of the reaction tube. The bottom of the quench port can be closed with a brass cover with a quartz window at the center. During quench, the cover is detached to allow the sample to fall through. Temperatures were measured with a type S Pt-Pt10Rh thermocouple located adjacent to the sample in the hot spot of the quench furnace. This allows the temperature to be measured at the same condition as the sample. The thermocouple was calibrated at the melting point of gold (1064.4°C) and palladium (1554°C).

2.4.3. Experimental Procedure

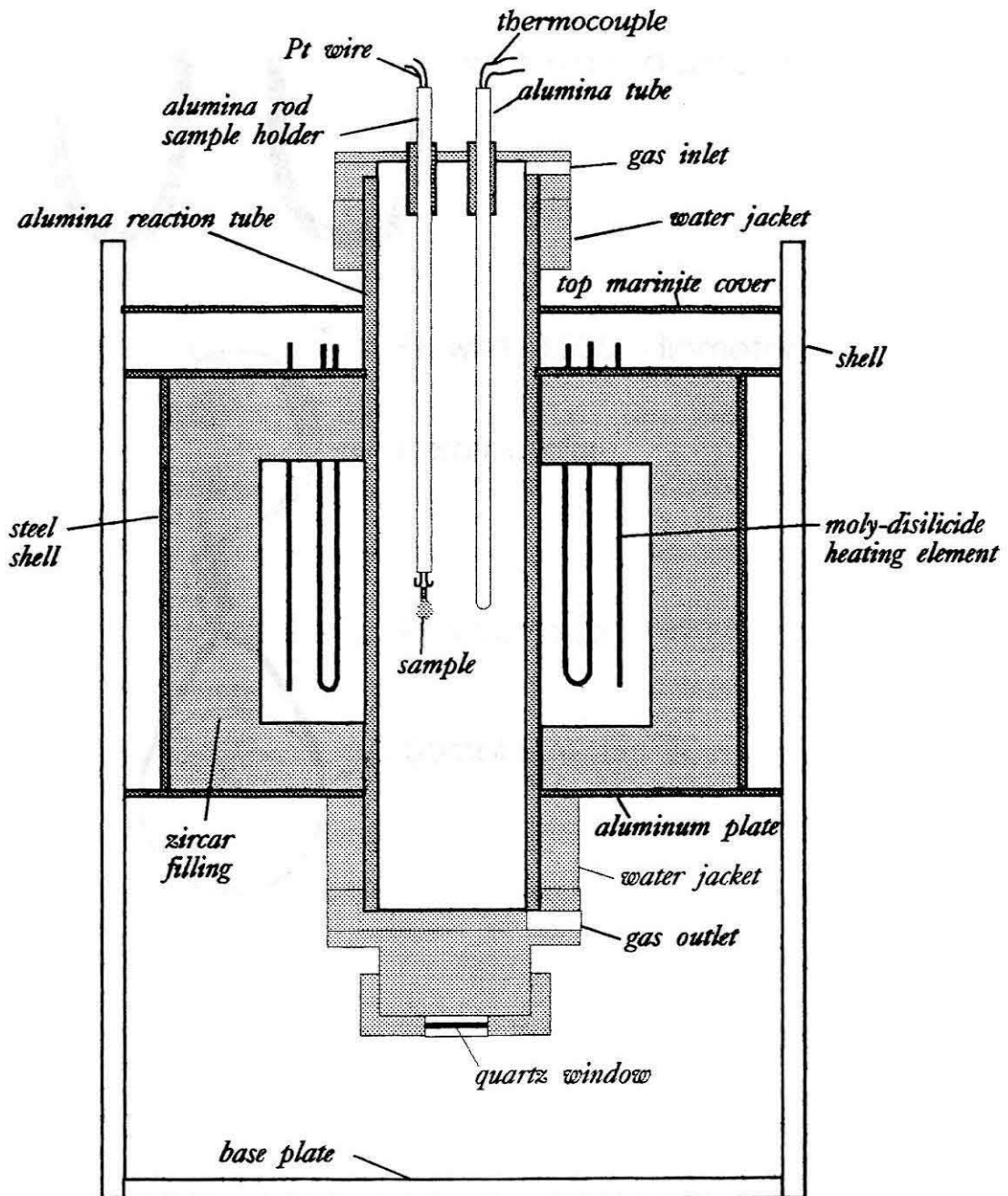
All experiments were conducted in air at 1 atmosphere total pressure in a vertical Deltech VT-31 quench furnace using Eurotherm models 990 temperature controller and 125 programmer. Experimental procedures were similar to those of Stolper (1982) and Stolper and Paque (1986). Samples were inserted into the furnace hot spot at the run temperature. For isothermal crystallization experiments, samples were held at the run

Deltech DT-31 Furnace

2000

Fig.2.2 Schematic drawing of the Deltech DT-31 vertical furnace.

Deltech DT-31 Vertical Furnace



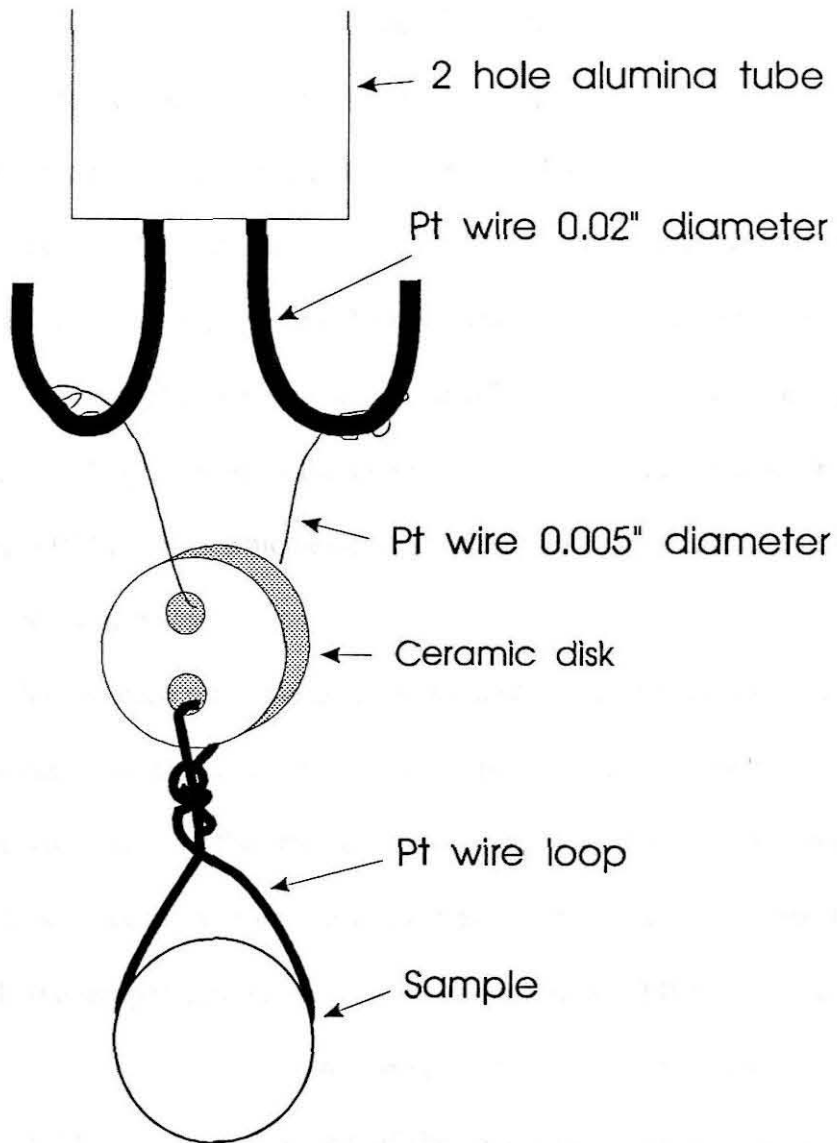


Fig. 2.3 Schematic drawing showing sample configuration.

temperature for 1-382 hrs. and then quenched into deionized water. For cooling rate experiments, samples were held at the initial temperature, T_{\max} , for 3 hrs., cooled at 20-100°/hr and then quenched from various temperatures into deionized water. All reported temperatures are believed accurate to within $\pm 5^{\circ}\text{C}$.

The sample consisted of glass (or crystalline) powder mounted within a Pt wire loop using a slurry of polyvinyl alcohol. The Pt wire containing the sample was looped through one hole of a two hole alumina disk (Fig.2.3). An additional (0.005" diameter) Pt wire was looped through the other hole and each end of the wire was attached on separate 0.02" Pt wires which extend, inside a two or four hole alumina tube, up through the top of the furnace.

Prior to each run sequence, the hot spot of the furnace was located by moving the thermocouple through a range of different positions in the reaction tube of a pre-heated furnace and reading the temperature at each position. The point of maximum temperature was marked on the outside end of the rod holding the thermocouple. In general, the temperature varied 2-3°C within a range $\pm 0.5\text{cm}$ of the hot spot.

The furnace temperature varied systematically by about 1-3 degrees over the course of 24 hours. At the end of the experiment, the sample was quenched into a beaker of water beneath the quench port by passing a current, using a variac, through the two thick Pt wires across which was suspended the thin Pt wire holding the sample. This caused the thin Pt wire holding the alumina rod and the sample to melt. The sample dropped through the furnace and the quench port into a beaker of water, cooling from the run temperature to room temperature in less than 10 seconds.

CHAPTER THREE

PETROGRAPHICAL AND CHEMICAL CHARACTERISTICS OF PLAGIOCLASE-OLIVINE INCLUSIONS

3.1 PETROGRAPHY

POIs are inclusions with igneous textures and characterized by the abundance of plagioclase and olivine in their mineral assemblages. They also contain variable amounts of spinel, fassaite, enstatite and diopside. Melilite, a major component in CAIs, is not present. Most POIs are spheroidal, ranging from 0.5 to 5 mm in diameter. The texture is most commonly sub-ophitic to intersertal with plagioclase and olivine phenocrysts in a fine-grained matrix. Textures similar to those observed in ordinary chondrules, such as barred olivine, porphyritic, radiating and granular, are also observed (see Figs.1a-e from Sheng *et al.*, 1991a in Appendix).

The occurrence of secondary phases containing Na and Fe such as nepheline, sodalite and hedenbergite is quite restricted in POIs. These phases compose less than 5% of the mode of all POIs and occur only near the rims of inclusions or along cracks and in interstitial regions within inclusions, and do not appear to be directly associated with plagioclase or the Na-rich mesostases. The unaltered appearance of plagioclase with clearly defined boundaries is in sharp contrast to the embayed and extensively veined

plagioclase and melilite frequently observed in Type B CAIs. POIs do not contain grossular or monticellite, two common secondary phases of Type B CAIs. Unlike the pervasive alteration of Type B CAIs, POIs do not appear to have been subjected to extensive post-crystallization open system alteration.

A common feature of many POIs is the presence of one or more clusters (up to 200 μm in diameter) of equigranular olivine crystals located near the periphery of inclusions (see Fig. 1f from Sheng *et al.*, 1991a in Appendix). These olivine clusters resemble granular olivine chondrules. The multi-layered rim sequences of oxides and silicates that surround most CAIs (Wark and Lovering, 1977) are not found in POIs, but sulfide-rich rims similar to those surrounding many ordinary chondrules are common. In some cases, aggregates of fine-grained olivine and pyroxene form accretionary rims on POIs, similar to those described by MacPherson *et al.* (1985).

The petrographic characteristics of POIs are summarized in Table 3.1. For simplicity of description, I have classified POIs into three groups. The trend from group 1 to group 3 is defined by the monotonic decrease in the modal abundances of spinel and plagioclase compensated by an increase in the abundance of olivine. The chemical compositions of POIs in the 3 groups change in accordance with the variations in mineralogy and are discussed in the following section.

Group 1 POIs contain abundant spinel (8-25% modal abundance) and plagioclase (20-65%). Inclusions 5ALLB6, BG82DH2 and ALA1-2 are similar in both mineral assemblage and texture. All have sub-ophitic textures with randomly oriented plagioclase laths. Subhedral to anhedral olivine and pyroxene terminate against or surround the

Table 3.1
PETROGRAPHIC FEATURES OF POI*

INCLUSION	D (mm)	TEXTURE	MAJOR PHASES (modal abundance)	MINOR PHASES [#]
Group 1				
(1) ALA1-2	1.7	sub-ophitic	pl(60),fas(15),ol(10),sp(9)	arm,ilm
(2) V477	2.1	sub-ophitic	fas(48),pl(37),sp(10)	ol
(3) 5ALLB6	2.7	sub-ophitic	pl(65),ol(20),sp(9),fas(4)	arm,ru,ilm, zir,pv
(4) BG82DH2	1.5	sub-ophitic	pl(55),ol(20),fas(15),sp(8)	arm,ru,ilm
(5) 3510	2.1	sub-ophitic	pl(60),ol(15),sp(10),en(10)	fas,sap
(6) BG82CLII	1.5	porphyritic and radiating	sp(25),pl(20),en(20),mes(20)	sap,ol
Group 2				
(7) BG82DH1A	4.0	sub-ophitic	pl(50),ol(30),fas(12),sp(10)	
(8) B14D	2.0	sub-ophitic	pl(60),ol(10),pi(15),di(5),sp(5)	
(9) LEO1009	0.6	porphyritic	pl(65),pi(25),sp(5)	ol,gl
(10) SA-1	2.3	sub-ophitic	pl(46),di(25),pi(14),sp(5),ol(6)	ne,ilm
(11) ADEL-1	0.5	sub-ophitic	pl(60),di(20),en(12),ol(5)	tr,sp
(12) BG82CH1	2.2	sub-ophitic	pl(60),en(20),di(10),ol(5)	sp
(13) BG82CLJa	1.8	porphyritic and radiating	pl(30),di(30),pi(20),mes(15)	ol,sp
(14) SA-1b	0.8	porphyritic	pl,ol,en	
(15) PPX	0.9	poikilitic	pl(40),ol(30),en(20)	sp
Group 3				
(16) A-47	2.1	barred with interstitial pl and di	ol(80),di(10),pl(8)	sp
(17) BG82CLJb	1.5	porphyritic	ol(75),pl(15),sp(5)	fas,pi
(18) BG82CLIb	1.5	granular	ol(80),di(10),pl(5)	pi
(19) BG82CLI	1.9	barred with interstitial pl and di	ol(65),pl(15),di(10),en(5)	
(20) REDEYE	4.8	porphyritic	ol(82),pl(10),di(5)	en,sp

* arm - armalcolite, di - diopside, en - enstatite, fas - fassaite, gl - glass, il - ilmenite, mes - mesostasis, ne - nepheline, ol - olivine, pi - pigeonite, pl - plagioclase, pv - perovskite, ru - rutile, sap - sapphirine, sp - spinel, tr - tridymite, zir - zirconolite

[#] minor mesostasis is present in all POI.

plagioclase. Olivines are commonly rimmed by Mg-rich pyroxene. Ti-rich fassaite is interstitial and is interpreted to be a late crystallizing phase. Spinel occurs as sub-rounded to euhedral crystals poikilitically enclosed in the other silicates. Many of the euhedral spinels appear to be included in the interstitial fassaite. Small grains (10-50 μm) of Ti-rich oxides, including armalcolite, rutile, ilmenite and perovskite, are associated with the interstitial fassaites. Several small grains of zirconolite ($\text{CaZrTi}_2\text{O}_7$) about 1 micron in diameter, associated with perovskite was observed in Allende inclusion 5ALLB6. This is only the second meteoritic occurrence of zirconolite. Zirconolite was reported by El Goresy *et al.* (1978) but was not documented.

Two other group 1 POIs, 3510 and BG82CLII, although quite different from each other in texture and modal mineralogy, both contain sapphirine ($\text{Mg}_2\text{Al}_4\text{SiO}_{10}$). 3510 consists of a coarse-grained (50-100 μm) mantle and a fine-grained (10 μm) core. Mineral phases in both rim and core are plagioclase, forsterite, spinel, and Al-enstatite. Subhedral to anhedral olivine and pyroxene terminate against euhedral plagioclase laths. Spinel is included in all three phases. BG82CLII has the least amount of plagioclase (20%) but the most abundant spinel (25%) among the group 1 POIs. Plagioclase and Al-enstatite occur as laths or prismatic crystals which radiate inward from the rim. A central zone of densely populated spinel marks a boundary between the core and the spinel-free mantle of the inclusion. In both of these inclusions sapphirine occurs as randomly oriented euhedral prisms (5x25 μm) embedded in an Na- (15% Na_2O) and Cl-rich (3%), Ca-poor (1.5% CaO) mesostasis (see Fig.2b from Sheng *et al.*, 1991a in Appendix). In 3510, sapphirine is localized in small pockets, whereas in BG82CLII it

is much more abundant and distributed in much larger regions.

Group 2 POIs contain minor spinel (<5%, with the exception of BG82DH1A) and abundant plagioclase (30-65%). Allende inclusions SA-1 and BG82DH1A have been described by Boctor *et al.* (1988; 1989) and Kennedy *et al.* (1989, 1991). These two inclusions plus BG82CH1, B14D and ADEL-1 all have sub-ophitic textures. ADEL-1 is an inclusion from the Adelaide chondrite and is the most silica-rich POI. A symplectic intergrowth of tridymite (or its polymorph) and plagioclase is found in regions interstitial to plagioclase laths in the interior of the inclusion. The few forsteritic olivines are rimmed by enstatite. A few small clusters of spinel are enclosed within plagioclase laths. These spinel grains appear to be strongly resorbed with corroded boundaries (see Fig.2a from Sheng *et al.*, 1991a in Appendix). BG82CLJa exhibits a radiating texture consisting mainly of plagioclase laths and tabular pyroxene grains. The pyroxenes are Fe-poor pigeonite surrounded by diopside. Spinel is rare, and where present, strongly resorbed. PPX contains granular olivines poikilitically enclosed in plagioclase. Ca-poor pyroxene grains are interstitial among plagioclase and spinel is rare.

Group 3 POIs have the highest abundance of olivine (>40%) with lesser plagioclase (<15%) and rare spinel. This group is characterized by porphyritic, granular and barred textures, commonly found in ferromagnesian chondrules. BG82CLJb is the only inclusion in this group that has a modest amount of spinel (5%). A cluster of spinel grains occurs in the center of the inclusion, enclosed by plagioclase. Olivine grains vary greatly in size, ranging from 10 to 200 microns in diameter. Larger grains developed near the rim of the inclusion grade into smaller grains towards the center.

Both A-47 and BG82CLI resemble barred olivine chondrules, except that plagioclase and diopside occur as anhedral grains interstitial to the olivine bars. Redeye consists of large olivine grains with interstitial plagioclase and pyroxene and is the only POI exhibiting chromium-rich ($\sim 30\%$ Cr_2O_3), rather than aluminous, spinel.

3.2 BULK CHEMISTRY

Bulk compositions of POIs are given in Table 3.2. POIs span a wide range in composition, reflected in a four-fold variation in CaO (4-17 wt. %), a three-fold variation in MgO (10-34 wt. %) and in Al_2O_3 (12-36 wt. %) and more than a ten-fold variation in Na_2O (0.6-6.8 wt. %). The most calcium- and aluminum- rich POI, ALA1-2, contains 44.8 wt. % $\text{CaO} + \text{Al}_2\text{O}_3$, whereas POI Redeye has only 6.2 wt. % $\text{CaO} + \text{Al}_2\text{O}_3$. Since Redeye is an extreme member among POIs, its composition was excluded from the preceding discussion. Corresponding to the classification outlined in the previous section, the $\text{CaO} + \text{Al}_2\text{O}_3$ content for the three POI groups are: 1) $\text{CaO} + \text{Al}_2\text{O}_3 > 40$ wt. %, 2) $20\% < \text{CaO} + \text{Al}_2\text{O}_3 < 40\%$, 3) $\text{CaO} + \text{Al}_2\text{O}_3 < 20\%$ (Fig.3.1). The difference in the $\text{CaO} + \text{Al}_2\text{O}_3$ content for the three groups is mainly a reflection of the modal abundances of spinel + plagioclase versus olivine.

The bulk chemical compositions of POIs are summarized in Fig.3.2. Representative analyses of Types B and C coarse-grained CAIs, fine-grained CAIs and CA chondrules are shown for comparison. It is evident from the data plotted in Fig.3.2 that with the exception of the olivine-rich POI Redeye, the bulk compositions of POIs

Table 3.2
POI BULK COMPOSITIONS⁺

	Na ₂ O	MgO	Al ₂ O ₃	SiO ₂	K ₂ O	CaO	TiO ₂	Cr ₂ O ₃	FeO	SUM
ALA1-2	2.9	10.0	32.0	38.4	0.1	12.8	1.5	0.3	1.5	99.5
V477	1.9	11.1	27.6	39.0	n.d.*	16.8	1.8	0.4	1.2	99.8
5ALLB6	1.4	13.7	31.6	38.1	n.d.	12.6	0.9	0.6	0.6	99.5
BG82DH2	1.5	14.9	30.9	38.1	0.1	11.3	0.7	0.3	1.7	99.5
3510	2.0	11.5	29.6	41.6	<0.1	12.4	0.4	0.3	1.5	99.3
BG82CLII	3.8	18.1	36.8	31.6	0.1	4.0	0.7	0.9	2.9	98.9
BG82DH1A	0.7	20.9	24.7	38.9	n.d.	11.4	0.1	n.d.	3.5	100.0
B14D	3.6	13.4	25.7	42.9	0.1	10.1	0.7	0.2	1.6	98.3
LEO1009	1.2	11.6	22.9	47.5	<0.1	9.3	0.9	0.6	4.8	98.8
SA-1	4.1	11.6	18.5	46.2	0.1	14.7	1.2	0.4	1.9	98.7
ADEL-1	0.9	9.6	18.4	50.7	n.d.	13.8	0.7	0.5	4.6	99.2
BG82CH1	3.6	15.0	17.3	45.8	0.2	11.0	0.7	0.5	3.5	97.6
BG82CLJa	6.8	14.3	17.3	45.5	0.2	9.6	1.3	0.5	2.4	97.9
SA-1b	5.8	19.9	18.1	43.1	0.5	5.1	0.7	0.5	5.2	98.9
PPX	2.4	24.1	15.2	43.5	0.1	5.8	0.4	0.5	6.5	98.5
A-47	1.3	33.1	13.7	42.2	n.d.	6.6	0.3	0.3	1.8	99.3
BG82CLJb	1.3	34.0	15.6	38.8	n.d.	4.3	0.3	0.6	4.1	99.0
BG82CLIB	1.2	28.5	12.6	43.5	n.d.	6.2	0.2	0.4	5.2	97.8
BG82CLI	2.0	31.6	12.4	40.9	0.1	5.9	0.4	0.3	4.8	98.4
REDEYE	1.0	44.6	3.9	41.7	0.1	2.3	0.1	0.4	5.6	99.7

⁺ EDS analysis by raster scan of the POI in the thin section.

* n.d. - not detected

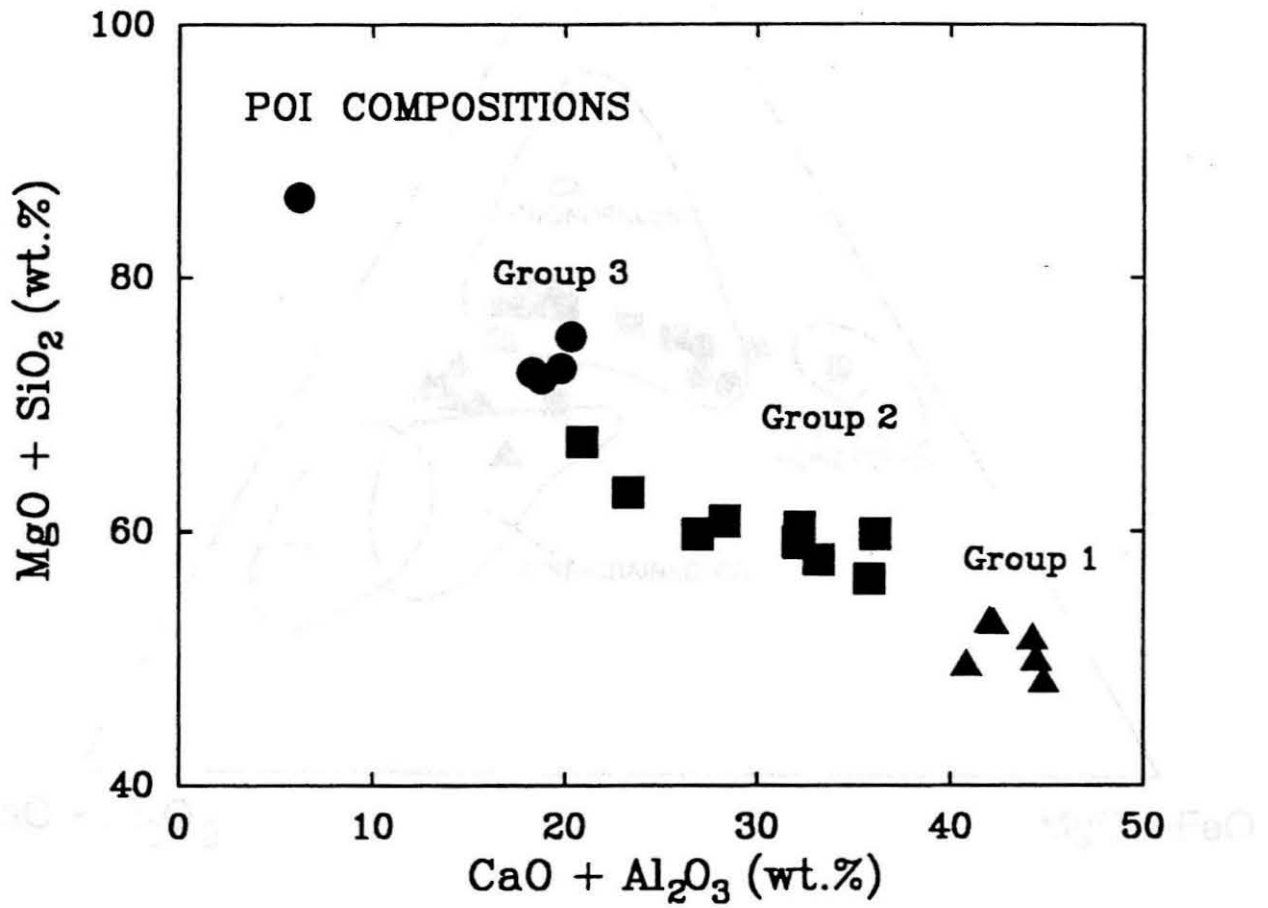


Fig.3.1 Difference in the amount of CaO+Al₂O₃ versus MgO+SiO₂ among the three groups of POIs.

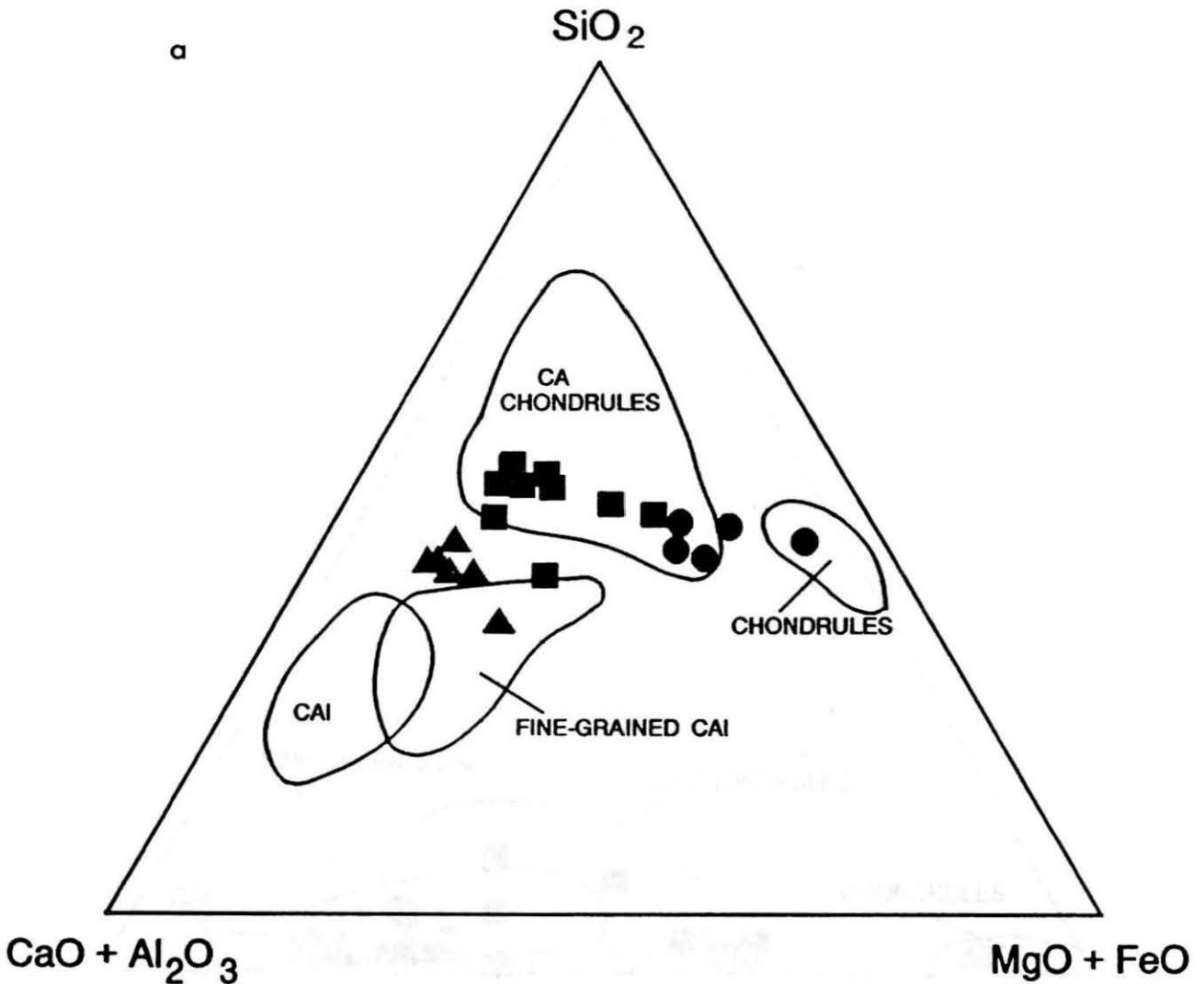
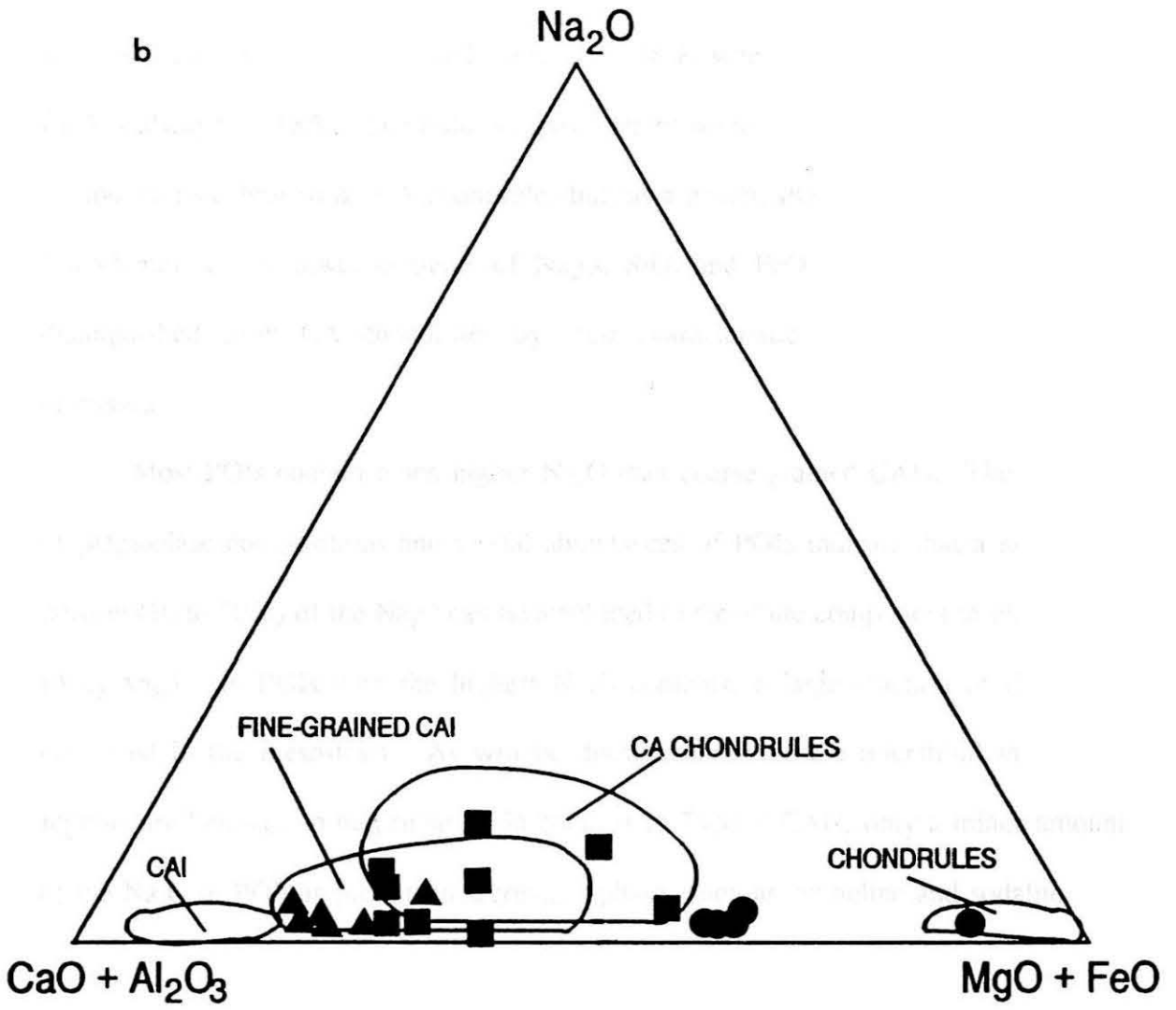


Fig.3.2 Bulk compositions of POIs (filled circles) compared with the compositional range of CAIs, fine-grained CAIs, ferromagnesian chondrules and CA chondrules. Filled triangles are group 1 POIs, squares are group 2 and circles are group 3 POIs. POIs have lower CaO and Al₂O₃ content than CAI but higher SiO₂ (a) and Na₂O (b). Their compositions overlap with fine-grained CAIs and CA chondrules. Their compositional differences with CAIs and ferromagnesian chondrules are obvious. Sources of data are: CAIs from Mason and Martin (1977) and McSween (1977); CA chondrules from Bischoff and Keil (1984); Fine-grained CAIs from Brigham et al. (1990) and Mason and Martin (1977); Ferromagnesian chondrules from McSween (1977).



are quite distinct from those of Types B and C CAIs and ferromagnesian chondrules. Relative to coarse-grained CAIs, the POIs are enriched in Na, Mg and Si and depleted in Al and Ca. All POIs have CaO contents < 18%, whereas in Types B and C CAIs, CaO is always > 18%. The bulk compositions of some POIs fall within the range of compositions exhibited by CA chondrules but, as a group, POIs are distinguished from CA chondrules by lower contents of Na₂O, SiO₂ and FeO. POIs are also readily distinguished from CA chondrules by their characteristic mineralogy, as will be discussed.

Most POIs contain much higher Na₂O than coarse-grained CAIs. The analyses of plagioclase compositions and modal abundances of POIs indicate that a significant portion (10 to 50%) of the Na₂O can be attributed to the albite component in plagioclase (An₈₂-An₉₈). In POIs with the highest Na₂O contents, a large fraction of the Na is contained in the mesostasis. As will be discussed later, these interstitial mesostasis regions are believed to be primary. In contrast to Type B CAIs, only a minor amount of the Na₂O in POIs is present in secondary phases such as nepheline and sodalite.

3.3 MINERAL CHEMISTRY

3.3.1 Plagioclase

Plagioclase compositions (Table 3.3) in POIs range from An₈₂ to An₉₈. Plagioclase contains small amounts of MgO (0.25-0.92 wt. %) and FeO (0-0.4 wt. %) but

TABLE 3.3
PLAGIOCLASE COMPOSITIONS

wt. % sample	Na ₂ O	MgO	Al ₂ O ₃	SiO ₂	CaO	FeO	SUM	An mole %	number of analyses
ALA1-2	0.61	0.65	36.78	43.18	19.02	0.08	100.00	96	3
5ALLB6*	0.26	0.25	35.95	43.34	19.43	0.11	99.35	97	12
BG82DH2*	0.50	0.44	35.43	44.08	19.14	0.12	99.72	95	15
3510*	0.54	0.39	35.85	44.64	19.15	0.10	100.67	95	8
BG82CLII	1.16	0.29	33.51	46.22	18.52	0.31	100.00	91	12
BG82DH1A	0.55	0.64	35.34	43.96	18.94	0.57	100.01	94	3
B14D	1.25	0.55	34.00	46.03	17.80	0.36	99.99	88	7
LEO1009	2.08	0.28	32.28	47.35	16.61	1.17	99.77	82	2
SA-1	0.94	0.54	34.48	45.24	18.49	0.33	100.00	92	3
ADEL-1	1.28	0.83	32.43	46.96	17.95	0.55	100.01	85	3
BG82CH1	1.70	0.79	32.47	46.92	17.13	0.50	99.50	85	3
BG82CLJa	1.23	0.64	33.89	45.68	18.11	0.42	99.97	89	13
SA-1b	1.47	0.36	34.04	46.10	17.63	0.40	100.00	87	2
PPX	0.29	0.33	35.88	43.42	19.39	0.10	101.41	97	2
A-47	0.87	0.56	35.02	45.03	18.33	0.19	100.00	91	2
BG82CLJb	1.56	0.35	33.51	46.00	17.82	0.71	100.00	87	2
BG82CLIb	1.18	0.50	33.40	46.05	18.61	0.27	100.01	91	3
BG82CLI	0.98	0.46	34.57	45.13	18.53	0.33	100.00	92	2
REDEYE*	1.25	0.35	33.25	45.95	18.40	0.35	99.55	92	2

* WDS analysis. All others EDS analysis.

no K_2O . Both Na_2O and MgO contents of plagioclase in POIs are higher than typically found in plagioclase in Type B CAIs, but the positive linear correlation between Mg and Na contents in plagioclase (see Fig.5 from Sheng *et al.*, 1991a in Appendix) is similar to that found in some Type B CAIs (Hutcheon *et al.*, 1978). No correlation between Fe and either Mg or Na in POI plagioclase was observed. Within each POI plagioclase compositions are nearly constant with only a subtle increase of ≤ 1 wt% Na_2O . Alteration of plagioclase crystals by low-temperature phases such as sodalite and nepheline is not observed except near cracks and near the rims of inclusions.

3.3.2 Olivine

Olivine compositions are highly variable among the different POIs, but are generally forsteritic, ranging from Fo_{63} to Fo_{99} (Table 3.4). Individual grains in the interior of POIs are only slightly zoned with rims that are marginally higher in iron content. The difference in FeO content between center and rim occasionally reaches 5 wt.% but is generally less than 1%. The more iron-rich olivines (Fo_{63} to Fo_{85}) are consistently found in olivine clusters embayed near the exterior margin of many POIs. These spherical clusters of equigranular grains are very similar in appearance and composition to granular olivine chondrules. In contrast to interior olivines, the cluster olivines are strongly zoned in FeO with more Fe-rich rims. The difference in FeO content between center and rim of individual grains typically exceeds 5%. Other than their high FeO content, there is no significant difference in their chemistry and Mg

TABLE 3.4
OLIVINE COMPOSITIONS

SAMPLE	MgO	Al ₂ O ₃	SiO ₂	CaO	TiO ₂	V ₂ O ₃	Cr ₂ O ₃	MnO	FeO	NiO	SUM	no. anal
ALA1-2	52.98	1.69	41.77	0.62	1.14	0.23	0.00	0.00	1.57	0.00	100.00	2
5ALLB6*	55.76	0.09	42.30	0.34	0.13		0.15	0.20	1.69	0.02	100.50	23
5ALLB6*c	51.95	0.04	41.20	0.30	0.04		0.06	0.12	7.54	0.02	101.27	8
BG82DH2	54.06	0.22	42.12	0.30	0.23	0.03	0.11	0.07	2.42	0.06	99.62	8
3510*	56.09	0.14	42.04	0.12	0.16		0.18	0.04	0.87	0.01	99.66	13
3510*c	50.90	0.03	41.27	0.18	0.06		0.06	0.06	8.11	0.08	100.75	4
BG82CLIIc	49.40	0.43	40.62	0.20	0.11	0.02	0.12	0.06	8.56	0.01	99.51	13
BG82DH1A	55.20	0.00	42.10	0.50	0.16	0.00	0.29	0.00	1.75	0.00	100.00	2
B14D*	54.84	0.04	41.67	0.17	0.13		0.05	0.08	3.35	0.02	100.35	17
B14D*c	47.25	0.07	39.54	0.13	0.08		0.04	0.12	14.24	0.06	101.53	8
SA-1	47.47	2.27	38.98	0.17	0.09	0.08	0.26		10.69		100.01	3
ADEL-1	51.91	0.21	43.63	0.35	0.04	0.00	0.60		3.27		100.00	6
BG82CH1	52.77	0.00	42.36	0.25	0.00	0.11	0.09	0.12	4.19	0.11	100.00	2
BG82CH1c	54.77	0.00	43.29	0.38	0.13	0.00	0.20	0.07	1.17	0.00	100.00	2
BG82CLJa	46.36	0.13	40.23	0.27	0.06	0.00	0.07	0.10	12.79		100.00	5
SA-1b	52.60	0.23	41.16	0.22	0.00	0.00	0.00	0.00	5.65	0.00	99.86	2
PPX	42.37	0.81	38.94	0.49	0.00	0.00	0.00		17.39		99.99	2
A-47	55.00	1.33	42.51	0.43	0.00	0.25	0.11	0.00	0.36	0.00	99.99	2
BG82CLJb	54.12	0.25	42.20	0.46	0.04	0.02	0.04	0.03	2.64	0.02	99.79	17
BG82CLIb	51.62	0.00	41.07	0.27	0.09	0.00	0.15	0.00	6.80	0.00	100.00	2
BG82CLI*	54.69	0.08	42.17	0.17	0.06	0.00	0.06	0.15	3.78	0.03	101.20	2
REDEYE*	52.08	0.47	41.35	0.38			0.48		4.38		99.00	4
Atom Proportions (normalized to four oxygens)												
	Mg	Al	Si	Ca	Ti	V	Cr	Mn	Fe	Ni	CAT	
ALA1-2	1.864	0.047	0.986	0.016	0.020	0.004	0.000	0.000	0.031	0.000	2.968	
5ALLB6*	1.953	0.002	0.994	0.008	0.002		0.003	0.004	0.033	0.000	3.001	
5ALLB6*c	1.857	0.001	0.988	0.008	0.001		0.001	0.002	0.151	0.000	3.010	
BG82DH2	1.917	0.006	1.002	0.008	0.004	0.001	0.002	0.001	0.048	0.001	2.990	
3510*	1.976	0.004	0.993	0.003	0.003		0.003	0.001	0.017	0.000	3.000	
3510*c	1.832	0.001	0.996	0.005	0.001		0.001	0.001	0.164	0.002	3.002	
BG82CLIIc	1.803	0.012	0.994	0.005	0.002	0.000	0.002	0.001	0.175	0.000	2.996	
BG82DH1A	1.947	0.000	0.996	0.013	0.003	0.000	0.005	0.000	0.035	0.000	2.998	
B14D*	1.941	0.001	0.989	0.004	0.002		0.001	0.002	0.066	0.000	3.007	
B14D*c	1.739	0.002	0.976	0.003	0.001		0.001	0.003	0.294	0.001	3.021	
SA-1	1.743	0.066	0.960	0.004	0.002	0.002	0.005		0.220		3.002	
ADEL-1	1.833	0.006	1.033	0.009	0.001	0.000	0.011		0.065		2.957	
BG82CH1	1.878	0.000	1.011	0.006	0.000	0.002	0.002	0.002	0.084	0.002	2.987	
BG82CH1c	1.920	0.000	1.018	0.010	0.002	0.000	0.004	0.001	0.023	0.000	2.978	
BG82CLJa	1.716	0.004	0.999	0.007	0.001	0.000	0.001	0.002	0.266		2.997	
SA-1b	1.888	0.007	0.991	0.006	0.000	0.000	0.000	0.000	0.114	0.000	3.006	
PPX	1.604	0.024	0.989	0.013	0.000	0.000	0.000		0.369		2.999	
A-47	1.923	0.037	0.997	0.011	0.000	0.005	0.002	0.000	0.007	0.000	2.981	
BG82CLJb	1.917	0.007	1.002	0.012	0.001	0.000	0.001	0.001	0.053	0.000	2.993	
BG82CLIb	1.861	0.000	0.993	0.007	0.002	0.000	0.003	0.000	0.138	0.000	3.004	
BG82CLI*	1.922	0.002	0.994	0.004	0.001	0.000	0.001	0.003	0.075	0.001	3.003	
REDEYE*	1.873	0.013	0.998	0.010			0.009		0.088	0.000	2.991	

*WDS analysis. All others EDS analysis. c- cluster olivine.

isotopic composition with respect to the olivine grains in the interior of the POIs.

3.3.3 Spinel

Spinel in POIs are magnesium-rich, generally containing less than 5% FeO (Fig.3.3). Iron contents of spinels within an individual POI can be variable and individual spinel grains are also zoned in FeO. In most cases the center of the grain contains less than 2% FeO. Within individual spinel the variation of FeO content from core to rim is generally less than 2%, but in rare cases such as in POI BG82CLII the difference can be as high as 5%. In contrast to spinels in CAIs, which commonly contain less than 0.2 wt. % Cr_2O_3 (Wark, 1983), the spinels in POIs have higher Cr_2O_3 contents, generally over 1% and as high as 5%. Spinel in 5ALLB6 have the widest range of Cr_2O_3 content, ranging from 0.2 to 10%. A distinguishing characteristic of spinel in POI 5ALLB6 is the presence of a 1-2 μm wide Cr-rich ($\text{Cr}_2\text{O}_3 > 5\%$) mantles or overgrowth on Cr-poor ($\text{Cr}_2\text{O}_3 < 0.5\%$) cores. A gradation of Cr_2O_3 content between core and mantle is observed. The low-Cr cores usually have a corroded appearance, whereas the Cr-rich mantles assume euhedral to subhedral forms (see Fig.2c from Sheng *et al.*, 1991a in Appendix). Spinel in the unique POI REDEYE contains 20~30 wt. % Cr_2O_3 . The Cr_2O_3 content of all spinels in POIs is unrelated to the amount of FeO. Spinel analyses are given in Table 3.5 and representative analyses are shown in Fig.3.3.

3.3.4 Pyroxene

TABLE 3.5
SPINEL COMPOSITIONS

	MgO	Al ₂ O ₃	SiO ₂	CaO	TiO ₂	V ₂ O ₃	Cr ₂ O ₃	FeO	SUM	no. of anal.
5ALLB6*	27.40	64.12	0.00	0.08	1.70	0.56	3.88	1.01	98.72	8
BG82DH2	24.25	66.84	0.66	0.21	0.73	0.42	1.37	4.90	99.38	4
3510	25.98	66.63	0.19	0.12	1.72	0.16	2.80	2.40	100.00	2
BG82CLII	24.31	68.27	0.45	0.11	0.29	0.07	1.73	4.61	99.83	6
BG82DH1A	24.53	68.66	0.32	0.16	0.33	0.15	1.06	4.78	100.00	3
B14D	16.59	63.44	1.90	0.57	0.35	0.21	1.92	15.01	99.99	2
LEO1009	26.53	70.80	0.34	0.11	0.54	0.00	0.00	1.68	100.00	2
ADEL-1	26.84	70.77	0.42	0.16	0.33	0.32	0.60	0.57	100.01	6
REDEYE	18.00	38.85			0.52	0.60	31.30	11.05	100.02	2
Atom Proportions (normalized to four oxygens)										
	Mg	Al	Si	Ca	Ti	V	Cr	Fe	Sum	
5ALLB6	1.003	1.855	0.000	0.002	0.031	0.011	0.075	0.021	2.998	
BG82DH2	0.886	1.931	0.016	0.005	0.013	0.008	0.027	0.100	2.988	
3510	0.938	1.902	0.005	0.003	0.031	0.003	0.054	0.049	2.985	
BG82CLII	0.882	1.958	0.011	0.003	0.005	0.001	0.033	0.094	2.987	
BG82DH1A	0.888	1.965	0.008	0.004	0.006	0.003	0.020	0.097	2.992	
B14D	0.630	1.906	0.048	0.016	0.007	0.004	0.039	0.320	2.970	
LEO1009	0.943	1.990	0.008	0.003	0.010	0.000	0.000	0.034	2.987	
ADEL-1	0.952	1.983	0.010	0.004	0.006	0.006	0.011	0.011	2.984	
REDEYE	0.749	1.277	0.000	0.000	0.011	0.013	0.690	0.258	2.999	

* WDS analysis. All others EDS analysis.

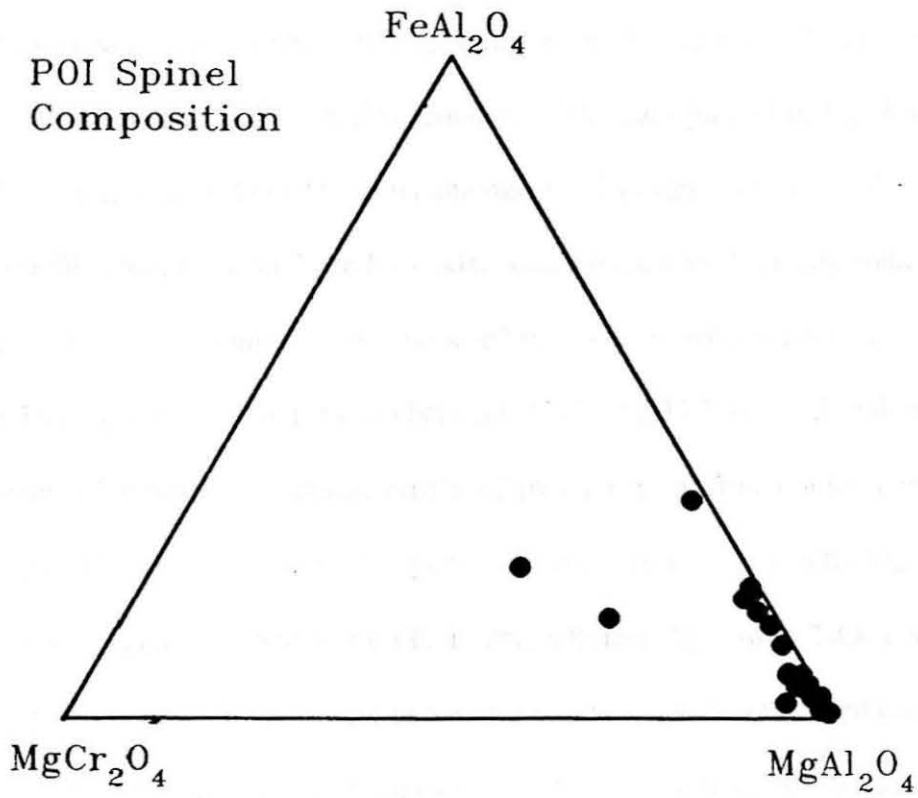


Fig.3.3 Projection of representative POI spinel compositions. Other oxide components were subtracted from spinel composition.

POIs contain a variety of different pyroxenes, including Al-, Ti-bearing fassaite, diopside, Al-rich enstatite and Fe-poor pigeonite (Table 3.6). Several different pyroxenes may occur in individual POI, especially in group 2 and 3 POIs. For example, in BG82CLJa, B14D and ADEL-1 either enstatite or pigeonite is mantled by diopside. Fassaite is a major phase in 4 of the 6 group 1 POIs but is uncommon in groups 2 and 3 POIs. Most fassaites are zoned with respect to Ti and Al and typically exhibit a linear relationship between the Al_2O_3 and TiO_2 contents. The data plotted in Fig.3.4 reveal a bimodal distribution of $\text{Al}_2\text{O}_3/\text{TiO}_2$ ratios among POI fassaites that clearly distinguishes fassaites in POIs from those in Type B1 CAIs. One population, typically found in POIs containing Ti-rich oxide minerals, is composed of fassaites with roughly equal weight Al_2O_3 and TiO_2 contents. This 1:1 ratio between Al_2O_3 and TiO_2 is not found in fassaites in other types of CAIs but is characteristic of pyroxenes in armalcolite-bearing lunar rocks (Sung et al., 1974). A second population, generally found in POIs together with Al-rich enstatite, pigeonite and diopside, is characterized by lower TiO_2 content and much higher $\text{Al}_2\text{O}_3/\text{TiO}_2$ ratios. These pyroxenes plot near the join between diopside and enstatite in Fig.3.5, many of the compositions lie within a field where no terrestrial pyroxene compositions exist. The more Al-rich fassaites of this population have compositions that fall within the range of fassaite compositions in Type B2 and C CAIs (Wark, 1987). Fassaites in POIs are also distinguished from those in Type B2 and C CAIs by their high MnO content, which is typically between 0.1 and 0.4% but may be as high as 1.0%. Fassaitic pyroxenes with similar MnO content have been found in Al-rich chondrules (Bischoff *et al.*, 1989).

TABLE 3.6
PYROXENE COMPOSITIONS

Wt.% Sample	MgO	Al ₂ O ₃	SiO ₂	CaO	TiO ₂	Cr ₂ O ₃	MnO	FeO	SUM	number of analysis
ALAI-2	17.22	7.11	47.47	20.40	6.77	0.47		0.50	99.94	3
5ALLB6	14.89	9.38	43.01	21.40	9.47	0.89	0.10	0.54	99.67	5
BG82DH2	30.72	3.06	54.25	6.41	2.58	0.87	0.21	1.15	99.26	5
BG82DH2	16.06	7.21	46.81	20.18	8.08	0.77	0.05	0.60	99.78	9
3510	34.38	8.07	53.16	0.62	2.81	0.56	0.03	0.36	99.99	4
BG82CLII	33.65	9.87	53.59	0.61	1.51	0.84	0	0.68	99.88	8
BG82DH1A	14.27	10.93	44.04	22.54	7.03	0.53		0.59	99.93	2
B14D	20.23	3.70	51.56	17.50	4.28	1.20	0.20	0.74	99.42	3
B14D	31.74	5.75	53.99	4.57	1.49	0.70	0.08	0.94	99.26	2
SA-1	18.65	5.57	51.28	21.09	2.30	0.66		0.21	99.77	3
ADEL-1*	36.52	1.16	58.11	2.07	0.28	0.57	0.10	0.78	99.58	3
BG82CH1	19.51	5.31	50.70	16.92	3.73	2.79	0	1.05	100	3
BG82CLJa	24.52	4.09	53.12	13.97	2.17	0.93	0.21	0.74	99.66	9
BG82CLJa	33.09	3.44	55.62	4.47	0.98	0.72	0.17	1.00	99.48	7
PPX	35.64	6.04	54.90	0.98	0.64	0.90	0	0.71	99.81	2
A-47	22.29	4.80	53.03	16.45	2.04	0.80	0	0.59	100	2
BG82CLJb	20.53	3.71	52.61	17.97	3.42	1.12	0	0.65	100	2
BG82CLib	38.13	1.19	58.15	0.63	0.16	0.49		1.25	100	3
BG82CLib	23.13	1.31	55.52	18.43	0.61	0.70	0	0.30	100	2
REDEYE	18.70	3.80	52.90	20.80	1.30	0.20		2.80	98.50	2
Atom Proportions (normalized to six oxygens)										
	Mg	Al	Si	Ca	Ti	Cr	Mn	Fe	CAT	
ALAI-2	0.927	0.303	1.714	0.789	0.184	0.014		0.015	3.945	
5ALLB6	0.814	0.406	1.577	0.841	0.261	0.026	0.003	0.017	3.945	
BG82DH2	1.592	0.125	1.886	0.239	0.067	0.024	0.006	0.033	3.972	
BG82DH2	0.868	0.308	1.696	0.784	0.220	0.022	0.002	0.018	3.918	
3510	1.73	0.321	1.795	0.022	0.071	0.015	0	0.010	3.966	
BG82CLII	1.679	0.389	1.793	0.022	0.038	0.022	0	0.019	3.963	
BG82DH1A	0.776	0.47	1.606	0.881	0.193	0.015		0.018	3.959	
B14D	1.082	0.156	1.850	0.673	0.116	0.034	0.006	0.022	3.939	
B14D	1.629	0.233	1.859	0.169	0.039	0.019	0.002	0.027	3.977	
SA-1	0.998	0.236	1.840	0.811	0.062	0.019	0	0.006	3.971	
ADEL-1*	1.848	0.046	1.973	0.075	0.007	0.015	0.003	0.022	3.989	
BG82CH1	1.040	0.224	1.813	0.648	0.100	0.079	0	0.032	3.935	
BG82CLJa	1.289	0.170	1.873	0.528	0.058	0.026	0.006	0.022	3.971	
BG82CLJa	1.694	0.139	1.910	0.164	0.025	0.020	0.005	0.029	3.986	
PPX	1.798	0.241	1.858	0.036	0.016	0.024	0	0.020	3.993	
A-47	1.173	0.200	1.873	0.622	0.054	0.022	0	0.017	3.962	
BG82CLJb	1.089	0.156	1.872	0.685	0.092	0.032	0	0.019	3.943	
BG82CLib	1.918	0.048	1.962	0.023	0.004	0.013		0.035	4.003	
BG82CLib	1.220	0.055	1.964	0.699	0.016	0.020	0	0.009	3.982	
REDEYE	1.000	0.161	1.898	0.800	0.035	0.006		0.084	3.984	

*WDS analysis. All others EDS analysis.

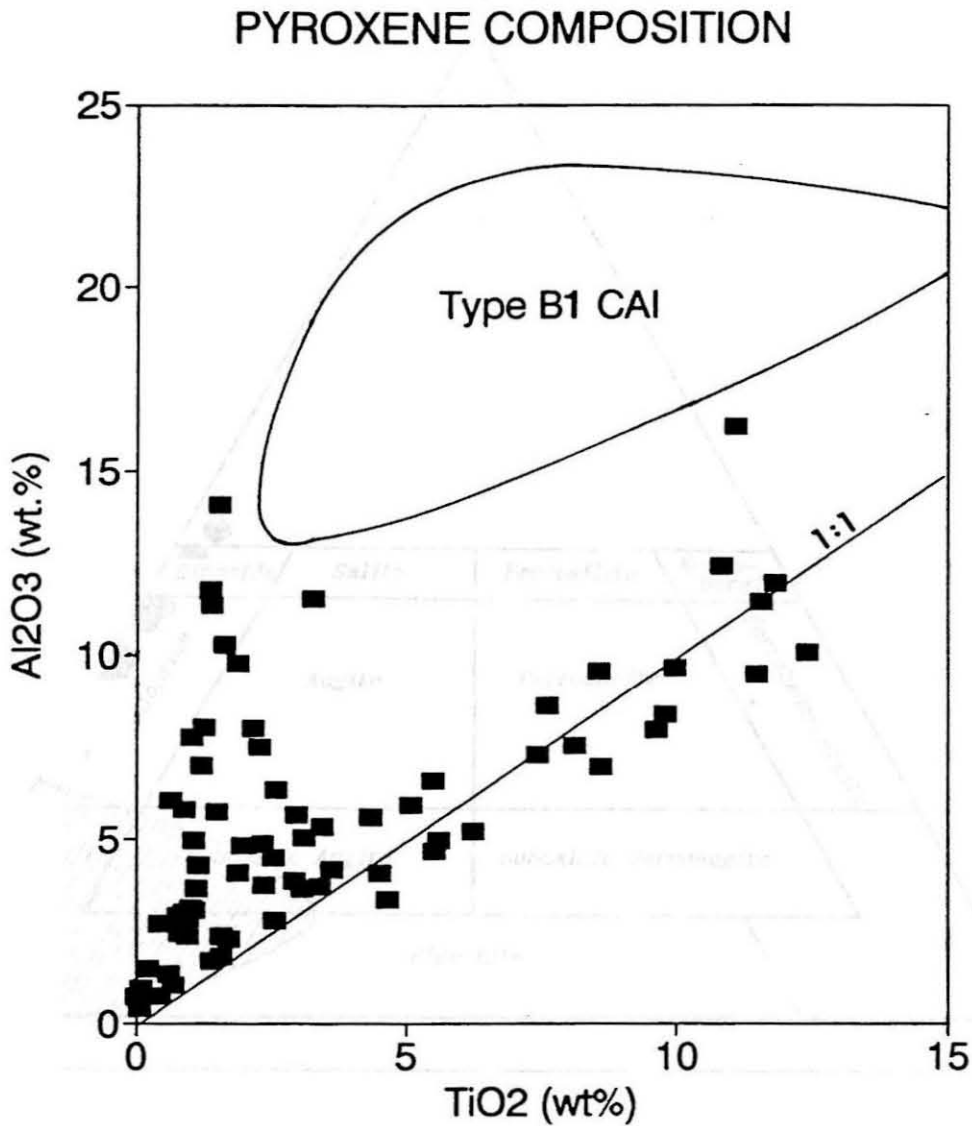


Fig.3.4 Plot of Al_2O_3 versus TiO_2 in POI pyroxenes. Ti-rich pyroxenes plot along the $\text{Al}_2\text{O}_3:\text{TiO}_2 = 1:1$ line. A second group show high $\text{Al}_2\text{O}_3/\text{TiO}_2$ ratios. They are characteristic of the Ti-poor pyroxenes in POIs. A comparison with fassaites of Type B1 CAI (Wark, 1987) is shown.

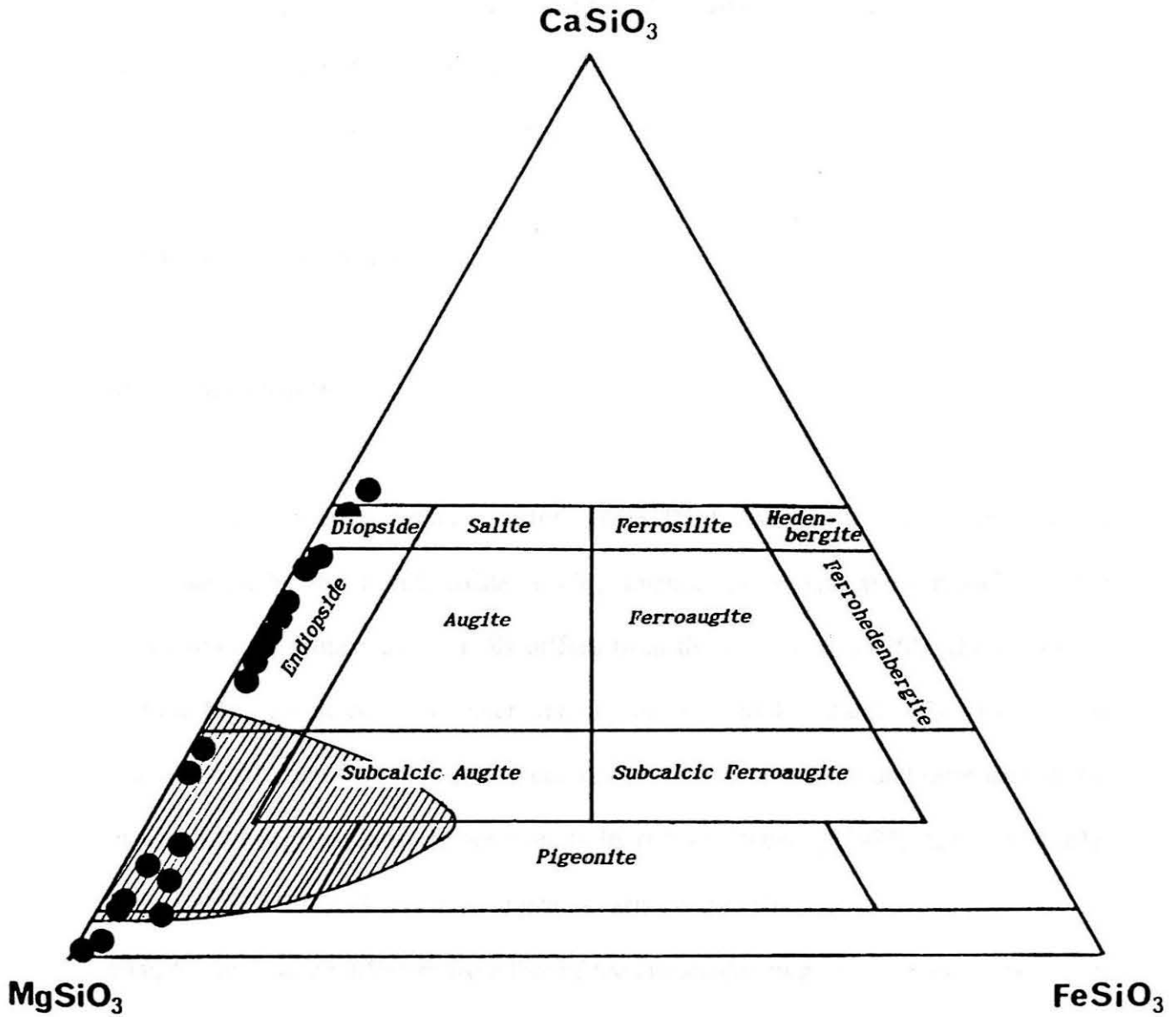


Fig.3.5 Projected composition of the Ti-poor pyroxenes in POIs. These compositions lie along the join between enstatite and diopside. Some plot in a region (hatched region) where no terrestrial pyroxene compositions were found. Ti and Al contents in these pyroxene were subtracted as $\text{CaTiAl}_2\text{O}_6$ component.

Calculations of Ti^{3+} versus Ti^{4+} in Ti-rich fassaites, made by assuming pyroxene stoichiometry, suggest that 60-80% of the total Ti is trivalent, similar to fassaites in Type B CAI. Such ratios suggest that POIs formed in a reducing environment similar to that inferred for CAI (Stolper, 1982; Beckett, 1986).

3.3.5 Accessory Phases

a) Armalcolite

Three group 1 POIs (5A11B6, BG82DH2, ALA1-2) contain armalcolite, accompanied by the Ti-rich oxides rutile, ilmenite, perovskite and zirconolite. The composition of armalcolite in POIs differs from the ideal formula ($Mg_{0.5}Fe_{0.5}Ti_2O_5$) in that the Mg/Fe ratio is much higher, ranging from 1.2 to 4.3 (Table 3.7). This ratio is also much different from that characteristic of armalcolite in lunar and terrestrial rocks, in which the Mg/Fe ratios ranges from 0.36 to 0.49 (Haggerty, 1973; Pedersen (1981). One group 2 POI (SA-1) also contains armalcolite (Boctor *et al.*, 1989) but its composition is quite different from that of the armalcolite in group 1 POIs. Whereas an ilmenite rim surrounding armalcolite is commonly observed in lunar basalts (El Goresy, 1976), no rims are found on the armalcolite in POIs. Armalcolite in 5ALLB6 exhibits submicron lamella of armalcolite, rutile and ilmenite (see Fig.2d from Sheng *et al.*, 1991a in Appendix), indicating the breakdown of armalcolite by the reaction

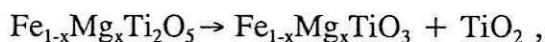


Table 3.7
ARMALCOLITE COMPOSITIONS*

Oxide wt. %	5ALLB6 ⁺ (10)	BG82DH2 ⁺ (5)	ALA1-2 ⁺ (3)	Lunar [#]	Disko [§]
MgO	10.68	16.99	13.75	6.93	8.40
CaO	0.98	2.41	0.69	0.32	0.10
MnO	n.a.	n.a.	n.a.	0.16	0.55
FeO	6.80	6.37	2.49	15.08	13.50
Al ₂ O ₃	1.21	1.57	3.78	1.61	1.25
V ₂ O ₃	1.41	0.60	0.96	n.a.	n.a.
Cr ₂ O ₃	3.68	0.83	0.26	2.44	0.22
SiO ₂	0.51	1.10	1.40	0.32	0.10
TiO ₂	74.23	70.25	76.67	74.82	75.20
ZrO ₂	0.30	n.a.	n.a.	<0.05	0.11
SUM	99.00	100.12	99.60	101.73	99.43
Number of cations normalized to 5 oxygens					
Mg	0.553	0.870	0.685	0.363	0.446
Ca	0.036	0.089	0.025	0.012	0.004
Mn				0.041	0.019
Fe	0.198	0.183	0.070	0.407	0.401
Al	0.050	0.064	0.149	0.067	0.053
V	0.039	0.017	0.026		
Cr	0.101	0.023	0.007	0.068	0.006
Si	0.018	0.038	0.047	0.011	0.004
Ti	1.941	1.815	1.927	1.976	2.017
Zr	0.005			0.001	0.002
SUM	2.941	3.099	2.936	2.946	2.952

* Average WDS analyses (number of analyses)

Data from: [#] Haggerty (1973); [§] Pedersen (1981); ⁺ This study.

where x is between 0 and 1. This reaction is rarely observed in lunar and terrestrial samples and may provide information on the low temperature subsolidus history of POIs.

b) Zirconolite

Zirconolite ($\text{CaZrTi}_2\text{O}_7$) occurs as micron-size, irregularly shaped blobs surrounding a small, $3\ \mu\text{m}$ perovskite crystal in an interstitial region between plagioclase and olivine in POI 5ALLB6. WDS analyses of the zirconolite total only to about 90 wt. % (7.57% CaO, 2.11% MgO, 0.27% FeO, 1.81% Al_2O_3 , 0.23% Cr_2O_3 , 29.27% ZrO_2 , 40.53% TiO_2 , 2.45% SiO_2 , and including 5.59% Y_2O_3 and 1.07% CeO). Although other REE were not analyzed, I have identified the presence of Nd, Gd, Dy, Er and Yb using a long counting time with the EDS. If the abundances of these elements are similar to those in lunar zirconolites (Haggerty, 1973; Meyer and Boctor, 1974), these REE would comprise the missing components in the electron probe analysis. The major differences in composition between terrestrial, lunar and POI zirconolites appear to be in their Ca and Fe contents. Terrestrial zirconolites show high CaO (>10%) and FeO (5%) (Lorand and Cottin, 1987), lunar zirconolites show high FeO (10%) and low CaO (<3%), whereas zirconolite in the POI has moderate CaO (7.5%) and very low FeO (0.3%). The low FeO in the Allende zirconolite appears to be related to the very low concentration of Fe in the inclusion.

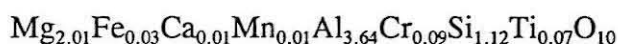
c) Sapphirine

Table 3.8
SAPPHIRINE COMPOSITIONS

Oxide wt. %	*BG82CLII	#3510	+Finero	§Mauson
MgO	23.58	23.13	21.5	19.89
CaO	0.15	0.22	0.52	1.13
MnO	0.12	n.d.	0.04	n.a.
FeO	0.52	0.27	3.90	3.16
Al ₂ O ₃	53.92	53.86	58.0	54.77
V ₂ O ₃	0.06	0.15	n.a.	n.a.
Cr ₂ O ₃	1.89	1.12	n.a.	n.a.
SiO ₂	19.49	18.50	16.0	16.71
TiO ₂	1.60	2.30	0.01	0.67
SUM	101.33	99.55	98.97	96.33
Number of cations normalized to 10 oxygens				
Mg	2.010	2.003	1.880	1.800
Ca	0.009	0.014	0.033	0.073
Mn	0.006		0.003	
Fe	0.025	0.013	0.190	0.160
Al	3.634	3.688	4.010	3.918
V	0.003	0.007		
Cr	0.085	0.051		
Si	1.115	1.075	0.939	1.014
Ti	0.069	0.101		0.031
SUM	6.956	6.952	7.055	6.986

* This study; average of 4 WDS analyses; # EDS analysis;
+ sapphirine in hornblende-granulitic facies rock from
Italian Alps (Lensch, 1971); § sapphirine from Antarctica
(Segnit, 1957).

Sapphirine was observed in the two Allende POIs BG82CLII and 3510. This is the first reported meteoritic occurrence of sapphirine. The composition of sapphirine, calculated from the average composition from four electron probe WDS analyses (cf., Table 3.8), is



and deviates from the ideal formula, $\text{Mg}_2\text{Al}_4\text{SiO}_{10}$. Variations in sapphirine compositions attributed to the coupled substitution of Mg and Si for Al have been observed in terrestrial samples and a number of different formulae have been proposed (Deer et al., 1978). Terrestrial sapphirine closely approaches a solid solution series between $\text{Mg}_8\text{Al}_{16}\text{Si}_4\text{O}_{40}$ and $\text{Mg}_7\text{Al}_{18}\text{Si}_3\text{O}_{40}$. However, the composition of sapphirine in the POI appears to be higher in MgO and SiO_2 than terrestrial sapphirine (Table 3.8). A significant difference in minor element abundances between Allende and terrestrial sapphirine is also observed. Allende sapphirine has much higher concentrations of TiO_2 and Cr_2O_3 , presumably due to the higher abundance of these elements in the inclusions. Synthetic sapphirine crystallized from a melt whose composition approximates compositions of sapphirine-bearing POI (see Chapter 5), is also enriched in MgO and SiO_2 relative to the ideal sapphirine composition, and has a composition corresponding to $\text{Mg}_{2.12}\text{Ca}_{0.01}\text{Al}_{3.74}\text{Si}_{1.10}\text{Ti}_{0.01}\text{O}_{10}$, very similar to that of natural POI sapphirine.

3.3.6 Glass and mesostasis

Many POIs contain optically isotropic or very fine grained regions in their interiors. These areas are localized either in interstitial regions or as matrix surrounding randomly oriented euhedral silicates. There is no clear evidence of reaction at mesostasis-crystal contacts. As shown in Table 3.9, these areas contain variable amount of Na₂O (1-18%), and in extreme cases can account for 90% of the total Na content in the bulk POI. In some cases, micron sized grains of sodalite and nepheline were observed in these regions. CaO is always depleted relative to the inclusion's bulk composition. Very high SiO₂ contents (63 and 91%) were observed in the interstitial glass/mesostasis region in two POIs. The compositions of residual melts derived by fractional crystallization from melts of the bulk compositions of the POIs, are similar to the compositions of the mesostasis, suggesting that the mesostasis regions are the product of fractional crystallization rather than low-temperature metamorphism. The trace element concentration and distribution among the crystalline phases and mesostasis also suggest closed system crystal/melt partitioning (see REE section).

TABLE 3.9
GLASS AND MESOSTASIS COMPOSITIONS*

wt. % sample	Na ₂ O	MgO	Al ₂ O ₃	SiO ₂	CaO	TiO ₂	Cr ₂ O ₃	FeO	SUM
ALA1-2	8.2	13.8	26.3	33.8	6.1	1.8	0.5	6.6	97.1
BG82DH2	3.0	13.7	23.2	46.7	10.8	1.1	0.3	0.7	99.5
3510	3.4	13.5	35.7	39.6	4.2	1.3	0.6	0.7	99.0
BG82CLII	15.8	7.3	26.5	43.9	1.5	0.4	0.8	0.5	96.7
B14D	11.1	8.8	32.7	35.0	5.7	0.2	0.1	3.2	96.8
BG8CCLJa	18.0	7.8	24.6	41.0	6.1	0.7	0.2	1.2	99.6
LEO1009	1.1	0.3	3.6	91.2	2.1	0.7	0.1	1.0	100.1
ADEL-1	1.3	1.9	16.8	63.3	9.2	0.8	0.3	5.7	99.3

* EDS analysis.

3.4. REE DATA

Rare Earth Elements (REE) were measured in plagioclase (5ALLB6, BG82CLII, and PPX), pyroxene (ALA1-2, 5ALLB6, BG82CLII, PPX, and BG82CH1), and mesostasis (5ALLB6, 3510, BG82CLII, B14D, and BG82CLJa). REE abundances for all minerals analyzed are given in Tables 3.10-3.13, and the chondrite-normalized REE patterns are shown in Figures 3.6-3.8. Each set of REE data represents ion microprobe analysis of individual 10 μm spots within a phase.

Mineral and glass standards with compositions similar to the phases analyzed were used to calculate sensitivity factors (Kennedy *et al.*, 1991). The sensitivity factor is the ratio of the concentration normalized secondary ion intensity of the element in question to the concentration normalized secondary ion intensity of the reference element (Beckett *et al.*, 1990). Mineral standards are Angra dos Reis fassaite and Moore County plagioclase. Glass standard contains trace elements concentration of about 1000 ppm and has major element composition of 60 mole % akermanite (Beckett *et al.*, 1990). Trace element contents of all standards have been measured by neutron activation analysis. Measurements of standards were performed at the start and end of each ion microprobe session.

Plagioclase analyses show LREE-enriched ($2-4 \times$ chondritic) patterns with positive Eu anomaly ($8-15 \times$ chondritic) relative to HREE ($0.1-1 \times$ chondritic). A striking feature is the plagioclase in BG82CLII exhibiting a pronounced Tm anomaly (Fig.3.6). A wide range of REE abundance is observed in pyroxenes. All pyroxenes

Table 3.10
Clinopyroxene

ppm	5ALLB6	5ALLB6	5ALLB6	5ALLB6	ALA1-2	ALA1-2
La	1.55±0.21	17.80±4.3	1.09±0.26	2.20±1.59	8.52±2.64	36.87±5.11
Ce	1.95±0.11	29.00±4.8	1.72±0.13	2.10±1.06	8.96±2.68	42.66±3.59
Pr	2.35±0.30	40.50±7.4	2.32±0.41	2.50±0.98	10.12±2.68	35.34±9.93
Nd	3.00±0.38	50.00±6.8	3.14±0.69	2.89±1.01	11.85±1.93	35.09±7.11
Sm	4.25±0.61	74.00±15.4	4.72±1.00	3.97±1.04	12.54±2.87	35.69±10.10
Eu	1.25±1.15	1.12±1.04	0.77±1.30	1.56±1.86	8.49±1.66	11.71±2.31
Gd	5.40±0.75	98.00±20.6	5.71±0.81	4.69±1.36	14.61±1.24	27.40±5.54
Tb	6.50±0.99	100.2±14.6	6.80±0.92	6.18±1.37	13.08±2.59	27.15±5.64
Dy	7.10±0.32	101.0±8.9	7.93±0.52	6.36±0.56	19.11±1.23	28.45±2.93
Er	7.60±0.49	101.0±14.6	9.02±0.94	6.32±0.91	19.77±1.74	28.63±2.26
Tm	7.00±0.94	100.0±39.4	9.20±1.70	5.20±1.30	20.14±3.05	41.41±4.17
Lu	8.10±2.10	101.5±34.4	8.80±2.30	6.50±2.58	22.67±4.98	28.28±5.25

Table 3.11
Low Ca Pyroxene

ppm	BG82CH1	PPX	BG82CLII	BG82CLII	BG82CLII
La	0.39±0.07	2.29±0.21	0.50±0.11	0.17±0.08	0.51±0.16
Ce	0.41±0.09	2.35±0.23	0.58±0.07	0.24±0.05	0.55±0.09
Pr	0.50±0.10	2.33±0.25	0.59±0.13	0.38±0.13	0.54±0.05
Nd	0.52±0.03	2.31±0.29	0.70±0.13	0.49±0.23	0.64±0.13
Sm	0.62±0.08	2.40±0.30	1.30±0.14	1.70±0.42	1.34±0.23
Eu	0.31±0.41	1.50±0.80	0.03±0.81	0.03±0.41	0.07±1.20
Gd	0.70±0.30	2.32±0.41	1.65±0.40	2.34±0.35	1.40±0.30
Tb	0.72±0.31	3.05±0.47	2.00±0.61	2.86±0.76	1.40±0.34
Dy	0.87±0.25	3.91±0.38	2.80±0.19	3.74±0.31	2.34±0.26
Er	1.16±0.18	5.19±0.62	1.10±0.15	1.71±0.33	0.86±0.18
Tm	1.51±0.81	5.69±0.70	12.00±1.70	16.25±1.64	9.60±1.90
Lu	1.91±1.10	7.45±1.10	1.00±0.73	0.91±0.57	1.34±0.61

Table 3.12
Plagioclase

ppm	PPX	BG82CLII	5ALLB6	BG82CLJa
La	3.52±0.12	4.05±0.10	2.90±0.21	0.71±0.66
Ce	3.16±0.11	4.20±0.05	2.35±0.17	0.96±0.34
Pr	2.41±0.19	3.15±0.24	2.00±0.20	0.75±0.62
Nd	2.61±0.27	3.20±0.25	1.60±0.26	0.61±0.42
Sm	2.11±0.43	2.90±0.85	1.40±0.27	0.77±0.64
Eu	7.60±1.10	10.70±2.37	14.00±3.30	10.37±1.77
Gd	0.76±0.30	1.32±0.49	1.23±0.42	0.16±0.33
Tb	1.26±0.33	0.67±0.70	0.86±0.40	0.16±0.34
Dy	0.81±0.28	0.59±0.23	0.82±0.13	0.22±0.32
Er	0.40±0.47	0.19±0.42	0.50±0.16	0.13±0.50
Tm	0.21±0.85	2.67±1.34	0.10±0.05	0.38±0.51
Lu	0.53±1.20	0.08±1.87	0.32±0.40	0.25±0.67

Table 3.13
Mesostasis

ppm	BG82CLII	BG82CLII	5ALLB6	BG82CLJa	3510	B14D
La	240±41	273±52	36.0±5.8	1.41±0.27	13.89±1.95	1.41±0.43
Ce	295±52	361±68	37.0±3.9	1.40±0.32	13.29±1.31	1.40±0.24
Pr	260±52	323±62	32.5±4.5	1.09±0.24	15.09±3.21	1.09±0.25
Nd	230±45	290±61	29.5±3.2	1.14±0.41	16.39±3.81	1.14±0.37
Sm	255±59	308±66	27.5±3.0	0.98±0.32	15.93±4.40	0.98±0.31
Eu	11.5±48	14.5±5.3	17.5±10.0	0.75±0.21	9.37±1.45	0.75±0.22
Gd	170±72	181±76	26.5±6.8	0.82±0.29	12.96±5.91	0.82±0.16
Tb	180±59	196±67	26.0±6.3	0.81±0.33	13.81±6.85	0.81±0.26
Dy	160±23	204±28	28.0±2.3	1.01±0.41	13.83±5.75	1.01±0.31
Er	40±9	48±10	29.5±3.0	1.10±0.29	12.83±6.91	1.10±0.89
Tm	275±67	376±83	26.5±4.2	1.23±0.28	11.18±8.13	1.23±0.62
Lu	12±18	2±40	28.0±12.9	1.44±0.77	12.71±8.00	1.44±0.63

are depleted in the light rare earth elements (LREE = $0.4-11 \times$ chondritic) and Eu ($0.03-8 \times$ chondritic) relative to heavy rare earth elements (HREE = $1-100 \times$ chondritic). The slightly higher LREE in one of the analysis of ALA1-2 is probably due to overlap of the ion beam on another phase. Lower REE abundances are found in pigeonite and aluminous enstatite (Fig.3.7a) while higher abundances are associated with Ca-rich clinopyroxene (Fig.3.7b). In inclusion 5ALLB6, the REE abundances of pyroxenes varies significantly. Interstitial pyroxenes, which were texturally identified to crystallized very late, are ten times higher in their REE abundances relative to earlier pyroxene (Fig.3.7b). In BG82CLII, the Tm anomaly, which is observed in its plagioclase, is also present its pyroxene (Fig.3.7).

The mesostasis of five POIs were analyzed. The REE abundances in the mesostasis vary significantly among POIs ($1-300 \times$ chondritic). While the REE patterns of the mesostasis in 3510, B14D, 5ALLB6, and BG82CLa are relatively flat, ranging from $1-40 \times$ chondritic, the mesostasis in BG82CLII is significantly different (Fig.3.8). Its REE pattern is highly enriched in LREE ($200-400 \times$ chondritic) and exhibits a distinct depletion of Eu ($\sim 15 \times$ chondritic) and positive Tm anomaly ($\sim 300-400 \times$ chondritic).

Since pyroxene, plagioclase, and mesostasis are the major REE carriers in POIs, I attempted to calculate the bulk REE pattern of three inclusions in which all three phases were analyzed. The REE patterns are calculated by summing the abundance of each element in all the three phases according to their estimated modal abundance in the inclusion. For the POIs PPX and 5ALLB6, the calculated bulk REE pattern is relatively

flat, and about $2-3 \times$ chondritic (Fig.3.9). Both show a positive Eu anomaly. This type of pattern has been identified in many coarse grained CAIs (see Boynton, 1984 and references therein) and is referred to as Group I by Mason and co-workers (Martin and Mason, 1974; Mason and Martin, 1977; Taylor and Mason, 1978). The positive Eu anomalies have been explained by (1) multiple episodes of condensation and isolation of grains from the solar gas. Removal of these grains after most of the REE had condensed resulted in an overabundance of the more volatile Eu in the remaining gas, which upon further condensation, would yield an Eu enrichment in the later grains; (2) the grains in these inclusions were a mixture of pre-existing material. The components which mixed together would have contributed REE and other trace elements according to mineral preference effects rather than volatility effects. The more pronounced Eu anomaly in the POIs may be due to oversampling of plagioclase. A different type of REE pattern is observed in BG82CLII. This type of REE pattern is typically found in fine grained CAIs, and was first identified by Tanaka and Masuda (1973). The bulk REE pattern of BG82CLII is fairly similar to that in its mesostasis. This result is due to the fact that most of the REE in the inclusion is contained in the mesostasis.

In all of the POIs analyzed, the plagioclase and pyroxene appear to exhibit complementary REE patterns. Late crystallizing phase contains higher REE abundance (e.g., pyroxene in 5ALLB6), suggesting REE enrichment in the melt with progressive crystallization. The Tm anomaly in BG82CLII is observed in all its constituting phases, suggesting that they all crystallized from a melt enriched in Tm. These observations are consistent with a closed system crystallization of the inclusions.

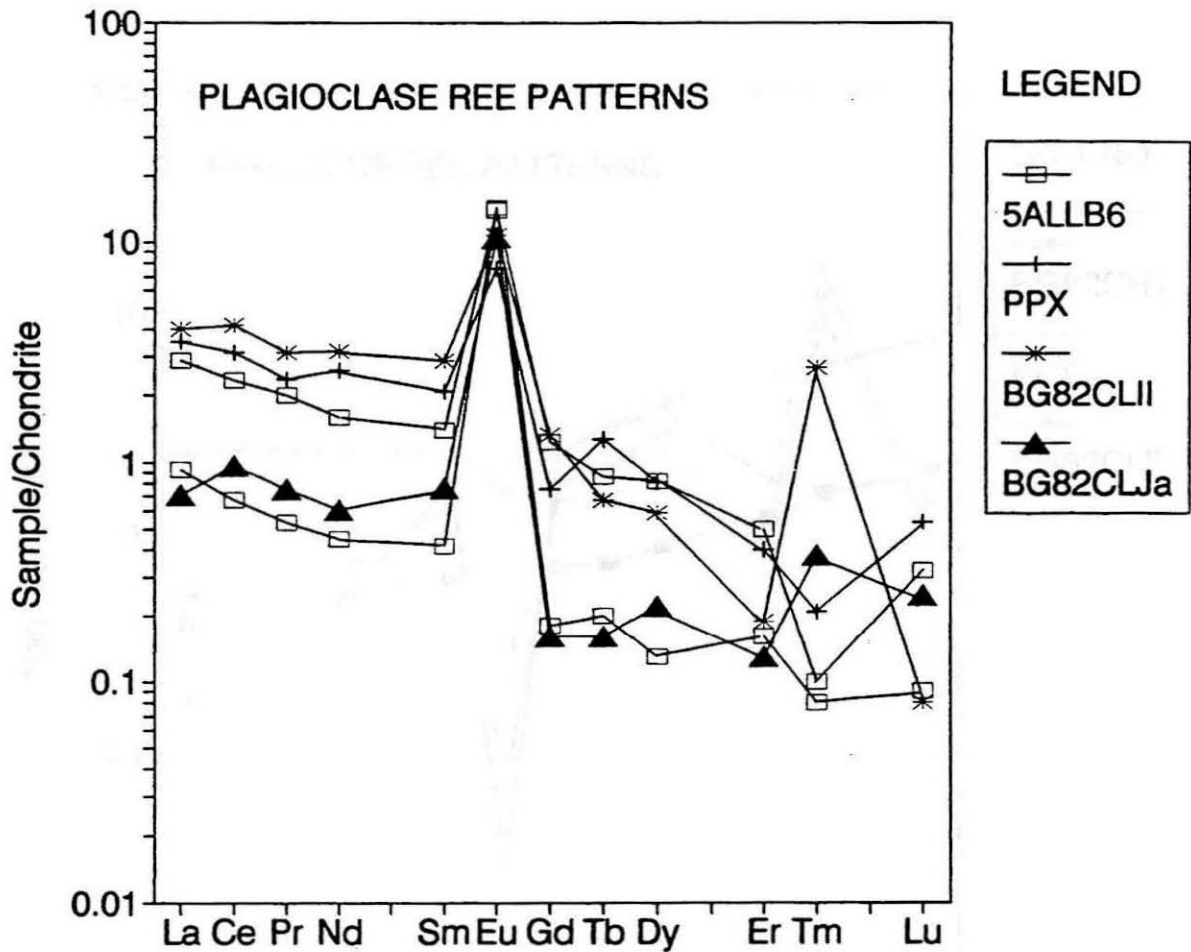


Fig.3.6 Chondrite-normalized REE abundances for plagioclase of 5ALLB6, PPX, BG82CLII, and BG82CLJa. Chondritic values from Anders and Grevesse (1989).

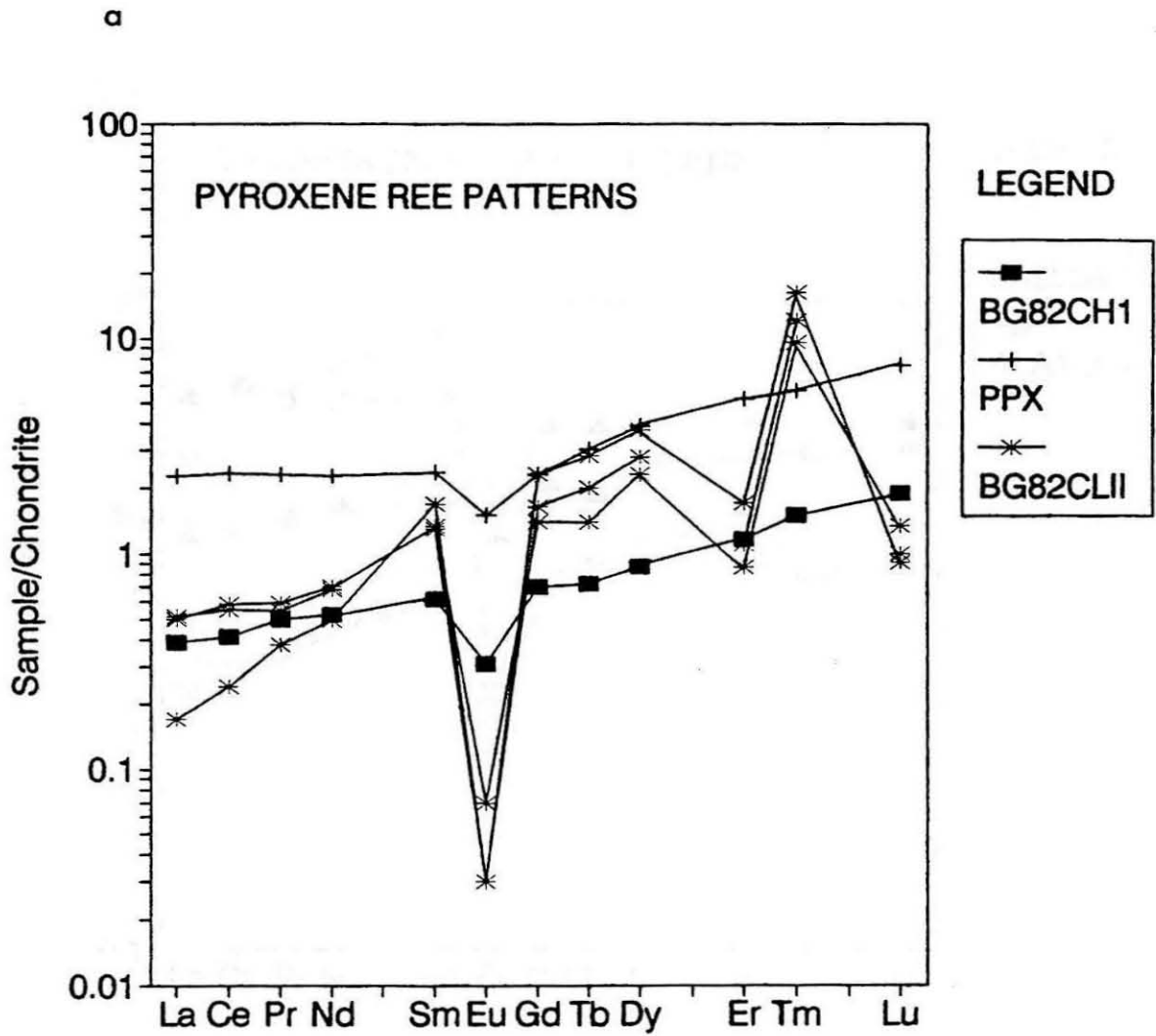
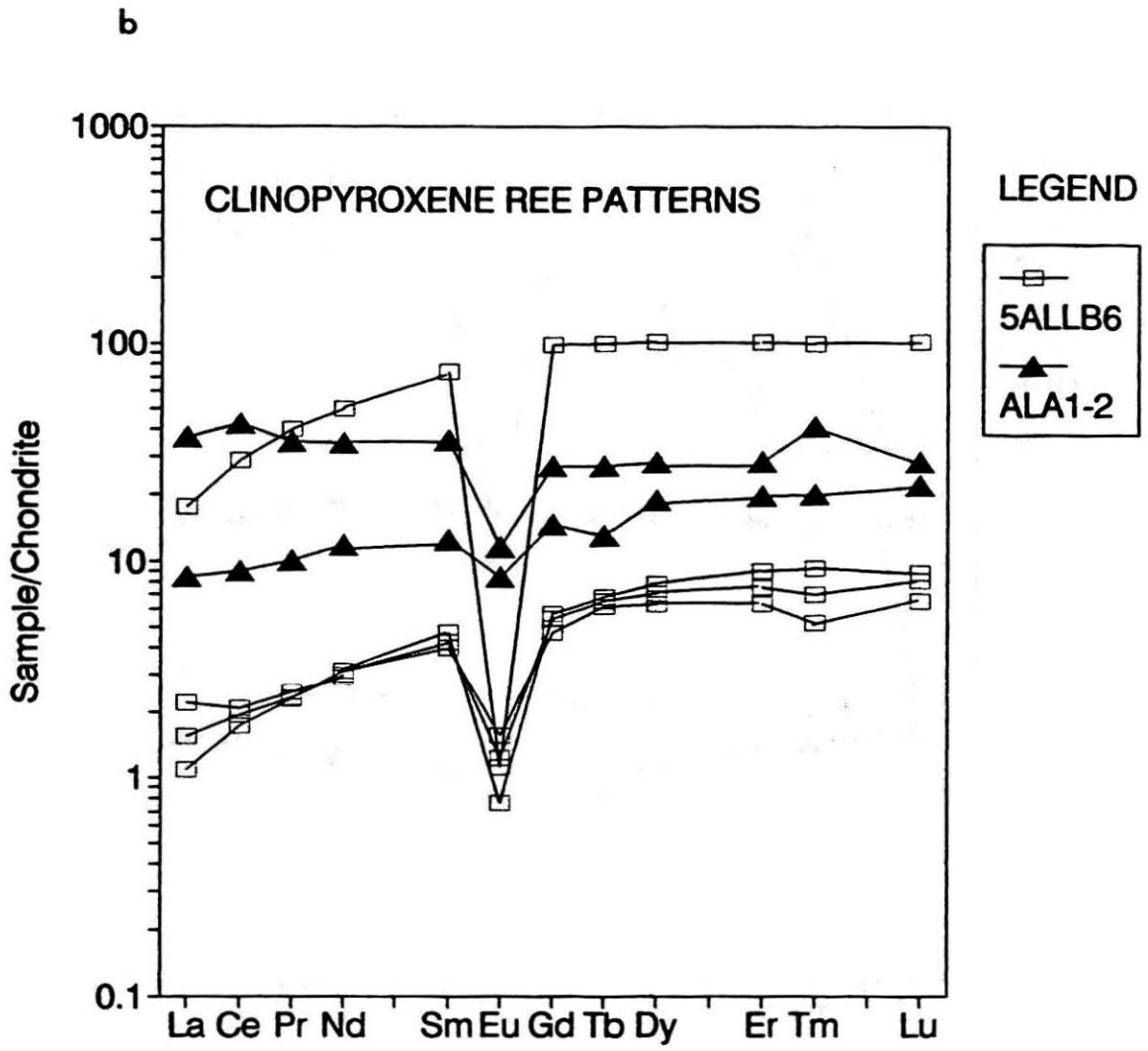


Fig.3.7 Chondrite-normalized REE abundances for a) low Ca pyroxene (BG82CH1, PPX, and BG82CLII) and b) clinopyroxene (5ALLB6 and ALA1-2).



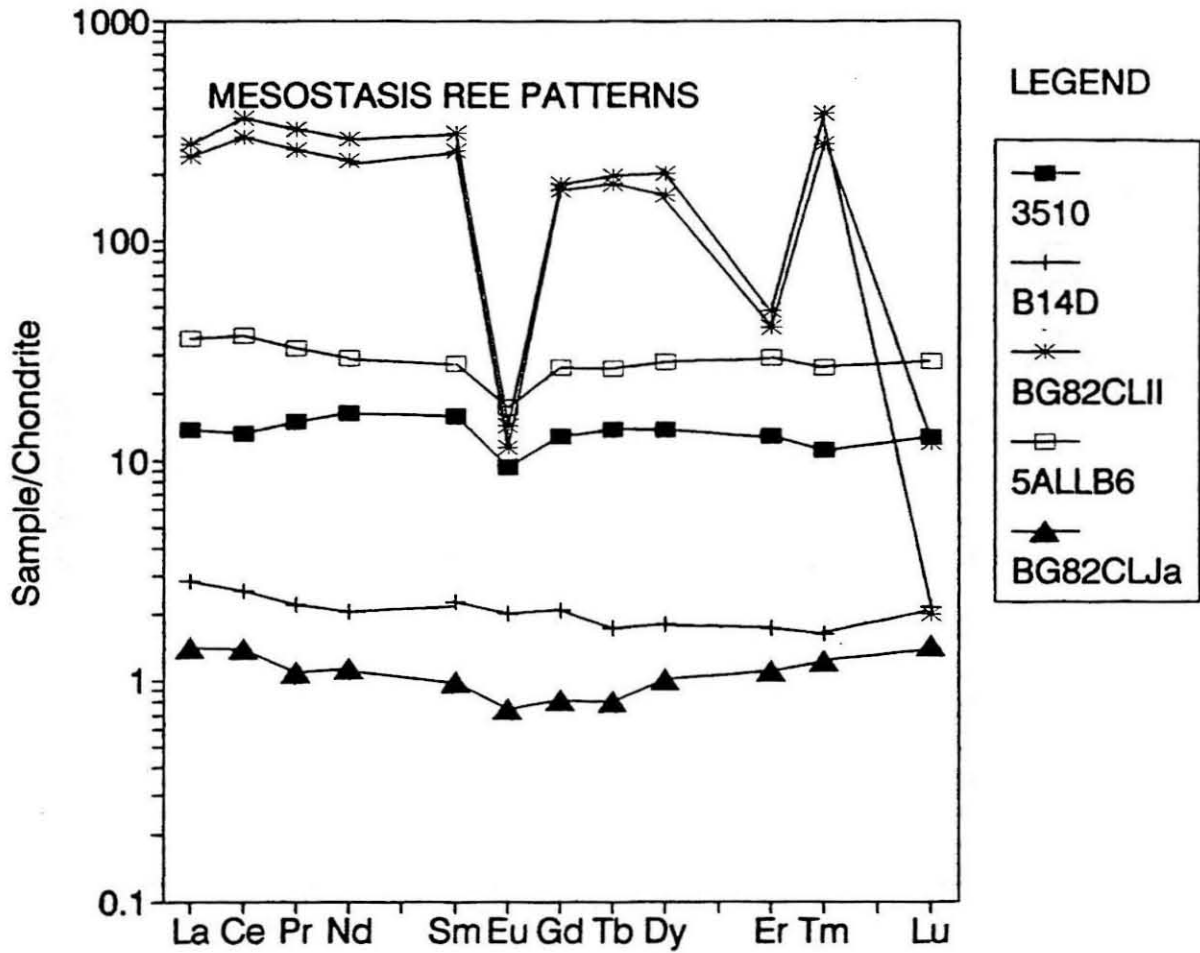


Fig.3.8 Chondrite-normalized REE abundances for mesostasis of 3510, B14D, BG82CLII, 5ALLB6, and BG82CLJa.

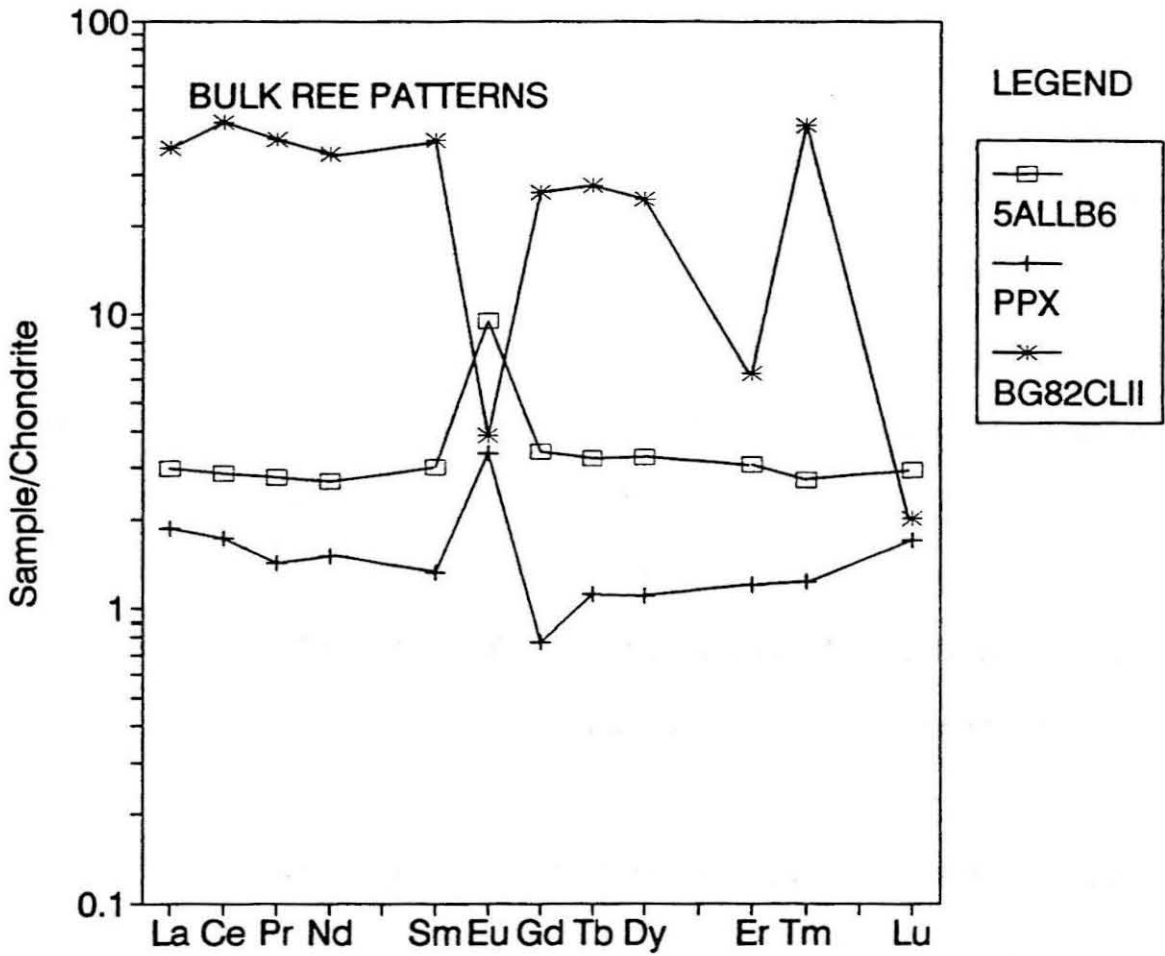


Fig.3.9 Chondrite-normalized REE abundances for bulk inclusions calculated from REE and modal abundances of constituent phases.

3.5. COMPARISON OF PLAGIOCLASE-OLIVINE INCLUSIONS WITH CAIS AND CA CHONDRULES

POIs constitute a distinct group of objects distinguished from both CAIs and chondrules by their mineralogy, chemistry and isotopic composition. Objects that have the closest resemblance in bulk composition to POIs are the Type C (or I) CAIs (Wark, 1987; Grossman, 1975) and CA chondrules (Bischoff and Keil, 1984). Type C CAIs are anorthite-rich (An_{99-100}) refractory inclusions with substantial amounts of fassaite and spinel, and can have melilite and olivine. POIs and CA chondrules are transitional Ca-Al-rich objects between CAIs and ferromagnesian chondrules. POIs consist of plagioclase (An_{82-98}), olivine (Fo_{63-99}), enstatite, clinopyroxene and nearly pure $MgAl_2O_4$ spinel in various proportions. Plagioclase is always a major component (>10 volume %) and sometimes the dominant (>60 volume %) phase in POIs. POIs are generally spheroidal ranging 0.5-5 mm in diameter. CA chondrules commonly consist of small (≤ 1 mm) chondrules containing elongated, partly skeletal crystals of fassaite and olivine embedded in a fine-grained Na-rich microcrystalline to glassy matrix. Sodic plagioclase (mean An_{80}) occurs occasionally while spinel is rare and usually Fe-rich (12-20 wt.% FeO). POIs are easily distinguished from both CA chondrules and Type C CAIs on the basis of their petrography and mineralogy and compose a distinct group unrecognized in previous studies. A comparison of the chemical features between POIs, Type C CAIs and CA chondrules as well as Type B CAIs is shown in Table 3.14.

Table 3.14 Comparison of POI with Type B, Type C CAI and CA Chondrule

	POI	Type C CAI	CA chondrule	Type B CAI
Bulk Chemistry (wt. %)	range (mean)	range (mean)	range (mean)	range (mean)
Na ₂ O	0.7-6.8 (2.5)	0.05-0.7 (0.2)	0.5-4.6 (4.5)	0.07-0.9 (0.3)
MgO	10-45 (19)	4-13 (7)	4-34 (14)	9-16 (10)
CaO	2-17 (10)	18-26 (22)	4-18 (7)	22-32 (27)
MnO	<0.2	-	0.02-0.4	-
FeO	0.6-6.5 (3)	0.1-0.9 (0.4)	2-14 (6)	0.3-1.7 (1.8)
Al ₂ O ₃	4-37 (22)	26-47 (32)	11-28 (17)	25-34 (31)
Cr ₂ O ₃	0.2-0.9 (0.45)	0.03-0.5 (0.13)	0.1-3.2 (0.5)	0-0.08 (0.05)
SiO ₂	36-50 (41)	21-41 (37)	40-57 (51)	25-35 (29)
TiO ₂	0.4-1.8 (0.7)	0.6-1.6 (1.1)	0.3-1.3 (0.7)	0.9-1.9 (1.5)
Modal Mineralogy (vol. %)				
spinel	0-25	2-25	minor	15-30
plagioclase	5-60	30-60	minor	5-25
melilite	none	10-25	none	5-20
olivine	10-70	minor	major	none
calcic pyroxene	0-30	10-30	major	35-60
low-Ca pyroxene	0-35	minor	major	none
Other phase				
armalcolite	rare	-	-	-
zirconolite	rare	-	-	-
rutile	rare	-	-	-
perovskite	rare	common	-	common
sapphirine	rare	-	-	-
glass	rare	-	common	-
refractory OA	rare	present	-	common
Mineral Chemistry				
plagioclase	An ₈₂₋₉₉	An ₉₉₋₁₀₀	An ₇₀₋₉₁	An ₉₉₋₁₀₀
olivine	Fo ₈₈₋₉₉		Fo ₇₃₋₉₉	
fassaite (wt. % TiO ₂)	2-13	2-12	0.6-4.3	3-11
(wt. % Al ₂ O ₃)	4-15	14-24	12-25	14-21
spinel (wt. % FeO)	0.3-5	0.1-1	12.4-19.8	
Texture	basaltic ophitic granular porphyritic radiating	basaltic ophitic	granular porphyritic skeletal radiating	zoned rim sequence spinel- framboid
Size (diameter mm)	0.5-5	0.5-7	0.1-0.2	4-13
Initial ²⁶Al/²⁷Al	<10 ⁻⁶	~10 ⁻⁶		~5×10 ⁻⁵
F_{Mg}	>0 or <0	0		0

CHAPTER FOUR

Mg ISOTOPE COMPOSITION

The Mg isotopic data were obtained on several different crystals of the major phases in each of the POI studied. The purpose was to establish the presence of isotopic effects due to either mass-dependent fractionation, general nonlinear effects or radiogenic $^{26}\text{Mg}^*$ from ^{26}Al decay. During the course of these analyses it became clear that particular attention to the isotopic homogeneity of POI was required. Measurements on spinel, olivine, pyroxene and plagioclase are summarized in Fig.4 and in Tables 4.1 and 4.2., where I present the Mg isotope fractionation (F_{Mg}) relative to a standard, the ^{26}Mg excess expressed as $\delta^{26}\text{Mg}$, and for plagioclase, the $^{27}\text{Al}/^{24}\text{Mg}$ ratio.

4.1. Mg Isotope Fractionation

4.1.1. Mg isotope fractionation in silicates

Mg isotopes of plagioclase in 12 POIs were analyzed, one of which was reported by Hutcheon (1982) and one from Papanastassiou *et al.* (1984). The data is shown

Table 4.1
Mg ISOTOPIC COMPOSITIONS OF POI PLAGIOCLASE

SAMPLE	F_{Mg} ‰ $\pm 2\sigma$ mean	$\delta^{26}Mg$ ‰ $\pm 2\sigma$ mean	$^{27}Al/^{24}Mg$ $\pm 2\sigma$ mean
plagioclase			
5ALLB6 plag1	1.5 \pm 3.3	5.8 \pm 5.6	166.8 \pm 5
5ALLB6 plag2	0.5 \pm 1.8	4.6 \pm 3.6	201.7 \pm 5
5ALLB6 plag3	0.9 \pm 1.3	4.2 \pm 3.1	222.3 \pm 5
5ALLB6 plag4	1.5 \pm 1.7	1.2 \pm 3.9	130.1 \pm 5
BG82CLJb plag1	1.4 \pm 1.5	-0.1 \pm 2.1	78.2 \pm 5
B14D plag1	1.0 \pm 1.3	2.3 \pm 2.2	85.2 \pm 5
B14D plag2	2.2 \pm 1.8	1.3 \pm 3.0	159.1 \pm 5
3510 plag1	†	4.3 \pm 2.3	58.7 \pm 5
3510 An 1*	-3.0 \pm 1.8	5.0 \pm 3.0	98 \pm 5
3510 An 2-1*	0.5 \pm 2.4	6.0 \pm 4.0	128 \pm 5
3510 An 2-2*	-2.1 \pm 1.8	7.0 \pm 3.0	103 \pm 5
3510 An 2-3*	-2.0 \pm 2.2	3.0 \pm 4.0	86 \pm 5
3510 An 5*	-2.2 \pm 2.0	2.0 \pm 4.0	114 \pm 5
BG82DH2 plag1	†	3.3 \pm 1.9	62.3 \pm 5
BG82DH2 plag2	1.2 \pm 1.3	1.0 \pm 2.3	86.7 \pm 5
PPX plag1	8.0 \pm 2.4	-2.1 \pm 4.9	183.3 \pm 5
PPX plag2	6.3 \pm 1.8	0.0 \pm 3.2	150.0 \pm 5
V477 plag1	4.0 \pm 1.6	-0.4 \pm 3.0	110.5 \pm 5
ADEL-1	3.0 \pm 1.0	-1.1 \pm 1.8	28.7 \pm 5
BG82CH1 plag1	4.6 \pm 1.4	-0.8 \pm 2.4	35.4 \pm 5
BG82CH1 plag2	3.7 \pm 1.6	0.3 \pm 2.6	40.0 \pm 5
BG82CH1 plag3	4.8 \pm 1.4	1.2 \pm 2.5	39.1 \pm 5
ALA1-2 plag1	-3.3 \pm 1.3	-0.6 \pm 4.9	177.9 \pm 5
BG82CLII plag1	1.8 \pm 1.5	-0.1 \pm 2.1	78.2 \pm 5
REDEYE plag1#	0.5 \pm 2.1	1.3 \pm 0.9	

* Ion probe isotope data from Hutcheon (1982); # Thermal ionization isotope data from Papanastassiou et al. (1984);

† F_{Mg} values not calculated.

Table 4.2
Mg ISOTOPIC COMPOSITIONS OF
OTHER PHASES

SAMPLE	F_{Mg} ‰ $\pm 2\sigma$ mean	$\delta^{26}Mg$ ‰ $\pm 2\sigma$ mean
olivine		
5ALLB6 ol1	-1.3 ± 0.8	0.9 ± 1.9
BG82CLJb ol1	-0.8 ± 1.0	0.6 ± 1.9
BG82CLJb ol2	-0.4 ± 1.2	0.1 ± 2.0
3510 ol1	0.3 ± 0.7	-2.1 ± 1.3
3510 ol*	0.4 ± 1.0	2.5 ± 1.2
3510 ol*	-0.8 ± 1.2	-0.8 ± 1.4
BG82DH2 ol1	-1.3 ± 0.8	2.4 ± 1.5
PPX ol1	-1.2 ± 0.8	-1.7 ± 1.5
BG82CLII ol1	-1.5 ± 0.9	0.9 ± 1.5
BG82CLJa ol1	1.0 ± 0.7	0.3 ± 1.2
ADEL-1 ol1	1.0 ± 0.9	-0.5 ± 1.6
REDEYE ol1	2.6 ± 1.1	-1.1 ± 0.2
REDEYE ol2	0.7 ± 1.8	-0.4 ± 0.2
spinel		
5ALLB6 sp1	6.4 ± 0.9	3.1 ± 1.8
5ALLB6 sp2	6.0 ± 1.1	0.0 ± 1.9
5ALLB6 sp3	3.7 ± 1.1	3.6 ± 1.8
5ALLB6 sp4	4.6 ± 1.0	0.1 ± 1.6
5ALLB6 sp5	4.2 ± 1.3	1.8 ± 2.1
5ALLB6 sp6	5.1 ± 1.0	0.5 ± 2.2
5ALLB6 sp7	5.0 ± 1.1	-0.1 ± 2.2
BG82CLJb sp1	5.4 ± 1.2	0.2 ± 2.0
B14D sp1	1.4 ± 0.9	0.9 ± 1.6
B14D sp2	0.3 ± 1.0	0.3 ± 1.7
3510 sp1	1.9 ± 1.3	1.1 ± 2.3
BG82DH2 sp1	4.9 ± 0.9	0.9 ± 1.7
BG82DH2 sp2	4.4 ± 1.2	2.4 ± 2.1
ALA1-2 sp1	-7.0 ± 1.1	1.9 ± 1.9
ALA1-2 sp2	-0.3 ± 1.0	0.1 ± 1.7
ALA1-2 sp3	-4.1 ± 1.0	2.3 ± 1.8
ALA1-2 sp4	-4.0 ± 1.0	0.8 ± 1.7
BG82CLII sp1	11.1 ± 1.1	2.2 ± 2.0
BG82CLII sp2	7.2 ± 1.1	2.4 ± 2.1
BG82CLII sp3	8.6 ± 1.0	0.3 ± 1.9
BG82CLII sp4	8.4 ± 1.2	1.3 ± 2.0
ADEL-1 sp1	-3.3 ± 1.0	2.7 ± 1.8
ADEL-1 sp2	-1.0 ± 0.9	0.6 ± 3.0
LEO1009 sp1	1.7 ± 1.0	0.9 ± 1.7
LEO1009 sp2	2.1 ± 1.0	1.8 ± 1.6

Table 4.2
Mg ISOTOPIC COMPOSITIONS OF
OTHER PHASES

pyroxene		
5ALLB6 px1	1.9 ± 0.9	3.3 ± 1.7
5ALLB6 px2	0.1 ± 1.0	3.0 ± 1.8
5ALLB6 px3	1.4 ± 2.4	-0.2 ± 4.0
5ALLB6 px4	5.2 ± 1.0	-0.3 ± 1.8
5ALLB6 px5	5.5 ± 1.2	-1.0 ± 2.0
5ALLB6 px6	4.0 ± 1.3	2.8 ± 2.1
BG82DH2 px1	2.1 ± 0.7	1.2 ± 1.1
BG82DH2 px2	3.9 ± 0.8	0.0 ± 1.4
ALA1-2 px1	-0.7 ± 0.9	1.5 ± 1.6
ALA1-2 px2	1.3 ± 0.9	-1.4 ± 1.6
BG82CLII px1	0.4 ± 0.9	3.2 ± 1.5
BG82CLII px2	1.8 ± 1.0	0.0 ± 1.7
BG82CLII px3	2.7 ± 0.9	-1.1 ± 1.6

* Data from Hutcheon (1982)

in Table 4.1. Most of the analyses show normal $^{25}\text{Mg}/^{24}\text{Mg}$. The exceptions are the plagioclase in PPX ($F_{\text{Mg}} = 6-8 \text{ ‰}$). Although plagioclase of BG82CH1 also show small enrichment of the heavier isotopes, the errors lie within the uncertainties of analyses of plagioclase standards (see Fig. 4.1). In the Mg isotope analyses of four POIs, pyroxenes of 5ALLB6 and BG82DH2 showed small enrichments of the heavier isotopes. All olivine analyses from nine POIs show normal Mg isotopes.

4.1.2. Mg isotope fractionation in spinel

The Mg isotopic composition of spinel was analyzed in nine POIs (Table 4.2). Spinel in six of the nine POIs show fractionated Mg isotopes (Fig.4.2). F_{Mg} values in these inclusions range from -7 to +11 permil per atomic mass unit (‰/amu). In individual inclusions F_{Mg} value is either positive or negative but not both. F_{Mg} values of spinel in 5ALLB6, BG82CLJb, BG82DH2, and BG82CLII are positive, ranging from 3.7 to 11.1 ‰ . In ALA1-2 and ADEL-1, the spinels are enriched in the lighter isotopes ($F_{\text{Mg}} = -1$ to -7 ‰). Spinels in B14D, 3510, and LEO1009 show normal values of Mg.

4.2. Summary of Mg Isotope Fractionation in POIs

The most striking feature of the isotopic data is the extent of Mg isotopic heterogeneity within and among the POIs. Seven of the fourteen inclusions examined in this study exhibit variations in F_{Mg} among coexisting phases. (The POI, SA-1, studied

by Kennedy *et al.* (1991), also contains internal variations in F_{Mg} but is excluded from the present discussion.) The predominant isotopic effect, present in seven POIs, is a significant difference in F_{Mg} between spinel and coexisting silicates (Fig.4.2). Differences in F_{Mg} between silicate phases are found in three POIs (Fig.4.1), two of which also contain isotopically heterogeneous spinel. In four POIs spinel is enriched in the heavier Mg isotopes relative to silicates, whereas in two inclusions spinel is enriched in the lighter Mg isotopes. The total range in F_{Mg} , -7 to +11 ‰/amu, is surprisingly large in view of the igneous textures of nearly all POIs and is much larger than the variation in F_{Mg} found in other (non-FUN) refractory inclusions. Within individual POI, F_{Mg} in spinel is not constant but may vary by up to 7 ‰/amu. Spinel containing isotopically fractionated Mg are found in all three petrographic groups of POIs but, in general, the most pronounced isotopic heterogeneity is found in those inclusions that have abundant spinel. For example, BG82CLII, which contains the most spinel (25%), also has the largest range in fractionation among its constituent phases, $-1 < F_{Mg} < 11$ ‰/amu. No correlation between F_{Mg} and spinel chemistry was observed. The evidence of Mg isotopic heterogeneity in silicate phases within POIs resembles that in spinels but occurs much less frequently. Variations in F_{Mg} among coexisting pyroxenes occur in 2 POIs, both belonging to petrographic group 1, while only one inclusion (PPX, a group 2 POI) contains plagioclase with a distinct F_{Mg} . Despite the scarcity, the magnitude of the differences in F_{Mg} among silicates is similar to that of differences between spinel and silicates. Fassaite pyroxenes in 5ALLB6 exhibit both the largest Mg fractionation and the greatest range of F_{Mg} among POI pyroxenes; F_{Mg} in fassaite ranges from 0 to 5.5

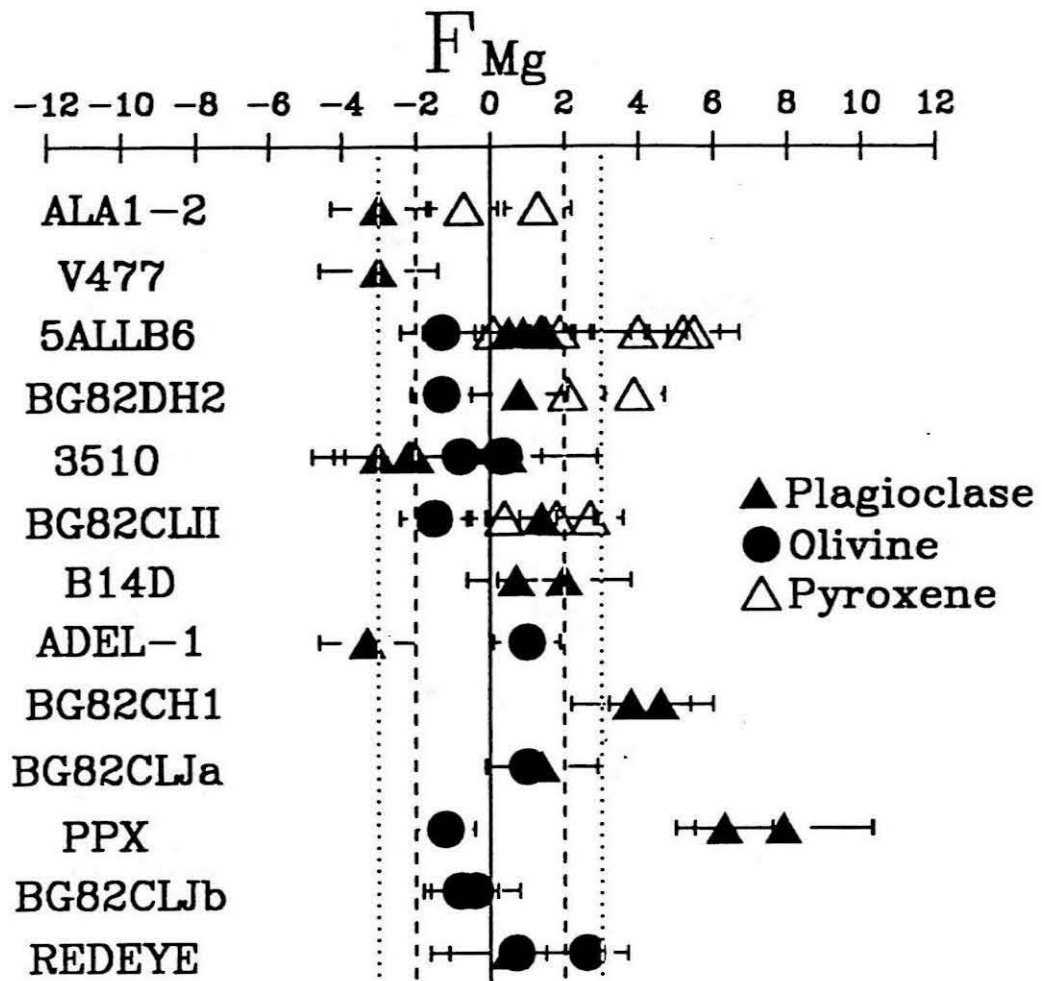


Fig.4.1 Mg isotopic fractionation plotted in permil for pyroxene, olivine and plagioclase from 13 POIs. Olivine, pyroxene and most plagioclase appear to be unfractionated. The dotted lines are the 2σ variation for normal plagioclase and the dashed lines for normal olivine and pyroxene.

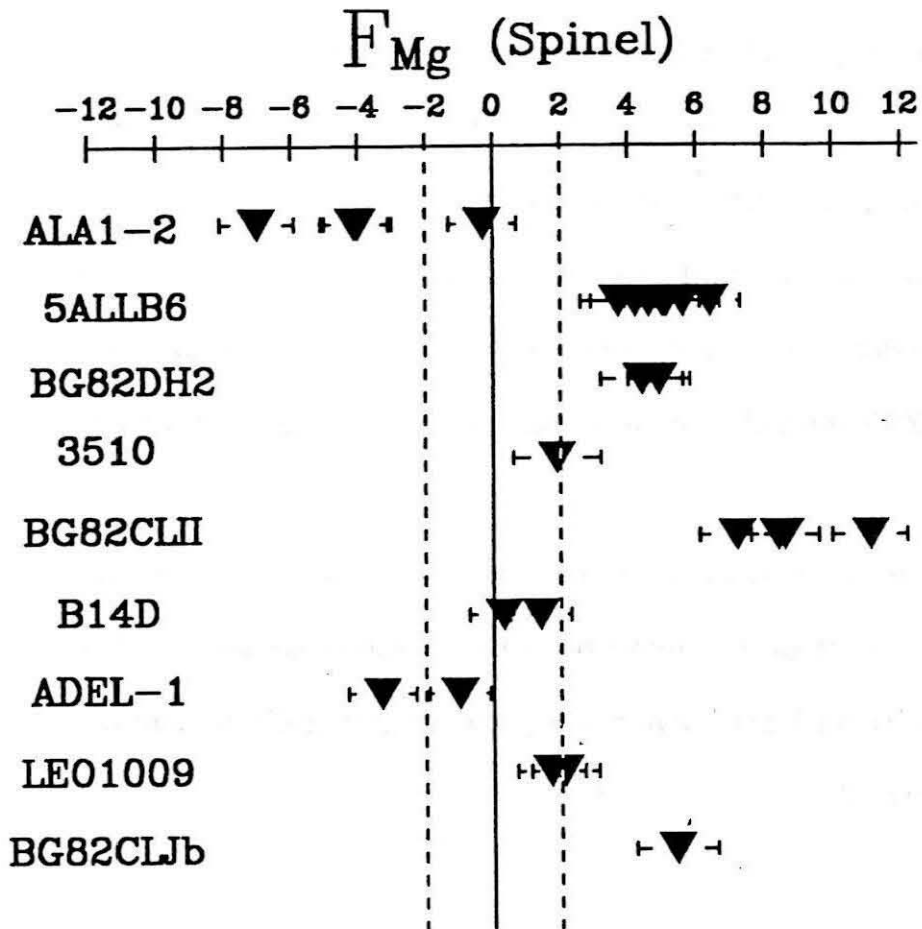


Fig.4.2 Mg isotopic fractionation plotted in permil for spinels of nine POIs. Spinel in six of the nine POIs are fractionated either heavy (BG82CLII, BG82CLJb, BG82DH2, and 5ALLB6) or light (ALA1-2 and ADEL-1). The dashed lines indicate the 2σ variation for normal spinel.

‰/amu compared to a range of 3.7 to 6.4 ‰/amu in spinel. One feature that distinguishes the isotopic record of pyroxene from that of spinel in both 5ALLB6 and BG82DH2 is the presence of some isotopically normal pyroxenes ($F_{Mg}=0$) in both POIs. All of the spinels in both inclusions, in contrast, have $F_{Mg} > 0$.

Isotopic fractionation effects in plagioclase are restricted to inclusion PPX. Plagioclase appears to be isotopically homogeneous with fractionation favoring the heavier Mg isotopes, $F_{Mg} \approx +7$ ‰/amu. Spinel is rare and very small in this inclusion and we were unable to obtain isotopic measurements of spinel. Olivine in PPX has $F_{Mg} \approx 0$.

In sharp contrast to spinel and pyroxene, olivine in all of the POIs contains isotopically normal Mg. The values of F_{Mg} cluster about zero, ranging from -1.5 to +1 ‰/amu. No significant variations in isotopic composition were found for interior olivine phenocrysts or for the more Fe-rich olivines located in the equigranular olivine clusters.

4.3. Excess $^{26}\text{Mg}^*$

Most POIs do not show evidence for radiogenic $^{26}\text{Mg}^*$. Only two POIs, 3510 and 5ALLB6, show small but significant enrichments in ^{26}Mg . The $^{26}\text{Mg}/^{24}\text{Mg}$ ratios in plagioclases in these two inclusions are correlated with the respective $^{27}\text{Al}/^{24}\text{Mg}$ ratios measured at the same point of analysis. Four of the six plagioclase analyses in 3510 indicate clear ^{26}Mg excesses (Fig.4.3). The linear correlation between the $^{26}\text{Mg}/^{24}\text{Mg}$ and $^{27}\text{Al}/^{24}\text{Mg}$ ratios suggests the *in situ* decay of ^{26}Al . The best fit slope of the isochron

for 3510 (Fig.4.3) and 5ALLB6 (Fig.4.4) corresponds to $^{26}\text{Mg}^*/^{27}\text{Al}=6.1 \times 10^{-6}$ and $^{26}\text{Mg}^*/^{27}\text{Al}=2.6 \times 10^{-6}$, respectively. In all the other POIs this ratio is less than 1×10^{-6} (Fig.4.5).

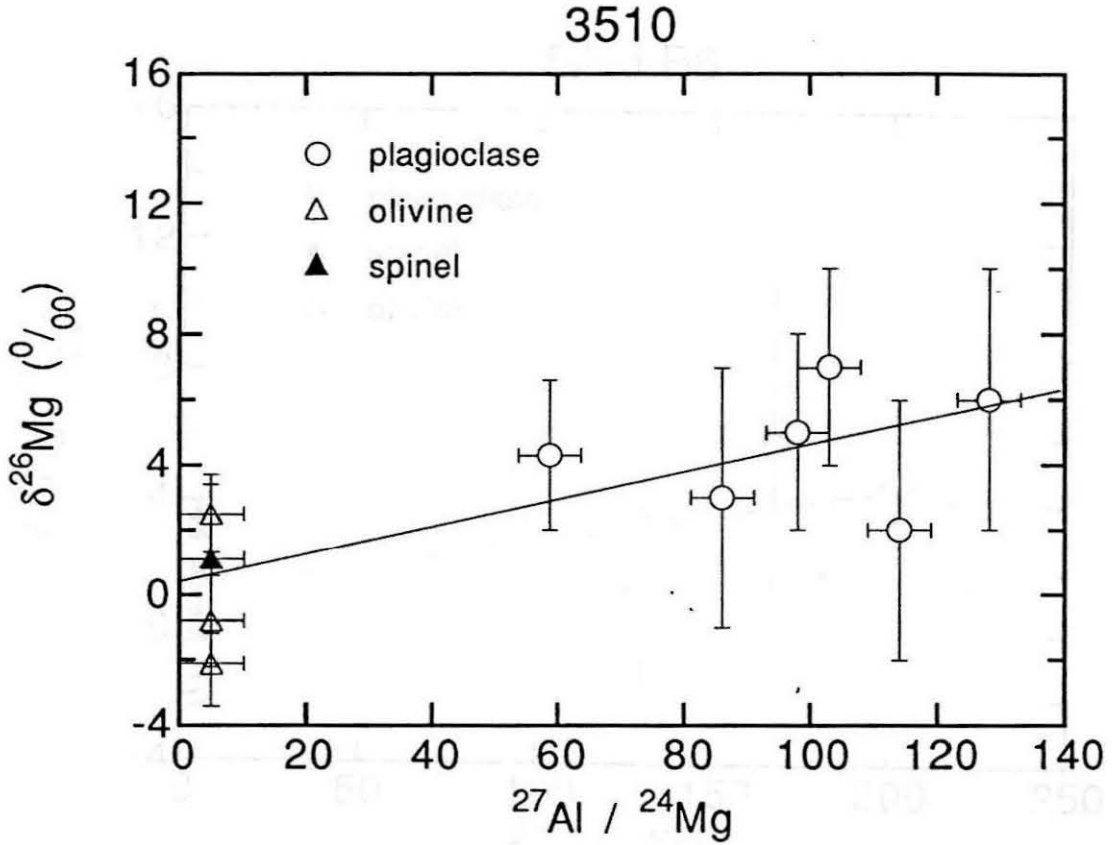


Fig.4.3 Mg isotopes of POI 3510 showing excess ^{26}Mg correlated with in-situ decay of ^{26}Al . The best fit slope of the isochron corresponds to $(^{26}\text{Al}/^{27}\text{Al})_0 = 5.8 \pm 0.2 \times 10^{-6}$.

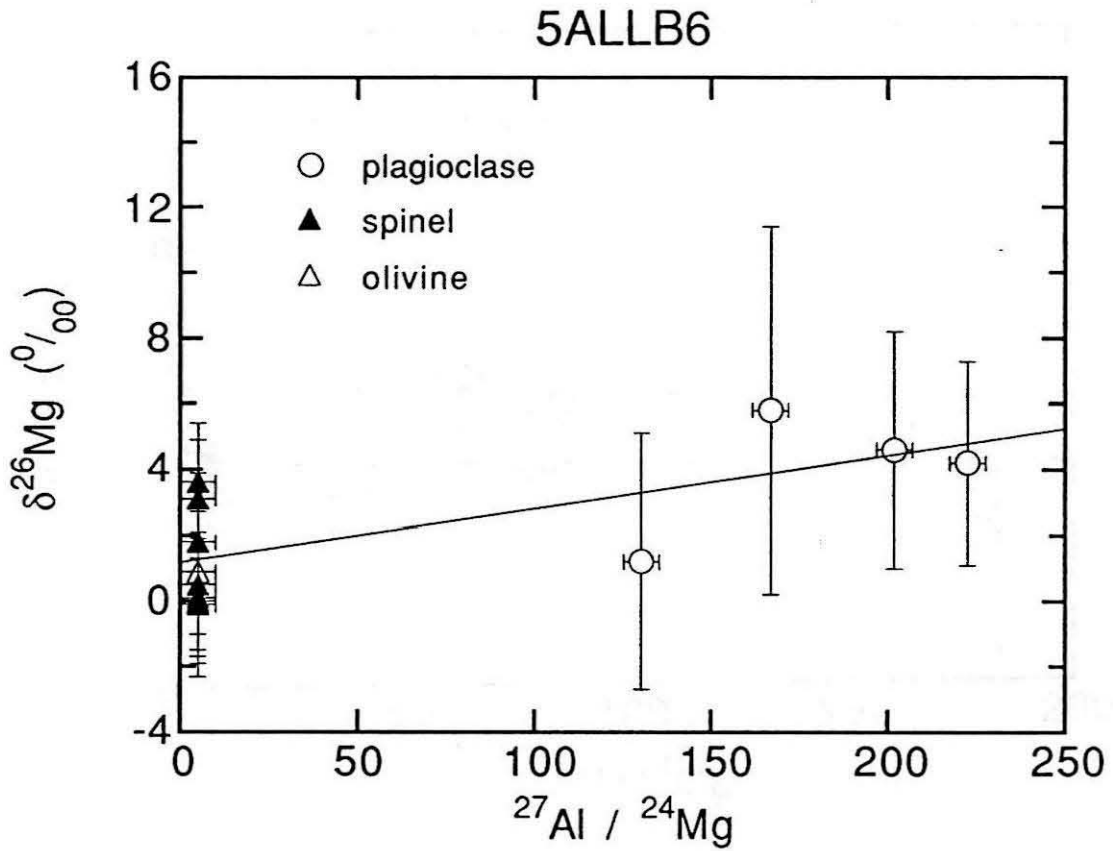


Fig.4.4 Mg isotopes of POI 5ALLB6 suggesting excess ^{26}Mg correlated with in-situ decay of ^{26}Al . The best fit slope of the isochron corresponds to $(^{26}\text{Al}/^{27}\text{Al})_0 = 2.2 \pm 0.7 \times 10^{-6}$.

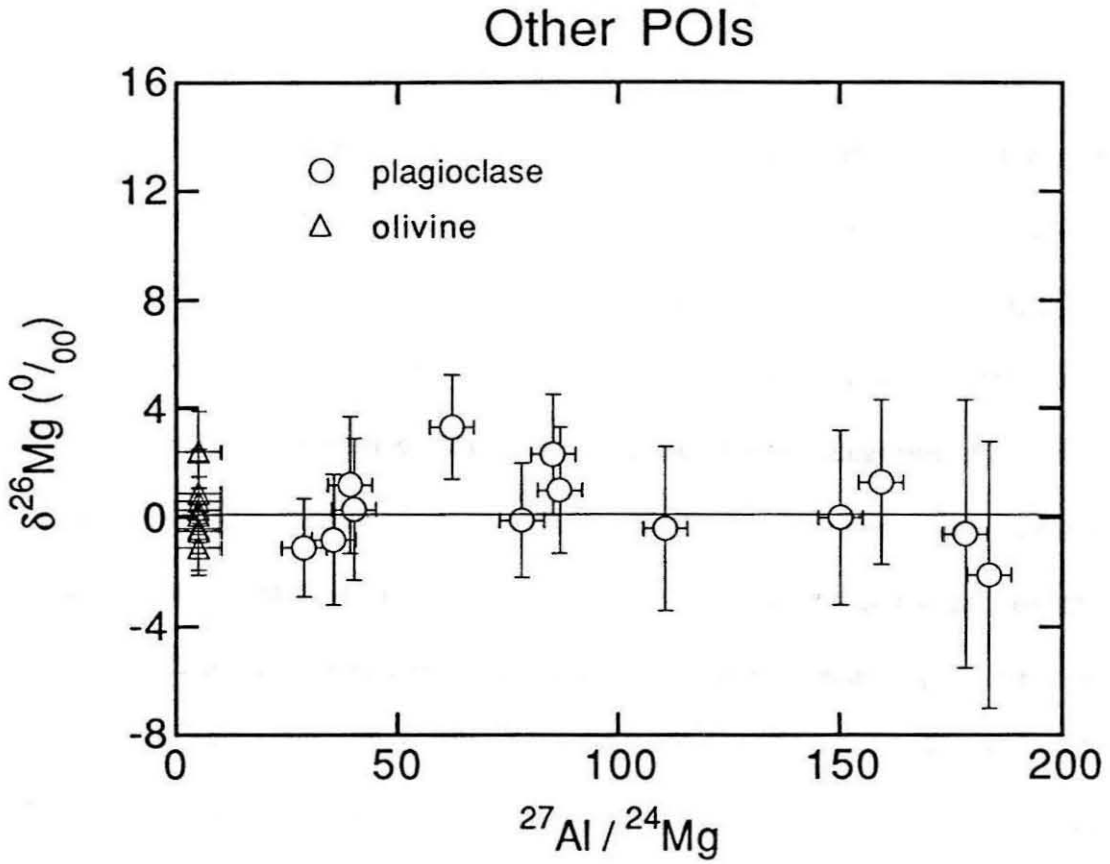


Fig.4.5 Mg isotopes of eight other POIs (BG82DH2, PPx, V477, BG82CH1, ALA1-2, BG82CLII, B14D, and ADEL-1) show no excess ^{26}Mg . The $(^{26}\text{Al}/^{27}\text{Al})_0$ ratio is less than 1.0×10^{-6} in all these inclusions.

CHAPTER FIVE

PHASE EQUILIBRIA STUDY

Recently, Ca- and Al-rich objects that appear transitional between CAIs and ferromagnesian chondrules have been observed in carbonaceous (Sheng *et al.*, 1991a), ordinary (Nagahara and Kushiro, 1982; Bischoff and Keil, 1983) and enstatite (Bischoff *et al.*, 1985) chondrites. The transitional Ca-Al-rich objects in chondrites can be classified based on the amount of plagioclase into two broad categories, Plagioclase-Olivine Inclusions (POIs) and CA chondrules (CACs). Although there has been considerable experimental effort to characterize the phase relations and dynamic crystallization behavior of CAIs (e.g., Stolper, 1982; Stolper and Paque, 1986) and dynamic crystallization experiments to elucidate the textures of ferromagnesian chondrules (Blander *et al.*, 1976; Planner and Keil, 1983; Lofgren and Russell, 1986), intermediate compositions relevant to these transitional objects have not been studied systematically.

Studies of phase relations for ferromagnesian chondrules have used either qualitative interpretations based on simple subsystems, or used synthetic analog of chondrule compositions applicable only to specific chondrules. In contrast, Stolper (1982) developed a spinel-saturated liquidus phase diagram that is remarkably successful in describing the crystallization behavior of many groups of coarse-grained CAIs. There

are four key reasons why this projection scheme works so well. First, spinel is generally the liquidus phase in CAIs and, with the possible exception of very late stage liquids, there is no reaction relation between spinel and melt that could drive the liquid composition off the saturation surface. Second, the spinel is essentially pure MgAl_2O_4 so there is no error in projection due to differences in composition between the phase crystallizing from the melt and the component (MgAl_2O_4) from which the melt composition is projected. Third, bulk compositions of most CAIs and their crystallization paths plot inside the ternary. In general, the crystallization behavior of bulk compositions that plot outside the ternary or under the saturation surface cannot be conveniently described using Stolper's projection for CAIs. Finally, the bulk compositions of CAIs are relatively simple, consisting mostly of CaO , MgO , Al_2O_3 and SiO_2 (CMAS). By projecting from one component, crystallization of spinel-saturated melts can be determined with the aid of a single ternary projection.

Like CAIs, the chemistry of POIs and CACs is relatively simple, consisting mainly of CMAS with lesser amounts of Na and Fe. Provided concentrations of Na and Fe are low enough, an approach similar to that of Stolper (1982) can be used to describe the crystallization behavior of POIs and CACs. In Fig. 1, bulk compositions of POIs and CACs with < 4 wt. % Na_2O and < 3 wt. % FeO are projected from spinel (Sp; MgAl_2O_4) onto the plane defined by the compositions of gehlenite (Ge; $\text{Ca}_2\text{Al}_2\text{SiO}_7$), anorthite (An; $\text{CaAl}_2\text{Si}_2\text{O}_8$) and forsterite (Fo; Mg_2SiO_4). Also shown are contours in weight percent of the spinel coordinate on the spinel saturation surface which describes the compositions of liquids that coexist with spinel and one or more additional solids. Bulk compositions

with spinel contents greater than that on the saturation surface and inside the ternary have spinel on the liquidus and the crystallization sequence can be readily determined using this figure (see Stolper, 1982, for a discussion). CAI compositions plot mostly in the Ge+Sp+liquid (L) or An+Sp+L fields (MacPherson *et al.*, 1988). However, only three of 44 POI and CAC bulk compositions plotted in Fig. 1, are both inside the ternary and above the spinel saturation surface. The liquid line of descent for five others plotting inside the ternary, intersect the spinel saturation surface after crystallizing small amounts of olivine. For the vast majority of POIs and CACs alternative projection schemes are needed in order to understand the phase relations of these inclusions.

In this chapter, I report the results of equilibrium crystallization experiments on representative POI bulk compositions at one atmosphere total pressure. Integration of our results with available phase equilibrium data from the literature provides a framework for the interpretation of mineral assemblages observed in POIs and some CACs. I have projected multiply saturated liquidus phase fields from spinel, forsterite and anorthite, respectively, onto relevant composition planes so that the crystallization behavior of POI and CAC compositions containing low amounts of Na₂O (< 4 wt. %) and FeO (< 3 wt. %) can be evaluated. I will initially look at the inclusions that comply to the above criteria but later we will also examine those with higher Na and/or Fe.

Phase assemblages predicted on the basis of phase equilibria are generally consistent with those observed in the meteoritic inclusions. POIs experienced a brief high temperature melting event in which relict phases were sometimes preserved. In many cases, phases identified as possibly relict on the basis of phase equilibria are also

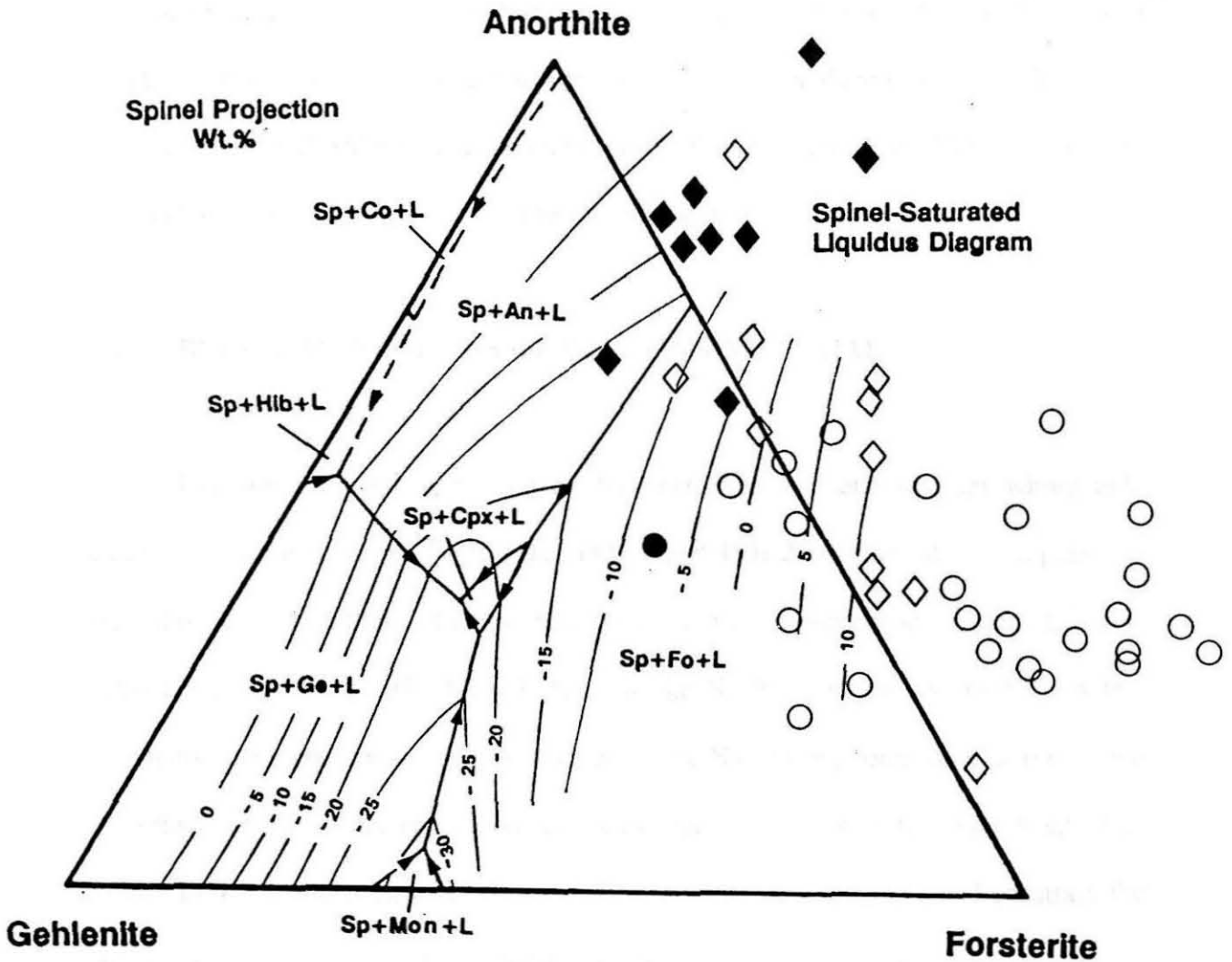


Fig.5.1 Spinel saturated liquidus diagram constructed by Stolper (1982). Contours denote wt.% spinel component above or below the anorthite-forsterite-gehlenite plane on the spinel saturation surface. Diamonds represent projected POI compositions (Sheng *et al.*, 1991a) and circles represent selected CA chondrule compositions (Nagahara and Kushiro, 1982; Bischoff and Keil, 1983; Bischoff *et al.*, 1985). Filled symbols indicate compositions that are above the spinel-saturation surface while open symbols represent compositions that are below the spinel-saturation surface. An-anorthite, Co-corundum, Cpx-clinopyroxene, Fo-forsterite, Ge-gehlenite, Hib-hibonite, L-liquid, Mon-monticellite, and Sp-spinel.

anomalous in their Mg isotopes (Sheng *et al.*, 1991a). In many CACs with abundant glass, the absence of plagioclase that were predicted to crystallize probably reflect rapid cooling of these chondrules and nucleation difficulty of plagioclase. Preliminary work on this experimental study was reported by Sheng *et al.* (1991b).

5.1. BULK COMPOSITIONS OF STARTING MATERIAL

Experiments were performed on five FeO-free synthetic samples whose bulk compositions are listed in Table 5.1. **POI-1** and **POI-2** correspond to compositions typical of spinel-rich POIs. Two Na-bearing starting mixes were made by adding 2 wt% (**POI-2Na2**) and 5 wt% (**POI-2Na5**) Na₂O to the Na-free composition **POI-2**. A few reconnaissance experiments were performed on the Na-bearing compositions to examine the effects of alkalis on phase boundaries in regions of interest for crystallization of POIs. **POI-3** was chosen to verify the stable equilibrium assemblage and constrain the position of the spinel+anorthite+forsterite+cordierite+liquid invariant point.

Table 5.1
Composition of starting material*

	Na ₂ O	MgO	Al ₂ O ₃	SiO ₂	CaO	TiO ₂	SUM
POI-1		15.50	34.76	40.18	9.12	0.51	100.07
POI-2		12.88	32.53	41.14	12.61	1.01	100.17
POI-2Na2	2.17	12.71	32.06	39.47	12.45	1.14	100.00 ⁺
POI-2Na5	5.03	12.43	31.27	38.14	11.92	1.21	100.00 ⁺
POI-3		22.52	21.11	51.41	4.96	1.05	101.05

* WDS analysis on starting glass composition.

⁺ Analyses were normalized to 100.

5.2. EXPERIMENTAL RESULTS

5.2.1. Crystallization Experiments

Results of isothermal crystallization experiments are tabulated in Table 5.2 and summarized in Fig.5.2. For bulk composition **POI-1**, the equilibrium crystallization sequence is spinel (1605-1613°C), followed by anorthite (1332-1343°C), and forsterite plus cordierite (~1260°C). The appearance temperature of anorthite was reversed (89I-13) by holding the sample at 1332°C for 12 hours to produce a phase assemblage of anorthite + spinel + liquid, raising the temperature to 1343°C, where it was held for 21 hours and quenched. The anorthite, which had crystallized during the first part of the experiment, dissolved during the second part of the experiment, demonstrating that 1343°C is above the appearance temperature of anorthite. The appearance of spinel + aluminous-enstatite (Al-enstatite), rather than cordierite + forsterite, in a 24 hour run at 1253°C (88I-9) is also noted. Most of the observed assemblage consists of spinel + Al-enstatite + anorthite with a small localized region in the run product containing spinel + Al-enstatite + anorthite + cordierite. Another run (89I-8) held at a subsolidus temperature of 1228°C for 208 hours has a crystalline assemblage of sapphirine + Al-enstatite + anorthite. Sapphirine appears as small micron sized euhedral prismatic crystals. When this assemblage is reheated at 1253°C and 1260°C, the run products recrystallize to form spinel + anorthite + forsterite + cordierite, suggesting that the sapphirine may have crystallized metastably. For **POI-2**, spinel is

Table 5.2
Experimental Results

Run #	T°(C)	Duration (hrs)	Starting material	Phases present [†]
POI-1				
88I-15	1613	2	gl	gl
88I-17	1605	2.7	gl	gl,sp
88I-16	1596	3	gl	gl,sp
88I-13	1527	3	gl	gl,sp
88I-6	1490	4.2	gl	gl,sp
88I-5	1462	5.8	gl	gl,sp
88I-4	1420	11.8	gl	gl,sp
88I-7	1391	14.5	gl	gl,sp
88I-11	1354	18.5	gl	gl,sp
88I-22*	1332/1343	12/20.8	gl+sp+an	gl,sp
88I-14	1332	12	gl	gl,sp,an
88I-2	1318	13	gl	gl,sp,an
88I-24	1311	21	gl	gl,sp,an
88I-8	1300	21	gl	gl,sp,an
88I-1	1271	26.3	gl	gl,sp,an
88I-23	1262	31	gl	gl,sp,an
89I-13	1228/1260	208/168	an+en+sap	gl,sp,an,fo,cd
88I-9	1253	24	gl	an,sp,en,cd
89I-9	1253	382	gl	an,fo,en,cd,sap
88I-10	1238	25.5	gl	an,en,sap
89I-8	1228	208	gl	an,en,sap

POI-2

88I-15	1613	2	gl	gl
88I-21	1552	3	gl	gl
88I-19	1546	3.3	gl	gl,sp
88I-20	1542	3	gl	gl,sp
88I-13	1527	3	gl	gl,sp
88I-6	1490	4.2	gl	gl,sp
88I-5	1462	5.8	gl	gl,sp
88I-4	1420	11.8	gl	gl,sp
88I-7	1391	14.5	gl	gl,sp
89I-10	1351/1381	23.5/9.3	gl+sp+an	gl,sp,an
88I-18	1372	11.5	gl	gl,sp,an
88I-11	1354	18.5	gl	gl,sp,an
88I-14	1332	12	gl	gl,sp,an
88I-24	1311	21	gl	gl,sp,an
88I-8	1300	21	gl	gl,sp,an
89I-2	1260/1281	168/23.5	gl+sp+an+fo	gl,sp,an
88I-1	1271	26.3	gl	gl,sp,an,fo
89I-13	1260	168	gl	gl,sp,an,fo
88I-9	1253	24	gl	gl,sp,an,fo
88I-10	1238	25.5	gl	sp,an,fo

POI-3

89I-1	1605	12	gl	gl
89I-2	1451	12	gl	gl
89I-18	1351	24.5	gl	gl,sp,fo
89I-17	1281	22	gl	gl,sp,fo,cd,en
89I-27	1277	33.5	gl	gl,sp,fo,cd,en
89I-19	1269	21	gl	gl,sp,fo,cd,en
89I-14	1260	24	gl	gl,sp,en,sap
89I-28	1250/1261	109/48.5	gl+an+fo+cd+en	gl,an,fo,cd,en
89I-28	1250	109	gl	gl,an,fo,cd,en

POI-2Na2

88I-15	1613	2	gl	gl
91I-1	1553/1450	3/0.5	gl+sp	gl
89I-6	1550	1.3	gl	gl,sp
89I-5	1542	3	gl	gl,sp
89I-4	1498	2.7	gl	gl,sp
89I-22	1343	20.8	gl	gl,sp
89I-24	1311	21	gl	gl,sp
89I-11	1288/1300	12.8/12.5	gl	gl,sp,pl
89I-11	1288	12.5	gl	gl,sp,pl
89I-2	1281	23.5	gl	gl,sp,pl,fo
89I-3	1233	35.3	gl	gl,sp,pl,fo
89I-7	1206	39.3	gl	gl,sp,pl,fo
90I-1c	1250/1237	26.5/18.5	gl+sp+fo	gl,sp
90I-1b	1237/1222	18.5/19.8	gl+sp+fo	gl,sp,fo
90I-1a	1222/1206	19.8/9	gl+sp+fo	gl,sp,fo

POI-2Na5

88I-15	1613	2	gl	gl
91I-1	1553/1450	3/0.5	gl+sp	gl
89I-6	1550	1.3	gl	gl,sp
89I-5	1542	3	gl	gl,sp
89I-4	1498	2.7	gl	gl,sp
88I-24	1311	21	gl	gl,sp
90I-1	1250/1237	26.5/18.5	gl+sp+fo	gl,sp
90I-1	1237/1222	18.5/19.8	gl+sp+fo	gl,sp,fo
90I-1	1222/1206	19.8/9	gl+sp+fo	gl,sp,fo
89I-3	1233	35.3	gl	gl,sp
89I-7	1206	39.3	gl	gl,sp,fo

POI-1C

 cooling rate = 100°C/hr

POI-1C1	1290	gl	gl,sp
	1200	gl	gl,sp,an,en

 cooling rate = 20°C/hr

POI-1C2	1195	gl	gl,sp
	1090	gl	gl,sp
	1042	gl	gl,sp,an,en

- * This entries for temperature and run time indicate that the experiment was held at the final temperature (1332°C) for 12 hours and at the initial temperature (1343°C) for 20.8 hours. The "starting material" entry refers to the phase assemblage present at the end of the first leg of the experiment.

- † gl = glass; an = anorthite; cd = cordierite; en = enstatite; fo = forsterite; pl = plagioclase; sap = sapphirine; sp = spinel.

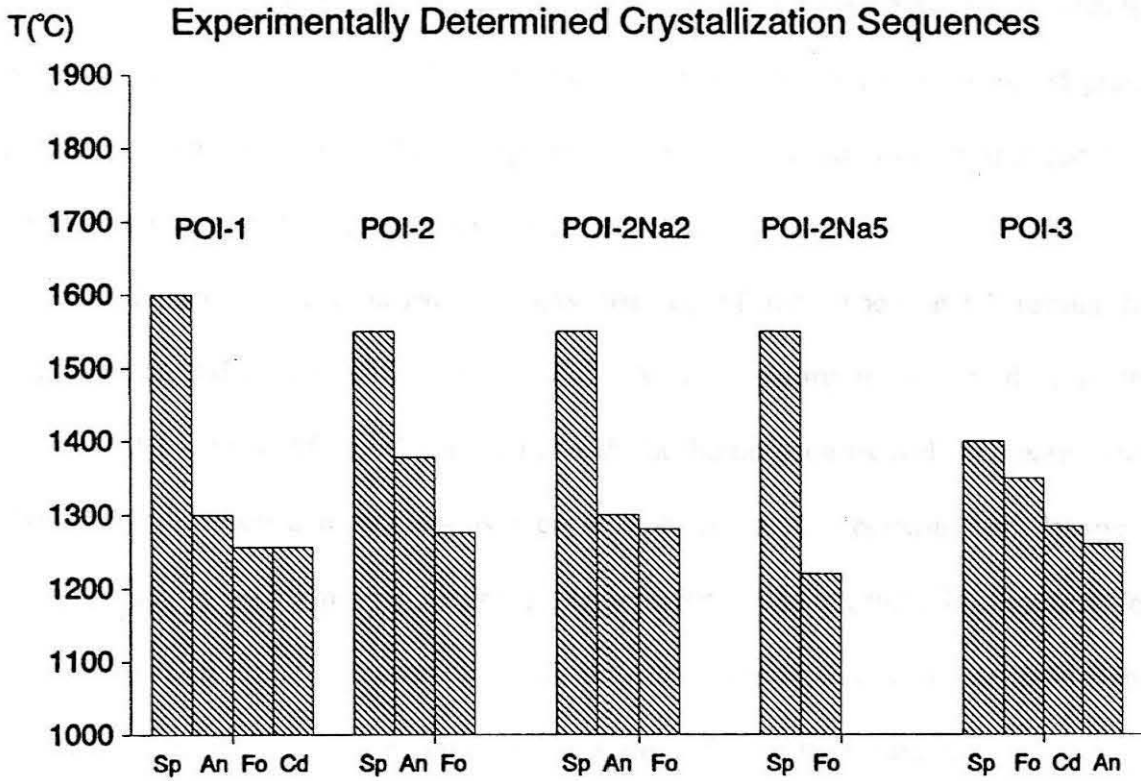


Fig.5.2 Summary of experimental runs on the 5 different starting compositions. Each bar represents the appearance temperature of a corresponding phase. Cd-cordierite and Pl-plagioclase. Other abbreviations as in Fig.1.

also the liquidus phase (1546-1552°C) followed by anorthite (1381-1391°C) and forsterite (1271-1281°C), the latter representing a reversal. For both **POI-1** and **POI-2**, most of the liquid is exhausted by the time the third phase crystallizes from the liquid. The crystallization sequence for **POI-3** is spinel (1351-1451°C) followed by forsterite (1351-1451°C), cordierite (1285-1301°C) and anorthite (1261-1269°C). Although Al-enstatite is present in all experiments below 1300°C, it is invariably found as corroded grains enclosed within cordierite. This suggests that Al-enstatite possibly crystallized as a metastable phase in these experimental runs.

Calculated modes, based on mass balance of the experimental results for composition **POI-2**, are shown in Fig.5.3. As temperature is decreased from the liquidus, the amount of spinel coexisting with the liquid progressively increases until about 1350°C, where anorthite begins to crystallize. A marked decrease in modal spinel occurs when the third phase, forsterite, crystallized. This feature is also true for composition **POI-1** and indicates spinel falls into a reaction relation with the liquid along part of the boundary curve for spinel + anorthite + forsterite + liquid.

A few reconnaissance experiments were performed to evaluate the effect of Na₂O on the phase equilibria for early crystallizing phases. Results are summarized in Fig.5.2. The crystallization sequence for **POI-2Na2** is spinel (1550-1553°C), followed by plagioclase (An₈₅) (1300-1311°C) and forsterite (1281-1288°C). Spinel is also the liquidus phase for composition **POI-2Na5** (1550-1553°C) with forsterite second (1237-1250°C). Plagioclase was not observed in any **POI-2Na5** experimental charges even for temperatures as low as 1206°C. The crystallization sequence for composition **POI-3** is

spinel (1351-1451°C), followed by forsterite and cordierite (1281-1351°C) and anorthite (1261-1269°C). This sequence indicates that there is a stability field for cordierite + spinel + liquid and that enstatite + spinel + liquid is not a stable assemblage.

Representative analyses of phases from run products are presented in Table 5.3. The anorthite analyses always contain small amounts of MgO (0.5-2%), probably due to contamination of the very small (a few microns wide) grains by surrounding crystals or glass. In the experiments with the Na-bearing composition, plagioclase contains 0.7-1.7% Na₂O. This is similar to the plagioclase composition from the experimental data of Pan and Longhi (1989) in the Na₂O-CaO-MgO-Al₂O₃-SiO₂ system, simulating compositions of alkaline basic lavas. The data are also comparable to the experimentally determined crystal-liquid partition coefficients between olivine and plagioclase in a tholeitic basalt magma (Yurimoto and Sueno, 1984). Experimentally determined $D_{CaO}^{ol,L}$ are similar to predicted concentrations based on experimentally determined olivine-liquid partition coefficients (Watson, 1979; Jurewicz and Watson, 1988). Synthetic enstatites have compositions along the binary Mg₂Si₂O₆-MgAl₂SiO₆ and are characterized by high Al₂O₃ (12-14%) contents similar to those observed in Al-enstatites of natural POIs (Sheng *et al.*, 1991a). Cordierite compositions are essentially stoichiometric Mg₂Al₄Si₅O₁₈ and spinel is stoichiometric MgAl₂O₄. Sapphire produced from my experiments is similar in composition to that observed in natural POIs (Sheng *et al.*, 1991a) but distinctly Mg-, Si-rich and Al-poor relative to terrestrial sapphirines. As shown in Fig.5.4, terrestrial sapphirine compositions (Deer *et al.*, 1978; Higgins *et al.*, 1979) can be well described by a solid solution series between Mg₈Al₁₆Si₄O₄₀ (2:2:1) and Mg₇Al₁₈Si₃O₄₀ (7:9:3)

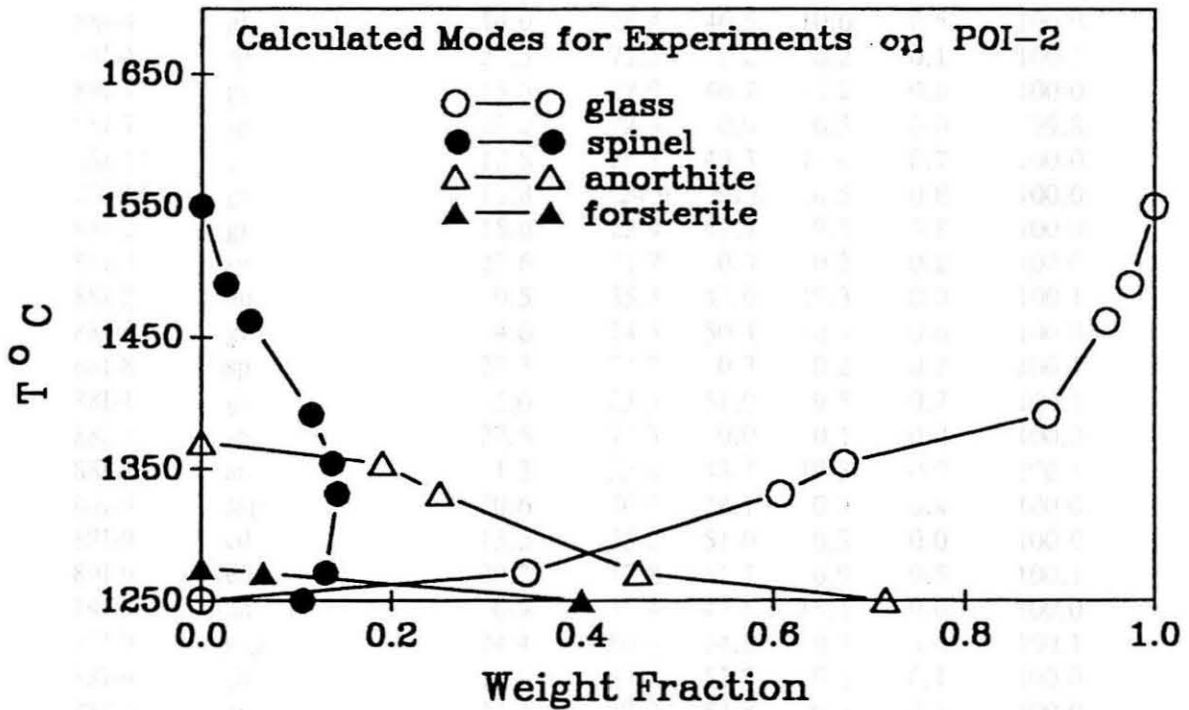


Fig.5.3 Calculated modes for runs on composition POI-2. A significant decrease in spinel occurs when anorthite and forsterite appears in the assemblage. This suggests that spinel is in reaction relation with the liquid on part of the Sp+An+Fo+L boundary curve and possibly in a region on the Sp+An+L surface.

Table 5.3
Representative analyses of experimental phases

Run #	Phase	Na ₂ O	MgO	Al ₂ O ₃	SiO ₂	CaO	TiO ₂	Total
POI-1								
88I-15	gl*		15.5	34.8	40.2	9.1	0.5	100.1
88I-16	gl		16.7	36.4	39.2	7.3	0.4	100.1
88I-6	gl*		14.7	31.8	42.6	10.3	0.6	100.0
88I-5	gl		14.0	30.1	44.8	10.3	0.8	100.0
88I-5	sp		27.1	72.8	0.0	0.1	0.0	100.0
88I-4	gl		14.0	28.4	46.5	10.6	0.5	100.0
88I-4	sp		27.3	72.3	0.2	0.2	0.1	100.1
88I-7	gl*		13.6	27.9	46.7	11.2	0.6	100.0
88I-7	sp		27.2	72.3	0.0	0.3	0.0	99.8
88I-11	gl		12.8	25.8	49.3	11.4	0.7	100.0
88I-14	gl		13.8	24.9	50.0	10.5	0.8	100.0
88I-2	gl		15.0	22.9	51.9	9.5	0.8	100.0
88I-2	sp		27.6	71.7	0.3	0.2	0.2	100.0
88I-2	an		0.5	35.3	45.0	19.3	0.0	100.1
88I-8	gl		14.6	24.3	50.4	10.1	0.6	100.0
88I-8	sp		27.3	71.7	0.7	0.2	0.2	100.1
88I-1	gl		15.6	23.3	51.0	9.5	0.7	100.1
88I-1	sp		27.6	72.3	0.0	0.1	0.0	100.0
88I-1	an		1.3	35.8	43.7	19.3	0.0	100.1
89I-9	sap		20.6	50.6	28.1	0.3	0.4	100.0
89I-9	cd		13.5	35.2	51.0	0.3	0.0	100.0
89I-9	en		29.2	17.8	51.7	0.9	0.5	100.1
89I-9	an		0.9	35.4	45.6	18.1	0.0	100.0
88I-9	sap		24.4	50.0	24.8	0.3	0.6	100.1
88I-9	cd		13.9	33.2	52.7	0.1	0.1	100.0
88I-9	en		34.4	12.0	52.8	0.5	0.3	100.0
88I-9	an		0.6	35.3	45.1	19.1	0.0	100.1
88I-9	sp		27.4	70.5	1.9	0.0	0.3	100.1
88I-9	fo		56.5	0.7	42.8	0.1	0.1	100.1
88I-10	sap		23.7	54.3	19.0	2.5	0.6	100.1
89I-8	en		33.2	13.9	51.5	0.7	0.8	100.1
89I-8	sap		23.0	51.6	23.1	1.5	0.9	100.1
POI-2								
88I-15	gl*		12.9	32.5	41.1	12.6	1.0	100.2
88I-6	gl		12.7	32.2	41.5	12.5	1.3	100.2
88I-6	sp		26.9	72.9	0.0	0.2	0.0	100.0
88I-5	gl		12.3	31.0	43.0	12.6	1.1	100.0
88I-5	sp		27.1	72.7	0.0	0.2	0.0	100.0
88I-4	gl		7.5	35.6	43.2	12.7	1.1	100.1
88I-7	gl		11.5	28.5	45.4	13.6	1.2	100.2
89I-10	gl		11.1	27.1	46.3	14.3	1.2	100.0
88I-18	gl		12.8	27.0	47.5	11.5	1.2	100.0
88I-14	gl		14.3	23.5	48.5	12.3	1.4	100.0

88I-8	gl	15.0	23.0	47.8	12.3	1.8	99.9
88I-8	sp	27.2	72.5	0.2	0.2	0.0	100.1
88I-8	an	0.6	36.1	43.5	19.7	0.0	99.9
88I-1	gl	15.8	21.9	49.1	10.9	2.3	100.0
88I-1	sp	27.6	71.5	0.6	0.2	0.2	100.1
88I-9	gl	15.2	21.4	51.5	8.2	3.8	100.1
88I-9	sp	27.1	71.8	0.5	0.3	0.3	100.0
88I-9	fo	55.4	0.8	43.5	0.3	0.0	100.0
88I-9	an	2.1	33.9	44.1	19.9	0.0	100.0

POI-3

89I-1	gl*	22.5	21.1	51.4	5.0	1.1	101.1
89I-2	gl	22.2	21.4	50.4	4.9	1.0	99.8
89I-17	gl	15.9	21.7	52.2	8.3	1.7	99.8
89I-17	cd	14.0	34.2	51.1	0.0	0.2	99.5
89I-27	gl	16.1	22.0	51.6	8.3	1.8	99.8
89I-27	fo	56.1	0.3	42.9	0.3	0.3	99.9
89I-19	gl	15.9	22.0	52.3	8.0	1.6	99.7
89I-14	en	33.5	14.6	51.1	0.4	0.4	100.0
89I-14	sp	27.2	71.9	0.7	0	0.2	100.0

POI-2Na2

88I-15	gl*	2.2	12.7	32.1	39.5	12.5	1.1	100.0
89I-6	sp		27.0	72.3	0.0	0.2	0.2	99.6
89I-6	gl	2.2	12.8	31.6	39.9	12.3	1.2	100.0
89I-5	gl	1.9	12.9	31.8	40.1	12.4	1.0	100.0
89I-4	gl	1.8	12.3	30.5	41.3	13.1	1.1	100.1
88I-22	gl	2.5	11.2	26.4	46.6	12.4	1.0	100.0
88I-22	sp		27.3	72.3	0.0	0.1	0.0	99.7
88I-24	gl	3.0	11.4	23.3	46.8	14.2	1.3	100.0
89I-11	gl	2.2	12.2	22.8	47.7	13.9	1.2	100.0
89I-11	pl	0.7	1.4	33.8	44.7	19.0	0.4	100.0
89I-2	gl	3.5	11.8	22.0	47.3	13.5	1.9	100.0
89I-2	fo		55.5	2.2	41.4	0.3	0.0	99.3
89I-2	pl	1.5	2.9	31.7	46.6	16.7	0.6	100.0
89I-3	pl	1.7	0.3	33.7	46.9	17.2	0.2	100.0
89I-3	gl	5.0	8.7	22.3	46.7	13.5	3.8	100.0
89I-3	fo		55.9	0.0	42.5	0.6	0.0	99.0
89I-7	pl	1.6	2.0	33.0	45.0	17.7	0.9	100.0

POI-2Na5

88I-15	gl*	5.0	12.4	31.3	38.1	11.9	1.2	100.0
89I-6	gl	3.6	12.2	30.9	40.0	12.3	1.0	100.0
89I-5	gl	2.8	12.4	30.9	40.2	12.7	0.9	100.0
89I-4	gl	4.3	12.5	29.9	42.0	10.4	0.8	100.0
88I-24	gl	4.4	9.7	24.3	42.2	14.4	1.0	91.6
89I-3	gl	5.7	9.3	22.9	46.5	14.4	1.1	100.0

POI-1C

C1-1290	gl	12.2	24.6	50.8	11.8	0.8	100.2
C1-1220	gl	11.9	22.8	52.8	12.0	0.6	100.0

C1-1100	sp	27.3	71.5	0.6	0.2	0.2	99.8
C1-1100	an	1.2	32.5	47.4	18.7	0.0	99.8
C1-1100	en	32.9	11.6	53.6	1.4	0.5	100.0
C2-1195	gl	11.7	22.5	53.3	12.0	0.5	100.0
C2-1090	gl	11.1	21.2	54.7	12.2	0.8	100.0
C2-1090	sp	27.6	72.0	0.3	0.1	0.0	100.0
C2-1042	gl	6.1	13.4	70.8	3.5	6.3	100.0

* WDS analysis. All others EDS analysis.

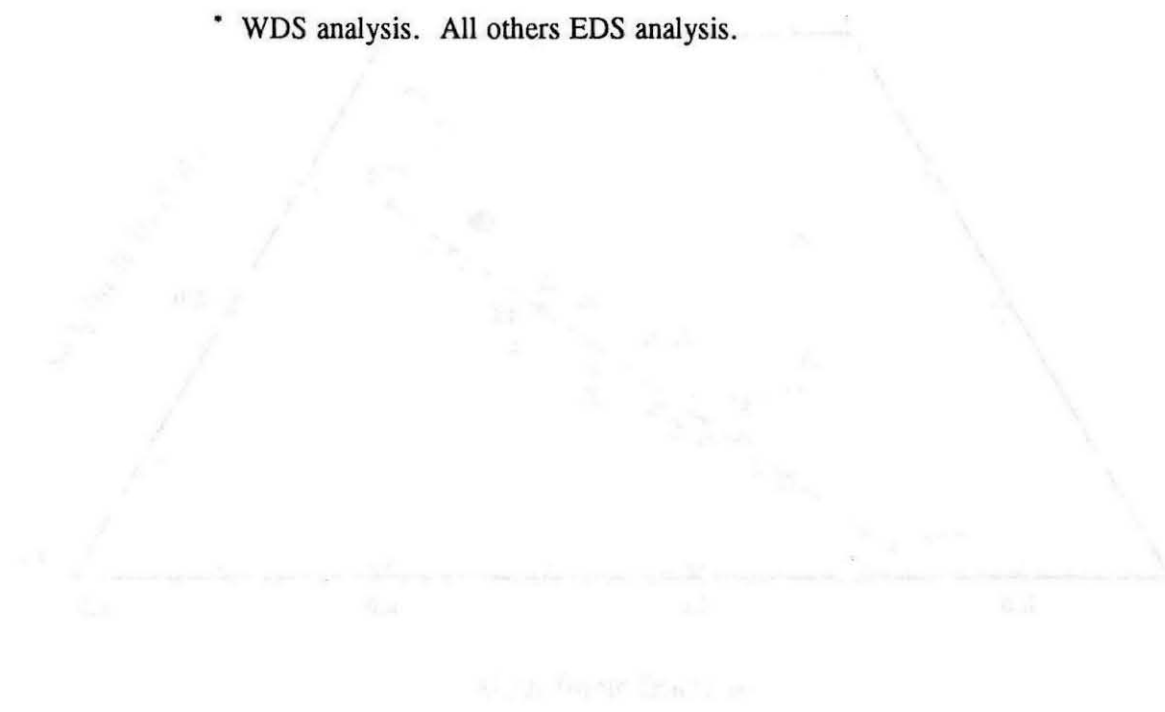


Fig. 2. Phase diagram of the Ca-Mg-Si system. The diagram shows the phase relationships between Ca, Mg, and Si. The vertices represent pure components: Ca at the top, Si at the bottom left, and Mg at the bottom right. The diagram shows various phase regions and reaction lines. Data points from the table are plotted on the diagram, showing the composition of different samples. For example, C1-1100 (sp) is located near the Ca-Si axis, while C2-1042 (gl) is located near the Si-Mg axis. The diagram illustrates the complex phase relationships between these three elements.

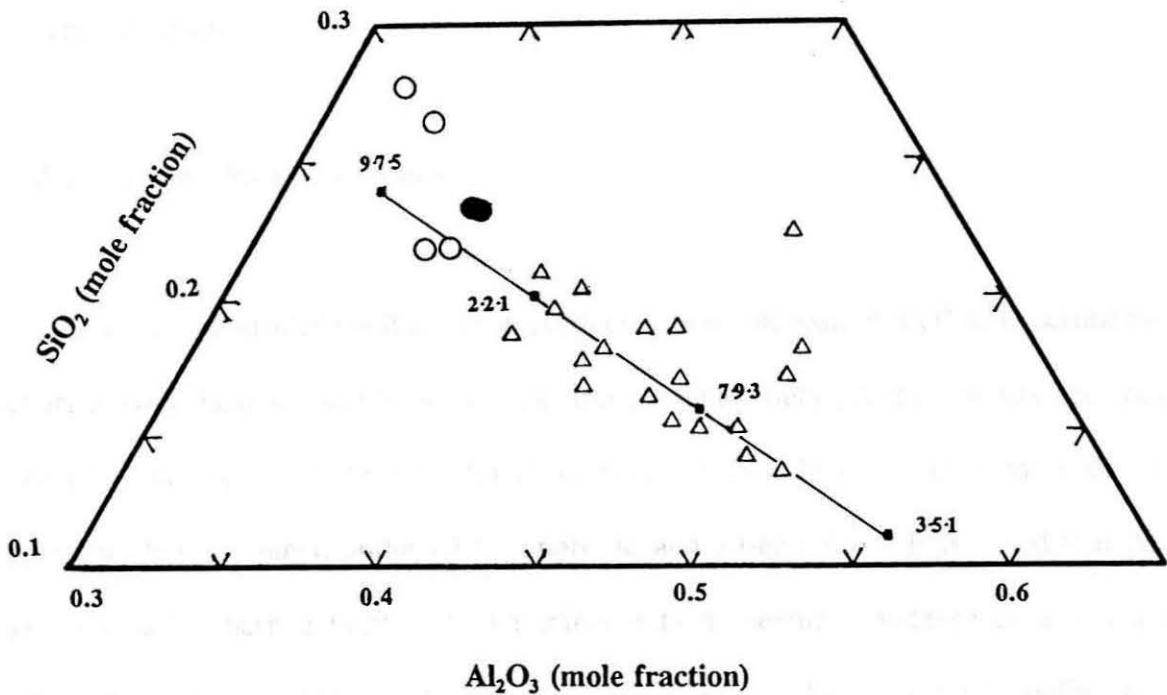


Fig.5.4 Compositions of sapphirine from natural POIs (filled circles; Sheng *et al.*, 1991a), from sapphirine in our experimental charges (open circles; this study), and terrestrial sapphirine (triangles) from the compiled data of Deer *et al.* (1978) and Higgins *et al.* (1979). Filled squares represent hypothetical sapphirine compositions where 2·2·1 denotes 2MgO·2Al₂O₃·SiO₂. It is apparent that natural POI sapphirines and those produced in our experiments are Mg-, Si-rich and Al-poor with respect to terrestrial sapphirines. Minor amount of other oxide components in sapphirine were subtracted from the sapphirine composition in the projection.

involving a coupled substitution of Mg and Si for Al. Sapphirine in our experiments and in POI have compositions between the 2:2:1 end-member and $\text{Mg}_9\text{Al}_{14}\text{Si}_5\text{O}_{40}$ (9:7:5). The differences between POI and terrestrial sapphirines probably reflect the conditions of their formation (igneous /metamorphic) as well as the bulk composition of their parental melt/rock.

5.2.2. Cooling Rate Experiments

In two controlled cooling rate experiments with composition **POI-1**, experimental charges were held at 1425°C within the spinel+liquid field for three hours and then cooled at rates of 20°C/hr and 100°C/hr, respectively. In both cases, the order of crystallization is spinel, followed by anorthite and Al-enstatite. It is noted that Al-enstatite is in sharp contact with the spinel with no textural evidence of a reaction relationship between them. The chemistry of phases produced in these cooling rate experiments (Table 5.3) is similar to that of phases crystallized in the isothermal experiments.

From my isothermal crystallization experiments, it appears that forsterite + cordierite is stable at low pressures relative to spinel + enstatite, a conclusion also reached by Schreyer and Schairer (1961), based on experiments on the system $\text{MgO}-\text{Al}_2\text{O}_3-\text{SiO}_2$. However, my experiments also clearly show that the metastable phase assemblage, spinel + Al-enstatite, is readily produced from glassy starting materials in the $\text{CaO}-\text{MgO}-\text{Al}_2\text{O}_3-\text{SiO}_2-\text{TiO}_2$ (CMAST) system. This feature should be kept in mind

when the results of phase equilibria are applied to meteoritic inclusions.

5.3. CONSTRUCTION OF PHASE DIAGRAMS

Methods for manipulating composition coordinates in n-dimensional composition space have been reviewed by Spear *et al.* (1982). The first step in constructing a phase diagram for the compositions of interest is to choose a compositional space that will best represent available phase equilibrium data graphically. Once the endmembers (coordinates) are decided, old coordinates (generally simple oxides) are transformed into new coordinates (composition of a mineral phase). The transformation of coordinate axes is performed by computing the elements of a composition vector in terms of any one of several different sets of components that might be chosen. For example, the phases of interest for compositions relevant to POIs are spinel, forsterite, anorthite, enstatite and diopside. Since these phases occupy only a small volume of the CMAS tetrahedron it would be more convenient to use just the relevant volume to represent POIs. One choice of components is the Sp-An-Fo-tridymite (Tr) volume. The relation of this subset to the CMAS tetrahedron is illustrated in Fig.5.5.

The first calculation involves mapping from one coordinate set into another. In the above case the old components are moles of the oxides CaO-MgO-Al₂O₃-SiO₂, and the new components are the end members spinel (MgAl₂O₄), anorthite (CaAl₂Si₂O₈), forsterite (Mg₂SiO₄) and tridymite (SiO₂). This may be done by simultaneous solution of the four mass balance equations for each oxide:

$$\begin{aligned}
 n_{CaO} &= n_{CaO}^{An} \\
 n_{MgO} &= 2n_{MgO}^{Fo} + n_{MgO}^{Sp} \\
 n_{Al_2O_3} &= n_{Al_2O_3}^{An} + n_{Al_2O_3}^{Sp} \\
 n_{SiO_2} &= 2n_{SiO_2}^{An} + n_{SiO_2}^{Fo} + n_{SiO_2}^{Tr} \quad ,
 \end{aligned}$$

where n is the number of moles of an oxide or a component. A general solution to the system of equations $A \cdot X = Y$ can be obtained by inversion of the coefficient matrix A and post-multiplication by the vector Y . Thus $A^{-1}Y = X$. The set of equations thus can be written as:

$$\begin{vmatrix} 1 & 0 & 0 & 0 \\ 0 & 2 & 1 & 0 \\ 1 & 0 & 1 & 0 \\ 2 & 1 & 0 & 1 \end{vmatrix} \cdot \begin{vmatrix} n_{An} \\ n_{Fo} \\ n_{Sp} \\ n_{Tr} \end{vmatrix} = \begin{vmatrix} n_{CaO} \\ n_{MgO} \\ n_{Al_2O_3} \\ n_{SiO_2} \end{vmatrix} \quad ,$$

where n_{An} , n_{Fo} , n_{Sp} and n_{Tr} are the number of moles of the end-member components.

Solution of the set of equations gives

$$\begin{aligned}
 n_{An} &= n_{CaO} \\
 n_{Fo} &= (n_{CaO} + n_{MgO} - n_{Al_2O_3}) / 2 \\
 n_{Sp} &= n_{Al_2O_3} - n_{CaO} \\
 n_{Tr} &= (n_{Al_2O_3} - 5n_{CaO} - n_{MgO} + 2n_{SiO_2}) / 2 \quad .
 \end{aligned}$$

Hence the coordinates calculated for the projections used in this study are as follows:

1. Projection of phases from spinel onto the plane Fo-An-Tr,

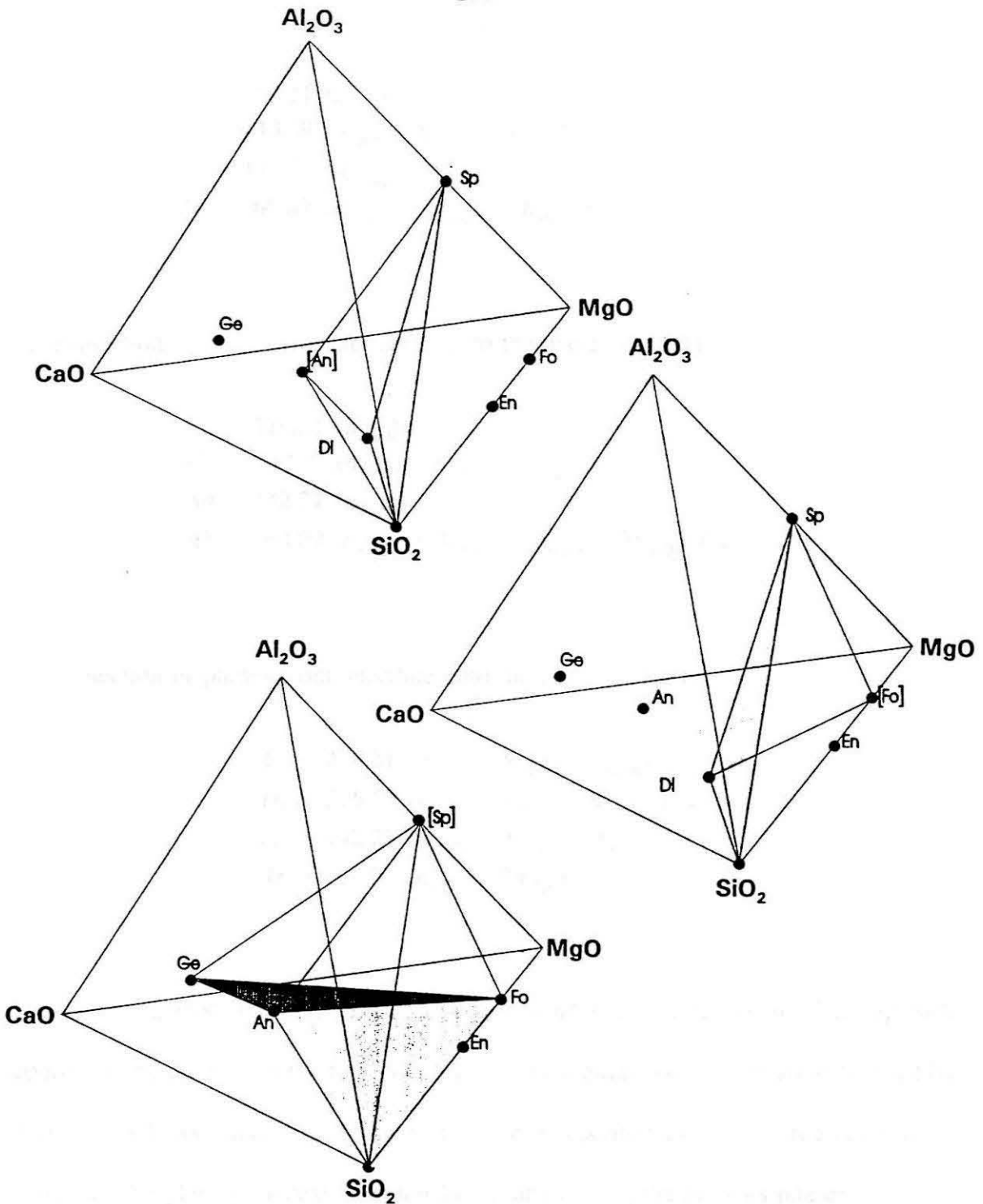


Fig.5.5 Schematic drawing illustrating the three projection schemes used in this study. The projected phase is denoted in brackets and the plane of projection is shaded. En-enstatite, Di-diopside. Other abbreviations given in previous figure captions.

$$\begin{aligned}
 An &= 278.21 (n_{CaO}) \\
 Fo &= 140.69 (n_{CaO} + n_{MgO} - n_{Al_2O_3}) / 2 \\
 Sp &= 142.27 (n_{Al_2O_3} - n_{CaO}) \\
 Tr &= 60.09 (n_{Al_2O_3} - 5n_{CaO} - n_{MgO} + 2n_{SiO_2}) / 2
 \end{aligned}$$

2. Projection of phases from forsterite onto the plane Di-Sp-Tr,

$$\begin{aligned}
 Di &= 216.55 (n_{CaO}) \\
 Fo &= 140.69 (n_{MgO} - n_{CaO} - n_{Al_2O_3}) / 2 \\
 Sp &= 142.27 (n_{Al_2O_3}) \\
 Tr &= 60.09 (n_{Al_2O_3} - 3n_{CaO} - n_{MgO} + 2n_{SiO_2}) / 2
 \end{aligned}$$

3. Projection of phases from anorthite onto the plane Di-Sp-Tr,

$$\begin{aligned}
 An &= 278.21 (n_{CaO} - n_{MgO} + n_{Al_2O_3}) \\
 Di &= 216.55 (n_{CaO} + n_{MgO} - n_{Al_2O_3}) / 2 \\
 Sp &= 142.27 (n_{MgO} + n_{Al_2O_3} - n_{CaO}) / 2 \\
 Tr &= 60.09 (n_{SiO_2} - 2n_{CaO})
 \end{aligned}$$

Oxides are in mole percent. Tetrahedral coordinates are calculated by dividing each coordinate by the sum of the four coordinates. Triangular coordinates are calculated by dividing each coordinate by the sum of the three coordinates. The three coordinates constitute the plane projected from the fourth phase (i.e., the liquidus phase).

5.4. PHASE DIAGRAMS FOR DETERMINING CRYSTALLIZATION SEQUENCES

My experimental data can be used in conjunction with available data from the literature to generate a database useful for interpreting phase relations for POI and CACs compositions. In the following section, phase diagrams for CMAS appropriate for depicting the crystallization sequences and phase relations of POIs and related objects are constructed. Relevant experimental data from Na- and Fe-bearing systems are then used to assess the effects of these components on the phase boundaries. I confine my applications to meteoritic inclusions for which the CMAS based phase diagrams are likely to constrain the igneous processes.

The Stolper projection depicted in Fig.5.1, together with three additional projections described below, are sufficient to predict the phase relations for most POIs and some CA chondrules. The data points in Figs. 5.6-5.8 represented by the open circles are from the literature, while filled circles in the figures are from this study (Table 5.4). Most of the data points are analyzed liquid compositions. Phase boundaries, isotherms, and constant spinel contours were drawn freehand through the scatter of liquid compositions on and near surfaces or boundaries. Berman's (1983) model for silicate melts was used to extrapolate contours into regions where no experimental data were available. Deviations between calculated and experimentally observed equilibrium temperatures for phase appearances average $\pm 33^{\circ}\text{C}$ (1σ) for the liquidus phase spinel, $\pm 24^{\circ}\text{C}$ for forsterite, and $\pm 40^{\circ}\text{C}$ for anorthite. The errors of the calculated components on respective surfaces are ± 3 wt.%. Sources of data used to construct the phase diagrams were from this study and from Bowen (1914), Andersen (1915), Rankin and Merwin (1918), Keith and Schairer (1952), Osborn and Tait (1952), Osborn *et al.*

Table 5.4

Data Used in Constructing Phase Diagram

#	assemblage	T(C)	Na2O	MgO	Al2O3	SiO2	CaO	TiO2	SUM
A1	an,sp	1444		8.02	31.52	43.13	17.34		100.01
A2	an,sp,fo	1320		16.90	22.36	48.45	12.30		100.01
A3	an,tr	1350		0.00	18.69	71.03	10.28		100.00
A4	an,fo,pr	1260		14.61	20.16	54.15	11.09		100.01
A5	an,tr,pr	1222		9.45	18.51	61.86	10.18		100.00
A6	fo,pr	1557		39.14	0.00	60.86	0.00		100.00
A7	fo,s	1446		26.36	19.79	42.97	10.88		100.00
B1	fo,di	1387		23.25	0.00	53.96	22.79		100.00
b1	sp,fo	1245	3.28	25.59	16.18	52.98	1.98		100.01
b2	sp,fo	1245	3.05	25.09	15.03	53.15	3.68		100.00
b3	sp,fo	1245	3.61	22.72	17.84	52.56	3.27		100.00
b4	sp,fo,an	1251	3.37	22.64	16.63	52.27	5.08		100.00
b5	sp,fo,an	1250	2.00	24.29	19.76	49.16	4.78		100.00
b6	sp,fo	1234	4.71	22.95	15.48	54.73	2.13		100.00
b7	sp,fo	1246	4.08	25.22	13.43	55.41	1.85		100.00
C1	an,tr	1368		0.00	18.70	71.02	10.28		100.00
D1	an,sp	1448		5.99	36.53	40.14	17.34		100.00
D2	an,sp	1448		6.40	34.30	40.43	18.87		100.00
D3	sp,fo	1553		30.93	18.99	41.21	8.87		100.00
D4	sp,fo	1544		29.64	19.06	40.82	10.48		100.00
D5	sp,an	1447		7.44	32.98	41.44	18.14		100.00
D6	sp,an,cd	1430		4.70	38.69	39.07	17.54		100.00
D7	an,cd	1513		2.07	39.21	40.04	18.69		100.01
GR1	an,tr,mu			5.00	21.80	67.30	5.70		99.80
GR2	sp,an,cd			5.00	35.00	42.00	18.00		100.00
Gt1	an,cd,mu	1550		0.00	37.00	47.50	15.50		100.00
Gt2	an,mu,tr	<1400		0.00	20.00	58.00	10.00		88.00
KS1	sp,co	1455		18.00	33.00	49.00	0.00		100.00
KS2	sp,mu,sa	1482		16.90	36.80	46.30	0.00		100.00
KS3	sp,sa,co	1453		17.40	33.50	49.10	0.00		100.00
L01	sp,fo	1358		18.50	21.80	47.00	12.00		99.30
L02	sp,fo	1341		17.80	22.00	48.00	12.30		100.10
L03	sp,fo	1326		16.60	22.00	48.20	12.20		99.00
L04	sp,fo	1318		15.50	20.80	47.00	16.40		99.70
L05	sp,fo	1316		15.60	21.50	47.00	16.00		100.10
L06	sp,fo	1313		15.60	21.80	47.80	14.60		99.80
L07	fo,an,sp	1312		15.30	21.40	47.10	16.60		100.40
L08	fo,an,sp	1303		15.90	22.30	49.20	12.70		100.10

Table 5.4
Data Used in Constructing Phase Diagram

#	assemblage	T(C)	Na2O	MgO	Al2O3	SiO2	CaO	TiO2	SUM
L09	fo,an,sp	1320		15.50	21.80	48.00	15.20		100.50
L10	fo,di,an	1270		13.40	15.70	49.40	21.60		100.10
L11	fo,di,an	1270		13.60	15.60	50.30	20.30		99.80
L12	fo,di,an	1263		13.40	15.60	50.40	19.50		98.90
L13	fo,di,an	1254		13.20	16.20	52.80	17.40		99.60
L14	fo,di,an	1243		12.50	15.40	53.50	16.00		97.40
L15	fo,an	1311		15.60	21.60	48.40	14.60		100.20
L16	fo,an	1309		15.20	20.90	46.80	17.30		100.20
L17	fo,an	1290		15.60	21.60	51.10	11.60		99.90
L18	fo,an	1269		14.30	20.10	53.70	11.40		99.50
L19	fo,an	1254		13.00	17.20	55.10	14.70		100.00
L20	fo,an	1265		13.80	19.60	53.70	11.10		98.20
L21	fo,an,pr	1254		12.70	17.20	55.60	13.50		99.00
L22	fo,an,oe	1243		12.40	15.80	54.40	15.10		97.70
L23	fo,an,pr,oe	1243		12.50	16.30	53.70	14.60		97.10
L24	an,pr	1265		13.00	19.00	56.40	11.10		99.50
L25	an,pr	1254		12.40	17.60	56.90	12.80		99.70
L26	an,pr	1243		12.40	16.40	55.20	14.30		98.30
L27	an,pr	1230		9.50	17.70	62.00	10.00		99.20
L28	an,pr,oe	1226		9.80	15.40	58.80	14.60		98.60
L29	an,oe,di	1226		10.20	15.40	59.10	15.20		99.90
L30	fo,an,pr	1263		14.00	19.00	54.90	11.60		99.50
L31	fo,an,di,oe	1240		12.50	15.50	55.50	16.40		99.90
L32	an,tr,di	1215		8.10	14.20	62.50	13.60		98.40
L33	an,tr,di	1211		4.80	14.50	62.40	18.00		99.70
L34	an,tr,di	1195		3.30	13.70	61.50	19.90		98.40
L35	an,tr	1234		8.80	17.60	63.20	9.30		98.90
L36	an,tr	1216		7.10	14.40	61.30	14.70		97.50
L37	an,tr,pr	1229		9.40	18.00	63.00	9.50		99.90
L38	an,tr,pr	1215		9.00	16.40	62.90	12.30		100.60
L39	an,tr,pr,oe	1211		8.50	15.10	62.70	13.00		99.30
L40	an,tr,oe	1211		8.60	15.30	62.80	13.30		100.00
L41	an,tr,oe,di	1195		8.30	14.50	60.20	13.30		96.30
L42	an,tr,di	1200		3.80	14.30	61.80	19.50		99.40
L43	an,tr	1223		6.70	15.60	63.40	14.20		99.90
L44	an,tr	1215		4.10	13.50	63.30	17.60		98.50
L45	an,tr,di	1211		5.10	14.30	60.80	16.20		96.40
L46	fo,pr	1371		20.40	14.20	56.10	8.30		99.00

Table 5.4
Data Used in Constructing Phase Diagram

#	assemblage	T(C)	Na ₂ O	MgO	Al ₂ O ₃	SiO ₂	CaO	TiO ₂	SUM
L47	fo,pr	1371		20.70	8.10	57.00	13.70		99.50
L48	fo,pr	1330		18.00	15.90	55.60	9.70		99.20
L49	fo,pr	1330		17.50	10.20	57.30	15.20		100.20
L50	fo,pr	1291		16.00	17.60	55.20	10.80		99.60
L51	fo,pr	1267		13.80	15.70	55.90	14.50		99.90
L52	fo,pr,oe	1267		13.40	14.90	55.60	15.90		99.80
L53	fo,pr,oe	1254		13.00	16.10	55.30	15.30		99.70
L54	fo,oe	1353		20.30	6.80	57.60	15.90		100.60
L55	fo,oe	1330		17.50	9.40	56.40	16.00		99.30
L56	fo,oe	1318		17.10	9.00	56.40	17.00		99.50
L57	fo,oe	1312		16.40	10.10	56.40	17.40		100.30
L58	fo,oe	1291		15.80	12.00	56.90	16.60		101.30
L59	fo,oe,pi	1330		18.00	8.60	56.80	16.80		100.20
L60	fo,pi	1353		20.70	5.40	57.60	17.40		101.10
L61	fo,pi	1353		21.00	4.40	57.50	17.60		100.50
L62	fo,pi	1335		18.80	7.70	56.10	16.80		99.40
L63	fo,pi,di	1335		18.50	6.60	57.10	17.80		100.00
L64	fo,pi,di	1321		18.60	7.10	56.60	17.40		99.70
L65	fo,pi,di	1319		17.90	8.20	56.80	17.60		100.50
L66	fo,oe,di	1322		17.50	8.60	57.10	17.60		100.80
L67	fo,oe,di	1318		17.50	8.50	56.80	17.20		100.00
L68	fo,oe,di	1313		17.00	9.10	56.00	17.60		99.70
L69	fo,oe,di	1305		17.00	9.60	57.70	17.40		101.70
L70	fo,oe,di	1305		16.70	9.60	56.90	17.50		100.70
L71	fo,oe,di	1291		15.80	11.20	56.60	17.30		100.90
L72	fo,oe,di	1287		15.30	11.80	56.50	17.10		100.70
L73	fo,oe,di	1277		14.70	12.60	55.60	16.40		99.30
L74	fo,oe,di	1267		13.80	13.20	55.60	16.90		99.50
L75	fo,oe,di	1254		13.00	15.20	55.60	16.00		99.80
L76	fo,pi,oe,di	1320		17.30	8.80	56.40	17.60		100.10
L77	fo,an,di	1275		13.40	15.70	49.60	21.50		100.20
L78	fo,an,pr	1263		14.60	19.90	54.30	11.20		100.00
L79	fo,an,di,oe	1240		12.40	15.20	55.40	17.00		100.00
LB1	oe,pr,fo	1445		27.47	0.00	59.81	12.72		100.00
LB2	oe,pi,fo	1410		24.53	0.00	59.75	15.72		100.00
LB3	pi,di,fo	1385		23.21	0.00	58.82	17.87		99.90
O01	an,co,sp	1315		14.00	25.00	52.00	9.00		100.00
O02	an,sp	1349		10.00	25.00	43.00	22.00		100.00

Table 5.4

Data Used in Constructing Phase Diagram

#	assemblage	T(C)	Na2O	MgO	Al2O3	SiO2	CaO	TiO2	SUM
O03	an,sp	1315		8.00	25.00	41.00	26.00		100.00
O04	sp,co	1440		18.00	30.00	51.00	1.00		100.00
O05	sp,mu	1490		8.00	35.00	47.00	10.00		100.00
O06	fo,sp	1472		24.00	15.00	38.00	23.00		100.00
O07	sp,an	1397		6.00	30.00	40.00	24.00		100.00
O08	sp,co,mu			12.00	30.00	52.00	6.00		100.00
O09	fo,sp	1600		34.80	20.00	39.40	5.80		100.00
O10	fo,sp	1500		27.90	20.00	42.70	9.40		100.00
O11	sp,an			13.60	25.00	46.30	15.10		100.00
O12	sp,an	1400		7.60	30.00	45.80	16.60		100.00
O13	fo,sp	1400		21.60	19.10	43.10	16.10		99.90
O14	fo,sp	1400		21.00	20.00	44.20	14.90		100.10
O15	fo,sp,an	1300		14.80	20.00	44.70	20.50		100.00
O16	sp,co,mu			10.50	30.00	52.00	7.50		100.00
O17	sp,co			19.50	30.00	50.50	0.00		100.00
O18	sp,co			15.00	30.00	51.50	3.50		100.00
O19	an,sp,mu	1350		8.00	30.00	50.00	12.00		100.00
O20	an,di	1267		10.00	15.75	49.50	24.75		100.00
O21	an,sp,co	1345		10.00	28.00	53.00	9.00		100.00
O22	an,co	1327		11.50	25.00	55.00	8.50		100.00
O23	an,sp	1400		4.20	35.00	35.90	24.90		100.00
OG1	fo,sp	1500		29.30	15.00	34.20	19.00	2.50	100.00
OG2	an,sp,fo	1290		14.50	20.00	45.00	20.50		100.00
OG3	an,pr,co	1300		15.00	20.00	45.00	20.00		100.00
OT1	an,fo,sp	1317		15.17	21.26	45.93	17.65		100.01
OT2	an,di,fo	1270		13.13	16.13	49.19	21.56		100.01
OT3	an,sp	1448		5.99	36.53	40.14	17.34		100.00
OT4	fo,an	1301		14.55	19.42	47.06	18.97		100.00
P01	sp,co	1349		10.00	28.67	52.66	8.67		100.00
P02	sp,an,co	1345		10.00	28.00	53.00	9.00		100.00
P03	sp,co,mu	1370		10.00	30.00	52.00	8.00		100.00
P04	sp,cd,mu	1485		10.00	37.00	48.50	4.50		100.00
P05	sp,an	1400		10.00	25.30	44.90	19.80		100.00
P06	sp,an	1380		10.00	23.50	43.80	22.70		100.00
P07	sp,an	1420		10.00	30.50	46.00	13.50		100.00
P08	an,co,tr	1245		10.00	18.50	63.00	8.50		100.00
P09	an,di,tr	1230		10.00	18.00	62.00	10.00		100.00
P10	an,sp	1400		10.00	25.30	44.90	19.80		100.00

Table 5.4
Data Used in Constructing Phase Diagram

#	assemblage	T(C)	Na2O	MgO	Al2O3	SiO2	CaO	TiO2	SUM
P11	sp,mu			10.00	34.00	50.00	6.00		100.00
R1	sp,fo,co	1370		25.00	23.00	52.00	0.00		100.00
R2	sp,cd	1570		16.00	43.00	41.00	0.00		100.00
R3	sp,fo	1450		30.00	23.00	47.00	0.00		100.00
R4	fo,pr,co	1360		25.00	21.00	54.00	0.00		100.00
S	sp,an	1381	0.50	10.36	25.65	42.00	12.09	0.97	91.57
S	sp	1354	0.08	11.99	24.93	44.87	10.01	0.53	92.42
S	sp,an	1354	0.05	13.48	28.08	39.75	10.34	1.07	92.78
S	sp,fo	1351		13.25	22.63	53.30	6.53	1.44	97.15
S	sp,an	1331	0.08	13.39	25.73	45.86	9.95	0.62	95.63
S	sp,an	1318	0.10	11.70	24.19	40.36	8.08	0.43	84.86
S	sp,an	1318	0.10	12.87	25.96	43.31	9.35	0.53	92.12
S	sp,fo	1316	4.41	12.72	23.20	51.51	5.83	1.36	99.03
S	sp,fo	1307	3.47	13.17	23.27	52.16	6.15	1.19	99.41
S	sp,an	1300	0.08	14.13	24.98	44.23	8.76	0.59	92.77
S	sp,fo,en	1294		18.44	22.19	51.34	5.63		97.60
S	sp,fo,en,sa	1294		18.14	22.44	51.81	5.55	0.99	98.93
S	cd,sp,fo	1285		12.70	22.04	53.76	7.34	1.72	97.56
S	sp,fo,cd,en	1281	0.28	14.99	20.64	47.86	6.80	1.37	91.95
S	fo,sp,cd,en	1281		15.92	21.74	52.18	8.26	1.71	99.81
S	sp,fo	1277	0.10	16.09	18.85	44.78	6.08	1.20	87.10
S	sp,an	1271	0.11	14.59	23.78	45.94	8.76	0.66	93.83
S	sp,an,fo	1271	0.07	11.57	25.23	41.66	11.02	1.13	90.67
S	sp,fo,cd,en	1269		15.86	21.98	52.30	7.97	1.59	99.70
S	sp,fo,cd,en	1269	2.47	14.62	19.96	48.71	5.17	1.05	91.99
S	sp,an,fo,cd	1261	0.30	13.37	18.51	45.45	7.28	1.85	86.77
S	fo,an,pr,cd	1260	0.30	16.10	21.70	51.04	8.51		97.65
S	sp,sa,en	1260		14.78	22.32	52.73	7.90	1.48	99.21
S	cd,fo,sp,en	1256		12.51	21.32	54.92	7.15	1.54	97.44
S	fo,sp	1256		12.75	22.41	53.46	7.90	1.37	97.89
S	sp,an,fo	1253	0.10	9.07	34.95	37.64	12.88	0.59	95.22
S	an,fo,pr,cd	1250		16.52	20.67	49.96	8.20		95.35
S	en,cd,an,sp	1249		14.58	21.85	52.03	8.60	2.67	99.73
S	sp,fo,cd			21.94	19.90	55.19	3.06		100.09
S	sp,fo,cd			17.21	21.79	53.05	8.04		100.09
S	sp,fo,cd			25.39	23.65	50.96	0.00		100.00
S	sp,fo,cd			19.38	21.31	53.51	5.81		100.01
S01	an,sp	1331		13.81	24.85	49.99	10.54	0.81	100.00

Table 5.4
Data Used in Constructing Phase Diagram

#	assemblage	T(C)	Na2O	MgO	Al2O3	SiO2	CaO	TiO2	SUM
S02	an,sp	1331	0.07	13.44	25.64	40.69	10.26	1.12	91.21
S03	an,sp	1318		14.99	22.86	51.86	9.47	0.82	100.00
S03	an,sp	1271		15.60	23.25	50.96	9.54	0.65	100.00
S04	an,sp	1354		13.28	24.78	47.59	13.40	1.32	100.37
S05	an,sp	1331		14.32	23.50	48.46	12.30	1.42	100.00
S06	an,sp	1300		15.01	23.02	47.83	12.33	1.80	99.99
S07	an,sp,fo	1271		15.66	22.05	49.74	10.67	1.89	100.01
S08	sp,an,fo	1271	0.08	13.28	23.68	42.08	9.80	1.46	90.37
S08	sp,pr,fo,an			15.79	20.62	53.76	9.83		100.00
S09	sp,an	1300	0.06	13.63	22.09	42.46	9.99	1.23	89.46
S10	fo,sp,an,pr			14.93	21.68	52.93	10.47		100.01
S11	sp,an,fo,cd	1250	0.22	14.04	18.76	48.12	7.65	3.64	92.43
S12	sp,an,cd			11.57	27.22	53.63	7.58		100.00
S13	an,fo,oe			20.80	12.28	53.51	13.41		100.00
Sc01	sp,fo,an	1305		15.00	19.40	44.70	20.90		100.00
Sc02	sp,an	1320		9.60	22.60	42.00	25.80		100.00
Sc03	sp,an	1300		8.00	22.70	41.20	28.10		100.00
Sc04	sp,an	1350		7.30	25.20	40.80	26.70		100.00
Sc05	sp,an	1400		6.20	30.50	39.60	23.70		100.00
Sc06	sp,an	1450		5.60	34.80	38.40	21.20		100.00
Sc07	sp,fo	1428		21.00	17.20	42.20	19.70		100.10
Sc08	sp,fo	1400		19.90	17.70	42.50	19.90		100.00
Sc09	sp,an,cd	1485		5.00	38.99	37.21	18.80		100.00
Sc10	sp,cd	1590		6.23	44.35	33.69	15.72		99.99
Sc11	an,sp,cd	1468		6.38	34.99	39.98	18.66		100.01
Sc12	an,cd	1485		1.98	39.10	40.17	18.75		100.00
Sc13	an,sp	1350		12.00	23.30	44.10	20.60		100.00
Sc14	an,sp	1400		8.80	28.80	42.50	19.90		100.00
Sc15	an,sp	1450		7.10	33.30	40.60	19.00		100.00
St01	sp,fo,an	1305		15.00	19.40	44.70	20.90		100.00
St02	fo,sp	1428		21.00	17.20	42.20	19.70		100.10
St03	fo,sp	1400		19.90	17.70	42.50	19.90		100.00
St04	fo,sp	1350		17.50	18.70	43.50	20.30		100.00
St05	an,fo,sp	1267		13.50	18.50	43.40	24.60		100.00
St06	fo,sp	1450		24.40	19.70	43.00	12.80		99.90
St07	fo,sp	1400		21.60	19.10	43.10	16.10		99.90
St08	fo,sp	1350		17.80	18.70	43.30	20.20		100.00
St09	fo,sp	1300		16.00	8.50	43.30	22.10		89.90

Table 5.4
Data Used in Constructing Phase Diagram

#	assemblage	T(C)	Na2O	MgO	Al2O3	SiO2	CaO	TiO2	SUM
St10	fo,sp			25.90	20.20	43.00	11.00		100.10
St11	fo,sp	1500		25.30	15.00	37.50	22.20		100.00
St12	fo,sp	1400		18.80	15.00	39.90	26.40		100.10
St13	fo,sp,me	1300		14.50	15.00	41.10	29.40		100.00
St14	fo,sp	1600		34.80	20.00	39.40	5.80		100.00
St15	fo,sp	1500		27.90	20.00	42.70	9.40		100.00
St16	fo,sp	1400		21.00	20.00	44.20	14.90		100.10
St17	fo,sp,an	1300		14.80	20.00	44.70	20.50		100.00
St18	fo,sp	1550		29.30	15.00	34.20	19.00	2.50	100.00
St19	fo,sp	1500		25.70	15.00	36.10	20.70	2.50	100.00
St20	fo,sp	1450		22.40	15.00	37.30	22.80	2.50	100.00
St21	fo,sp	1400		19.40	15.00	38.50	24.60	2.50	100.00
St22	fo,sp	1350		16.90	15.00	39.40	26.20	2.50	100.00
St23	fo,sp	1300		14.80	15.00	40.20	27.50	2.50	100.00
St24	fo,sp,me	1275		13.30	15.00	40.80	28.40	2.50	100.00
Sy1	sp,cd,mu	1575		15.00	42.00	43.00	0.00		100.00
Sy2	sp,fo,co	1370		25.00	23.00	52.00	0.00		100.00
Sy3	fo,co,pr	1364		24.00	21.00	55.00	0.00		100.00
Y1	sp,fo	1450		24.40	19.70	43.00	12.80		99.90
Y2	sp,an	1400		9.90	27.20	43.20	19.80		100.10
Y3	sp,an			8.30	31.40	43.10	17.20		100.00
Y4	sp,fo			25.90	20.20	43.00	11.00		100.10

A1-A7 Andersen

D1-D7 Devries

KS1-KS3 Keith and Schairer

LB1-LB3 Longhi and Boudreau

OG1-OG3 Osborn and Gee

P1-P11 Prince

S Sheng et al.

St1-St24 Stolper

Y1-Y4 Yang

B Bowens

GR1-GR2 Gutt and Russel

C Clark

Gt1-Gt2 Gentile

L1-L79 Longhi

O1-O23 Osborn

OT1-OT4 Osborn and Tait

R1-R4 Rankin

Sc1-Sc15 Schairer

Sy1-Sy3 Schreyer

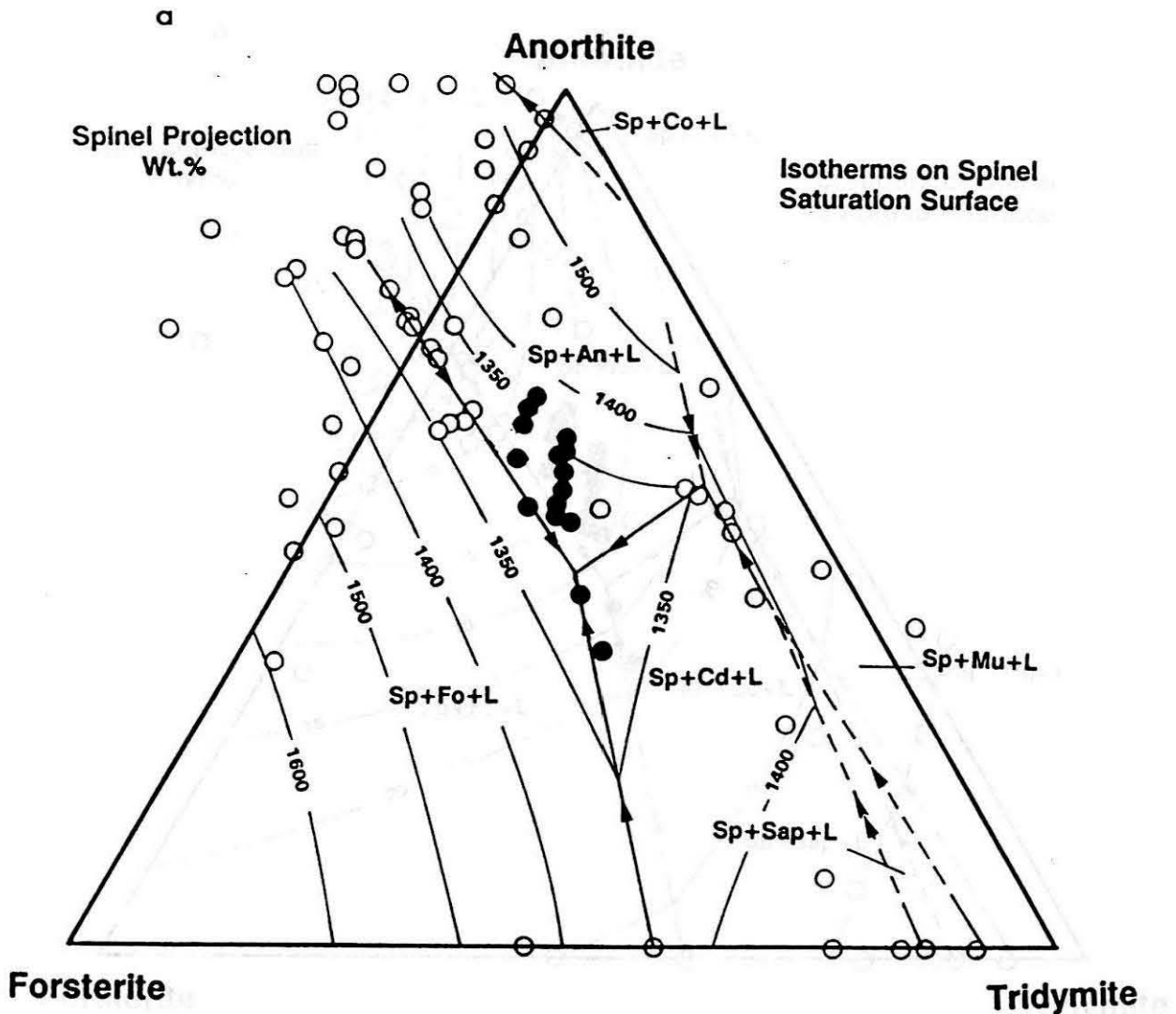
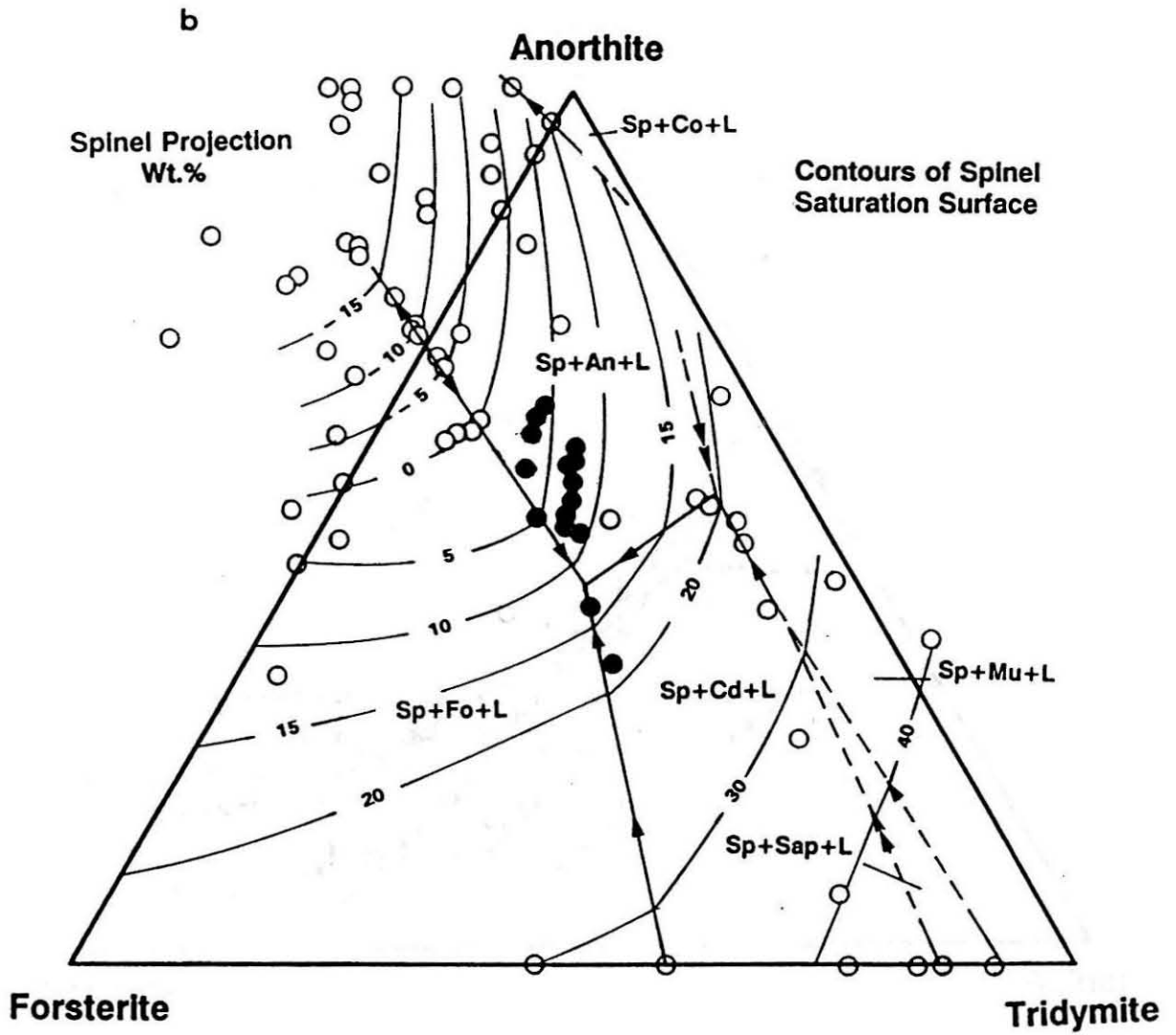


Fig.5.6 a) Isotherms on the spinel saturation surface projected onto the plane An-Fo-Tr. Filled circles are experimental data from this study, open circles are data from various literature sources (see text). b) Contours in wt.% Sp for liquidus on the spinel saturation surface. Oxides are given in mole percent. The projected data points are normalized to the three coordinates of the projection plane. Mu-mullite and Sap-sapphirine. Other abbreviations are given in previous figure captions.



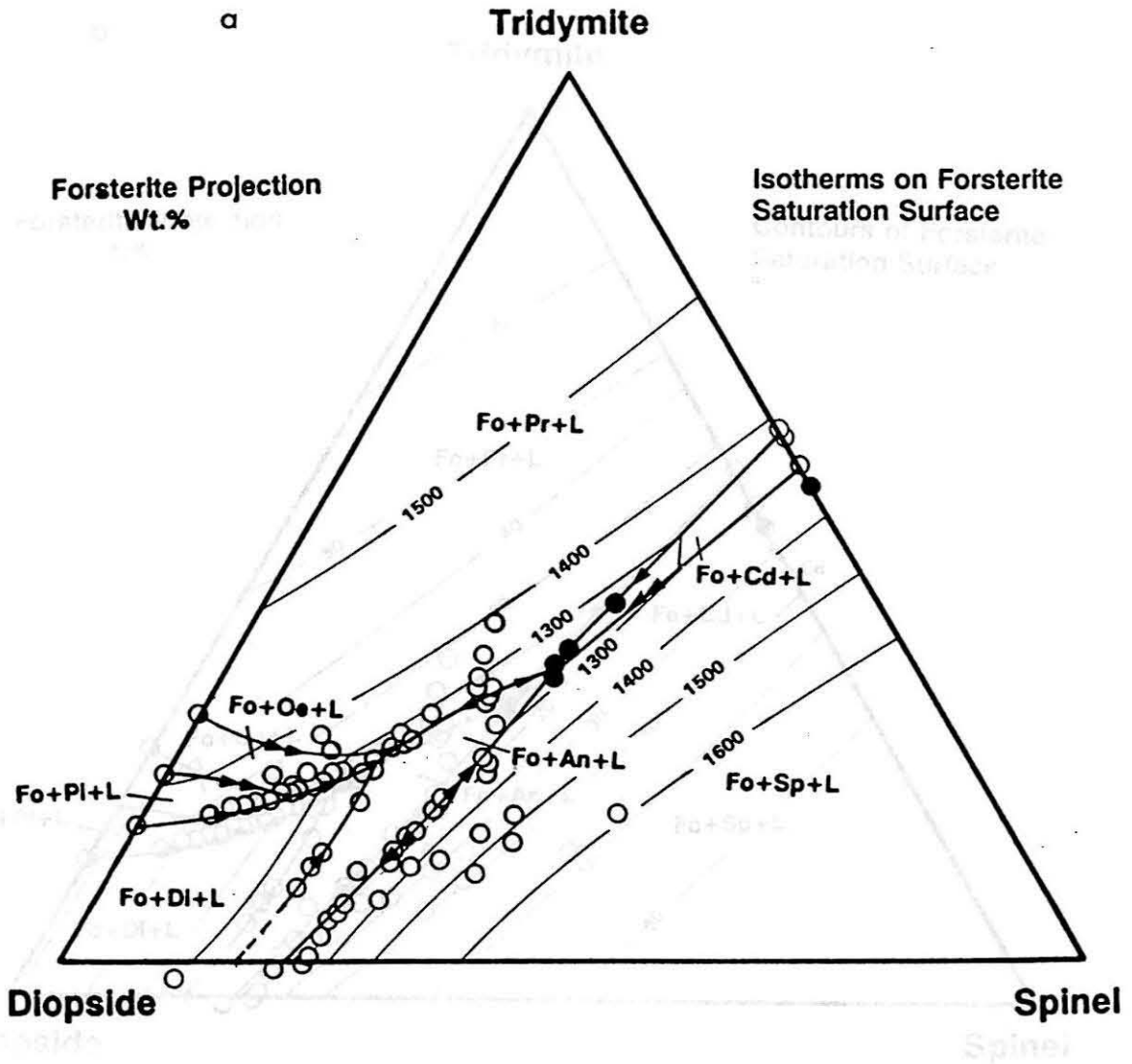
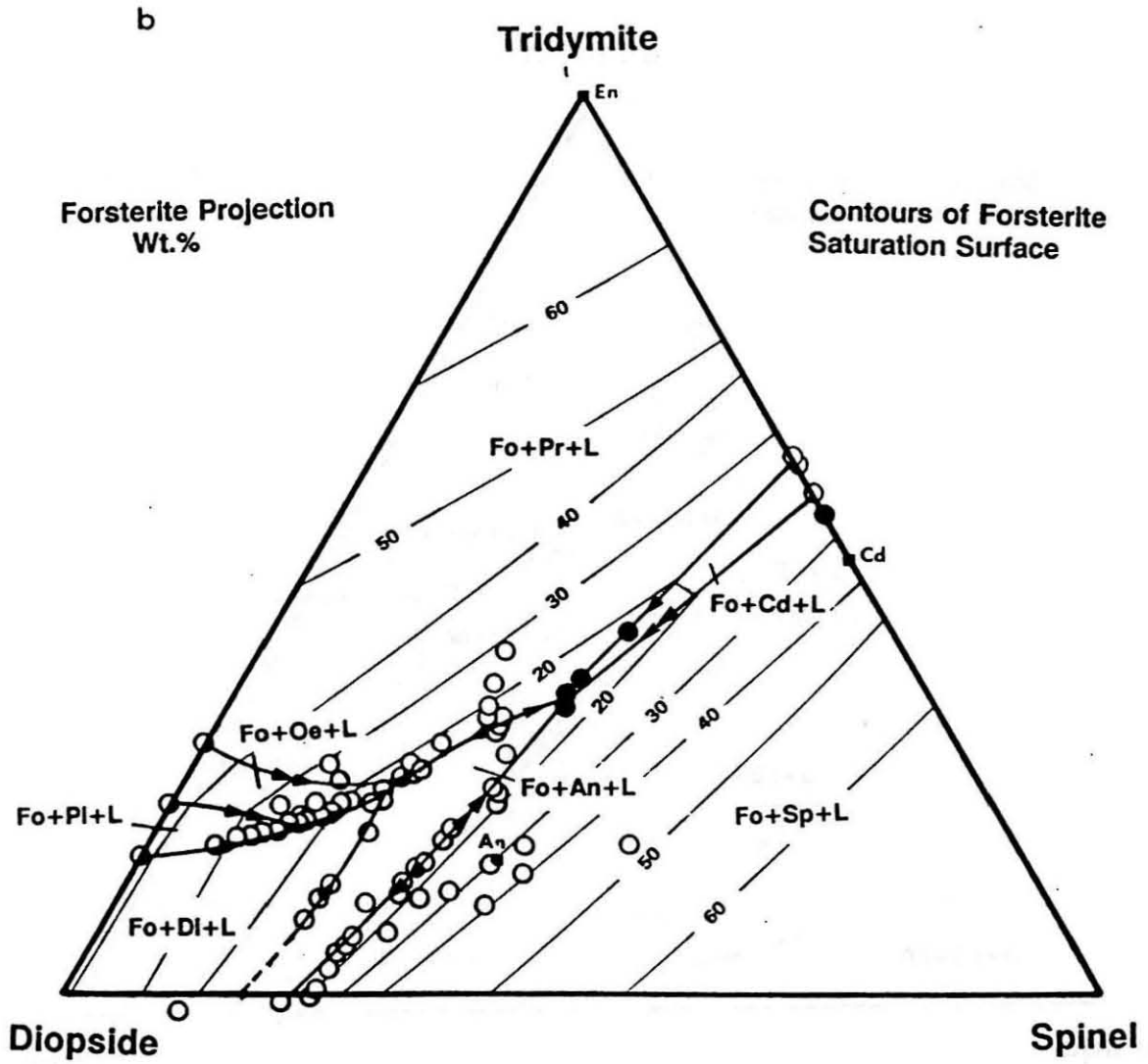


Fig.5.7 a) Isotherms on the forsterite saturation surface projected onto the plane Di-Sp-Tr. b) Contours in wt.% Fo for liquids on the forsterite saturation surface. Di-diopside, Oe-orthoenstatite, pi-pigeonite, and pr-protoenstatite. Other abbreviations are given in previous figure captions.



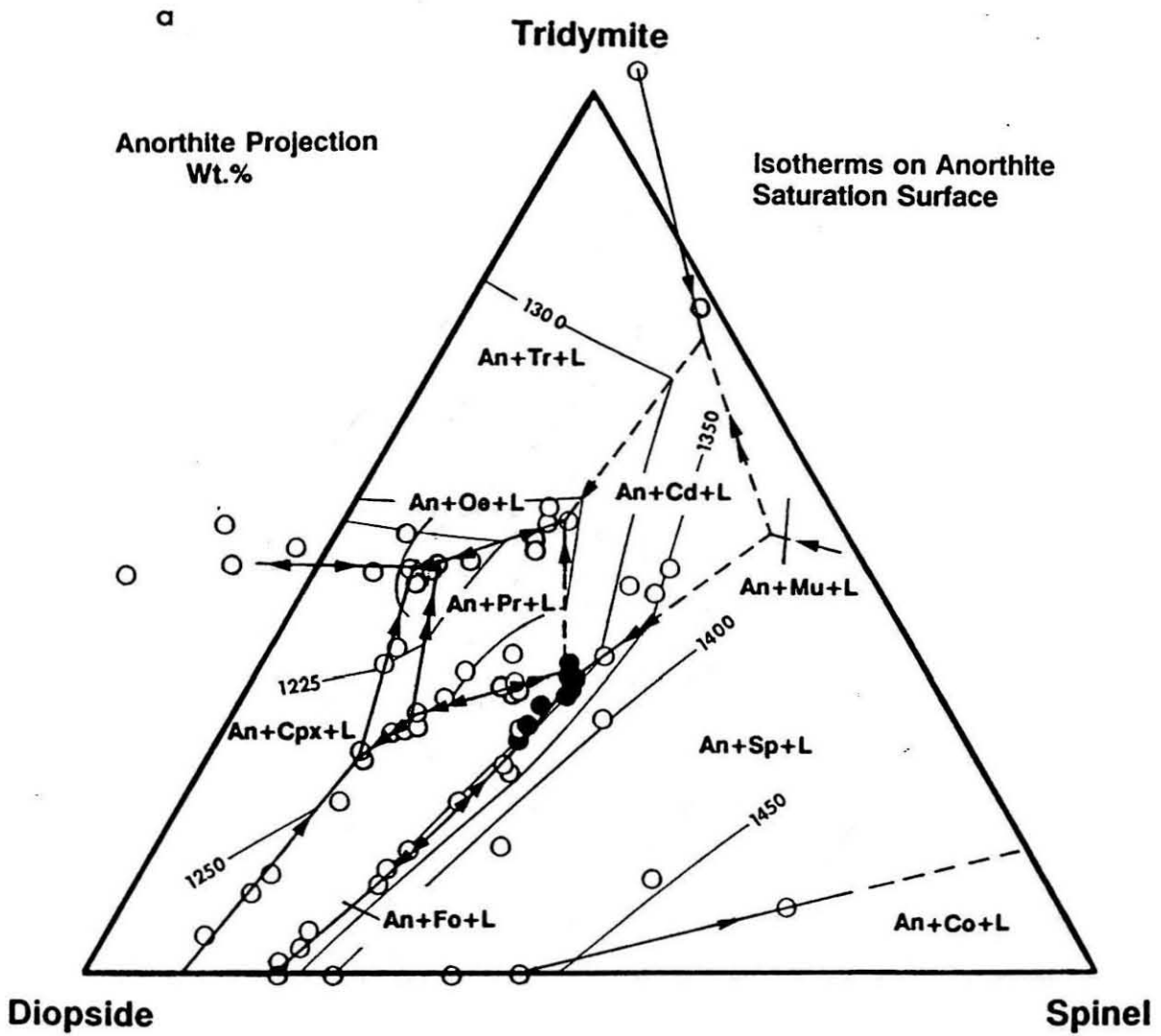
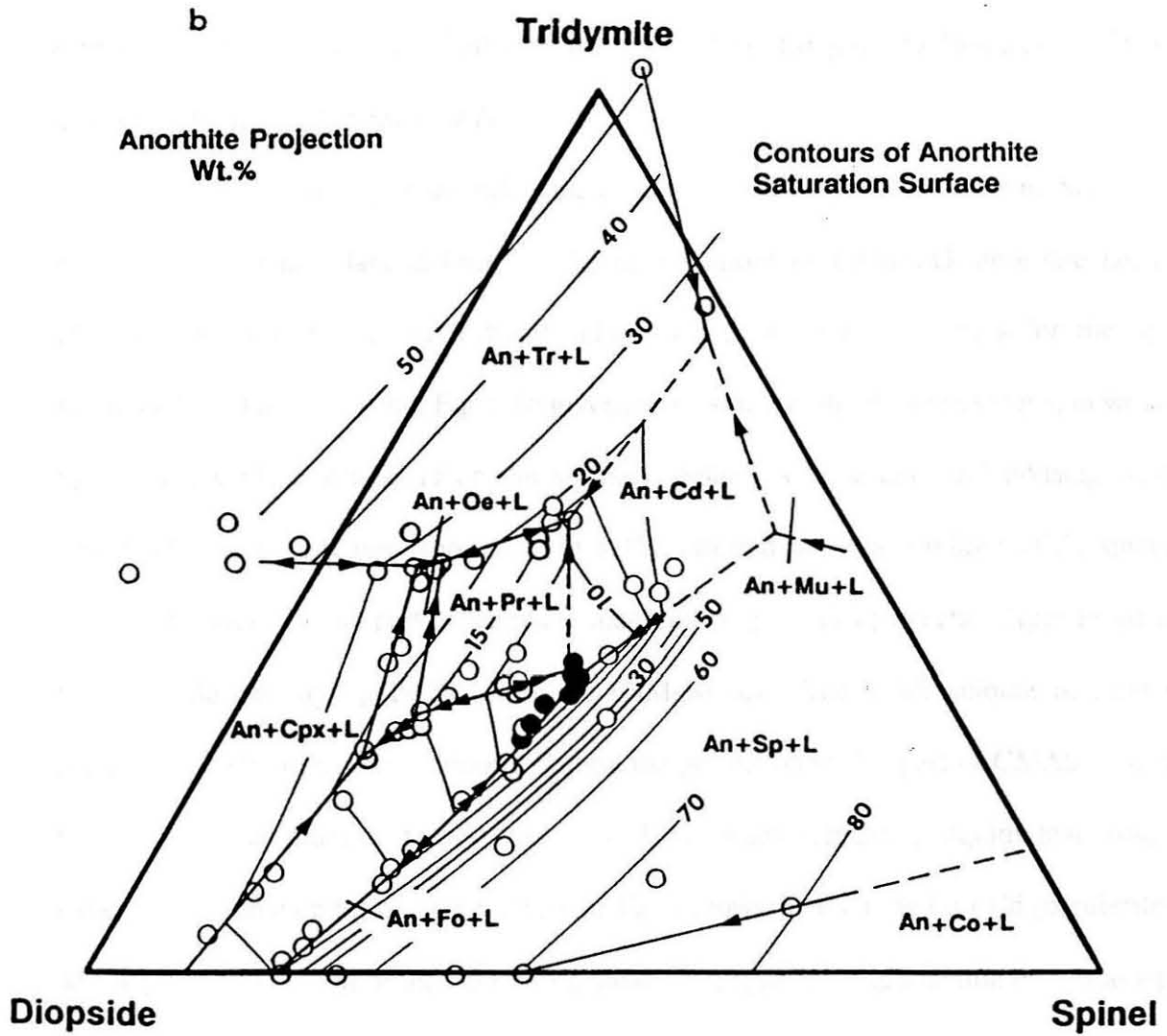


Fig.5.8 a) Isotherms on the anorthite saturation surface projected onto the plane Di-Sp-Tr. b) Contours in wt.% An for liquids on the anorthite saturation surface. Tr-trydimite. Other abbreviations given in previous figure captions.



(1954), Prince (1954), DeVries and Osborn (1957), Schreyer and Schairer (1961), Clark *et al.* (1962), Gentile and Foster (1963), Osborn and Gee (1969), Schairer and Yoder (1969), Yang *et al.* (1972), Gutt and Russell (1977), Longhi and Boudreau (1980), Stolper (1982), and Longhi (1987).

In Fig.5.6, multiply saturated melt compositions are projected from $MgAl_2O_4$ spinel (Sp) onto the plane defined by the compositions of $CaAlSi_2O_8$ anorthite (An), Mg_2SiO_4 forsterite (Fo), and tridymite (Tr). Fig.5.6a shows isotherms for the Sp-saturated liquidus surface and Fig.5.6b gives corresponding liquid compositions, in wt. % Sp above the plane An-Fo-Tr on the surface. Spinel is in reaction relationship with liquid in the hachure region (shown in Fig.5.11), inferred from the topology of the spinel saturation surface in that part of the phase diagram. Fig.5.7 is a projection from Fo onto the plane defined by Sp-Tr-Di (diopside; $CaMgSi_2O_6$). The small amount of larnite present in forsterite has only minor effect on the projection in this part of CMAS. There is a thermal maximum on the Fo+An+Sp+L boundary separating liquids that would evolve, depending on the composition of the liquid, toward either the Fo+Cd (cordierite; $Mg_2Al_4Si_5O_{18}$) +L field or the Fo+Di+L field. There are also subtraction curves along Fo+Oe+Pr+L and Fo+Oe+Pig+L but these are of limited relevance to the petrogenesis of POIs and CACs.

Fig.5.8 is the projection of anorthite saturated melt compositions from An onto the plane Sp+Tr+Di. The An+Fo+Sp+L boundary and much of the Fo+An+L fields are common to Figs.5.7 and 5.8 but the different projections give them a somewhat different appearance. The invariant point An+Fo+ ortho-enstatite (Oe) + proto-enstatite

(Pr) is a reaction point where both forsterite and proto-enstatite are in reaction relation with the liquid. This can be inferred from projection of their composition relative to the topology of the saturation surface. Liquid compositions that project within the region bounded by Di-En-Tr would evolve toward the An+Tr+Oe+Pr invariant point.

5.4.1. Effect of Na₂O and FeO on the Phase Boundaries

Figs.5.1 and 5.6-5.8 were derived from liquid compositions in the system CMAS. POI and CAC compositions however often contain significant amounts of Na₂O and FeO, so it is necessary to examine how much the addition these components will shift the phase boundaries. The direction of shift caused by the addition of Na₂O is shown in Fig.5.9 based on data from Pan and Longhi (1989) and the present study. Increasing Na₂O causes the Sp+Fo+L (liquid) field to expand relative to the Sp+Cd+L and the Sp+ plagioclase (Pl)+L fields. Similar shifts are observed in the other projections. From my experimental data on Na-bearing compositions (**POI-2Na2** and **POI-2Na5**), the crystallization temperature of spinel is unaffected by the addition of up to 5 wt. % Na₂O, but that of plagioclase drops dramatically from 1380°C in **POI-2** (Na-free) to 1300°C (2% Na₂O), to less than 1206°C (5% Na₂O). The forsterite crystallization temperatures for **POI-2** and **POI-2Na2** are within error of each other. However, with 5% Na₂O in the starting composition, the crystallization temperature of forsterite dropped to ~1240°C. Fig.5.10 shows the effect of adding ~6 wt. % FeO (Longhi and Pan, 1988). There are dramatic shifts in Fo+Pr+An+L and Fo+An+Sp+L boundary curves and

it is unlikely that the Fe-free phase diagrams (Figs.5.1, 5.6-5.8) will give an adequate representation of the crystallization of melts containing as much as 6 wt.% FeO. Based on the above analysis, I limit the discussion of meteoritic inclusions to those bulk compositions containing <4 wt.% Na₂O and <3% FeO. It should be noted that FeO and Na₂O become progressively enriched in the melt during crystallization so that only the early part of the crystallization sequence can be described quantitatively.

In projecting bulk compositions of meteoritic inclusions, the FeO content is subtracted as fayalite and the Na₂O content is subtracted as nepheline. Most of the oxidized Fe in POIs and CACs is present in olivine. However, a significant proportion of the Na₂O in POIs (up to 50%) is contained in plagioclase, the projection does introduce an error in the projection of POIs on the projected plane. However, for most of the compositions we will project through this scheme, this error does not affect the interpretation on their phase assemblage and crystallization sequence. The agreement of texturally derived crystallization sequence with that predicted by the related phase diagram for the projected POI compositions supports the validity of the projection scheme.

5.4.2. Crystallization Sequences of POIs

Sheng *et al.* (1991a) provided detailed descriptions of 20 POIs of which 11 inclusions have < 4 wt.% Na₂O and <3 wt.% FeO. I compare phase assemblages and texturally inferred crystallization sequences for these POIs and two CACs described by

Nagahara and Kushiro (1982) with the predictions based on phase diagrams developed in this work. I also predict crystallization sequences for CACs analyzed by Bischoff and Keil (1983), and Bischoff *et al.* (1985), although the lack of corresponding petrography prevents detailed comparisons between predicted and observed phase assemblages.

The appropriate phase diagram for describing the phase relations of a given meteoritic inclusion should meet two basic criteria. First, the phase diagram should be projected from the composition of a liquidus, or near liquidus, phase for the inclusion. This means that the bulk compositions must lie above or at least very close to the saturation surface for the projected phase. Second, the inclusion's bulk composition should plot in a part of the phase diagram where the crystallization sequence can be easily followed. In practice, this usually means that the projected point plots inside the projected pseudo-ternary diagram. Of the 18 low Na, low Fe POIs (Sheng *et al.*, 1991a) and CACs (Nagahara and Kushiro, 1982; Bischoff and Keil, 1983) for which there is petrographic data, four plot above the spinel saturation surface and inside the Fo-Ge-An ternary (i.e., the Stolper diagram), six in the Sp projection onto Fo-An-Tr, four in the Fo projection onto Di-Tr-Sp, and four in the An projection onto Di-Tr-Sp. Although the POI ADEL-1 has 4.6 wt. % FeO, most of the Fe is comprised by Fe-rich metal nuggets concentrated in olivine-rich regions near the periphery of the inclusion. The compositions of olivine and pyroxene are low in FeO (<2 wt. %) suggesting that these phases crystallized from a low Fe melt. If these Fe-rich nuggets are subtracted from the bulk composition, the FeO content of the inclusion is less than 2 wt. %. Therefore this inclusion is included in the discussion. In the following, we will discuss the

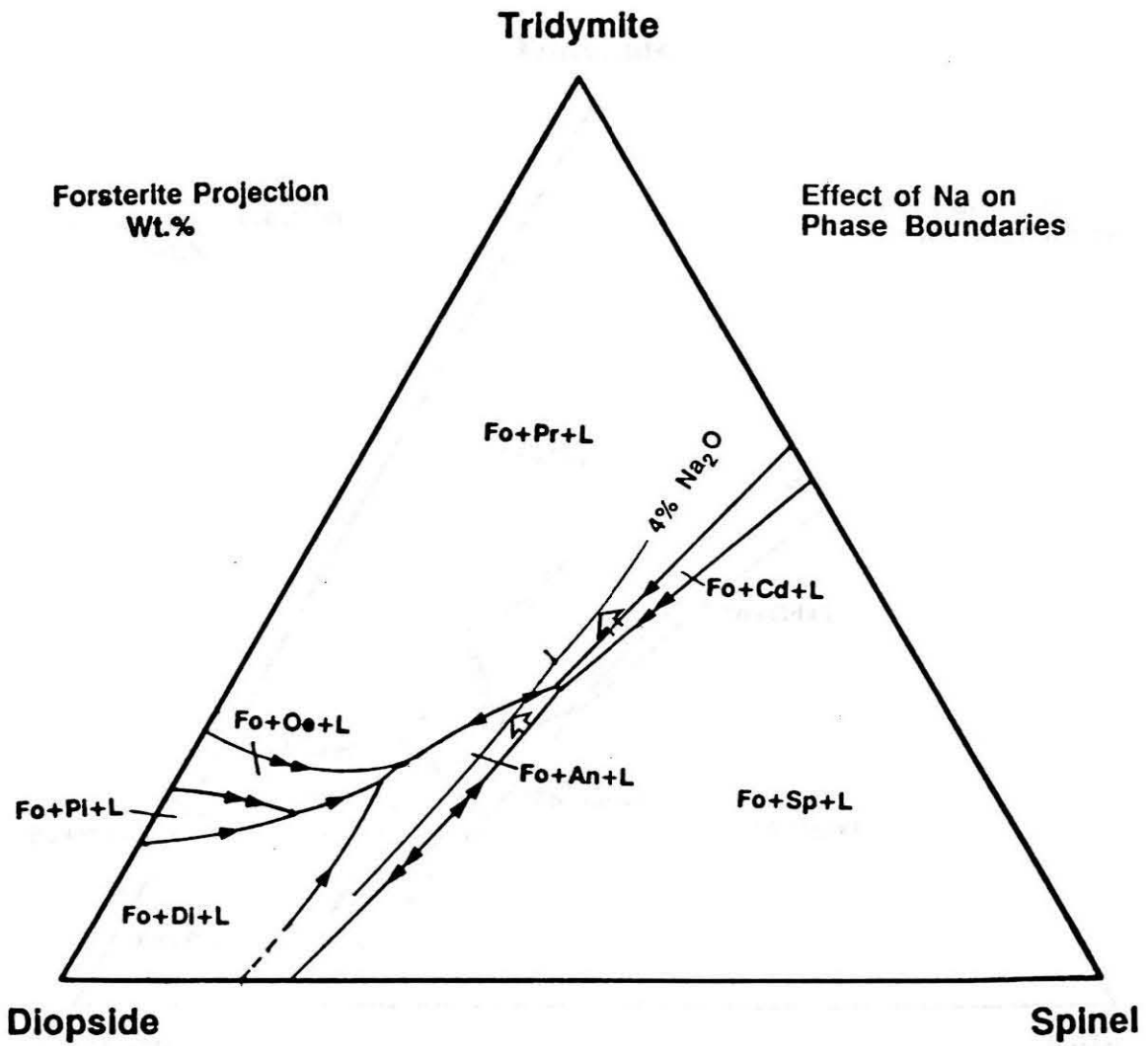


Fig.5.9 Shifts of the phase boundaries in the Fo projection onto the plane Tr-Di-Sp due to the addition of 4 wt.% Na₂O. Similar effects are seen in the other projections.

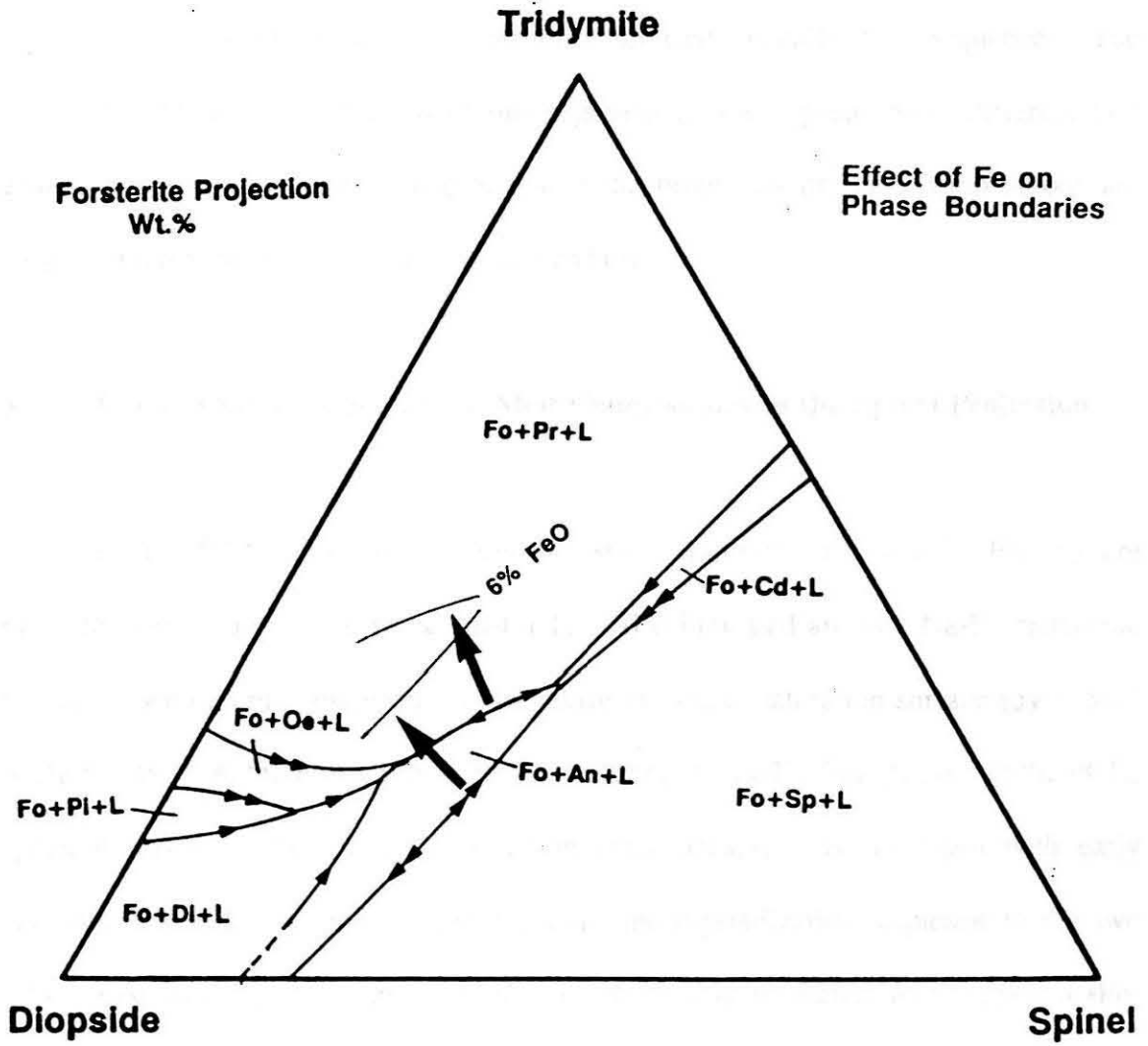


Fig.5.10 Shifts of the phase boundaries in the Fo projection onto the plane Tr-Di-Sp due to the addition of 6 wt. % FeO.

crystallization paths for liquid compositions that fall in the specific regions of the phase diagrams where the natural compositions are plotted, and compare the predicted crystallization sequences with the texturally inferred crystallization sequence. The different symbols in the phase diagrams represent bulk compositions of different POI groups and CA chondrules. The errors in the projection of their compositions are roughly approximated by the size of the symbols.

a) Crystallization Sequences of Melt Compositions in the Spinel Projection

In Fig.5.11, bulk compositions of spinel saturated melts (cf., Fig.6b) are projected from Sp onto the plane An-Fo-Tr. Also indicated are low Na-Fe meteoritic inclusions whose bulk compositions plot above the spinel saturation surface (by ~5-20 wt. % Sp) and are, therefore, predicted to have spinel as the liquidus phase. In the POIs, spinel grains are poikilitically enclosed in other phases, thus consistent with early crystallization. Based on bulk compositions, the crystallization sequence in the two CACs described by Nagahara and Kushiro (1982) is predicted to be Sp→An→Fo. Plagioclase is not observed in these inclusions but glass is ubiquitous. The absence of plagioclase may be a consequence of the well-known difficulty of plagioclase nucleation (Gibb, 1974). Since POIs of similar composition contain plagioclase but no glass, these two CACs probably cooled faster or were heated to higher temperatures than comparable POIs.

The key feature of Fig.5.11 for interpreting the crystallization behavior of POIs

and CACs is the presence of a thermal divide formed by the spinel-olivine-plagioclase plane. The exact position of this plane shifts with the plagioclase composition, $\sim \text{An}_{90}$ for POIs, as shown in Fig.5.11. Spinel saturated liquids on the Tr-rich side of the Fo+Plag+Sp plane will evolve toward the invariant point Sp+An+Fo+Cd+L while those on the Tr-poor side will move away from Tr and evolve towards the Cpx+Sp+L field shown in Fig.5.1. This behavior is independent of whether plagioclase or olivine is the second phase to crystallize and represents a fundamental test for the application of projections such as Fig.5.11 to POIs and CACs. Those inclusions with bulk compositions plotting on the Tr-poor side of the Plag+Fo+Sp plane should contain fassaite but no orthopyroxene or cordierite. From Fig.5.11, every meteoritic inclusion clearly plotting on the Tr-poor side of the Plag+Fo+Sp plane [A1, A2, 2, 7] contains Cpx, whereas none of the inclusions clearly plotting on the Tr-rich side [5, 6, 8] has any Cpx. The fact that POIs whose bulk compositions plot very close to the olivine+plagioclase+spinel plane contain fassaite suggests that these inclusions are on the Tr-poor side of the plane. At first glance, it appears that fractional crystallization of POIs on the Tr-rich side of the Plag+Fo+Sp plane will lead to the appearance of cordierite, a phase never observed in the POIs we studied, but not of enstatite, which is common (Sheng *et al.*, 1991a). The only cordierite-bearing inclusion described by Fuchs (1969) also contains spinel, plagioclase, and olivine, and therefore falls into the category of POIs. The presence or absence of cordierite for inclusions, whose bulk compositions should crystallize cordierite upon fractional crystallization, possibly reflect a difference in their cooling history. However, crystallization sequences for these compositions are

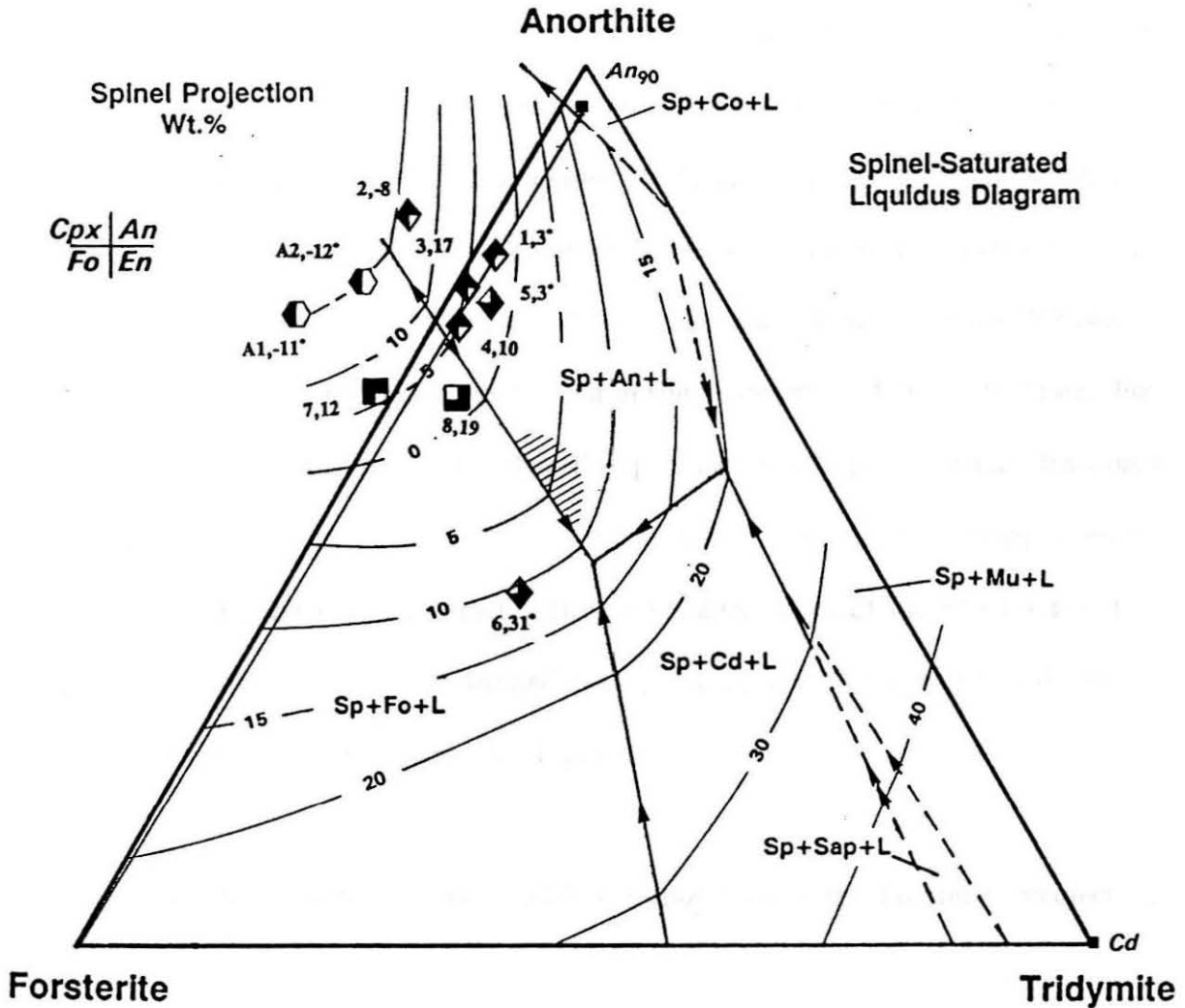


Fig.5.11 Spinel saturated liquidus phase diagram projected onto the An-Fo-Tr plane. Only POIs that have spinel as the liquidus phase are shown. Diamonds represent group 1 POIs, squares represent group 2 POIs, and hexagons represent CACs. Sectors in each symbol denote the presence (filled) or absence (unfilled) of the phase which is labeled at each corner. Numbers and the * sign beside each symbol denote, respectively, the I.D. number, weight percent spinel component above the projection plane and the presence of glass or mesostasis. Other abbreviations given in previous figure captions. 1: A1A1-2, 2: V477, 3: 5ALLB6, 4: BG82DH2, 5: 3510, 6: BG82CLII, 7: BG82DH1A, 8: B14D.

complicated by the fact that spinel is in a reaction relationship with liquid at the $Sp+An+Fo+Cd+L$ invariant point, along the $Sp+An+Fo+L$ boundary curve, and in the hachure region on the spinel saturation surface. Fractional crystallization can therefore result in the melt being driven off the spinel saturation surface so that Fig.5.11 can no longer be used to follow the liquid line of descent. Whether or not this occurs depends on the bulk composition, the amount of spinel present, and the cooling rate. For POIs on the Tr-rich side of the Plag-Fo-Sp plane in Fig.5.11, perfect fractional crystallization will generally crystallize enstatite before cordierite even at equilibrium. This can be seen by following fractional crystallization paths of the $Sp+Fo$ saturated liquids plotting in the triangle formed by Sp , An_{90} , and the $Fo+An+Cd+Sp+L$ invariant point in the Fo projection of Fig.5.12.

b) Crystallization Sequences of Melt Compositions in the Forsterite Projection

In Fig.5.12, bulk compositions of forsterite saturated melts (cf. Fig.5.7b) are projected from Fo onto the plane Sp-Di-Tr. Low Na and Fe meteoritic inclusions whose bulk compositions plot above or close enough to the forsterite saturation surface that upon fractional crystallization the melt will eventually evolve onto the saturation surface are also plotted. In the cases where the bulk compositions plot above the forsterite saturation surface, forsterite is predicted to be the liquidus phase. For those that plot slightly below the saturation surface, forsterite will be the second phase to crystallize, preceded by one of the other phases depending on the phase field within which the bulk

composition is plotted. The thermal maximum on the Fo+An+Sp+L boundary separates liquids plotted within the Fo+Sp+L field that will crystallize enstatite from those that will crystallize diopside upon fractional crystallization. The exact location of this thermal maximum depends on the composition of plagioclase. Since the Fo+Sp+An+L boundary on both sides of the thermal maximum is a reaction curve, the liquid will, at some point along the curve, move across the Fo+An+L phase field and crystallize either diopside or enstatite depending on which side of the thermal maximum the liquid evolved from. The three inclusions within the Fo+Sp+L field plot on the Tr poor side of the thermal maximum, therefore, are predicted to crystallize diopside rather than enstatite. The two CACs [N15, P11] of Bischoff and Keil (1983) contain olivine and fassaite but not plagioclase. Both contain abundant Ca-rich mesostasis, thus the absence of plagioclase is possibly due to nucleation difficulty.

Six CACs are plotted in the Fo+Pr+L phase field. Only two of them plot above the forsterite saturation surface and thus will have forsterite as the liquidus phase. Four others plot below the forsterite saturation surface, but are close enough to the surface that upon crystallization the melt will evolve upon the forsterite saturation surface and crystallize forsterite. Phase assemblages were reported by Bischoff and Keil (1983) for two of the chondrules [B13, S3]. The CAC B13 was reported to consist of olivine and Ca-rich mesostasis and S3 of olivine, pyroxene and Ca-rich mesostasis. The absence of expected plagioclase in these two CACs is likely an indication of rapid cooling and nucleation difficulty of plagioclase. The phase assemblages of the other CACs were not reported. Since their bulk compositions plot below the forsterite saturation surface it is

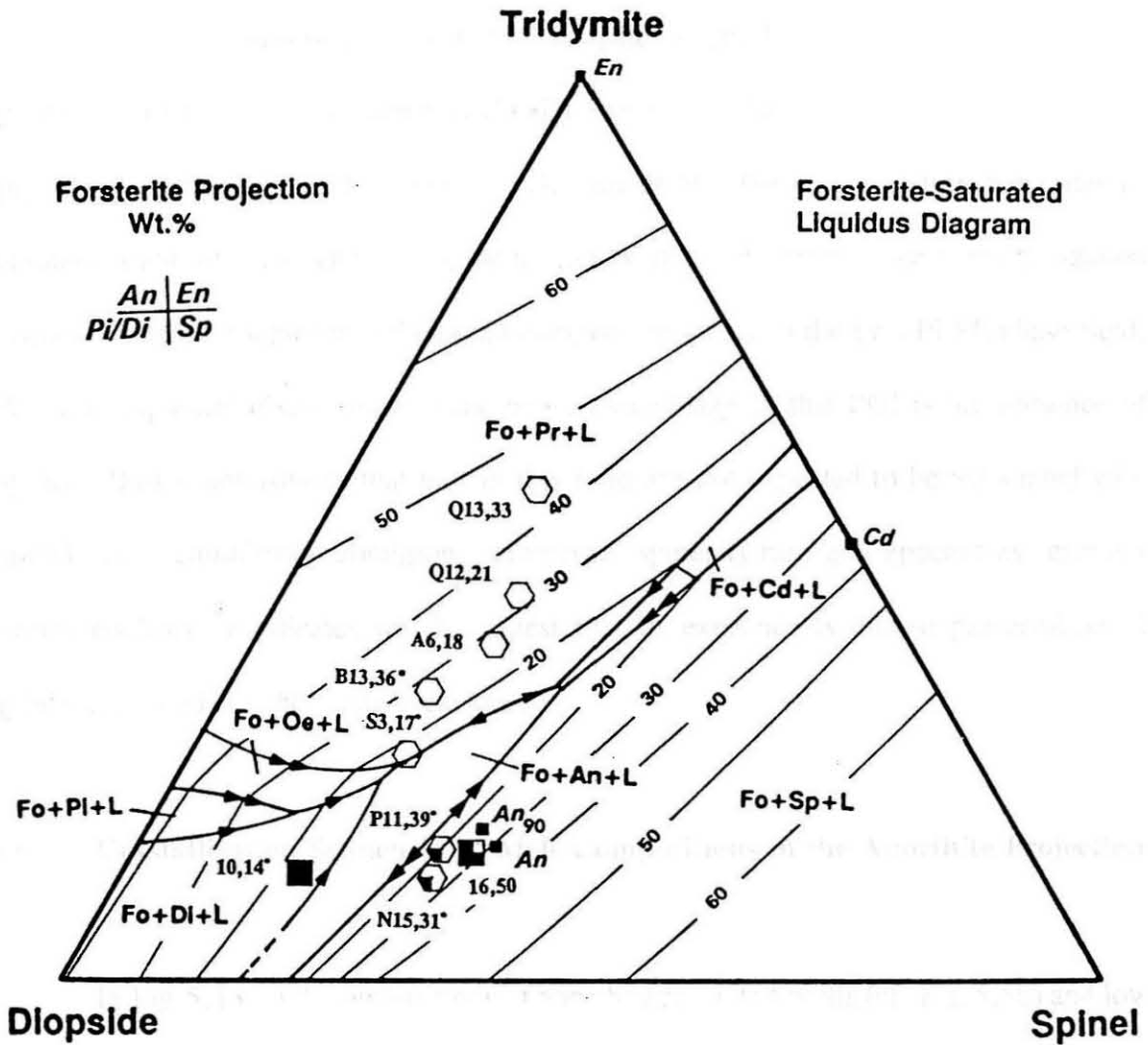


Fig.5.12 Forsterite saturated liquidus phase diagram projected onto the plane Tr-Di-Sp. Only POIs with bulk compositions above or near the olivine saturation surface are plotted in this projection. Circle represents Group 3 POI. Contours are in wt. % forsterite component. En-enstatite. Other abbreviations given in previous figure captions. 10: BG82CH1, 16: A-47.

expected that they should have enstatite on their liquidus.

The bulk composition of one POI [10] lies in the Fo+Di+L phase field. The predicted crystallization sequence is Fo→Di→An→Oe. The pyroxenes, however, show pigeonite crystals enclosed in diopside (Boctor et al., 1989), suggesting the order of crystallization of pyroxene is pigeonite followed by diopside. This crystallization sequence could be achieved if the liquid compositions were in the Fo+Pi+L phase field. A more important discrepancy of the phase assemblage in this POI is the presence of spinel. Bulk compositions that plot in this field are not expected to be associated with spinel under equilibrium condition. However, spinel is rare and appears as resorbed grains enclosed in silicates which suggest that its existence is due to preservation of grains that predates the melting episode.

c) Crystallization Sequences of Melt Compositions in the Anorthite Projection

In Fig.5.13, bulk compositions of anorthite saturated melts (cf. Fig.5.8b) and low Na and Fe meteoritic inclusions whose bulk compositions plot above or near the anorthite saturation surface are projected from An onto the plane Sp-Di-Tr. Bulk compositions that plot above the anorthite saturation surface are predicted to have anorthite as the liquidus phase. For those that plot slightly below the saturation surface, anorthite will be the second phase to crystallize, preceded by one of the other phases depending on the phase field within which the bulk composition is plotted. The phase fields of interest for these inclusions are An+Fo+L, An+Cpx+L, An+Oe+L, and An+Pr+L. Liquid

compositions that plot in the $An+Fo+L$ phase field will crystallize anorthite followed by forsterite. The liquid will then move away from the projected endmember composition Fo until either clinopyroxene or orthopyroxene crystallizes, depending on the position of the initial bulk composition of the liquid relative to the tie lines between Fo and the invariant points $An+Fo+Cpx+Oe+L$ and $An+Fo+Oe+Pr+L$. The invariant point $An+Fo+Oe+Pr$ is a reaction point, where either Fo or En is in reaction relation with the liquid and the liquid will move along the $An+Pr+Oe+L$ phase boundary towards the $An+Pr+Oe+Tr$ invariant point, or will move across the $An+Oe+L$ phase field. Liquid compositions plotting within the $An+Pr+L$ field will crystallize anorthite followed by proto-enstatite and evolve toward either $An+Pr+Cd+L$, $An+Pr+Oe+L$, or $An+Pr+Tr+L$ boundary curve depending on the position of the liquid composition relative to the $Tr-En$ tie line. Liquid compositions in the $An+Oe+L$ field will crystallize anorthite followed by ortho-enstatite. Depending on the liquid composition, the liquid will evolve on either $An+Oe+Tr+L$ or $An+Oe+Cpx+L$ boundary curve and towards the $An+Oe+Cpx+Tr+L$ invariant point.

The bulk composition of the POI [11] plots in the vicinity of the invariant point $An+Fo+Pr+Oe+L$. The inclusion consists of mainly plagioclase, with rounded olivine grains mantled by enstatite, tabular enstatite mantled by clinopyroxene and interstitial polymorph of SiO_2 . The inferred crystallization sequence from the textural relation of these phases is $An+Fo \rightarrow En \rightarrow Cpx \rightarrow Tr$. This is consistent with the predicted crystallization of this liquid composition based on the phase diagram. However, we also observed rare grains of spinel in this POI. The spinel appears as small, highly corroded grains

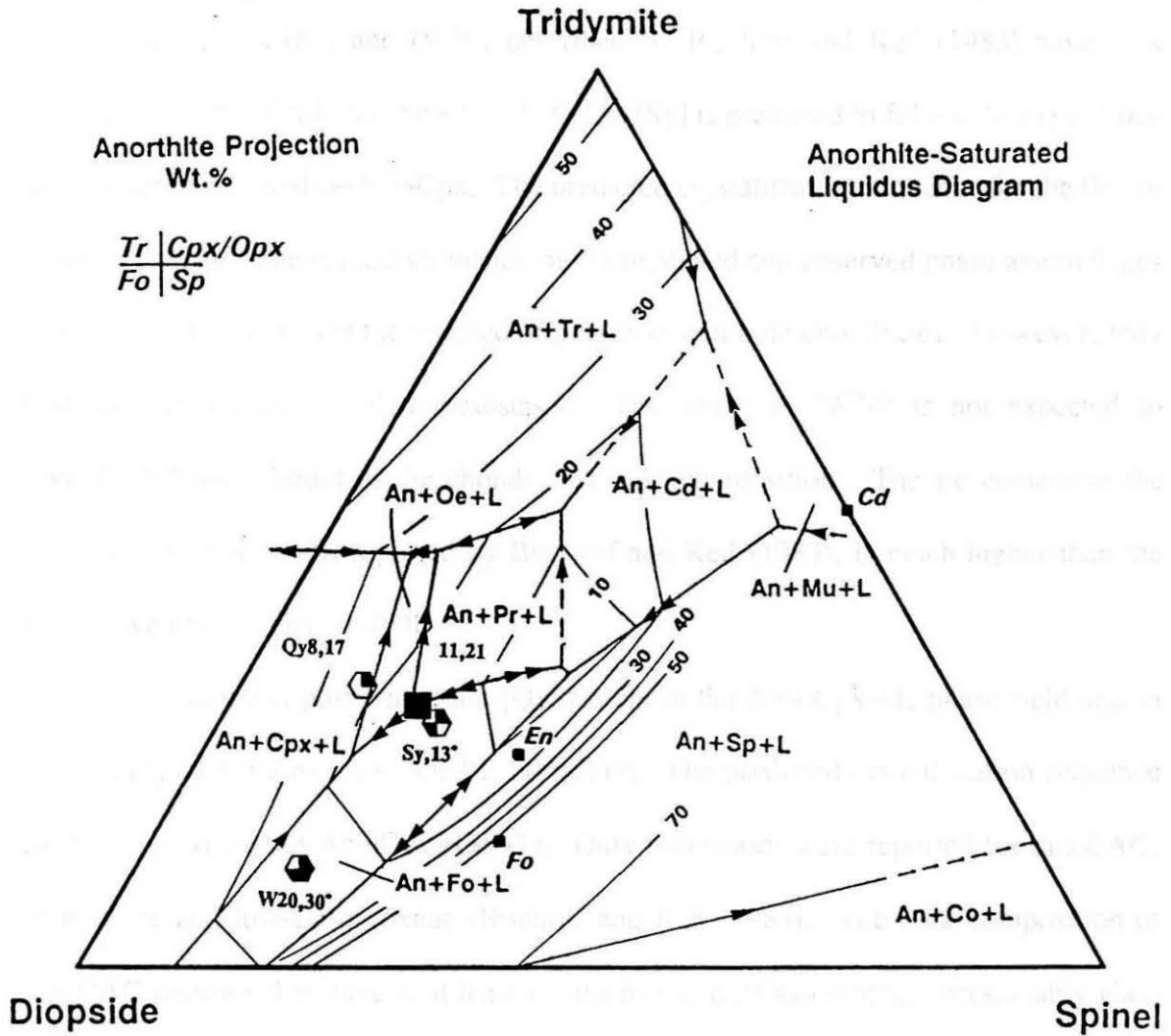


Fig.5.13 Anorthite saturated liquidus phase fields projected onto the Tr-Di-Sp plane. Contours are in wt.% anorthite component. Abbreviations given in previous figure captions. 11: ADEL-1.

included in plagioclase laths. Spinel is not allowed to exist under equilibrium condition in a melt of this composition.

Two CACs [Sy] and [W20] described by Bischoff and Keil (1983) have bulk compositions that plot in the An+Fo+L field. [Sy] is predicted to follow the crystallization sequence of An→Fo→En→Cpx. The predicted crystallization sequence for the [W20] is An→Fo→Cpx. The main discrepancy of the predicted and observed phase assemblages in the above two CACs is the absence of plagioclase in both chondrules. However, they both contain Ca and Al-rich mesostasis. The spinel in [W20] is not expected to crystallize from a liquid of the chondrule's bulk composition. The Fe content in the spinel (~20wt.% FeO), reported by Bischoff and Keil (1983), is much higher than the spinels we encountered in POIs.

The bulk composition of the [Qy8] plots in the An+Cpx+L phase field and in the vicinity of the An+Cpx+Oe+L boundary. The predicted crystallization sequence for this composition is An→Cpx→Oe→Tr. Only two phases were reported for this CAC, plagioclase and low-Ca pyroxene (Bischoff and Keil, 1983). The bulk composition of this CAC requires that there is at least a third phase in its assemblage, presumably glass or mesostasis.

5.5. IMPLICATIONS FOR PETROGRAPHIC CLASSIFICATION

Sheng *et al.* (1991a) divided POIs into three groups based on mineralogy. Group 1 are spinel rich inclusions and group 3 are olivine rich. Group 2 inclusions are

intermediate between group 1 and 3 POIs and generally contain more pyroxenes. Group 1 POIs (represented by diamonds in Fig.5.11) are characterized by abundant spinel. All inclusions of this group described by Sheng *et al.* (1991a) have spinel on their liquidus. It is suggested from their phase assemblages, that two of the six group 1 POIs will follow crystallization paths that can be described in this phase diagram, and the crystallization paths of the other four can be visualized in Stolper's (1982) projection. The POIs whose compositions plot on the silica rich side of the plagioclase-forsterite tie line can crystallize orthopyroxene while those on the silica poor side can crystallize clinopyroxene. For those POIs that have bulk compositions plotting near the plagioclase-forsterite tie line, the crystallization paths can be distinguished by the presence of either clinopyroxene or orthopyroxene.

Group 2 POIs (represented by squares in the phase diagrams) comprise half of the POIs we studied. Spinel is generally rare and resorbed. The presence of spinel in two group 2 POIs contradicts the predicted phase assemblages from their bulk compositions. We have observed that melts from their bulk compositions are spinel-undersaturated.

Group 3 POIs (represented by circles in the phase diagrams) are dominated by olivine and will have olivine on the liquidus. With the exception of A-47 these POIs are Fe-rich (4.1-5.6 wt. % FeO). However, as will be discussed in the following section, it appears that even for the Fe-rich POIs, a reasonable sense of their crystallization paths still can be depicted.

The phase diagrams we constructed can also be used for interpretation of the phase relations of some CACs (represented by hexagons). The phase relations of

selected CAC compositions for which there is data on their phase assemblage are, in general, consistent with the prediction from the phase diagram. A major inconsistency between the observed and predicted phase assemblages is the absence of plagioclase in several CACs that were expected to contain plagioclase based on the phase diagrams. These CACs contain Ca-rich glass or mesostasis, some of which have stoichiometric plagioclase composition (Bischoff and Keil, 1983). This may reflect faster cooling rates in CACs relative to POIs and the difficulty of plagioclase nucleation (Gibb, 1974).

5.6. EVALUATION OF POIs WITH HIGHER Fe AND/OR Na

Although the compositions of some POIs exceed the limitations we set on their FeO or Na₂O contents, we have nevertheless evaluated them to see how well their phase assemblages and crystallization sequences can be predicted based on the phase diagrams. The texturally inferred crystallization sequence of BG82CLI (4.8 wt. % FeO) is consistent with that predicted from its bulk composition except for the absence of spinel. BG82CLJb (4.1 wt. % FeO) exhibits a phase assemblage that is consistent with the predicted crystallization sequence of Fo→Sp→An→Cpx. The inferred crystallization sequence for PPX (6.5 wt. % FeO) is compatible to the sequence of Fo→Sp→An→En predicted from the phase diagram. REDEYE (5.6 wt. % FeO) is predicted to have the crystallization sequence of Fo→An→Di→En, identical to the texturally inferred crystallization sequence with the exception of the presence of Cr-rich (20-30% Cr₂O₃) spinel in this POI. Analysis of Cr contents in spinels and coexisting Cr-doped glasses

with compositions similar to POIs and CAIs suggests a partition coefficient of Cr between spinel and coexisting liquid of approximately 40. The partition coefficient of Cr between olivine and a basaltic liquid is about 1 (Leeman and Scheidegger, 1977). These data suggest that the Cr-rich spinels and olivines (0.5% Cr₂O₃) in REDEYE can coexist in a melt containing ~0.5% Cr₂O₃. The predicted crystallization sequence for the Na-rich POI BG82CLJa (6.8 wt.% Na₂O) is consistent with observed assemblage except for the presence of rare and strongly resorbed spinel. Even when we accounted for the Na-effects on the phase boundaries, it still is apparent that spinel is not allowed to crystallize from a melt of the inclusion's bulk composition.

The predicted crystallization sequence for BG82CH1 is Fo→An→Di→En. While the general textural feature is consistent with the prediction, the inclusion contains spinel, which is not expected to crystallize from liquids of its bulk composition. It is noted that spinel is rare and occurs as small resorbed crystals enclosed in plagioclase.

Although the amount of FeO or Na₂O in these POIs limits the application of our phase diagrams to the interpretation of their phase relations, it appears that their texturally inferred crystallization sequence follow that predicted from the phase diagrams. This may be due to the coincidence that the projections of their compositions fall in a region where the general trend of their liquid line of descent is not affected by the shifts in the phase boundaries due to the addition of FeO or Na₂O in the system.

CHAPTER SIX

Mg SELF-DIFFUSION EXPERIMENTS

The very existence of isotopic heterogeneities in the spinels of POIs implies that the maximum temperature was low enough and the cooling rate fast enough to prevent reequilibration. A determination of the conditions under which isotopic heterogeneities would have been preserved requires a knowledge of the self-diffusion rate of Mg in spinels. Therefore, experiments to determine the self-diffusion coefficients of Mg in spinel single crystals at temperatures reflecting possible melting conditions of POIs were designed. The only available Mg diffusion data in MgAl_2O_4 are those of Lindner and Åkerström (1958). They used a radiotracer (^{28}Mg) precipitated on a polycrystalline aggregate of spinels.

A common technique for the preparation of a diffusion couple in simple solids is to coat the diffusing species onto the surface of the sample by means of electroplating or chemical precipitation (Coles and Long, 1973; Reed and Wuensch, 1979; Cygan and Lasaga, 1985). The sample is then annealed to allow species in the thin film to diffuse into the sample. Some of the potential drawbacks to this technique are that the thin film and the crystal are in very different chemical and physical states, and the boundary between them may not be well defined. Imperfections along this contact could serve as a major obstruction to the diffusing species and thus limit the reliability of the data. The

thin film method usually does not permit a check on the mass balance of the species transported between the two phases. Another potential problem is that if the thin film has one or more components that are volatile in the enclosing gas, differential volatilization may occur at the surface. In order to avoid these problems, an experimental approach was designed by which volume diffusion in both phases is maintained. The technique permits precise determination of the activation energy and is applicable to many other systems (cf., Jurewicz and Watson, 1988; Watson *et al.*, 1985; Freer *et al.*, 1982) in which elements with multiple usable isotopes (e.g., Mg, Ca) can be used as tracers. The measured Mg diffusion rates for spinel are used to establish the temperatures and time scales which control isotopic homogenization of Mg in refractory inclusions found in some meteorites. A preliminary report of this approach has been given (Sheng *et al.*, 1991c).

6.1. ANALYTICAL TECHNIQUE

The determination of diffusion coefficients usually requires isotopic or chemical analysis with high spatial resolution, as produced by depth profiling using secondary ion mass spectrometry. In our experiments we found that at the temperatures of interest, diffusion of Mg in spinel (and melt) was sufficiently fast that isotopic profiles $\sim 40\mu\text{m}$ long were developed in spinel in less than 24 hr. The length of the profiles enabled us to measure the variations in Mg isotopic composition along a traverse normal to the diffusion interface in both spinel and glass. Depth profiling techniques required in many

isotopic tracer experiments (cf., Coles and Long, 1973; Reed and Wuensch, 1979; Cygan and Lasaga, 1985) were not necessary.

The Mg isotopic compositions in spinel and glass were determined with the PANURGE ion microprobe. To maximize the spatial resolution of the ion probe analyses, the ^{16}O primary beam was focused to a diameter of $\sim 5 \mu\text{m}$. An aperture inserted in the sample image plane allowed only secondary ions emitted from an $8 \mu\text{m}$ diameter region centered on the point of analysis to enter the mass spectrometer. Isotopic profiles were measured by moving the sample under computer control in predetermined movements, while holding the position of the primary beam fixed. In addition to the Mg isotopes, the $^{28}\text{Si}^+ / ^{24}\text{Mg}^+$ ratio was recorded to provide a sensitive indicator of the presence of glass. The 2σ error for measured $^{25}\text{Mg} / ^{24}\text{Mg}$ ratios is $\pm 3\%$ and $\pm 2\%$ for $^{26}\text{Mg} / ^{24}\text{Mg}$.

The data analysis required two types of corrections for instrumental mass-dependent fractionation. Since the $^{26}\text{Mg} / ^{24}\text{Mg}$ ratio in the ^{25}Mg -doped glass was approximately (within $\pm 3\%$) normal, measured $^{25}\text{Mg} / ^{24}\text{Mg}$ ratios in each phase were corrected for fractionation using a power law after normalizing to $^{26}\text{Mg} / ^{24}\text{Mg} = 0.13955$ (Brigham, 1990). In order to compare measured $^{25}\text{Mg} / ^{24}\text{Mg}$ ratios in spinel and glass, and thus determine the composition, at the boundary, an 8 ‰ correction was applied to the data from glass to correct for differences in "intrinsic" instrumental fractionation between spinel and glass. This correction was determined by measurements in spinel and isotopically normal glass. The distances between the sputtered holes from the ion microprobe analyses were determined on a high precision (resolution $\sim 0.1 \mu\text{m}$)

measuring stage attached to an optical microscope. The isotope ratios at the boundary were determined by extrapolating the measured data in both spinel and glass on different sides of the border to the boundary. Chemical compositions of spinel and glass were measured with WDS. The concentrations of each Mg isotope species in spinel and melt are calculated from measured isotope ratios and total Mg concentrations in each phase and expressed in terms of moles per cubic centimeter, where the density of the melt was calculated using the method of Lange and Carmichael (1987).

6.2. EXPERIMENTAL METHOD

We investigated Mg self-diffusion in MgAl_2O_4 (spinel) using isotopic tracers. The diffusion couple consists of a single crystal gem quality spinel with a normal isotopic composition and spinel saturated, ^{25}Mg -doped, $\text{CaO-MgO-Al}_2\text{O}_3\text{-SiO}_2$ melts representative of POI compositions. The spinel crystal was sawed into thin slabs $\sim 300 \mu\text{m}$ thick and one side polished to a smooth, flat surface with $1 \mu\text{m}$ diamond paste. The polished spinel slabs were annealed in air for 24 hrs. at 1500°C . ^{25}Mg doped glasses were produced by first mixing ^{25}MgO powder ($^{25}\text{MgO} > 98.7\%$: Oak Ridge National Laboratory) with appropriate amounts of CaCO_3 , MgO , Al_2O_3 , and SiO_2 and then grinding under ethanol in an agate mortar. The mixtures were decarbonated at 800°C for 12 hours followed by melting in Pt crucibles in a Del-Tech VT-31 furnace at 1550°C for 24 hours in air and quenched in deionized water. Each bulk composition was chosen based on phase equilibria studies (Sheng *et al.*, 1991b) to be in equilibrium with spinel

at the desired temperature for the diffusion experiment. Glass chips were analyzed after melting and verified to be both chemically and isotopically homogeneous by electron probe and ion probe measurements. Mg isotope ratios measured in the glass are consistent with the amount of isotope tracer added into the mixture.

Preparation of the diffusion couple is shown schematically in Fig.6.1. Chips of the ^{25}Mg doped glass were placed in a cylindrical Pt crucible of 3 mm diameter. The glass chips were remelted inside the crucible to produce a nearly bubble-free glass. Chemical and isotopic compositions of the glass were not changed by the remelting. The remelted glass was then reequilibrated at a temperature slightly ($\sim 5\text{-}10^\circ\text{C}$) below the spinel saturation temperature of the melt composition to ensure chemical equilibrium. The melt was quenched in air to prevent fracturing of the glass. Observation of this reequilibrated glass under the optical microscope showed spinel grains crystallized from the melt but had settled down to the bottom of the crucible (Fig.6.2). The open end of the crucible was sawed off and the glass polished to a flat surface. The preannealed and polished spinel slab was placed against the polished surface of the glass and tied together by Pt wire. This couple was then placed into the hot spot of preheated Del-Tech furnace adjacent to a thermocouple, and held at the temperature of interest for periods of 0.5 to 20 hours. Samples were removed through the top of the furnace and allowed to cool slowly in air, to avoid fracturing spinel or glass. All experiments were conducted in air at one atmosphere. This procedure produces a well defined, wetted contact between spinel and a bubble-free, spinel saturated melt. Assuming that there is no convection in the melt, diffusion coefficients in both melt and crystal can be determined.

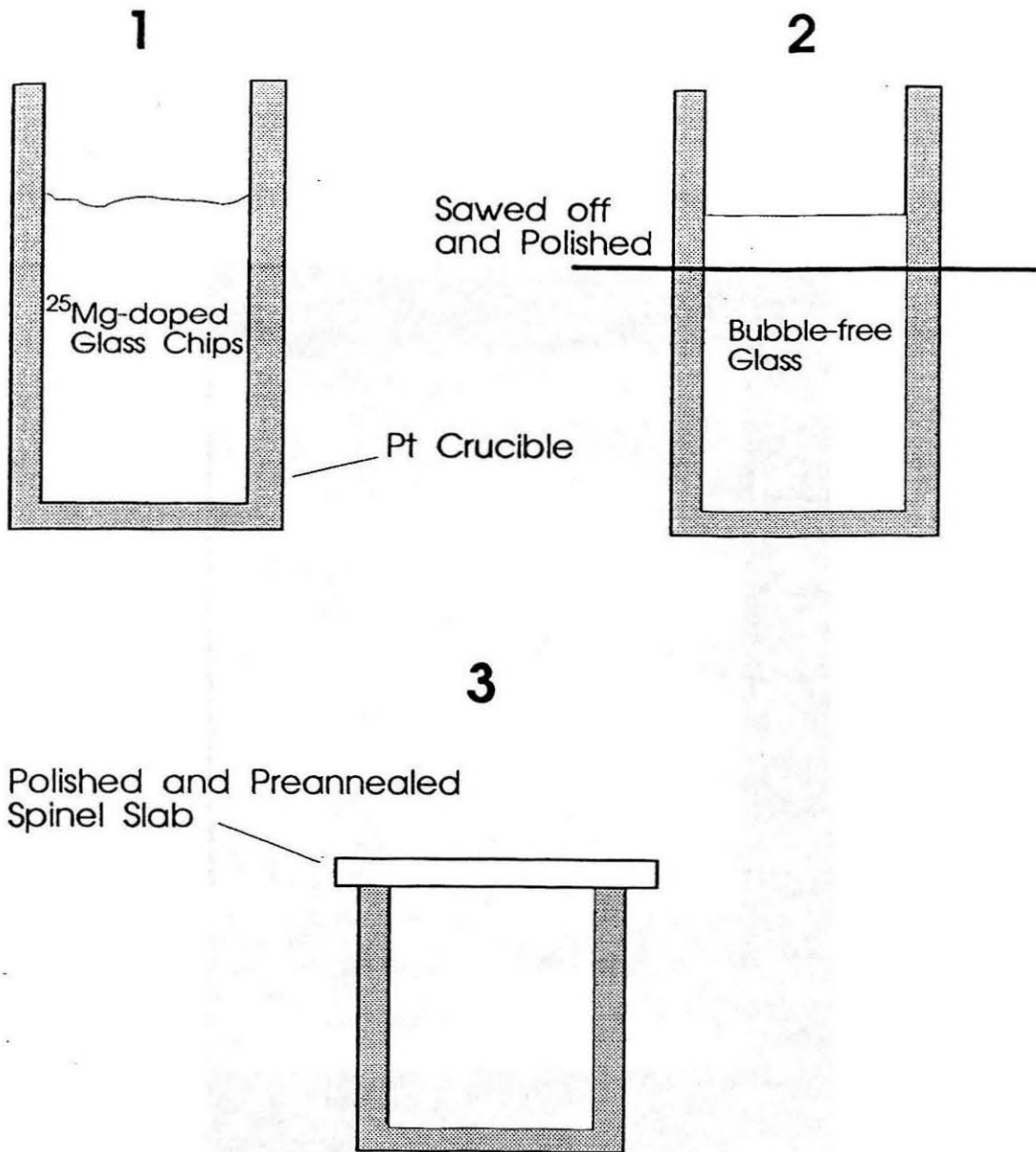


Fig. 6.1 Schematic illustration showing the preparation of the diffusion couple. Chips of homogenized ^{25}Mg -doped glass is remelted inside Pt crucible to produce bubble free glass. It is then reequilibrated at a temperature slightly below the spinel-saturation temperature of the melt composition to ensure chemical equilibrium. The glass is polished after the open end is sawed off. A polished and preannealed spinel slab is placed against the polished glass. The glass and spinel slab is fastened together with Pt wire and then placed into a furnace to the temperature in which the melt was equilibrated.

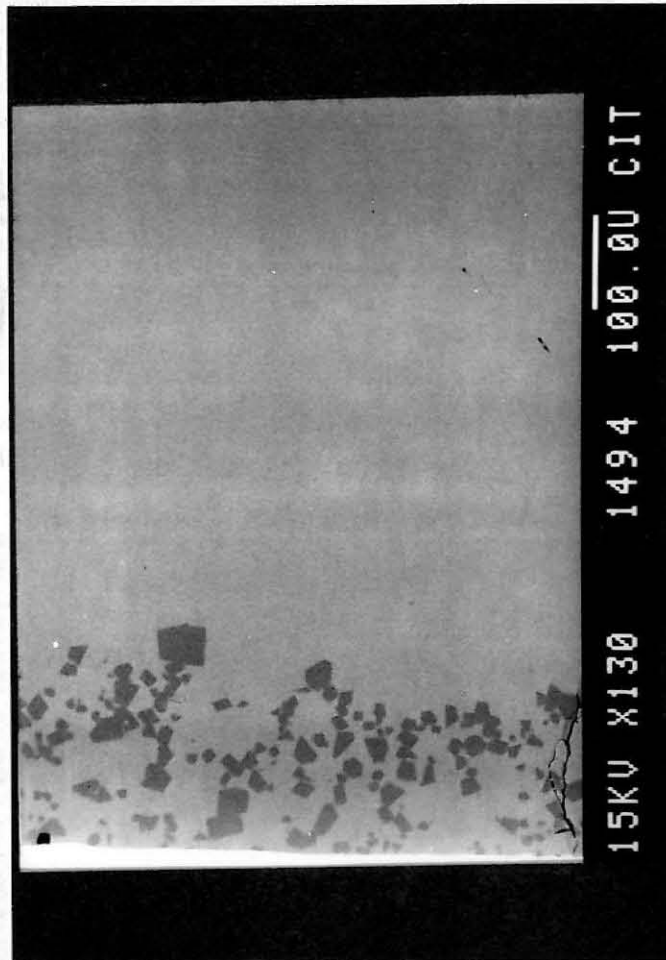


Fig.6.2 SEM backscattered image showing spinels that had crystallized and settled to the bottom of the Pt crucible during re-equilibration of the melt at a temperature below the spinel-saturation temperature of the liquid composition.

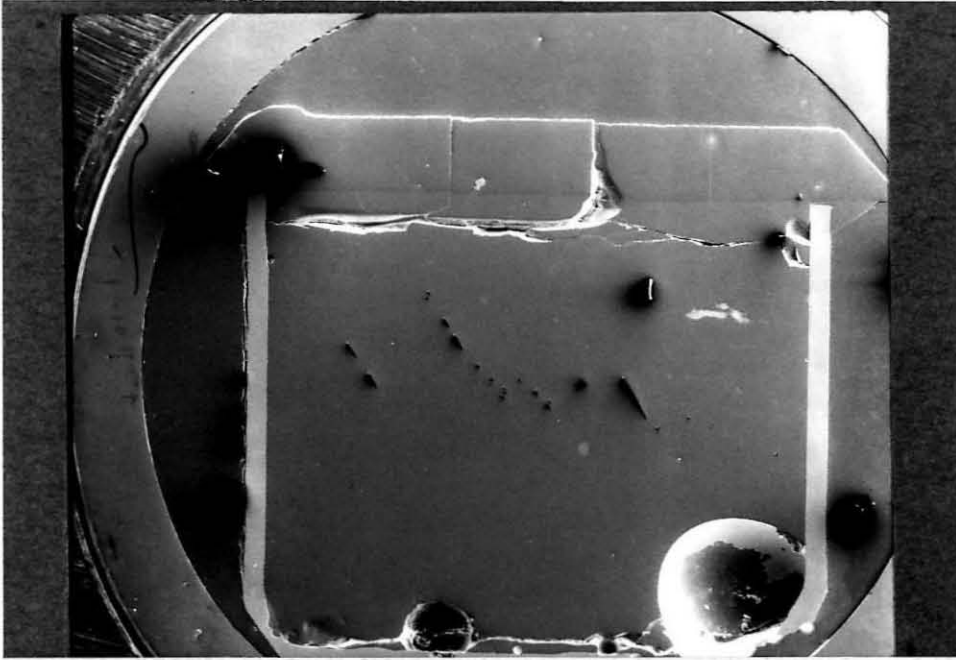


Fig.6.3 SEM secondary electron (SEI) image of one run product showing a cross section of the spinel slab welded to the glass contained inside Pt crucible. The inner diameter of the Pt crucible is 3 mm.

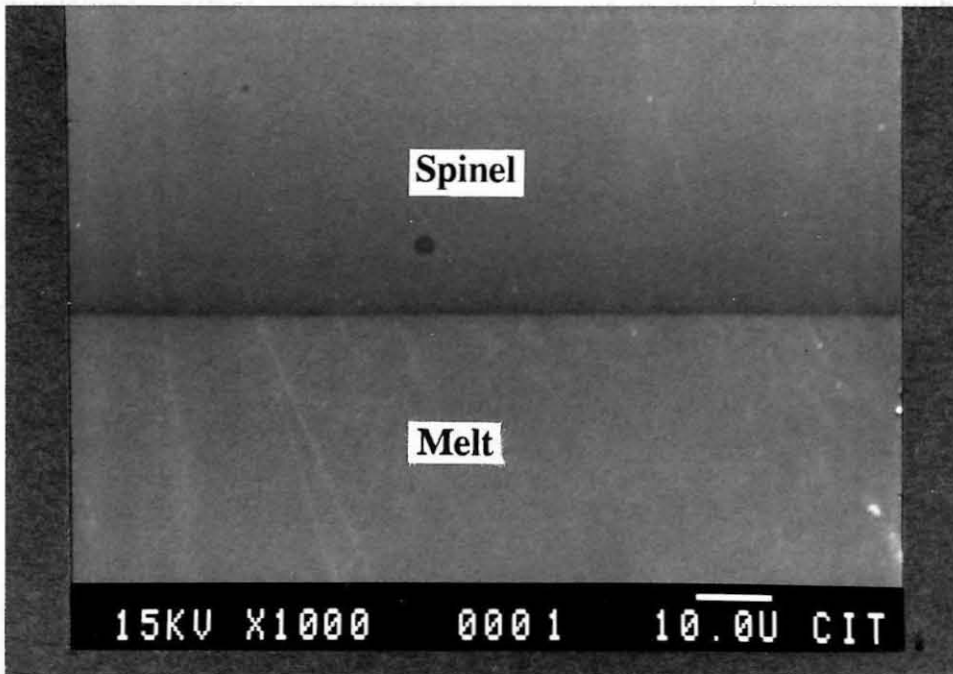


Fig.6.4 An enlarged secondary electron image shows the wetting of melt on spinel surface yielded a sharp welded contact between the two phases.

Figure 6.3 is a secondary electron image (SEI) of one run product showing the spinel slab welded onto the ^{25}Mg doped glass contained within a Pt crucible. As shown in the enlarged SEI in Fig.6.4, wetting of the melt on the spinel surface yielded a boundary of spinel to glass that was a sharp welded contact. This is an illustration of a contact in which the two phases are in chemical equilibrium.

6.2. Mathematical Treatment

The data for the experimental conditions described above was treated as diffusion in an infinite composite medium taking into account the complementary diffusion of ^{24}Mg , ^{25}Mg and ^{26}Mg in both spinel and melt with the total concentration of Mg in each phase maintained constant. The two phases are thus in bulk chemical equilibrium but with isotopic exchange. The conditions are schematically illustrated in Fig.6.5 showing the concentration distribution of total Mg and of the different isotopes in the two phases before and after the diffusion experiment. For the three isotope species ^{24}Mg , ^{25}Mg , ^{26}Mg we assign the indices $i=1, 2, 3$ respectively. The number concentrations of these species, C_i , in the two media, spinel (R) and melt (L), satisfy the condition

$$C_1^L + C_2^L + C_3^L = \Sigma^L = C_1^{L_0} + C_2^{L_0} + C_3^{L_0} \quad (1a)$$

and

$$C_1^R + C_2^R + C_3^R = \Sigma^R = C_1^{R_0} + C_2^{R_0} + C_3^{R_0} \quad , \quad (1b)$$

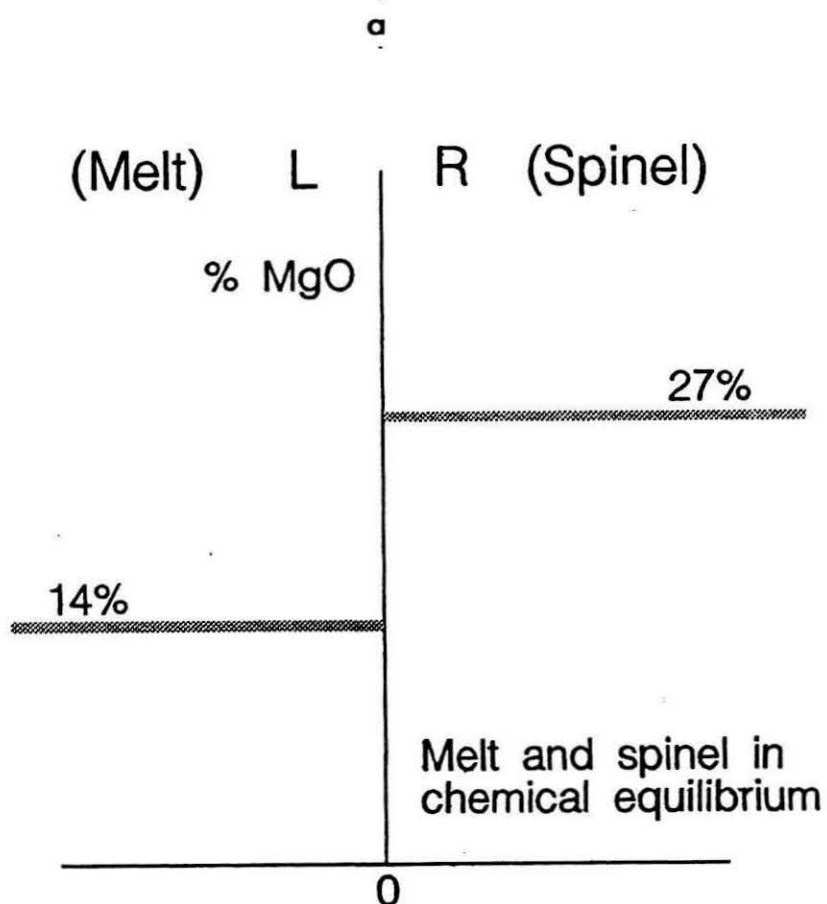
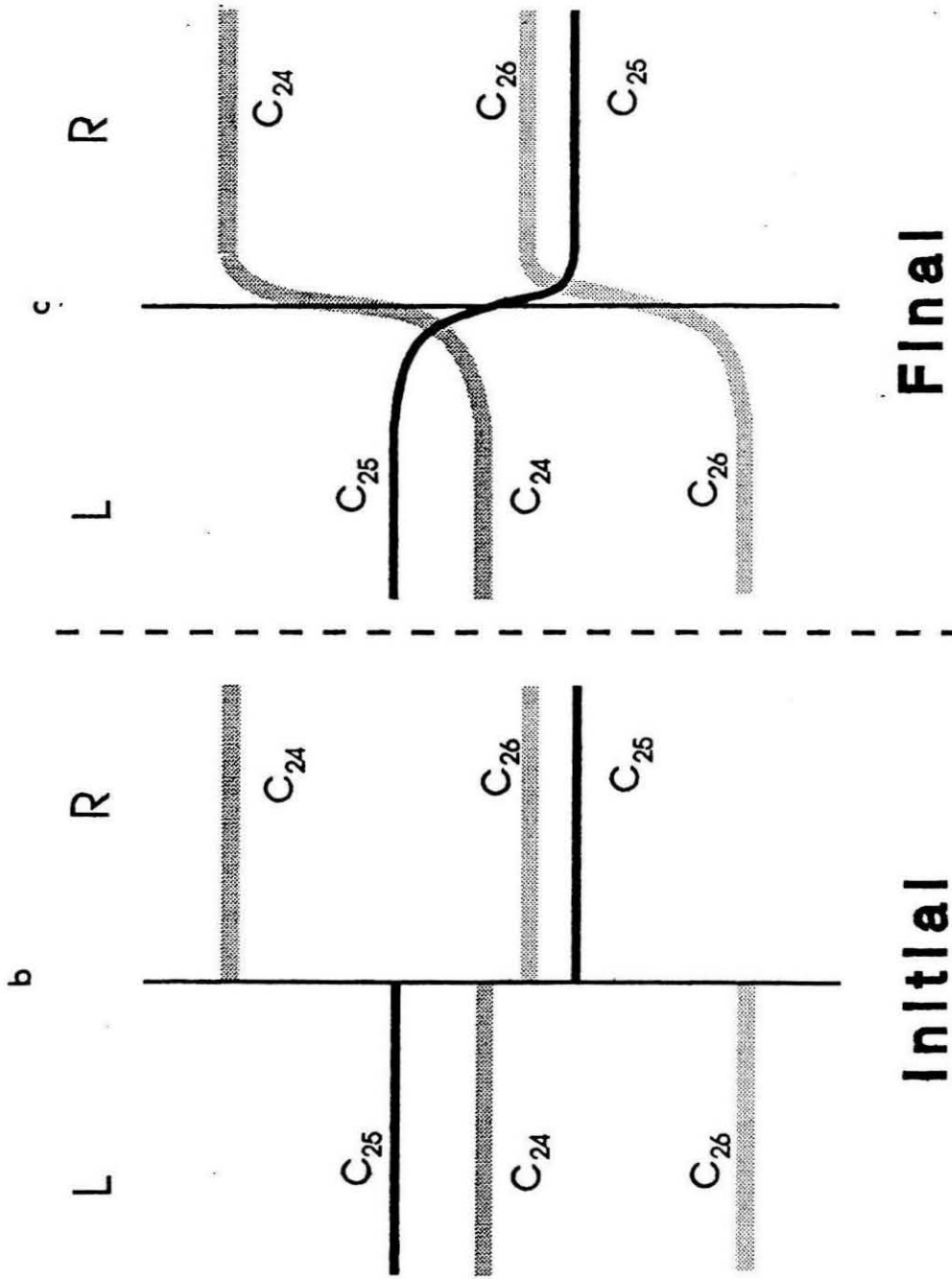


Fig.6.5 Schematic drawing illustrating a) the composition of the melt is in chemical equilibrium with spinel at the run temperature therefore the total Mg in both spinel and melt remain constant throughout the experiment. b) The concentration of Mg isotopes in spinel and melt before and c) after diffusion experiment. The concentration profiles of Mg isotopes in both spinel and melt can be modeled by simple one dimensional diffusion equations.



where C^{L0} and C^{R0} denote the initial concentration of species C_i in L and R respectively and Σ^L and Σ^R are the total concentrations of the isotope species in phase L or R. Provided that there is no convection, and no growth or dissolution of spinel (i.e., no moving boundaries), the relevant transport equations for constant diffusion coefficients are

$$\frac{\partial C_i^L}{\partial \tau} = D_L \nabla^2 C_i^L \quad (2a)$$

and

$$\frac{\partial C_i^R}{\partial \tau} = D_R \nabla^2 C_i^R, \quad (2b)$$

where D_L and D_R are, respectively, the diffusion coefficients for the species in phases L and R, and τ is the time. This is a reasonable assumption given that the bulk compositions of both phases are constant. From (1) and (2)

$$\frac{\partial C_1^L}{\partial x} + \frac{\partial C_2^L}{\partial x} + \frac{\partial C_3^L}{\partial x} = 0 \quad (3a)$$

and

$$\frac{\partial C_1^R}{\partial x} + \frac{\partial C_2^R}{\partial x} + \frac{\partial C_3^R}{\partial x} = 0 \quad (3b)$$

The continuity of flux for each species through the spinel-liquid interface requires that

$$D_L \left. \frac{\partial C_i^L}{\partial x} \right|_{x=0} = D_R \left. \frac{\partial C_i^R}{\partial x} \right|_{x=0} \quad (4)$$

at $x=0$ and as the isotopic composition must be continuous at $x = 0$, $\tau > 0$:

$$\frac{C_i^L}{C_1^L + C_2^L + C_3^L} = \frac{C_i^R}{C_1^R + C_2^R + C_3^R} \quad (5)$$

If the initial conditions are

$$\begin{aligned} C_i^L(x,0) &= C_i^{L_0} \quad , \quad x < 0 \\ C_i^R(x,0) &= C_i^{R_0} \quad , \quad x > 0 \quad , \end{aligned} \quad (6)$$

the solutions are of the form (cf., Jost, 1952; Crank, 1975)

$$C_i^L(x,\tau) = A_i^L + B_i^L \operatorname{erf} \left(\frac{x}{2\sqrt{D_L\tau}} \right) \quad (7a)$$

and

$$C_i^R(x,\tau) = A_i^R + B_i^R \operatorname{erf} \left(\frac{x}{2\sqrt{D_R\tau}} \right) \quad (7b)$$

From equations (3) and (7)

$$B_1^L + B_2^L + B_3^L = 0 \quad (8)$$

and

$$B_1^R + B_2^R + B_3^R = 0 .$$

From equations (4) and (7)

$$B_1^L = \alpha B_1^R , \quad B_2^L = \alpha B_2^R , \quad B_3^L = \alpha B_3^R . \quad (9)$$

Here
$$\alpha \equiv \sqrt{\frac{D_R}{D_L}} . \quad (10)$$

From equations (5) and (7)

$$\left. \frac{C_i^L}{\Sigma^L} \right)_{x=0} = \frac{A_i^L}{\Sigma^L} = \frac{A_i^R}{\Sigma^R} = \left. \frac{C_i^R}{\Sigma^R} \right)_{x=0} . \quad (11)$$

From the initial conditions we can write (7) as

$$C_i^{L_0} = A_i^L - B_i^L$$

and (12)

$$C_i^{R_0} = A_i^R + B_i^R ,$$

from which we can derive

$$\begin{aligned} C_i^{L_0} &= A_i^L - \alpha B_i^R \\ &= \frac{\Sigma^L}{\Sigma^R} A_i^R - \alpha B_i^R \end{aligned} \quad (13)$$

From equations (12) and (13) we can write

$$C_i^{L_0} + \alpha C_i^R = \left(\frac{\Sigma^L}{\Sigma^R} + \alpha \right) A_i^R \quad (14)$$

Hence we can solve

$$A_i^L = \frac{\Sigma^L}{\Sigma^R} \frac{(C_i^{L_0} + \alpha C_i^{R_0})}{\left(\frac{\Sigma^L}{\Sigma^R} + \alpha \right)} \quad A_i^R = \frac{(C_i^{L_0} + \alpha C_i^{R_0})}{\left(\frac{\Sigma^L}{\Sigma^R} + \alpha \right)} \quad (15)$$

and

$$B_i^L = \frac{\alpha \left(C_i^{R_0} \frac{\Sigma^L}{\Sigma^R} - C_i^{L_0} \right)}{\left(\frac{\Sigma^L}{\Sigma^R} + \alpha \right)} \quad B_i^R = \frac{\left(C_i^{R_0} \frac{\Sigma^L}{\Sigma^R} - C_i^{L_0} \right)}{\left(\frac{\Sigma^L}{\Sigma^R} + \alpha \right)} \quad (16)$$

Substituting equations (10), (15), and (16) into equation (7), the formal solution to this problem becomes

$$\frac{C_i^L}{\Sigma^L} = \frac{C_i^{L_0} + \alpha C_i^{R_0}}{\Sigma^R \left(\frac{\Sigma^L}{\Sigma^R} + \alpha \right)} - \frac{\alpha \left(C_i^{R_0} \frac{\Sigma^L}{\Sigma^R} - C_i^{L_0} \right)}{\Sigma^L \left(\frac{\Sigma^L}{\Sigma^R} + \alpha \right)} \operatorname{erf} \left(\frac{x}{2\sqrt{D_L \tau}} \right) \quad (17a)$$

and

$$\frac{C_i^R}{\Sigma^R} = \frac{C_i^{L_0} + \alpha C_i^{R_0}}{\Sigma^R \left(\frac{\Sigma^L}{\Sigma^R} + \alpha \right)} + \frac{\left(C_i^{R_0} \frac{\Sigma^L}{\Sigma^R} - C_i^{L_0} \right)}{\Sigma^R \left(\frac{\Sigma^L}{\Sigma^R} + \alpha \right)} \operatorname{erf} \left(\frac{x}{2\sqrt{D_R \tau}} \right) \quad (17b)$$

Given a solution in one region (L or R) equation (17) can be used immediately to construct a solution in the other phase. At the boundary $x = 0$, we have

$$\frac{C_i^R(0)}{\Sigma^R} = \frac{C_i^L(0)}{\Sigma^L} \equiv \zeta = \frac{C_i^{L_0} + \alpha C_i^{R_0}}{\Sigma^R \left(\frac{\Sigma^L}{\Sigma^R} + \alpha \right)}, \quad (18)$$

where ζ is a constant. The value of ζ at the boundary thus depends only on the initial chemical and isotopic composition of the system and the diffusion coefficient in each phase via α . Note that if $\alpha = 1$ and $\Sigma^R = \Sigma^L$ then we obtain the usual result:

$$\frac{C_i^L(0)}{\Sigma^L} = \frac{C_i^R(0)}{\Sigma^R} = \frac{1}{2} \frac{C_i^{L_0} + C_i^{R_0}}{\Sigma^L} \quad (19)$$

Using the transform

$$\frac{x}{2\sqrt{D_R\tau}} = \operatorname{erf}^{-1} \left[\frac{\Sigma^R}{A_i^R} \left(\frac{C_i^R}{\Sigma^R} - \frac{A_i^L}{\Sigma^L} \right) \right], \quad (20)$$

(cf., equation 17b) we can plot the inverse error function versus $x/\sqrt{\tau}$. The slope of the best fit line determines the diffusion coefficient D_R .

Errors in the ion probe measurements of $^{25}\text{Mg}/^{24}\text{Mg}$ ratios were incorporated into the diffusion coefficient by an error propagation technique. A linear regression of the diffusion data was performed to determine the activation energy and pre-exponential factor. The associated error in each diffusion coefficient was included in this regression using the method of Williamson (1968).

6.4. EVALUATION OF THE DIFFUSION COUPLE

6.4.1. Treatment of the Diffusion Couple

In all experiments, spinel could be treated as an infinite medium. However, in some preliminary experiments with a rather limited amount of melt relative to the crystal (runs at $T = 1302, 1354, \text{ and } 1497^\circ\text{C}$), we found that the $^{25}\text{Mg}/^{24}\text{Mg}$ isotope ratio of the glass measured at the point furthest away from the spinel-glass boundary was significantly lower than the initial ratio of the glass prior to the experiments. This indicates that the amount of Mg in the melt and hence the mass of the melt in these

experiments was inadequate to treat it as an infinite medium, greatly complicating any attempt to extract diffusion coefficients. In subsequent experiments, we ensured that sufficient glass was present so that the liquid could be treated as an infinite reservoir and verified that $^{25}\text{Mg}/^{24}\text{Mg}$ measured in the glass far from the spinel following the diffusion anneal corresponded to that of the initial glass.

6.4.2. Importance of Chemical Equilibrium during Diffusion Experiment

The chemical and isotopic composition of the glasses and spinel are given in Table 6.1. If spinel and melt are in chemical equilibrium for each run, then Mg diffuses only in response to the isotopic disequilibrium. That this condition was fulfilled during our experiments was tested by measuring the chemical and isotopic compositions along diffusion profiles normal to the interface.

The importance of establishing chemical equilibrium during the course of the diffusion experiment can be demonstrated by the experimental result shown in Fig.6.6. The spinel to glass boundary in this experiment, where the melt was over saturated with respect to spinel, shows a serrated contact due to spinel growth. The irregular contact between the two phases indicates that bulk chemical disequilibrium existed at some point during the experiment. The diffusion coefficient of Mg determined from the measured isotope abundance profile in spinel from this experiment is not consistent with the data from our other experiments and is not included in our discussion.

Table 6.1
Compositions of Starting Material

	MgO	Al ₂ O ₃	SiO ₂	CaO	Sum	²⁵ Mg/ ²⁴ Mg	²⁵ C ₀	ΣMg
1553GI	11.69	32.29	43.71	12.76	100.55	0.90530	0.00299	0.00679
1497GI	13.23	33.06	43.35	10.82	100.56	1.47665	0.00433	0.00767
1495GI	13.81	30.84	44.39	10.92	99.96	0.81343	0.00334	0.00803
1415GI	14.08	28.60	47.34	10.06	100.08	1.18216	0.00416	0.00817
1354GI	13.12	25.81	49.32	11.10	100.35	1.47809	0.00431	0.00761
1302GI	13.17	25.16	51.78	10.47	100.58	1.47841	0.00431	0.00764
1261GI	14.58	22.76	54.45	7.97	99.76	0.85726	0.00423	0.00848
Spinel	28.20	72.63	0.03	0.02	100.88	0.12633	0.00254	0.02541

Oxides are in wt. %, initial ²⁵Mg (²⁵C₀) and total Mg (ΣMg) concentrations are in moles/cc.

Zhang *et al.* (1989) derived a quantitative way to assess the growth or dissolution rate during diffusion experiments using a diffusion controlled growth (or dissolution) model. Using their model, the effects of chemical disequilibrium between melt and coexisting solid can be estimated.

For spinel, the major component that controls the saturation of the mineral is Al₂O₃. Assuming the saturation concentration of Al₂O₃ is exactly 30%, and the actual Al₂O₃ concentration in the melt is 30.1% (slightly oversaturated). The minimum growth distance can be estimated by assuming diffusion-controlled growth,

$$L = 2a\sqrt{D_m t}$$

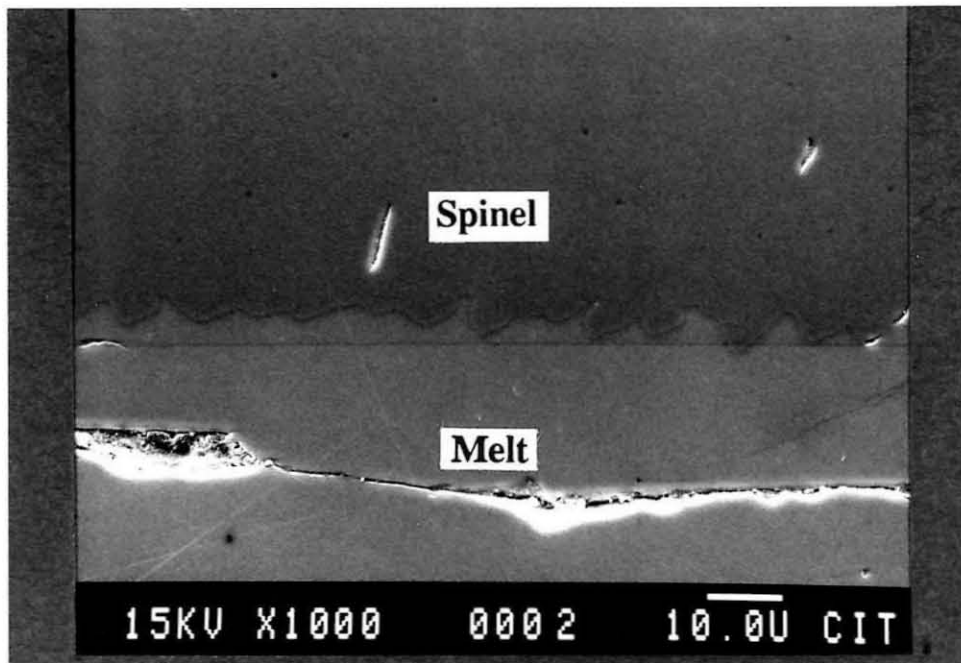


Fig.6.6 SEI image of a serrated spinel to glass boundary which is the result of chemical disequilibrium between the two phases. The melt composition was spinel oversaturated at the run temperature of this experiment.

Here L is growth distance, D_m is the diffusion coefficient in the melt, t is the run duration, and a is a parameter that is dependent on composition by the relation:

$$b = \frac{C_i - C_0}{C_s - C_0} = \sqrt{\pi} a e^{a^2} \operatorname{erfc}(a) \quad .$$

Here C_i is the actual concentration of Al_2O_3 , C_s is the Al_2O_3 concentration in spinel (see Zhang *et al.*, 1989).

Assuming $C_s = 70\%$, then $b \approx 0.0025$, $a \approx 0.001$. For $D_m = 10^{-7} \text{cm}^2/\text{s}$ and $t = 3600\text{s}$, $L \sim 0.4 \mu\text{m}$. If $D_m = 10^{-6} \text{cm}^2/\text{s}$ and $t = 3600\text{s}$, then $L \sim 1 \mu\text{m}$. For a worst case scenario where the actual concentration of Al_2O_3 is 31% and the saturation concentration of Al_2O_3 is 30%, then $a \approx 0.017$ and $b \approx 0.01$. If $D_m = 10^{-6} \text{cm}^2/\text{s}$, then in one hour, $L = 12 \mu\text{m}$. Hence depending on the accuracy of compositional control, D_m and t , the growth distance could be significant. This also holds for the dissolution rate where the melt is initially undersaturated at the run temperature with respect to spinel.

6.5. RESULTS

Diffusion experiments were performed at seven different temperatures. The results are listed in Table 6.2. The experiments at 1553, 1494, 1415 and 1261°C were conducted under conditions in which both spinel and melt can be treated as infinite sources. The value of the isotopic concentration at the boundary can be quite accurately determined from the set of diffusion profiles in the two phases. The measured data in

spinel is fitted to obtain the diffusion coefficient (D_{sp}). The diffusion coefficient in coexisting melt (D_m) is then calculated from D_{sp} and α .

The results for these experiments are shown in Figs. 6.7-6.17. Figure 6.7 shows the chemical profiles measured in the glass for the experimental run at $T = 1495^\circ\text{C}$. The chemical profiles in the glass from WDS analysis measured to within $5\ \mu\text{m}$ of the boundary show no significant variations in compositions of the chemical species and partially justify the assumption that spinel and melt were in chemical equilibrium. Isotopic abundance profiles for this run measured in both spinel and glass, with only a portion of the diffusion profile in the glass, is shown in Fig.6.8. The $^{28}\text{Si}^+/^{24}\text{Mg}^+$ ratios monitored during these analyses show the sharp drop off of Si across the glass to spinel boundary. Fig.6.9 is the variation of $C_{25}/\Sigma\text{Mg}$, where C_{25} is the concentration of ^{25}Mg in moles/cc and ΣMg the total Mg concentration, across a traverse in the spinel showing a penetration distance of about $50\ \mu\text{m}$. Figure 6.10 shows the least square best fit of the data through equation 20 to determine D_{sp} . The corresponding ion probe traverse for the melt in this same experiment is shown in Fig.6.11. Variations in C_{25} in the glass are smaller in magnitude but extend to much greater distances ($\sim 2\text{mm}$). Using the measured data and equation 17a, the diffusion coefficient in the melt is determined through the relations 10, 17b, and 18. The calculated diffusion profiles in both regions are shown by the curves in Figs.6.8, 6.9 and 6.11. The agreement between the calculated profiles and the measured data for both spinel and melt is very good and serves as a fundamental check on the application of our diffusion model to the experimental data. The results from experiments at other temperatures (Figs.6.12-6.17)

a

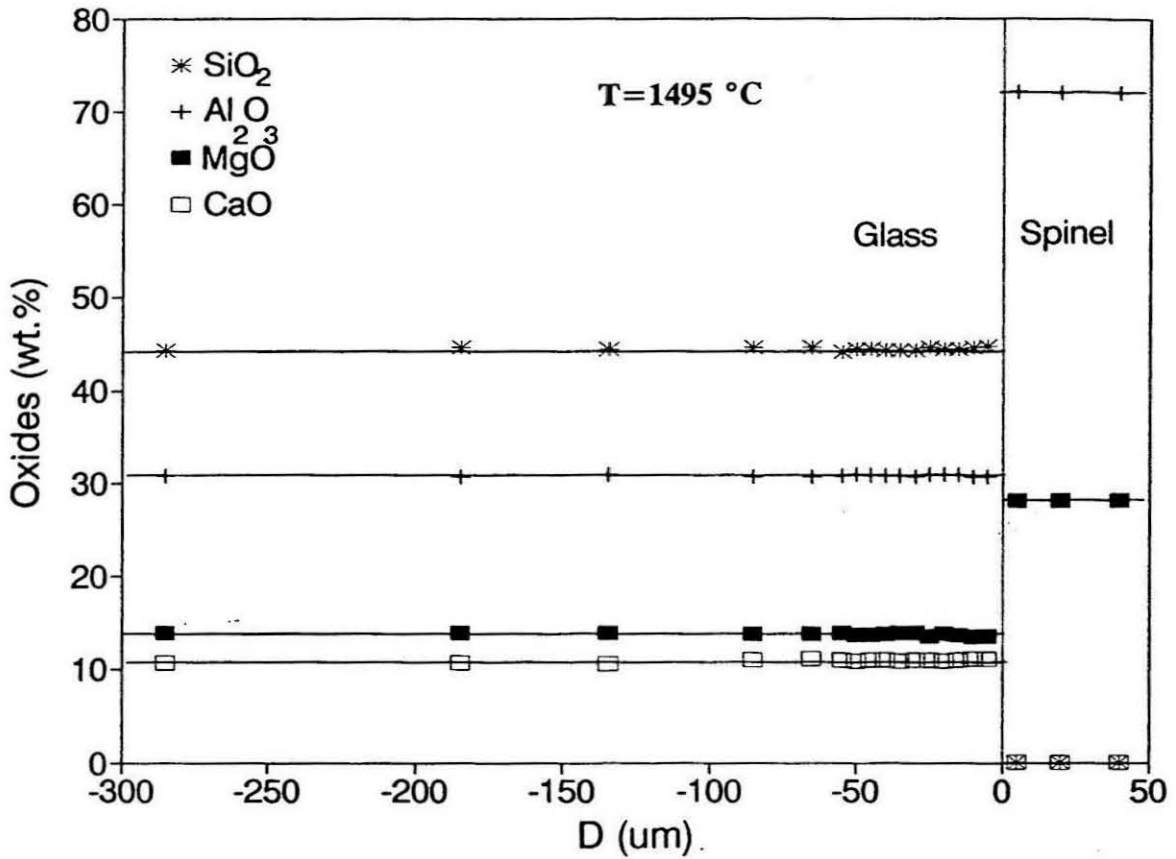
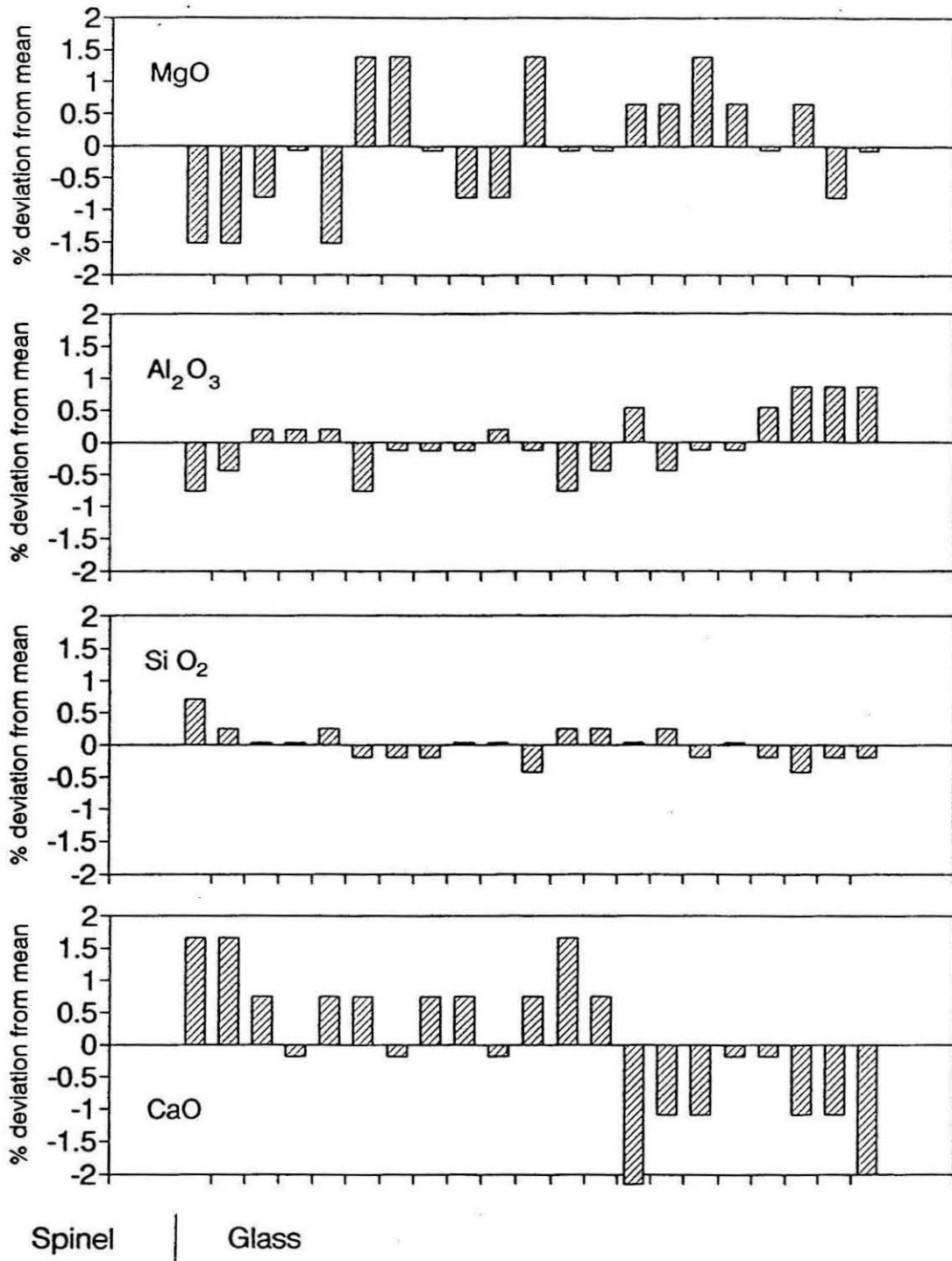


Fig.6.7 a) Chemical profiles from WDS analysis showing concentrations of MgO, Al₂O₃, SiO₂, and CaO in the melt as a function of distance from the spinel-melt interface. b) The percent deviation of each analysis from the mean concentration of respective oxides in the glass is shown in the four bar graphs. The relatively constant concentrations of these oxides indicate that spinel and melt is in chemical equilibrium.

b



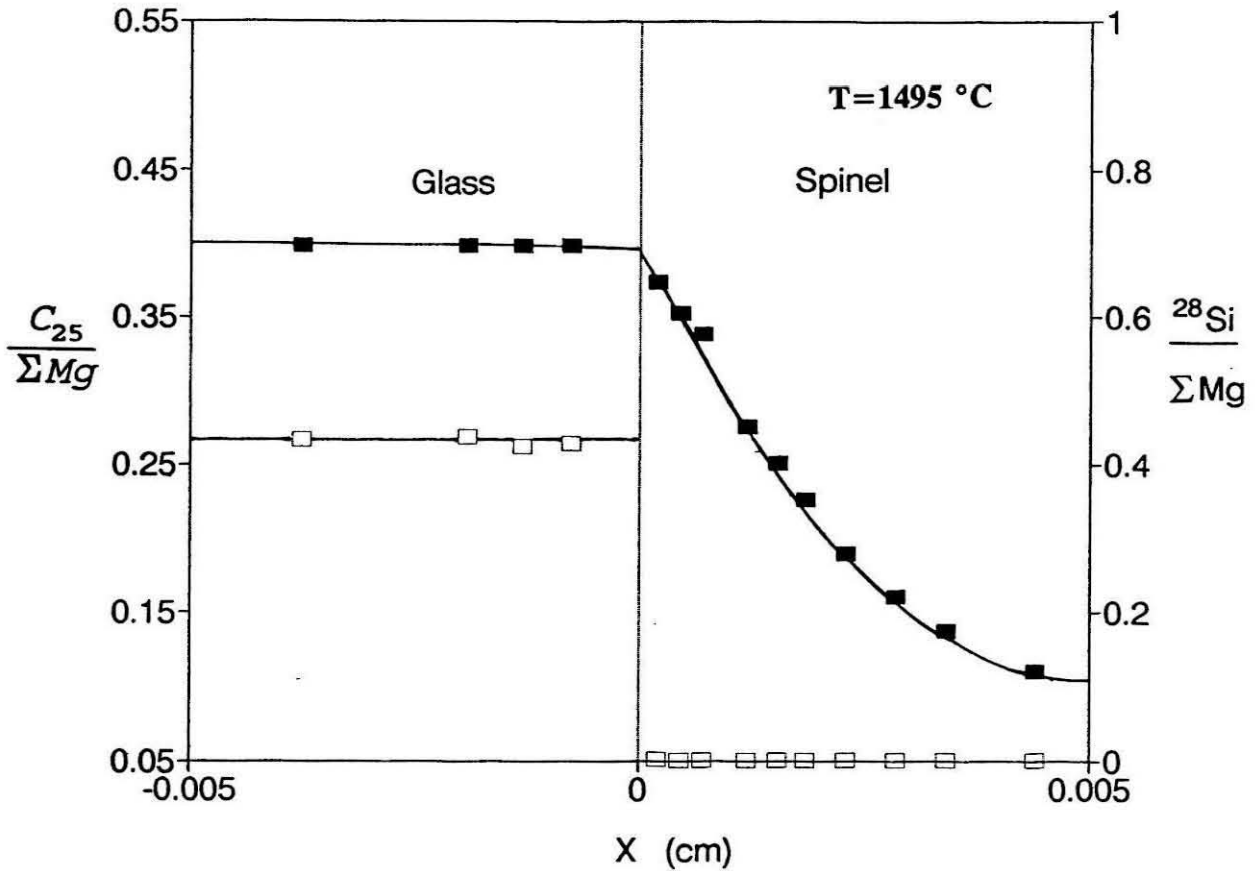
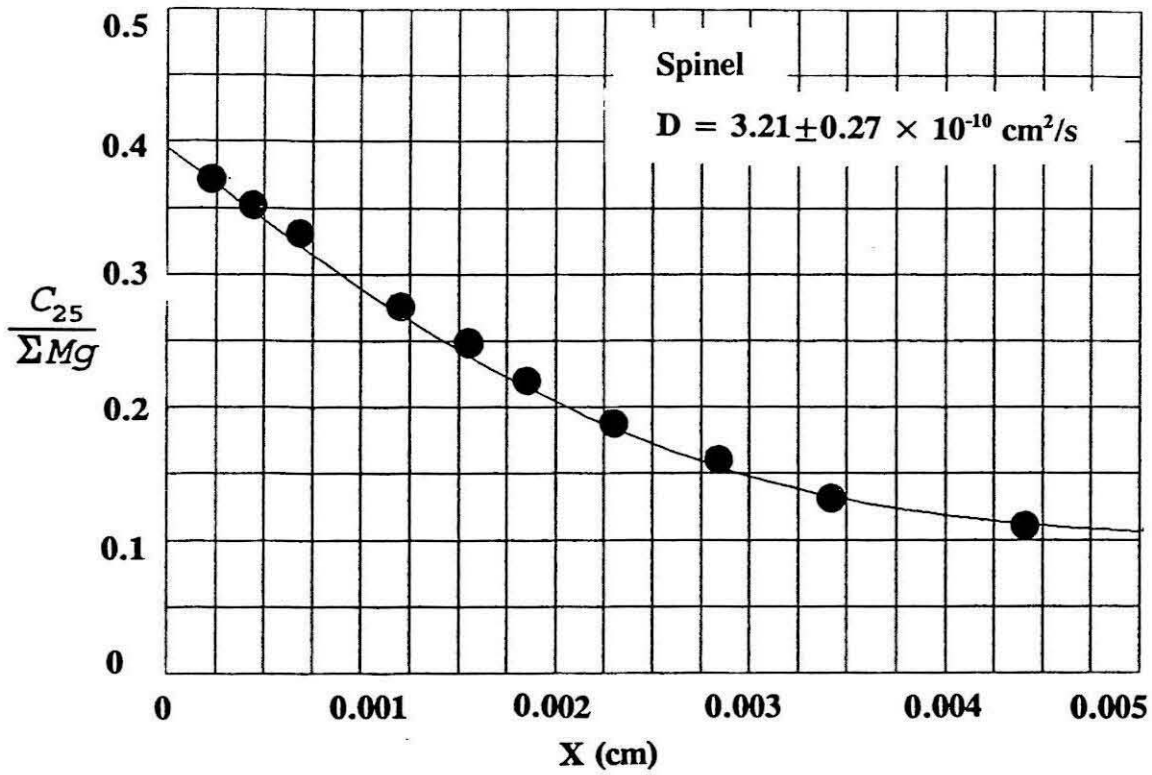


Fig.6.8 Concentration variation of $^{25}Mg/\Sigma Mg$ (filled square) in spinel and melt following diffusion experiment held at 1495°C for 2 hr. Mg isotope ratios are analyzed with an ion microprobe focussed to an ion beam diameter of about 5 μm . $^{28}Si/^{24}Mg$ ratio (open square) is monitored to verify the spinel-melt boundary. The boundary value is determined by extrapolating the measured data in spinel and melt to the boundary. Mg isotope ratios are converted to moles per cubic centimeter and normalized to total Mg.



T=1495 °C Run Duration = 2 hr.		
x (cm)	$^{25}\text{Mg}/^{24}\text{Mg}$	$C_{25}/\Sigma\text{Mg}$
0.00020	0.67938 ± 0.00160	0.37351 ± 0.00055
0.00045	0.62038 ± 0.00184	0.35250 ± 0.00068
0.00070	0.58397 ± 0.00327	0.33882 ± 0.00126
0.00120	0.43351 ± 0.00159	0.27558 ± 0.00073
0.00155	0.38243 ± 0.00124	0.25127 ± 0.00061
0.00185	0.33298 ± 0.00086	0.22613 ± 0.00045
0.00230	0.26690 ± 0.00194	0.18977 ± 0.00112
0.00285	0.21811 ± 0.00083	0.16065 ± 0.00051
0.00340	0.18194 ± 0.00060	0.13768 ± 0.00039
0.00440	0.14194 ± 0.00045	0.11076 ± 0.00031
0.00530	0.12976 ± 0.00039	0.10223 ± 0.00028

Fig.6.9 The concentration profile in spinel shows penetration distance of about 50 μm . The diffusion coefficient derived from a best fit of the measured data is $3.21 \pm 0.27 \times 10^{-10} \text{ cm}^2/\text{s}$. The fitted curve is the calculated diffusion profile using equation 17b.

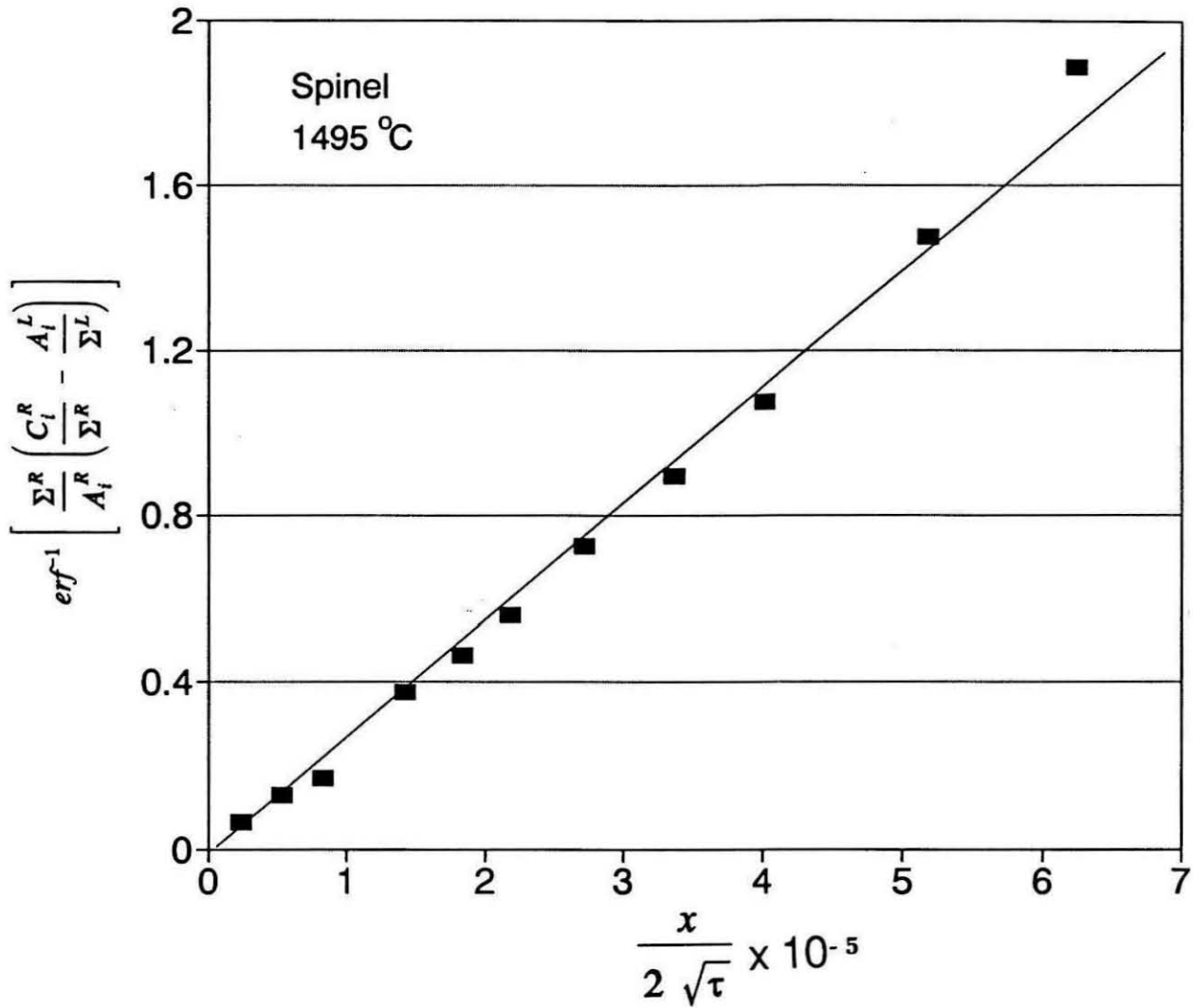


Fig.6.10 Measured Mg isotope data in spinel are fitted through an inverse error function (equation 13). The slope of the best fit line determines the diffusion coefficient of Mg in spinel (D_R).

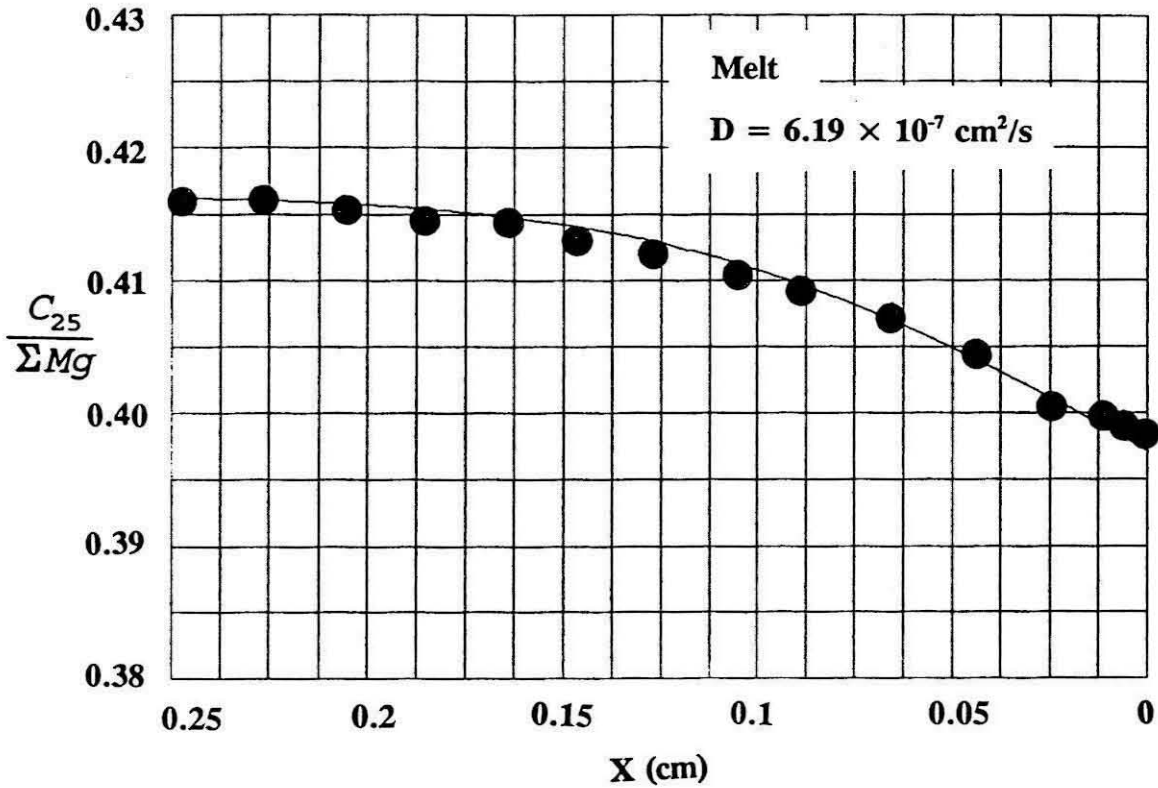
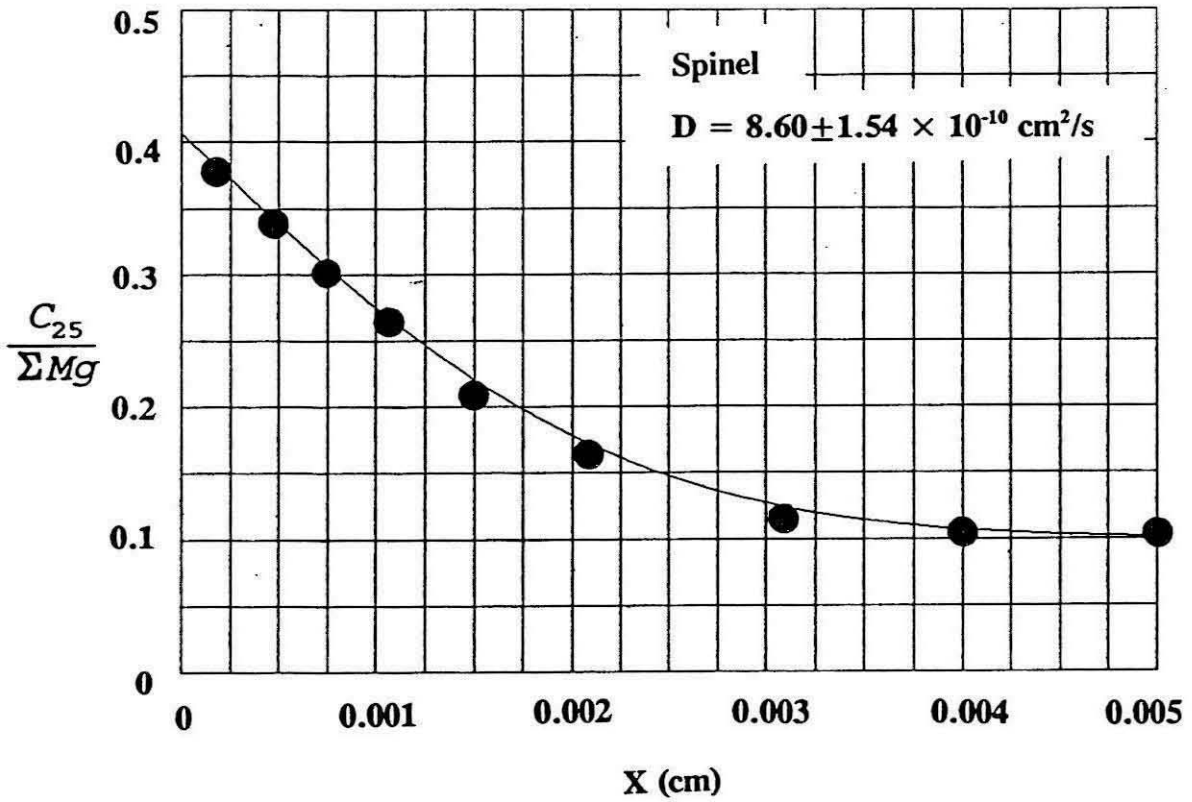


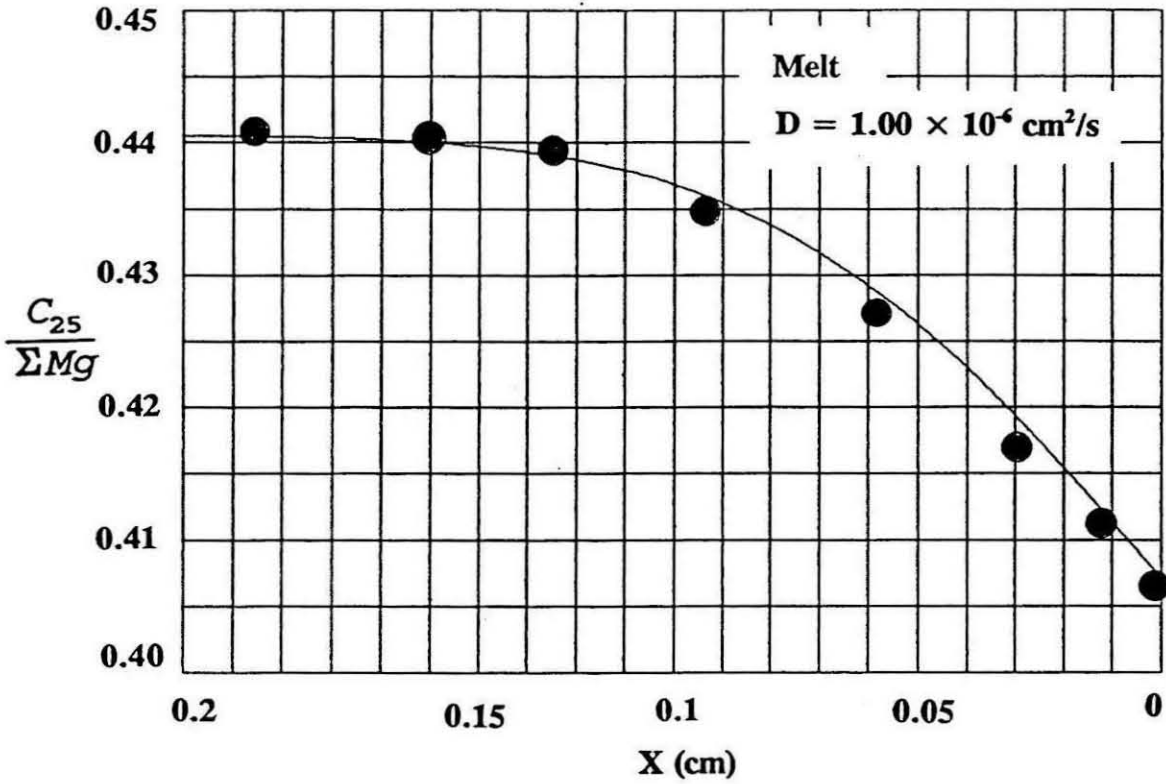
Fig.6.11 Concentration profile in glass shows diffusion distance of over 2000 μm . The diffusion coefficient of Mg in the melt calculated from D_R and α is $6.19 \times 10^{-7} \text{ cm}^2/\text{s}$. The fitted curve is calculated from equation 17a.

T=1495 °C Run Duration = 2 hr.		
x (cm)	$^{25}\text{Mg}/^{24}\text{Mg}$	$C_{25}/\Sigma\text{Mg}$
-0.00075	0.75489±0.00278	0.39848±0.00088
-0.00130	0.75505±0.00215	0.39853±0.00068
-0.00190	0.75561±0.00200	0.39870±0.00064
-0.00375	0.75553±0.00257	0.39868±0.00082
-0.00570	0.75686±0.00287	0.39910±0.00091
-0.01085	0.76307±0.00188	0.40106±0.00059
-0.02580	0.76720±0.00267	0.40236±0.00084
-0.04580	0.77564±0.00275	0.40499±0.00086
-0.06650	0.78260±0.00238	0.40715±0.00073
-0.08630	0.78870±0.00208	0.40902±0.00064
-0.10620	0.79325±0.00255	0.41042±0.00078
-0.12660	0.79718±0.00158	0.41161±0.00048
-0.14680	0.80110±0.00192	0.41280±0.00058
-0.16700	0.80709±0.00273	0.41461±0.00082
-0.18670	0.80731±0.00242	0.41467±0.00073
-0.20670	0.80967±0.00217	0.41538±0.00065
-0.22670	0.81296±0.00231	0.41637±0.00069
-0.24640	0.81265±0.00292	0.41627±0.00087
-0.26280	0.81343±0.00257	0.41651±0.00077



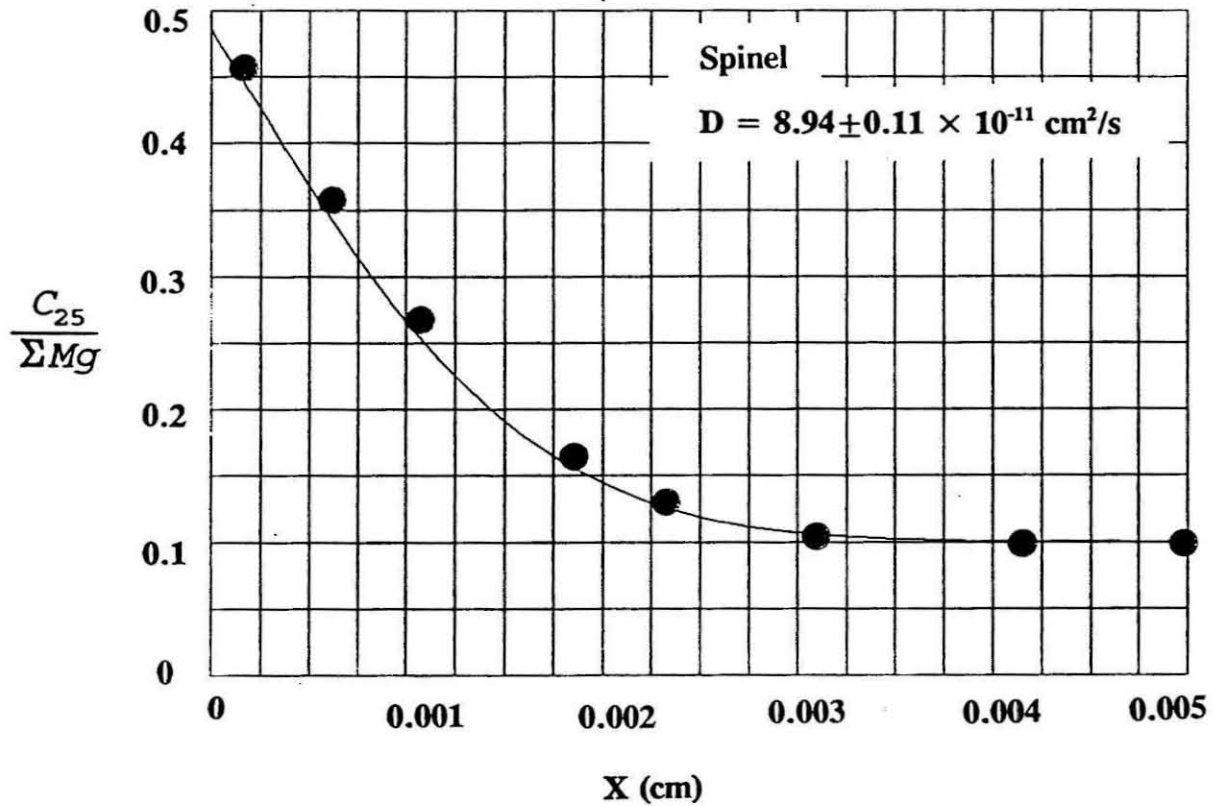
T=1553 °C Run Duration = 0.5 hr.		
x (cm)	$^{25}\text{Mg}/^{24}\text{Mg}$	$C_{25}/\Sigma\text{Mg}$
0.00015	0.68122±0.00183	0.37414±0.00063
0.00045	0.59468±0.00259	0.34291±0.00098
0.00075	0.49548±0.00274	0.30304±0.00117
0.00105	0.40364±0.00242	0.26156±0.00116
0.00150	0.29373±0.00228	0.20494±0.00127
0.00210	0.21902±0.00115	0.16121±0.00071
0.60310	0.14474±0.00040	0.11270±0.00028
0.00400	0.12951±0.00038	0.10205±0.00027
0.00505	0.12826±0.00051	0.10117±0.00036
0.00560	0.12775±0.00046	0.10081±0.00033

Fig.6.12 Measured ^{25}Mg concentration (C_{25}) in spinel for the experimental run at 1553°C.



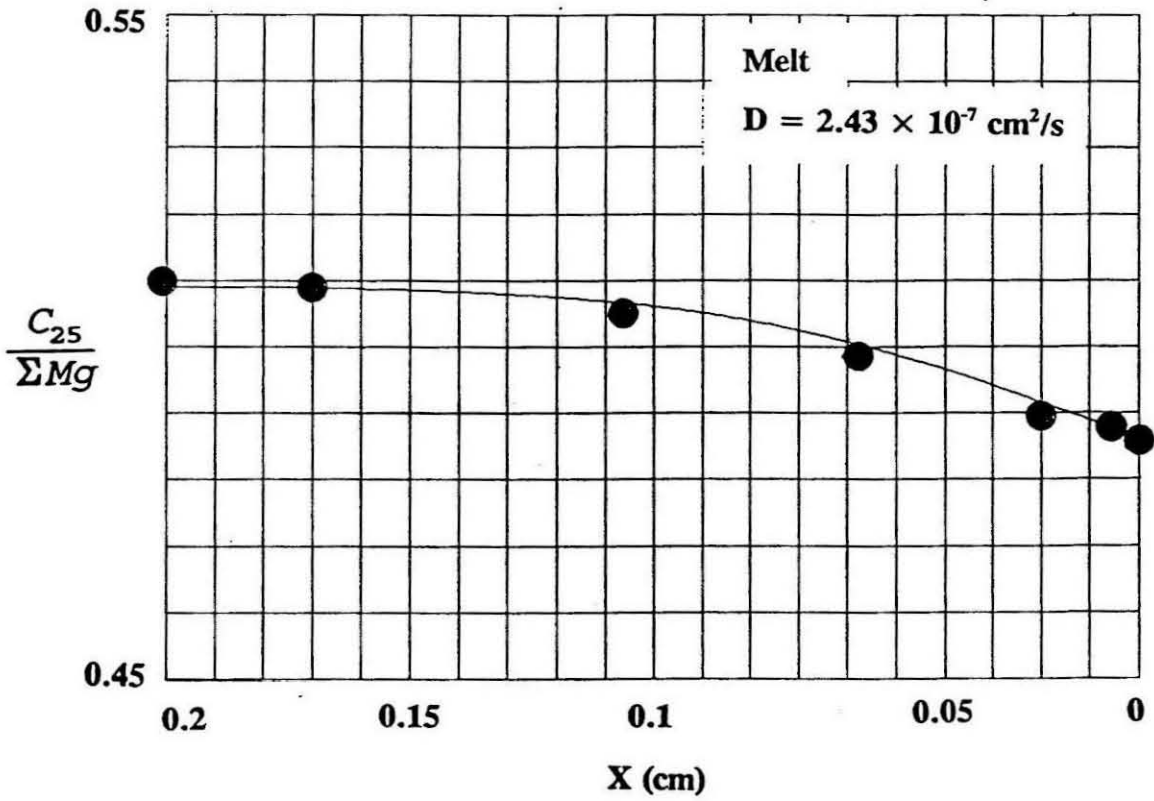
T=1553 °C Run Duration = 0.5 hr.		
x (cm)	$^{25}\text{Mg}/^{24}\text{Mg}$	$C_{25}/\Sigma\text{Mg}$
-0.00020	0.77811 ± 0.00190	0.40256 ± 0.00060
-0.00500	0.77583 ± 0.00339	0.40397 ± 0.00106
-0.01175	0.78466 ± 0.00218	0.41037 ± 0.00067
-0.03180	0.81664 ± 0.00345	0.41645 ± 0.00103
-0.06070	0.85157 ± 0.00318	0.42513 ± 0.00092
-0.09510	0.88087 ± 0.00307	0.43400 ± 0.00086
-0.12620	0.89182 ± 0.00430	0.43975 ± 0.00119
-0.15620	0.89879 ± 0.00515	0.44248 ± 0.00141
-0.18540	0.90403 ± 0.00578	0.44416 ± 0.00157

Fig.6.13 Measured ^{25}Mg concentration (C_{25}) in glass for the experimental run at 1553°C.



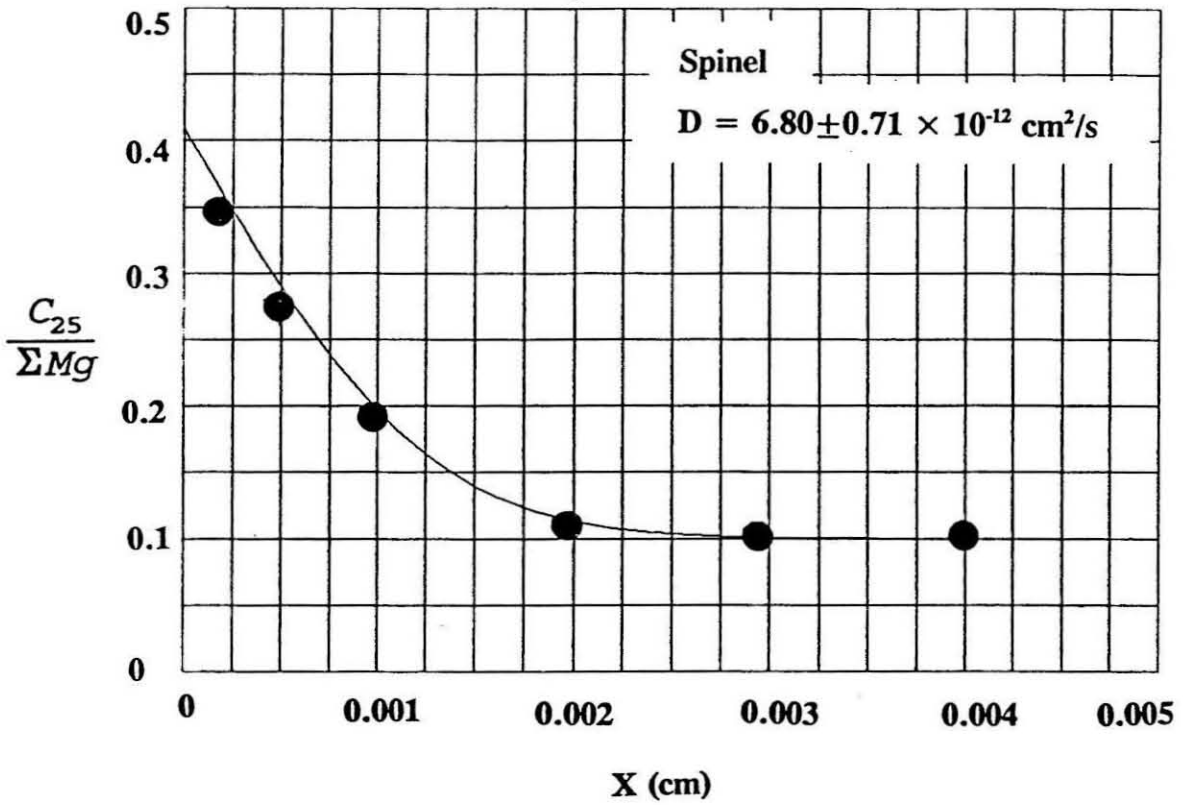
T=1415 °C Run Duration = 2 hr.		
x (cm)	$^{25}\text{Mg}/^{24}\text{Mg}$	$C_{25}/\Sigma\text{Mg}$
0.00015	0.99047 ± 0.00311	0.46500 ± 0.00078
0.00070	0.64775 ± 0.00543	0.36242 ± 0.00194
0.00120	0.42939 ± 0.00240	0.27368 ± 0.00111
0.00185	0.24033 ± 0.00237	0.17417 ± 0.00142
0.00235	0.17562 ± 0.00099	0.13353 ± 0.00065
0.00310	0.13533 ± 0.00051	0.10615 ± 0.00036
0.00415	0.12704 ± 0.00050	0.10030 ± 0.00036
0.00500	0.12675 ± 0.00028	0.10010 ± 0.00020

Fig.6.14 Measured ^{25}Mg concentration (C_{25}) in spinel for the experimental run at 1415°C.



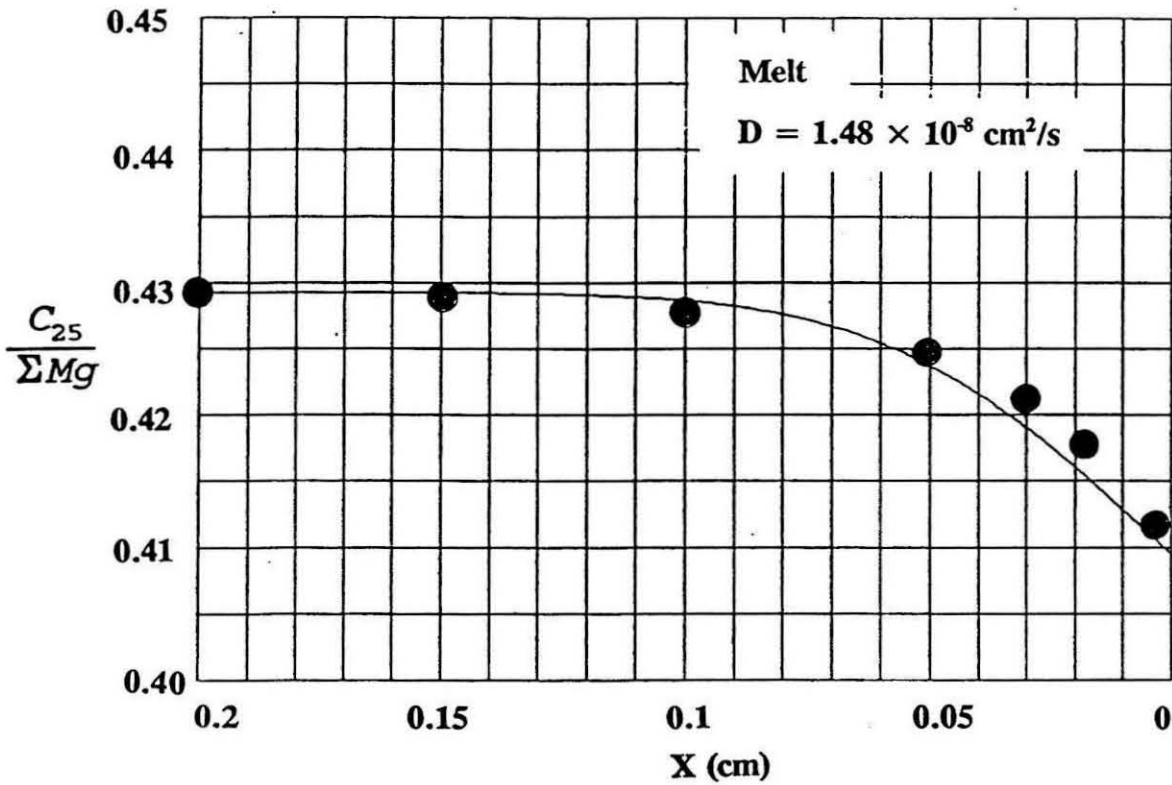
T=1415 °C Run Duration = 2 hr.		
x (cm)	$^{25}\text{Mg}/^{24}\text{Mg}$	$C_{25}/\Sigma\text{Mg}$
-0.00030	1.06708 ± 0.00239	0.48559 ± 0.00056
-0.00145	1.07429 ± 0.00283	0.48727 ± 0.00066
-0.00500	1.07551 ± 0.00239	0.48755 ± 0.00056
-0.01890	1.08117 ± 0.00356	0.48886 ± 0.00082
-0.05840	1.11676 ± 0.00270	0.49696 ± 0.00061
-0.10820	1.15195 ± 0.00276	0.50471 ± 0.00060
-0.17040	1.17623 ± 0.00305	0.50993 ± 0.00065
-0.20830	1.18099 ± 0.00252	0.51094 ± 0.00053

Fig.6.15 Measured ^{25}Mg concentration (C_{25}) in glass for the experimental run at 1415°C.



T=1261 °C Run Duration = 20 hr.		
x (cm)	$^{25}\text{Mg}/^{24}\text{Mg}$	$C_{25}/\Sigma\text{Mg}$
0.00015	0.59048 ± 0.00390	0.34131 ± 0.00149
0.00045	0.41612 ± 0.00505	0.26832 ± 0.00245
0.00095	0.25765 ± 0.00326	0.18441 ± 0.00191
0.00195	0.14333 ± 0.00050	0.11173 ± 0.00035
0.00290	0.12764 ± 0.00036	0.10073 ± 0.00026
0.00390	0.12645 ± 0.00034	0.09988 ± 0.00024
0.00630	0.12673 ± 0.00034	0.10008 ± 0.00024
0.00850	0.12757 ± 0.00065	0.10068 ± 0.00046

Fig.6.16 Measured ^{25}Mg concentration (C_{25}) in spinel for the experimental run at 1261 °C.



T=1261 °C Run Duration = 20 hr.		
x (cm)	$^{25}\text{Mg}/^{24}\text{Mg}$	$C_{25}/\Sigma\text{Mg}$
-0.00100	0.80670 ± 0.00296	0.41254 ± 0.00090
-0.00430	0.80760 ± 0.00238	0.41281 ± 0.00072
-0.01900	0.82108 ± 0.00162	0.41683 ± 0.00048
-0.03090	0.84102 ± 0.00181	0.42464 ± 0.00053
-0.05105	0.84287 ± 0.00194	0.42517 ± 0.00056
-0.10075	0.84926 ± 0.00200	0.42702 ± 0.00058
-0.14950	0.85213 ± 0.00170	0.42810 ± 0.00049
-0.20120	0.85481 ± 0.00118	0.42861 ± 0.00034

Fig.6.17 Measured ^{25}Mg concentration (C_{25}) in glass for the experimental run at 1261°C.

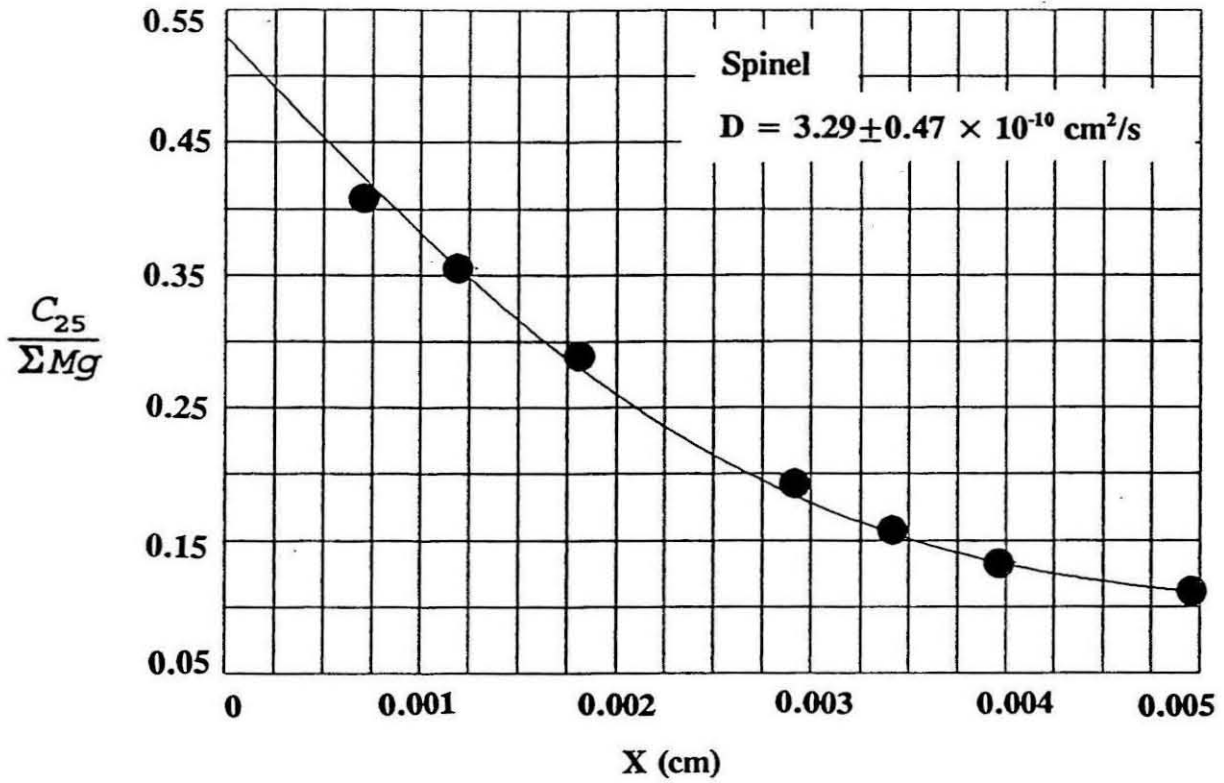
show equally good fits to the measured data.

In three previous experiments at 1497, 1354, and 1302°C, the diffusion profiles were measured only in spinel. The results for these three experiments are given in Figs. 6.18-6.20. It can be seen that the fits of the measured data to calculated curves are also very good. The reason for not measuring the Mg isotope concentrations in the glass phase for these experiments will be discussed in a later section. It will be shown that using the data from these three experiments can be justified. I wish to emphasize that the results for activation energy and pre-exponential factor are unchanged if these data are omitted.

Table 6.2
Experimental Results

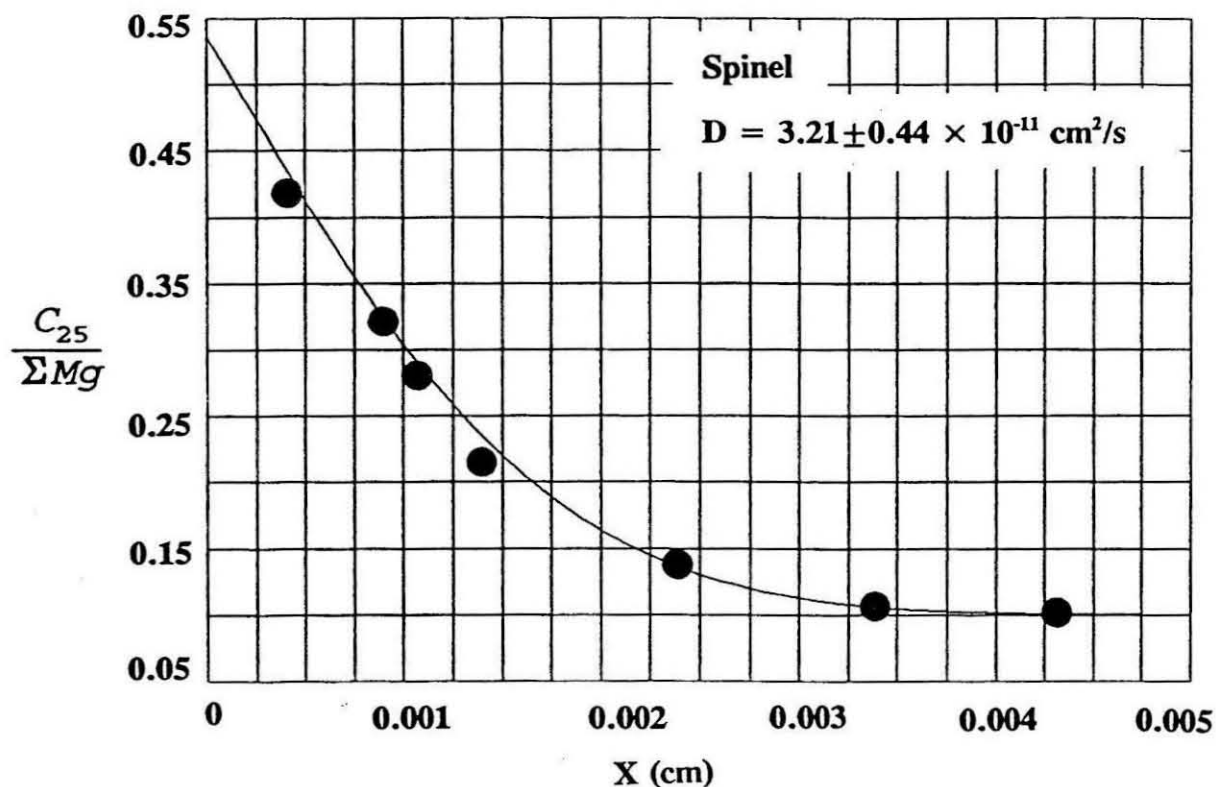
T (°C)	t (hr)	α	$D_R(\text{cm}^2/\text{s}) \pm 2\sigma$	$D_L(\text{cm}^2/\text{s})$
1553	0.5	0.0293	$8.60 \pm 0.15 \times 10^{-10}$	1.00×10^{-6}
1497	2		$3.29 \pm 0.47 \times 10^{-10}$	
1495	2	0.0227	$3.21 \pm 0.27 \times 10^{-10}$	6.19×10^{-7}
1415	2.5	0.0192	$8.94 \pm 1.11 \times 10^{-11}$	2.43×10^{-7}
1354	8.17		$3.21 \pm 0.44 \times 10^{-11}$	
1302	14.33		$1.38 \pm 0.14 \times 10^{-11}$	
1261	20	0.0215	$6.80 \pm 0.71 \times 10^{-12}$	1.47×10^{-8}

D_R is the diffusion coefficient of Mg in spinel, α is the square root of D_R over D_L , where D_L is the diffusion coefficient of Mg in coexisting melt.



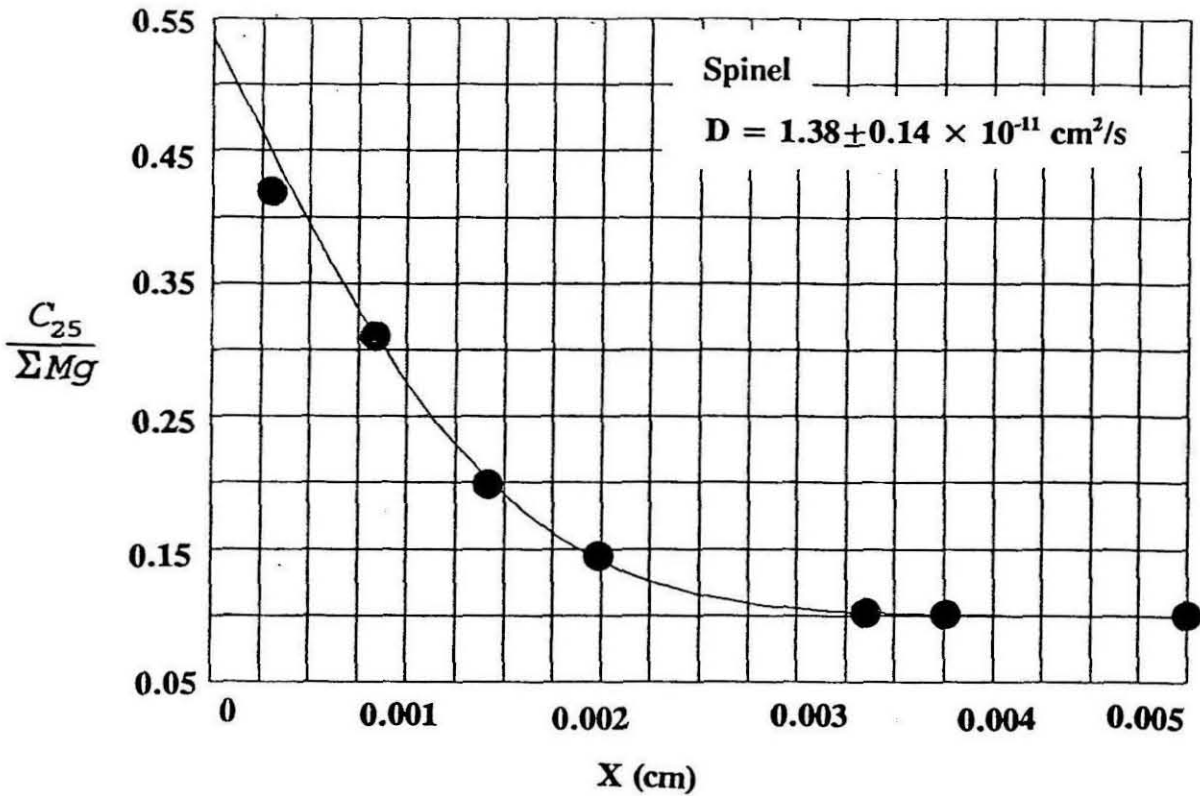
$T=1497^\circ\text{C}$ Run Duration = 2 hr.		
x (cm)	$^{25}\text{Mg}/^{24}\text{Mg}$	$C_{25}/\Sigma\text{Mg}$
0.00072	0.79155 ± 0.00159	0.40990 ± 0.00049
0.00126	0.62765 ± 0.00140	0.35517 ± 0.00051
0.00181	0.47274 ± 0.00117	0.29307 ± 0.00051
0.00290	0.27473 ± 0.00076	0.19425 ± 0.00043
0.00345	0.21426 ± 0.00070	0.15826 ± 0.00044
0.00394	0.18011 ± 0.00057	0.13648 ± 0.00037
0.00495	0.13881 ± 0.00042	0.10858 ± 0.00029
0.00598	0.12841 ± 0.00026	0.10127 ± 0.00018
0.00685	0.12677 ± 0.00033	0.10011 ± 0.00023

Fig.6.18 Measured ^{25}Mg concentration (C_{25}) in spinel for the experimental run at 1497°C .



T=1354 °C Run Duration = 8.167 hr.		
x (cm)	$^{25}\text{Mg}/^{24}\text{Mg}$	$C_{25}/\Sigma\text{Mg}$
0.00040	0.81829 ± 0.00284	0.41796 ± 0.00085
0.00089	0.54738 ± 0.00403	0.32448 ± 0.00162
0.00138	0.31066 ± 0.00085	0.21422 ± 0.00046
0.00110	0.35692 ± 0.00344	0.27851 ± 0.00175
0.00242	0.18306 ± 0.00120	0.13841 ± 0.00078
0.00341	0.13510 ± 0.00043	0.10599 ± 0.00030
0.00440	0.12729 ± 0.00034	0.10048 ± 0.00024

Fig.6.19 Measured ^{25}Mg concentration (C_{25}) in spinel for the experimental run at 1354°C.



T=1302 °C		Run Duration = 14.33 hr.	
x (cm)	$^{25}\text{Mg}/^{24}\text{Mg}$	$C_{25}/\Sigma\text{Mg}$	
0.00030	0.82770 ± 0.00315	0.42074 ± 0.00093	
0.00085	0.50635 ± 0.00346	0.30764 ± 0.00146	
0.00140	0.27976 ± 0.00109	0.19711 ± 0.00062	
0.00195	0.19860 ± 0.00065	0.14841 ± 0.00041	
0.00335	0.12871 ± 0.00041	0.10149 ± 0.00029	
0.00375	0.12768 ± 0.00051	0.10076 ± 0.00036	
0.00500	0.12681 ± 0.00040	0.10013 ± 0.00028	

Fig.6.20 Measured ^{25}Mg concentration (C_{25}) in spinel for the experimental run at 1302°C.

6.6. ACTIVATION ENERGY OF Mg IN SPINEL AND MELT

The temperature dependence of the diffusion coefficient for Mg self diffusion in spinel is obtained from the Arrhenius relation $D = D_0 \exp(-E/RT)$ (21). As can be seen (Fig.6.21), the data exhibit a good linear relationship on a $\log D$ versus $1/T$ plot. It follows that a single diffusion mechanism appears to govern the transport in spinel crystals. The activation energy (E) and pre-exponential factor D_0 derived by a linear regression of the experimental diffusion data are, respectively, 384 ± 7 KJ and 74.6 ± 1.1 cm^2/s . Our result is somewhat different from that reported by Lindner and Åkerström (1958). The temperature dependent diffusion coefficients calculated from equation 21 indicate an order of magnitude difference between the data from this study and that of Lindner and Åkerström at the temperatures pertinent to melting of POIs. Since their experiments were conducted on polycrystalline spinel aggregate, the faster rate from their data possibly reflect some combination of grain boundary and volume diffusion.

The activation energy for Mg in the melts is deduced from the four experiments in which diffusion data for the melts is available. The activation energy derived from this analysis is 343 ± 25 kJ and the pre-exponential factor is 7790.5 ± 1.3 cm^2/s . Although the melts are of different bulk compositions (Table 6.1), the linear relation of the diffusion coefficients derived from an Arrhenius plot (Fig.6.22) suggests that the diffusion coefficient is not a strong function of composition, thus a constant D_m can be assumed for all POI compositions of interest.

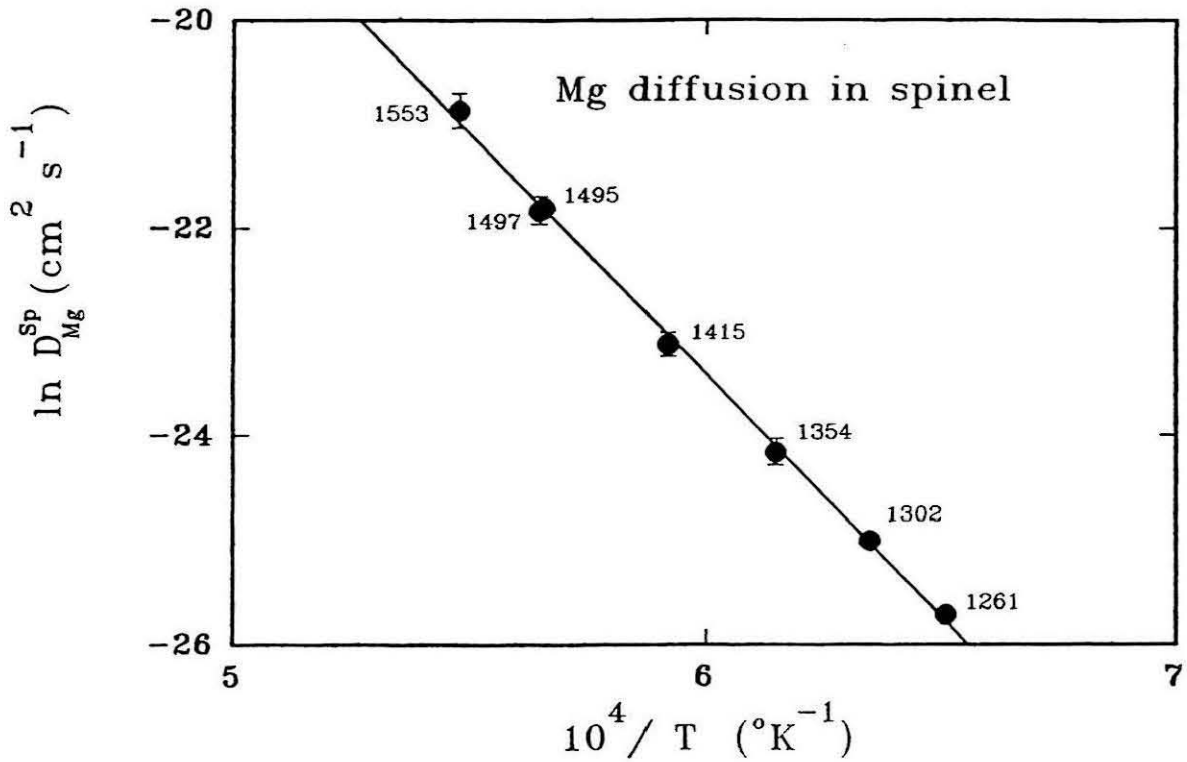


Fig.6.21 Temperature dependence of the diffusion coefficient for Mg self diffusion in spinel can be obtained from the Arrhenius relation $D = D_0 \exp(-E/RT)$. The activation energy $E = 384 \pm 7$ kJ and pre-exponential factor $D_0 = 74.6 \pm 1.1$ cm^2/s is derived by a linear regression of the diffusion coefficient obtained from experimental data at different temperatures.

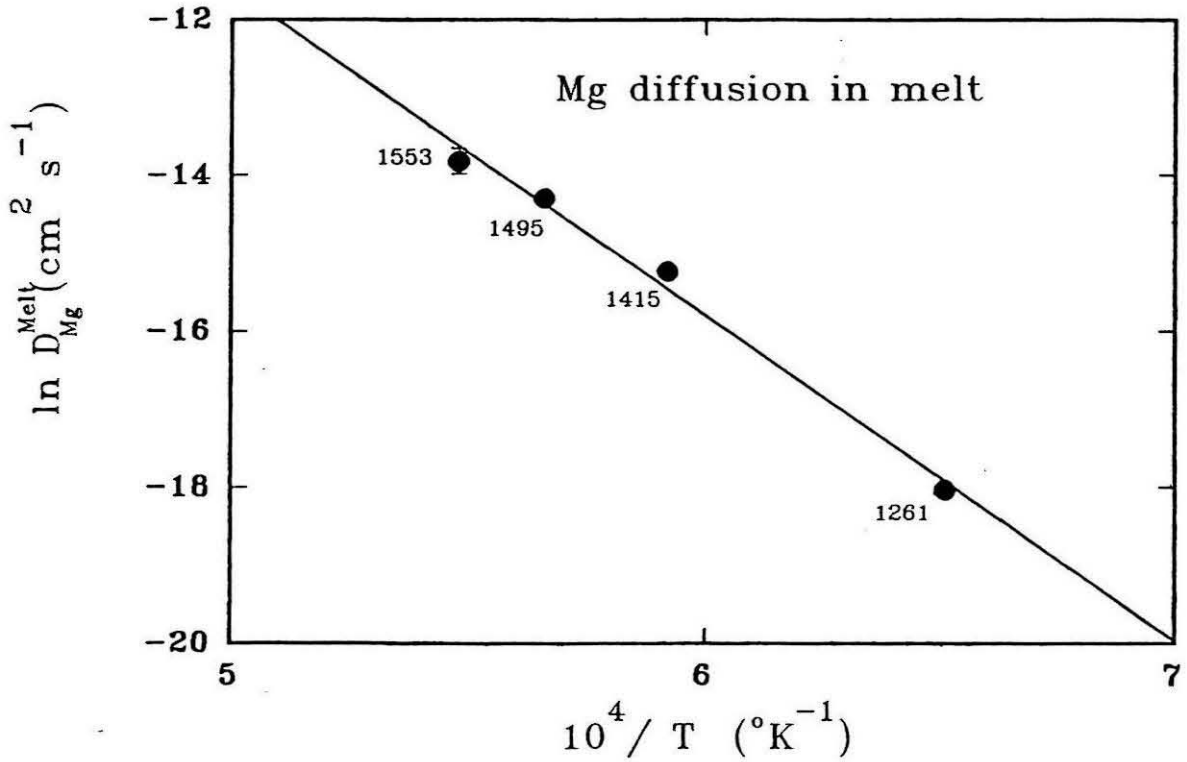


Fig.6.22 The diffusion coefficients in the melt, calculated with the constraints imposed by the solutions from Mg diffusion in coexisting spinel, is used to determine the activation energy of Mg in the silicate melt. From the available data in four experiments, the activation energy and pre-exponential factor is 343 ± 25 kJ and 7791.9 ± 1.3 cm^2 respectively.

6.7. EFFECTS OF THE BOUNDARY CONDITION

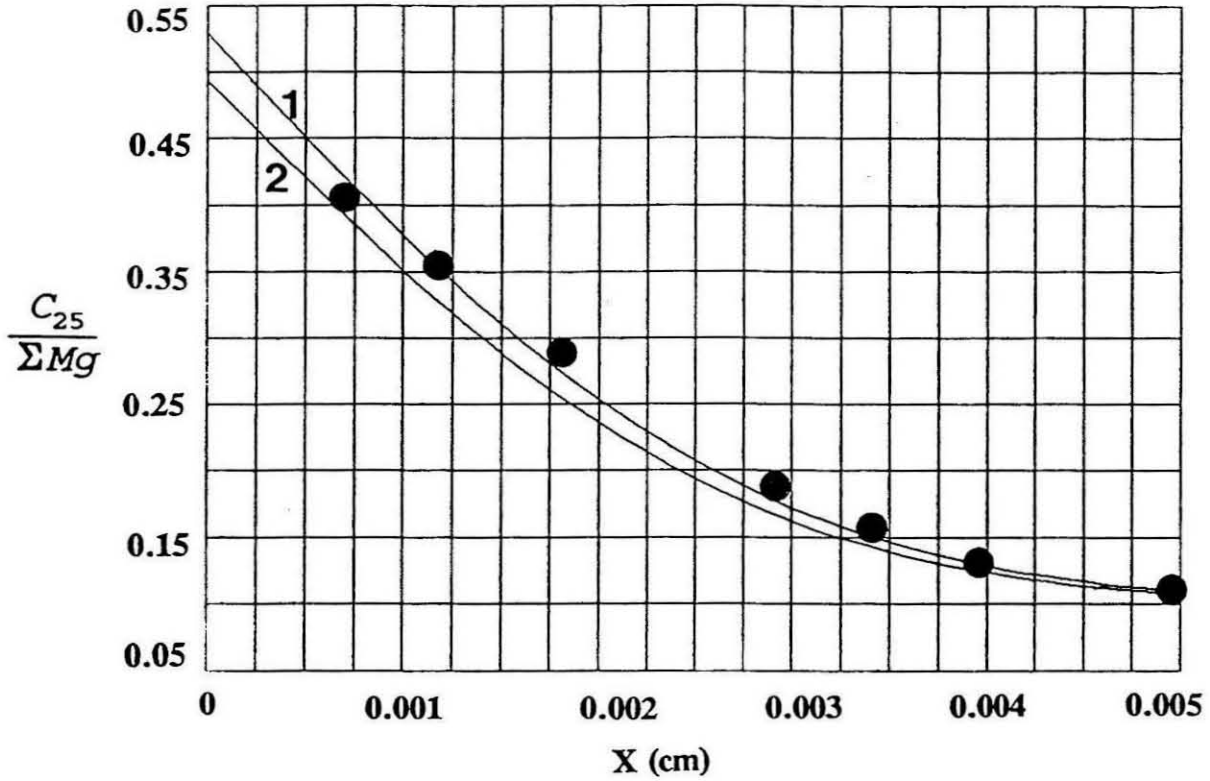
A necessary parameter for the derivation of diffusion coefficients from equation 17 is the concentration of the isotope species at the boundary. The accuracy of this boundary value will affect the diffusion coefficients derived from a least square best fit. Since the treatment of the diffusion equation also allows the determination of diffusion coefficients of a species for one phase from the diffusion coefficient of that species in coexisting phase, the effect of uncertainties in the boundary value to the diffusion coefficient of the species in each phase needs to be evaluated.

In the experiments at 1553, 1495, 1415, and 1261°C, the diffusion profiles in both phases were measured. The boundary values were extrapolated from measured data on both sides of the boundary to the boundary, thus these values were fairly well defined. This is supported by the fact that the fit of the measured data to the theoretical profiles in both phases is quite good (Fig.6.9-6.17). In the three other experiments (1497, 1354, and 1302°C), the diffusion profiles in the melt were not measured because the amount of melt was not sufficient to treat it as an infinite source for the diffusion species. A major concern is whether the diffusion coefficients for these three experiments, extracted from the measured data in spinel, can be justified. The experiment at 1495°C in which an infinite source for both phases was achieved was conducted to see whether there is a significant difference in the diffusion coefficient to that for the experiment at 1497°C. As can be seen in Figures 6.9 and 6.18, the diffusion coefficients derived from these two experiments are quite consistent ($3.21 \pm 0.27 \times 10^{-10}$ and $3.29 \pm 0.47 \times 10^{-10}$ cm²/s,

respectively). The analysis shows that slight variations in the boundary value have only small effects on the diffusion coefficient of spinel. However, when this same variation of the boundary value is used to calculate the diffusion coefficient in the melt using equation 10, the difference is significant. As shown in Figures 6.23-6.25, while the differences in the diffusion coefficients of spinel varies slightly ($\sim 10\%$ for $\sim 20\%$ variation in the boundary value), there is approximately an order of magnitude difference in the calculated diffusion coefficients for coexisting melts.

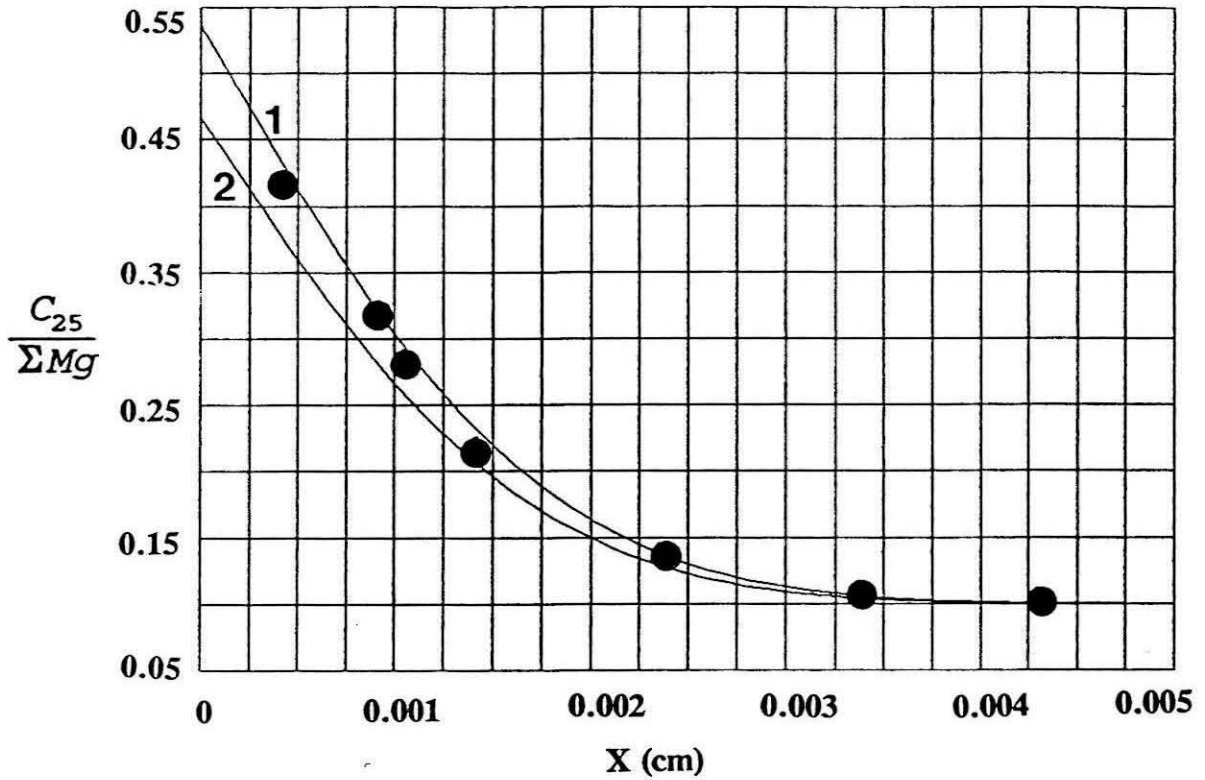
The variation of diffusion coefficients in the melt, due to the different boundary values used, is shown in the Arrhenius plot (Fig.6.26). From each boundary value, one can determine an α value. The line in the graph is the best fit line for the diffusion coefficients from the four experiments in which both spinel and melt data were measured. The two different symbols for each temperature represent the calculated two diffusion coefficients of each melt, using the two different α values (see Figs.6.23-6.25), for each of the three experiments where melt data were not measured (i.e., runs at 1497, 1354, and 1302°C). The difference in the values for each temperature also illustrates the uncertainties of the diffusion coefficients in the melt if the boundary values were determined solely from the measured data in spinel. It can readily be seen that these uncertainties are very significant. However, when these different boundary values were used to derive the diffusion coefficients for spinel, they still fit fairly well in an Arrhenius plot (Fig.6.27). The different effects of the boundary value on the diffusion coefficients in spinel and coexisting melt can be attributed to the fact that there is a steep gradient in the diffusion profile of spinel, in sharp contrast to that in the melt (see

Fig.6.8). As a consequence, slight variations of the boundary value would not significantly change the fit to the measured data in spinel but would result in a much enhanced effect upon the diffusion coefficient calculated for coexisting melt. For example, the diffusion coefficient in spinel at 1354°C calculated from a best fit of the measured data, using a boundary value $^{25}\text{Mg}/\Sigma\text{Mg} \sim 0.535$, is $3.21 \times 10^{-11} \text{ cm}^2/\text{s}$, while using $^{25}\text{Mg}/\Sigma\text{Mg} \sim 0.470$ the diffusion coefficient is 3.04×10^{-11} . However, this variation on the boundary value when translated into the diffusion coefficient of corresponding glass gives a much greater uncertainty. From the boundary values given above, the calculated diffusion coefficients for glass are, respectively, 7.78×10^{-8} and $4.55 \times 10^{-9} \text{ cm}^2/\text{s}$. Generally speaking, from the boundary value determined through measured profile in the melt, the diffusion coefficient in spinel can be calculated fairly accurately through equation 10. However, the reverse is not true. Because of these uncertainties resulting from the functional difference shown in equation 17, I did not attempt to extract the diffusion coefficients for coexisting melt using the data for the three experiments where the isotope concentrations in the melt were not directly measured.



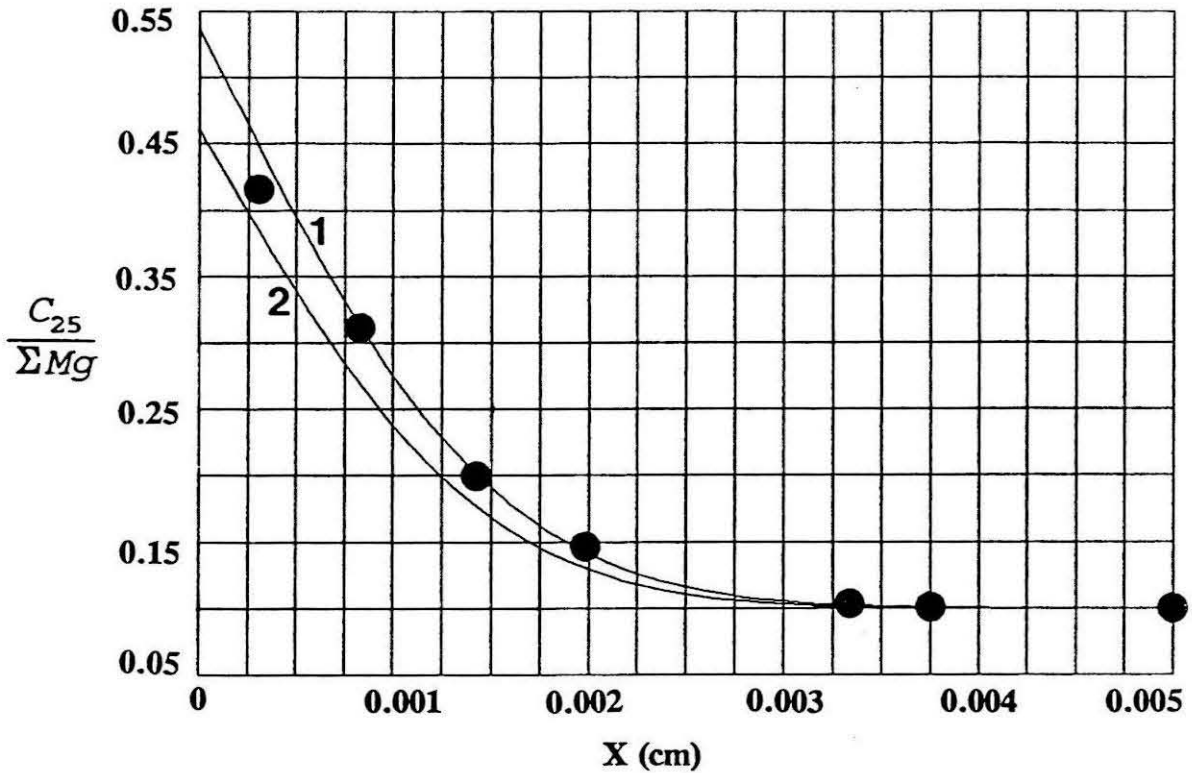
T=1497 °C Run Duration = 2 hr.			
	D_{Sp}	α	D_m
1	3.29×10^{-10}	0.0248	5.35×10^{-7}
2	3.12×10^{-10}	0.0541	1.07×10^{-7}

Fig.6.23 Demonstration of the effect of boundary value on the diffusion coefficient calculated from a best fit of the measured data in spinel using equation 17. The diffusion coefficient for spinel (D_{sp}) at 1497°C, from curve 1 and 2, vary slightly, but the diffusion coefficient in coexisting melt (D_m) calculated through α differ by a factor of five.



T=1354 °C Run Duration = 8.167 hr.			
	D_{Sp}	α	D_m
1	3.21×10^{-11}	0.0203	7.78×10^{-8}
2	3.04×10^{-11}	0.0817	4.55×10^{-9}

Fig.6.24 Small variation is observed for D_{sp} at 1354°C with change on the boundary value. D_m of coexisting melt, however, varies by more than an order of magnitude.



T=1302 °C Run Duration = 14.33 hr.			
	D_{sp}	α	D_m
1	1.38×10^{-11}	0.0193	3.73×10^{-8}
2	1.22×10^{-11}	0.0910	1.47×10^{-9}

Fig.6.25 In the data for the experiment at 1302°, it is again observed that D_{sp} is not significantly affected by variation on the boundary value, in sharp contrast to the difference in D_m of coexisting melt.

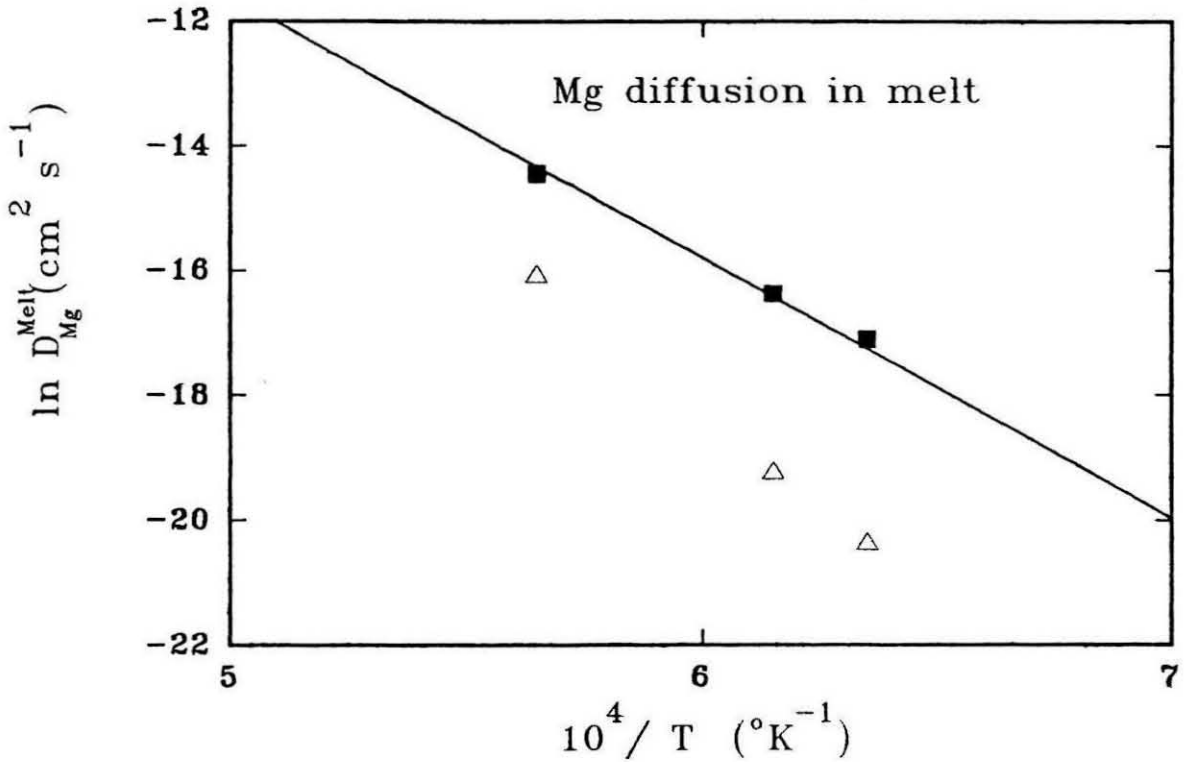


Fig.6.26 Diffusion coefficients of melts calculated from the two different α values (i.e. different boundary values) given in Figures 6.22-6.24 plotted in the Arrhenius diagram. The line is the best fit line in Figure 20. The diffusion coefficients calculated from different α values show very large uncertainties.

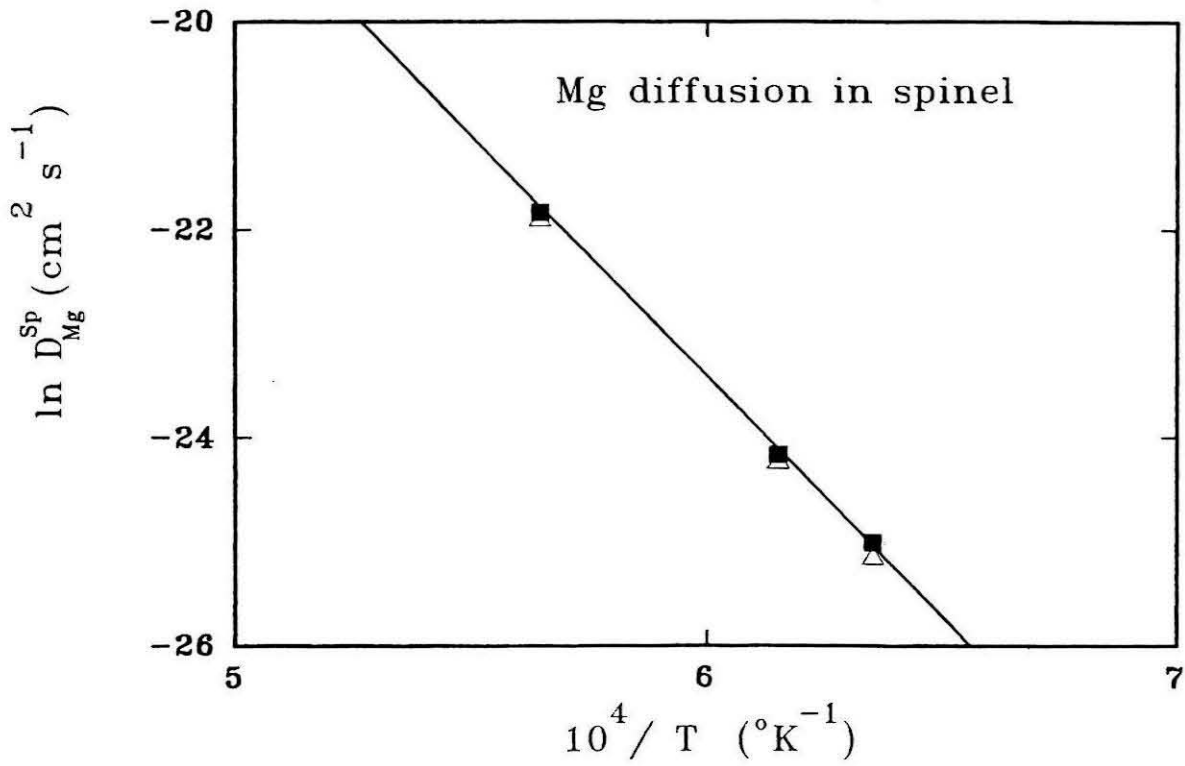


Fig.6.27 Diffusion coefficients of spinel calculated using the two different boundary values in Figures 6.22-6.24 showed negligible variation in the Arrhenius diagram. The best fit line is derived in Figure 19.

6.8. EXTRACTING DIFFUSION COEFFICIENT FROM COEXISTING PHASE

The diffusion experiment that I used is an isotope exchange technique for phases in chemical equilibrium. This allows precise and simultaneous determination of diffusion coefficients in both phases. Since the diffusion coefficients in the coexisting phases are related by common parameters, it is possible to determine the diffusion coefficient of a species in the second phase from the measured data in the first phase and the initial and boundary values. One advantage of this technique is that the determination of a diffusion coefficient, which is limited by the slow diffusion rate of that species in the host phase, can be determined from the diffusion coefficient of the same species in a coexisting phase (e.g., melt) in which the diffusion rate may be several orders of magnitude faster. As a test, we used the diffusion coefficient of Mg extracted from a best fit to the measured data in the melt for the experiment at 1495°C and calculated the diffusion coefficient of Mg in spinel through the parameter α . The diffusion coefficients of Mg in spinel derived from a best fit of the measured data in spinel and from that derived from the data in the coexisting melt are $3.21 \pm 0.27 \times 10^{-10}$ and $3.01 \pm 0.40 \times 10^{-10}$ cm²/s, respectively. This result shows these two approaches to be in reasonable agreement given the uncertainties in the analysis. Therefore, using this experimental technique and the treatment of the diffusion equation, indirect measurement of the diffusion species can be in a coexisting phase. This type of experiment may have broader application and can be applied to other elements (including Si and O) and other mineral systems. It is believed that diffusion coefficients of 10^{-14} cm²/s can be readily measured by the procedures described here.

CHAPTER SEVEN

ORIGIN OF PLAGIOCLASE-OLIVINE INCLUSIONS

In the preceding chapters, petrographical, chemical, and isotopic data of POIs and associated mineral phases have been presented in detail. Experimental studies on compositions resembling that of POIs were conducted to provide a framework to describe phase relations and crystallization paths for melts that cover a wide composition range, including POIs and CACs. Mg isotopic heterogeneity, which was found to be common in POIs, provided the motivation to initiate Mg self diffusion experiments in spinel and coexisting melts. Results from this study provided data to place constraints on the thermal history of these inclusions.

The igneous texture and spheroidal shape of POIs are consistent with crystallization from liquid droplets. Phase relations in most POIs are consistent with crystallization from melts of their bulk compositions. However, there are several features that preclude formation by equilibrium crystallization or fractional crystallization from an initially homogeneous liquid. A major challenge is the reconciliation of the broad textural, chemical, mineralogical, and phase equilibria evidence suggestive of an overall igneous origin as compared with the more subtle but common isotopic evidence, and occasional phase assemblage evidence, suggesting the presence of relict phases and incomplete melting.

7.1. INTERPRETATION OF TEXTURAL AND CHEMICAL FEATURES

The petrographical observations strongly suggest that POIs experienced an igneous history. The subophitic texture common to many POIs is similar to that found in rocks known to have crystallized from rapidly cooled melts. The porphyritic, barred, and radiating textures also found in several POIs are commonly observed in chondrules and these textures have been re-produced in experimental studies (Lofgren, 1980; Lofgren and Russell, 1986; Tsuchiyama *et al.*, 1980).

Experimentally determined phase equilibria in systems appropriate to POI bulk compositions also support the interpretation that POIs crystallized from a melt. Both the mineral assemblages and the inferred sequence of crystallization in most of the natural POIs are consistent with laboratory experiments on chemically similar synthetic systems.

The bulk chemistry of CAIs is usually attributed to early (high temperature) condensation from a solar gas. In comparison with CAIs, the POIs (which are also rich in refractory elements) exhibit higher contents of the more volatile elements such as Na, Fe, and Cr (see Table 3.14). The fact that these elements are mainly contained in the unaltered primary phases (plagioclase, olivine, pyroxene, and spinel), indicates that they either were present or were incorporated in the POI precursor during melting, and were not "added later" by some gas exchange mechanism. The Na in the plagioclase of POIs is what one would expect for bulk compositions with 1-5 wt. % Na₂O, consistent with the observed Na contents in POIs. The concentrations of trace elements are qualitatively in agreement with experimental data of crystal/melt partitioning (Yurimoto and Sueno,

1984; Colson *et al.*, 1988). Thus, to the extent that the bulk composition of the POI system can be approximated by the synthetic systems, the experimental data on the elemental distribution between crystals and melt are in good agreement with our data on natural and synthetic POIs and suggest that substantial Na, Fe, and Cr were present in the POI parent melts during crystallization of the major silicates.

The majority of the chemical and mineralogical properties of 16 of the 20 POIs examined are compatible with an igneous origin. However, in four group 2 POIs the presence of spinel contradicts the experimentally determined phase equilibria. Spinel should not crystallize at equilibrium from melts of the respective bulk compositions of ADEL-1, BG82CH1, SA-1 and BG82CLJa. In ADEL-1, BG82CH1 and BG82CLJa, spinel is rare and strongly resorbed, and only occurs included within plagioclase. In SA-1 spinel occurs as rare inclusions in plagioclase, olivine and pyroxene. The extent of disequilibrium in ADEL-1 is emphasized by the presence of both spinel and tridymite in close proximity. Phase equilibria data (Longhi, 1987; Longhi and Pan, 1988) clearly show that these two phases are incompatible, and textures suggest that spinel is a relict phase. The strongly resorbed character of the spinels, with serrated and embayed boundaries, can readily be explained by reaction with a spinel-undersaturated liquid. The preservation of relict spinels in such a liquid at high temperature is possible only as a result of isolation of the spinels from the liquid by inclusion in early crystallizing plagioclase crystals. Relict spinel that remained in contact with the liquid would rapidly dissolve, explaining the low abundance of spinel in these POIs. The preservation of relict spinel is also the most plausible explanation for the Cr-rich mantles on Cr-poor

spinel in inclusion 5ALLB6. Although spinel can be the earliest phase to crystallize in this inclusion, the large difference in Cr_2O_3 contents between core and mantle suggests that the coexisting spinels could not have crystallized from a single homogeneous melt. Based on the partitioning of Cr among spinel, olivine, and melt (see Chapter 5), it is apparent that the Cr-poor spinel core could not have crystallized together with the olivines from a liquid, whereas the Cr-rich spinel rims could. The petrographic and chemical evidence indicate that the Cr-rich rims were late overgrowth on the Mg spinel core.

7.2. IMPLICATIONS OF IGNEOUS TEXTURE VERSUS Mg ISOTOPE HETEROGENEITY

Ion microprobe analysis shows that at least seven POIs are isotopically heterogeneous in Mg. Four of these seven are group 1 inclusions, two are group 2 inclusions, one of which was reported by Kennedy et al. (1991), and another is a group 3 POI. The presence of spinels with distinct Mg isotopic compositions suggests that some spinels are relict and carry the isotopic signature of a different source region. Relict phases can be identified by differences in isotopic composition (F_{Mg}) or by their occurrence in inclusions whose bulk composition does not allow crystallization of the phase. The compositions of the group 1 POIs are spinel-saturated and thus relict spinels cannot be identified petrographically. However, difference in F_{Mg} between coexisting spinel and silicates and among spinels of up to 11 ‰/amu, strongly suggest that some

spinel is a relict. Four group 2 POIs have spinel-undersaturated compositions and phase equilibria considerations require spinel to be a relict phase. Spinel is rare and small ($\leq 2\mu\text{m}$) in this group of inclusions, making isotopic measurements very difficult. In two spinel-undersaturated POIs, the observed differences in F_{Mg} between spinel and silicate support the identification of spinel as a relict phase.

As shown in Fig.4.2, the isotopic fractionation of spinels in POIs can favor enrichment in either the lighter Mg isotopes or in the heavier Mg isotopes, but never both in the same inclusion. Fractionation effects in silicates, found in only 3 POIs, have similar magnitude but always exhibit positive F_{Mg} values. This Mg isotopic signature clearly distinguishes POIs from both refractory inclusions and chondrules. With the exception of crystals in the Wark-Lovering rims of some CAIs, most coarse-grained CAIs and chondrules are isotopically homogeneous in their $^{25}\text{Mg}/^{24}\text{Mg}$ ratios (MacPherson *et al.*, 1988). Types A, B and C CAIs generally exhibit little evidence of Mg isotopic fractionation and when isotopic fractionation is present, F_{Mg} is always positive. However, the occurrence of Mg isotope heterogeneity between spinel and silicates in a coarse-grained CAI was recently reported by Goswami *et al.* (1991) and Srinivasan *et al.* (1991). These observations indicate that many refractory objects (including some CAIs) were the result of multiple stages of processing of originally isotopically heterogeneous aggregates. Large, positive isotopic fractionation is found in FUN inclusions but most FUN CAIs are also isotopically homogeneous (Wasserburg *et al.*, 1977; Esat *et al.*, 1978; Clayton *et al.*, 1984). An important exception are the purple, spinel-rich Allende inclusions, some of which exhibit both large isotopic

fractionation and variations in F_{Mg} among coexisting phases (Brigham *et al.*, 1988; Brigham, 1990). Isotope fractionation in these inclusions is always positive and the isotopic heterogeneity is believed to reflect partial isotopic exchange during alteration. Many fine-grained inclusions, in contrast, are fractionated favoring the lighter Mg isotopes and are usually isotopically heterogeneous within individual inclusions (Brigham 1990). The POIs are thus distinguished from these types of inclusions as the first group of objects to exhibit both positive and negative Mg isotopic fractionation, and the first group of igneous-textured inclusions to exhibit heterogeneity in F_{Mg} with such frequency.

A major challenge posed by the data is to understand the preservation of large Mg isotope heterogeneities in a class of objects whose textures would otherwise suggest crystallization from a homogeneous melt. Two possible models can be constructed within the constraints imposed by our data. One model assumes that each inclusion is an aggregate of grains from different sources that were not homogenized by subsequent thermal processes. Spinel containing isotopically fractionated Mg was one such precursor phase and was not completely melted, reacted, or isotopically exchanged during POI formation, thus retaining some part of its original isotopic signature. A requirement of this model is incomplete melting/reaction of the precursor material during POI formation and insufficient time for isotopic homogenization. In this model, the following conditions can be considered:

- a) Spinel and melt achieved chemical equilibrium during melting.

If spinel and melt can reach chemical equilibrium during melting (i.e., the bulk composition of the POI melt was spinel saturated at the temperature of melting), some

precursor spinels could be preserved. If spinel and melt were also in isotopic equilibrium, no isotopic variations would be observed among the resulting phases. In the case where spinel and melt were in isotopic disequilibrium, the preservation of "relict" isotopic signature in the spinel would depend on the duration of the melting event and the cooling rate. With decreasing temperature, more spinels would crystallize from the melt. These "newly" crystallized spinels would have acquired the isotopic composition of the melt.

b) Spinel and melt were out of chemical equilibrium during melting.

If the bulk composition of the POI melt does not allow spinel formation, spinels that were present in the precursor aggregate would dissolve. To preserve these spinels, the duration of melting must be either short enough and the cooling rate fast enough that the spinels had not enough time to react completely away. Alternatively, the spinels were isolated from the melt by inclusion in a saturation phase (e.g., plagioclase or olivine). If these spinels were also in isotopic disequilibrium with coexisting melt or with its enclosing phase, preservation of these "relict" identities depends on the diffusion rates of the isotope species.

The alternative model proposed assumes that the inclusions formed from a single homogeneous source containing isotopically fractionated Mg. Partial isotopic reequilibration with an isotopically normal gas took place via sub-solidus gas-solid exchange which gave rise to the observed heterogeneity. This type of model has been used to explain the oxygen isotopic heterogeneities in CAIs. This model requires large differences in Mg diffusion rates between spinel and silicates.

7.3. MODEL FOR POI FORMATION

Based on the available data and the diffusion rate of Mg in spinel determined in this study, I believe there are several lines of evidence that strongly favor formation of POIs by aggregation of isotopically dissimilar materials followed by partial melting. In this section the essential characteristics of POIs are critically examined and a model for the formation of POIs is presented.

The data show large Mg isotopic heterogeneity between major Mg-rich silicates and oxides in POIs; spinel and host silicates show variations in F_{Mg} of up to 11 ‰/amu on a spatial scale of tens of microns. If POIs originally formed as homogeneous melts containing isotopically fractionated Mg, which at some late stage reacted with a gas phase with normal Mg, the observed variations in F_{Mg} require that Mg diffuse much faster in olivine and pyroxene than in spinel. Since the silicates in POIs are typically 10 to 50 times larger in size than the spinels, the Mg self-diffusion coefficients in olivine and pyroxene must be ~ 100 times larger than that in spinel to preserve the fractionated Mg in spinels and replace the Mg in silicate phases to produce the observed isotopic heterogeneity. However, data from this study indicate that Mg self-diffusion in spinel is very rapid ($D=7.638 \times 10^{-11}$ cm²/s at 1400°C), whereas the value for forsterite is 9.323×10^{-12} cm²/s at 1400°C (Freer, 1981), contrary to the requirements of this model. If the Mg isotopic heterogeneity were due to partial isotopic reequilibration during late stage alteration, in which some phases (e.g., silicates) were more susceptible to chemical and isotopic exchange with a gas phase, one would expect to observe some correlation

between the magnitude of isotopic exchange and the severity of alteration. However, no such correlation is observed in the POIs. In contrast to CAIs, most POIs, in fact, show remarkably little evidence of mineralogical alteration. Alteration of plagioclase to nepheline and sodalite or spinel to feldspathoid plus olivine, two common occurrences of secondary metamorphism in CAIs, is rare in POIs. No correlation between spinel chemistry and F_{Mg} was observed. The more Fe-rich spinels do not, in general, have lower F_{Mg} , as might be expected if diffusive exchange with a nebular gas at lower temperature were pervasive with the gas having normal Mg and a high Fe content. Thus, it is unlikely that POIs originated as homogeneous melts and obtained their isotopic heterogeneity as the result of diffusive gas-solid exchange.

The formation of POIs from an assemblage of chemically and isotopically heterogeneous materials requires that the inclusions were never completely melted/reacted, allowing the most refractory phase (e.g., spinel) to preserve its original isotopic signature. Both our petrographic observations of natural POIs and the results of our experimental phase equilibria studies of melts with compositions similar to the more Ca-Al-rich POIs are consistent with this essential requirement. Five of the seven isotopically heterogeneous POIs have spinel as the liquidus phase. Relict spinels included in a melt of this composition could, therefore, survive if the partial melt of the POI precursor were spinel-saturated, if the maximum temperature to which the POI was heated was below the spinel liquidus, or if the heating event were sufficiently brief to inhibit spinel dissolution and isotopic reequilibration between spinel and the melt. In a spinel-oversaturated melt, corresponding to group 1 POIs, it is possible that spinel crystallized

from the melt could coexist with isotopically anomalous, relict spinel in the same POI. Partial dissolution of some relict spinel also may occur during partial melting. Spinel crystallized from the melt would have a Mg isotopic composition reflecting that of the melt, whereas partially reacted, relict spinel would undergo some isotopic exchange with the melt and acquire an isotopic composition intermediate between those of the primary, relict spinel and the melt. The large range in F_{Mg} , observed in several POIs, is considered a reflection of the presence of several generations of spinels. The remaining POI containing isotopically heterogeneous spinel, ADEL-1, belongs to petrographic group 2 and spinel does not appear in the crystallization sequence. The highly resorbed appearance of the rare spinel found in this inclusion, provides independent evidence that spinel is a relict phase.

Phase equilibria prohibits the presence of relict pyroxenes in group 1 POIs since they would be the first phase to melt for these bulk compositions. The variation of F_{Mg} among pyroxenes in two group 1 POIs most plausibly can be attributed to the partial dissolution of relict spinel (with $F_{Mg} > 0$) and incorporation of some isotopically fractionated Mg in late crystallizing pyroxene. This scenario leads to the prediction that measured values of F_{Mg} in pyroxene must lie between the maximum F_{Mg} of relict spinel and the average F_{Mg} of the silicate precursor. In this case pyroxene with high F_{Mg} is possibly related to a local parcel of melt that contained dissolved spinels with fractionated Mg.

The one inclusion containing plagioclase with isotopically fractionated Mg, PPX, is a group 2 POI and contains almost no spinel. The large difference in F_{Mg} between

plagioclase and olivine requires that either plagioclase is a relict phase, that olivine acquired its normal Mg isotopic composition by sub-solidus exchange with the nebular gas, or that relict spinel dissolved in plagioclase. Phase equilibria considerations permit the presence of relict plagioclase but petrographic observations of plagioclase laths intergrown with olivine phenocrysts suggest that both phases crystallized from the melt. Although the rate of Mg diffusion in plagioclase is unknown, the lack of alteration in POIs does not favor sub-solidus exchange with a nebular gas. It is more likely that dissolved relict spinels provided local enrichments of fractionated Mg isotopes. The amount of spinel in plagioclase must be limited by the MgO content of plagioclase.

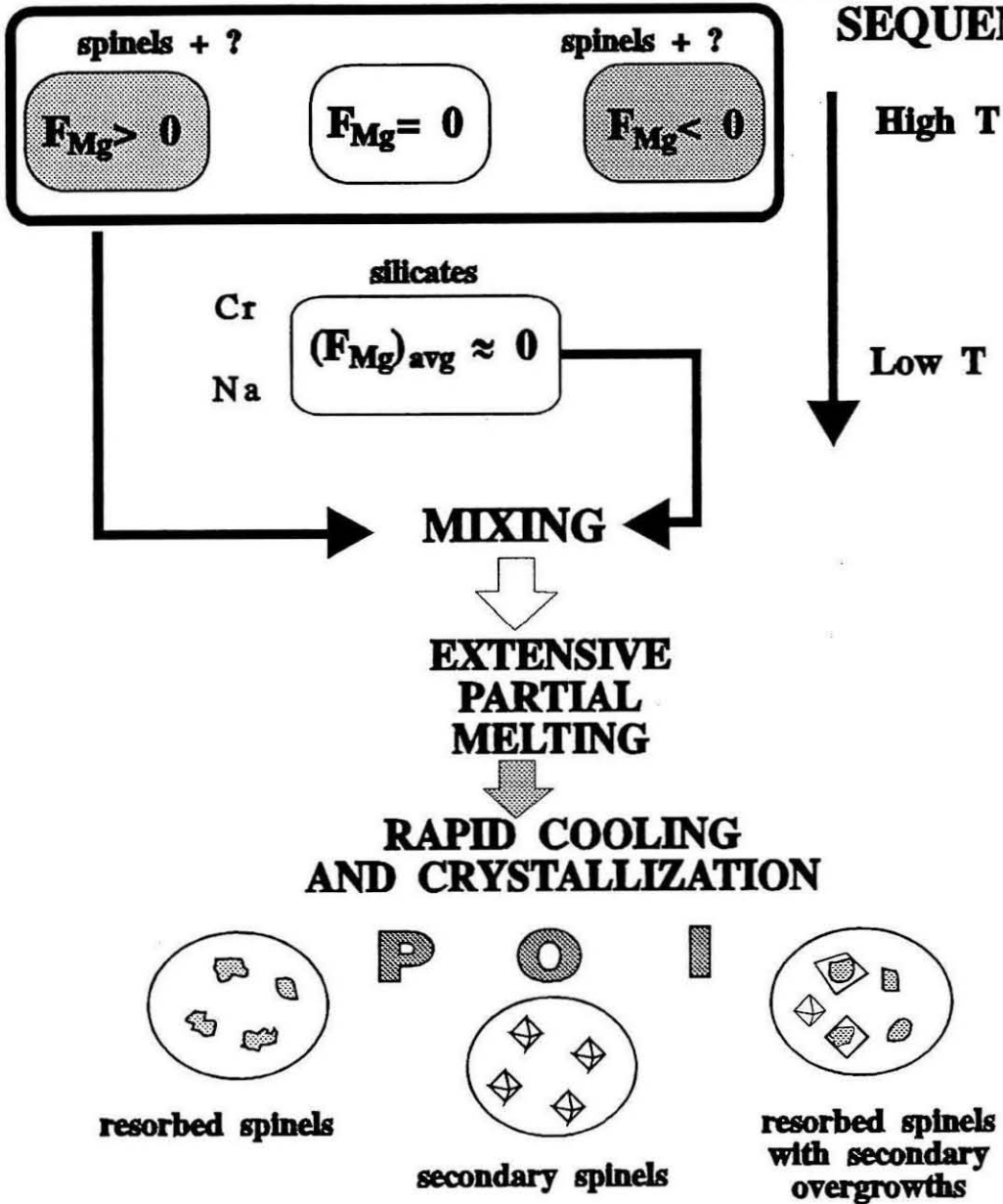
The preferred scenario for the origin of POIs consists of the following events (illustrated in Fig.7.1). (1) Formation of spinel containing isotopically fractionated Mg; spinel may contain isotopically fractionated Mg with $F_{Mg} > 0$ or $F_{Mg} < 0$, or may contain normal Mg. Some silicates may also have been present. (2) Formation of a separate silicate precursor material representing a wide range of bulk compositions but containing significant Na and Cr, and little refractory siderophiles. Some of these silicates must be produced by gas/solid fractionation during condensation/evaporation to produce Group II REE abundances (Sheng et al., 1991a). The silicate precursor material may have contained components with isotopically fractionated Mg but the average composition of most silicates was near $F_{Mg} = 0$. The observation of plagioclase containing isotopically fractionated Mg in one POI attests to the presence of silicate precursors with $F_{Mg} > 0$ or the local dissolution of fractionated relict spinel. (3) Mixing of spinel and separate silicate precursor components. (4) A heating episode that melted the silicates but only

partially reacted or melted spinel. The Fe-rich olivine clusters embedded at the rims of many POIs are believed to be material accreted from another source during the final solidification of the POIs. (5) Relatively rapid cooling and little subsequent alteration to preserve isotopic heterogeneity. In some cases mesostasis or glass is preserved as a quench product of the melting event.

The similarities in major element composition and in the extent of Mg isotopic heterogeneity between the POIs and fine-grained Ca-, Al-rich inclusions suggest that the POI precursor material may be related to fine-grained inclusions. The observation of a Group II REE pattern in one POI, BG82CLII, (Sheng *et al.*, 1991a) also provides support for this argument. However, this POI contains spinel with large positive F_{Mg} , whereas most fine-grained inclusions are enriched in the lighter Mg isotopes. In fact, all but two of the fractionated POIs are enriched in the heavier Mg isotopes. This behavior shows that even though POIs and fine-grained CAIs share many common chemical characteristics, there still exist essential differences prohibiting a simple and

Fig.7.1 Proposed model for formation of POIs. The POIs are considered to be formed from materials that originated from different Mg isotopic reservoirs. These materials with different Mg isotope fractionation (F_{Mg}) were mixed and subsequently melted/partially melted and rapidly cooled. Some relict spinels preserved their original Mg isotope signature.

CONDENSATION SEQUENCE



direct relationship.

7.4. ^{26}Al AS A RELATIVE CHRONOMETER

The existence of excesses of ^{26}Mg ($^{26}\text{Mg}^*$) and of a correlation between $^{26}\text{Mg}^*$ and Al in some meteoritic samples has been confirmed by many investigations. The magnitude of the enrichments in $^{26}\text{Mg}^*$ is strongly correlated with the Al/Mg ratio (Lee *et al.*, 1976; Lee *et al.*, 1977; Hutcheon, 1982), while most samples have $^{25}\text{Mg}/^{24}\text{Mg}$ ratios within a few permil of the terrestrial value. This evidence strongly suggests that these enrichments were due to the addition of $^{26}\text{Mg}^*$ to normal Mg by the *in situ* decay of now extinct ^{26}Al . The short half life of ^{26}Al ($\tau_{1/2} \sim 7.2 \times 10^5 \text{y}$) implies that ^{26}Al must have been produced within a few million years of the formation of these meteoritic samples. If ^{26}Al was present in the solar system at the time refractory inclusions formed, it must have been incorporated into their constituent phases together with normal ^{27}Al . Subsequent decay of ^{26}Al to $^{26}\text{Mg}^*$ produced enhanced $^{26}\text{Mg}/^{24}\text{Mg}$ ratios, the magnitude of which was proportional to the Al/Mg ratio in a particular mineral phase.

If we assume the presence of ^{26}Al in the early solar system, its use as a chronometer relies on knowledge of the initial $^{26}\text{Al}/^{27}\text{Al}$ ratio ($(^{26}\text{Al}/^{27}\text{Al})_0$), corresponding to the first formation of solid bodies. While the value of $(^{26}\text{Al}/^{27}\text{Al})_0 \approx 5 \times 10^{-5}$ is typical for many CAIs, there are numerous other meteoritic samples that show lower ratios, including some that have $(^{26}\text{Al}/^{27}\text{Al})_0 \approx 0$ but with initial values $(^{26}\text{Mg}/^{24}\text{Mg})_0$ above terrestrial value (see Wasserburg and Papanastassiou, 1982; Hutcheon, 1982;

Papanastassiou *et al.*, 1977). This raises a key issue of whether ^{26}Al was widespread and uniform throughout the solar system or was heterogeneously distributed. If ^{26}Al were heterogeneously distributed, then it cannot serve as a precise chronometer but only provides an indication of very early formation for those samples that show evidence of $^{26}\text{Mg}^*$. The different $(^{26}\text{Al}/^{27}\text{Al})_0$ in various samples reflect the initial value of the parcel of material from which they formed.

If we assume that ^{26}Al was initially uniformly distributed in the solar system and consider a scenario in which repetitive thermal events occurred in the early history of the solar system and heated or melted the dust particles, then it is possible that the ^{26}Al clock was repeatedly reset prior to its total decay. The different $(^{26}\text{Al}/^{27}\text{Al})_0$ values in different inclusions would indicate reprocessing of the sample after some time had elapsed. Melting of inclusions after the initial addition of ^{26}Al to the solar system, but while ^{26}Al was still alive, would result in lower $(^{26}\text{Al}/^{27}\text{Al})_0$ with enriched $^{26}\text{Mg}/^{24}\text{Mg}$. If significant material with normal Mg was incorporated prior or during melting, the enrichment of $^{26}\text{Mg}/^{24}\text{Mg}$ in these inclusions could be concealed beyond the detection limits of the analysis. If melting of inclusions with high Al/Mg occurred after ^{26}Al has totally decayed, one would observe in these inclusions a $(^{26}\text{Al}/^{27}\text{Al})_0$ value near zero, but with enriched $^{26}\text{Mg}/^{24}\text{Mg}$. Therefore, in the scenario described above, it is not necessary to assume heterogeneity in the distribution of ^{26}Al in the early solar system to account for the various $(^{26}\text{Al}/^{27}\text{Al})_0$ values observed in different inclusions. These differences can be explained as the superimposed result of subsequent thermal event(s) (which occurred within a few million years of the injection of ^{26}Al in the solar system) that reprocessed

earlier formed material. If it is assumed that ^{26}Al was initially distributed homogeneously in the solar system, then the rare occurrence and significantly lower abundance of $^{26}\text{Mg}^*$ in POIs relative to CAIs would imply that POIs formed at least 2.9 million years later than CAIs.

7.5. COMPARISON OF ISOTOPIC HETEROGENEITY IN POIs AND CAIs

The Mg isotopic heterogeneity on a microscopic scale in POIs is analogous to observations of oxygen isotope heterogeneity in refractory inclusions (Clayton *et al.*, 1977), where spinel and pyroxene and melilite exhibit strikingly different oxygen isotopic compositions. However, the oxygen in spinels is enriched in ^{16}O and the differences in $\delta^{18}\text{O}$ between spinel and silicates do not reflect mass-dependent fractionation as found for Mg in POIs. Oxygen in Type B CAIs follows the relationship

$$\delta(^{18}\text{O}/^{16}\text{O})_{\text{spinel}} - \delta(^{18}\text{O}/^{16}\text{O})_{\text{melilite}} \approx -30\text{‰}.$$

This equation describes the largest and most widespread isotopic effect in terms of heterogeneity within a single, morphologically well-defined group of inclusions. In most CAIs, the Mg isotopic composition was found to be the same (and indistinguishable from terrestrial) in spinel, pyroxene, and melilite from the same CAI where the oxygen was highly anomalous for the spinel and pyroxene but much closer to "normal" for the melilite. Most CAIs are generally assumed to have formed from an ^{16}O -rich reservoir and to have acquired their oxygen isotopic heterogeneity through gas-solid diffusive exchange with a gas containing essentially normal oxygen. In this model the isotopic

heterogeneity arises from presumed large differences in the rates of oxygen diffusion in spinel, pyroxene, and melilite. The minerals melilite and to some extent pyroxene were assumed to be susceptible to reaction with an ^{16}O -depleted nebular gas, producing a large shift in the oxygen isotope composition of the melilite, but only small shifts in the other phases. It is noted that the extent of the shifts in oxygen isotopes is directly related to the degree of alteration of the mineral phase. Although this model is widely accepted, recent experimental measurements of oxygen diffusion rates in spinel, diopside and melilite (Yurimoto *et al.*, 1989; McKeegan and Ryerson, 1990) require a reexamination of the critical assumptions. Divergent laboratory data for oxygen self-diffusion in different phases have led to contradicting views as to the ability of the gas-solid exchange model to explain the oxygen isotopic heterogeneity. Oxygen diffusion rates reported by Yurimoto *et al.* (1989) are two to four orders of magnitude lower than rates previously reported (Hayashi and Muehlenbachs, 1986), leading them to question the diffusion controlled model for oxygen isotopic differences between melilite and spinel/pyroxene in CAIs. McKeegan and Ryerson (1990), based on their new data, also questioned the production of the oxygen isotopic anomalies in CAIs by diffusive exchange. Clearly, the justification of this model depends on accurate diffusion data.

Oxygen isotope compositions were not analyzed for POIs. Oxygen diffusion data (see Freer, 1980; 1981) suggest that if there was oxygen isotopic exchange between POI and nebular gas, we should observe a significant difference in the oxygen isotopic composition between spinel and plagioclase and olivine. The absence of pervasive alteration in POIs suggests that post formational reaction between POI and nebula gas

was not substantial, thus shifts in oxygen isotopes probably would not be observed even if there were differences in the oxygen isotopic compositions of POIs and the ambient gas. Alternatively, it might have been that the temperature of the nebular gas was too low for diffusive exchange to be in effect subsequent to POI formation. It is also likely that the oxygen isotope exchange between solids and gas occurred before the formation of POIs, thus evidence of oxygen heterogeneity that might have existed in POI precursor was erased upon melting. This needs to be evaluated by oxygen isotope analysis of POIs.

The proposed POI formation model underscores a major difference in the way in which POIs and CAIs obtained their respective Mg and oxygen isotopic heterogeneity. The Mg isotopic heterogeneity of POIs reflects the inherited Mg isotopic variability of relict spinel, whereas the oxygen isotopic heterogeneity in CAIs is most plausibly produced during post-crystallization exchange between silicates and the nebular gas.

7.6. EXPERIMENTAL CONSTRAINTS ON THE THERMAL HISTORY OF POIs

7.6.1. T_{\max} for POIs

The existence of isotopic anomalies places a number of constraints on the thermal history of POIs. Since bulk POIs have $F_{\text{Mg}} \sim 0$, any spinel that crystallized from the bulk melt also would have $F_{\text{Mg}} \sim 0$. The common existence of relict spinel with $F_{\text{Mg}} \neq 0$

included in a host that crystallized from a melt, means that the maximum temperature (T_{\max}) to which POIs were subjected was high enough to cause extensive melting, but below the appearance temperature of spinel at least for some inclusions. In addition, the heating event was insufficiently long to homogenize the Mg isotopes. Thus, some precursor spinels in these inclusions survived the melting event.

The results of the phase equilibria study also provide criteria to identify relict phases in individual POI assemblage. For melt compositions in which spinel is not allowed to crystallize at any temperature under equilibrium conditions, the presence of resorbed spinel in that assemblage requires the spinel to be a relict phase. This is the case for many of the spinel-bearing group 2 POIs. If these spinels initially possessed an isotopically different signature, the characteristic would be preserved, as in ADEL-1, provided that they were not given sufficient time to reequilibrate.

In group 1 POIs, the phase equilibria criteria cannot be used for identification of spinel as a relict phase since melts corresponding to the bulk compositions of these inclusions are spinel saturated. However, Mg isotopic analyses indicate that in most of these inclusions, the spinels are not in isotopic equilibrium with their coexisting silicates. If the maximum melting temperature (T_{\max}) was within the spinel stability field but the time at T_{\max} was so short that relict spinels could not approach equilibrium with the melt, the cores of these spinels would reflect the compositions of the original spinel, while the rims would assume the Mg isotope signature of the melt. Thus, ignoring diffusion effects, the spinel core and rim would have different isotopic identities. Due to the small size of most spinels in POIs, it was not possible to discriminate the core from the rim

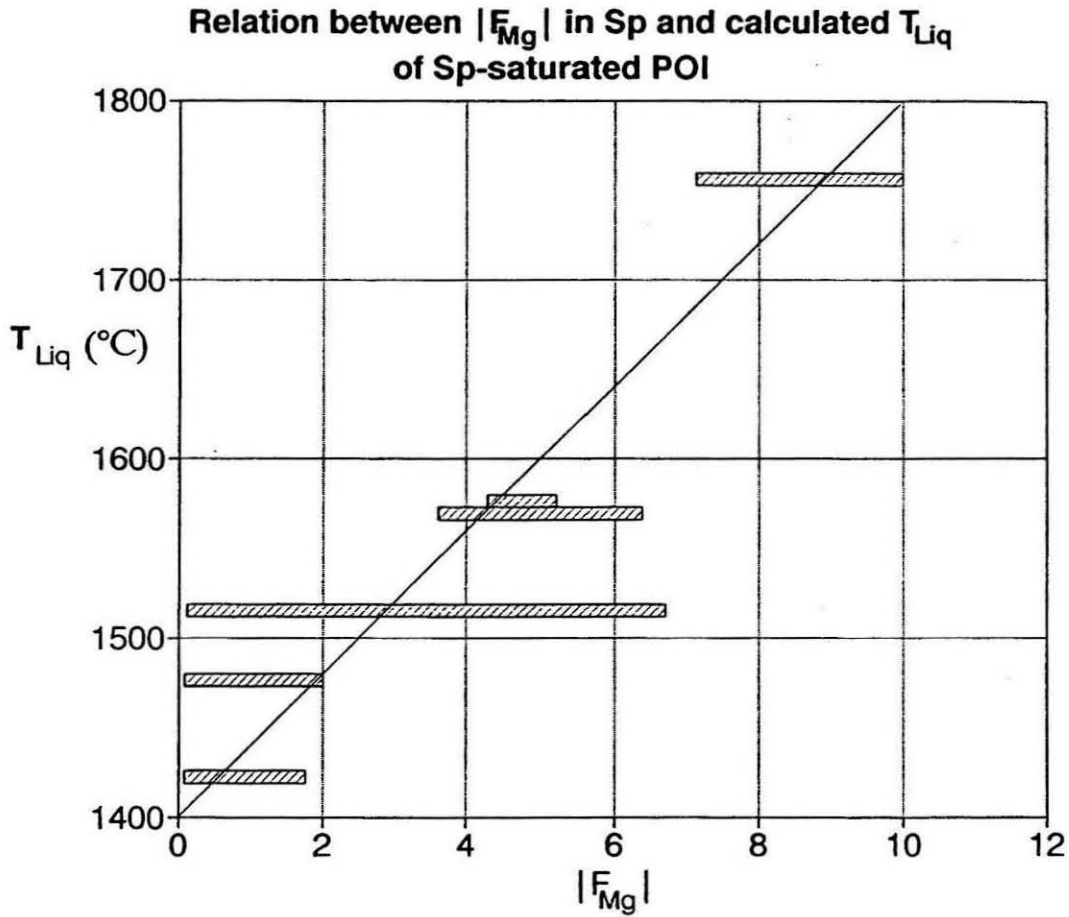


Fig.7.2 Correlation between the range of Mg isotope fractionation ($|F_{Mg}|$) observed in spinels of individual POI and the calculated liquidus temperature (T_{Liq}) for a melt of the bulk composition of corresponding POI.

in the ion microprobe analysis. The analysis reflects the average value of the sputtered volume of the spinel. If all relict spinels in each POI initially had similar F_{Mg} , then, depending on the relative volume of relict and overgrowth spinel analyzed, one would expect a variation in the F_{Mg} of spinels within a POI; the more relict spinel preserved, the more likely one was to observe values reflecting mostly the relict core.

The liquidus temperature of POIs calculated using a model by Berman (1983) places a limit on the T_{max} for those inclusions that preserved relict spinel. Based on phase equilibria analysis, the appearance temperature of silicates in group 1 POI melts ($\leq 1400^{\circ}C$) is much lower than that for spinel ($> 1430^{\circ}C$). The rare occurrence of isotopically fractionated Mg in silicates is likely an indication that the temperature of the melting event was near or above the temperature of first appearance of the silicates. As shown in Fig.7.2, the calculated liquidus temperatures for the group 1 POIs varies from about 1430 to 1750 $^{\circ}C$. The appearance temperature of silicates in these POIs is about 1325-1400 $^{\circ}C$. Since the modal abundance of the spinels in these POIs ranges from 5-25%, any temperature above 1400 $^{\circ}C$ would result in mostly ($>75\%$) melted POIs. For some inclusions, a temperature of 1350 $^{\circ}C$ would be sufficient to make them mostly melted. Calculations show that T_{max} could be as high as 1700 $^{\circ}C$ for one inclusion (containing 25 wt% spinel) and yet still preserve 5 wt% relict spinel. Such a high melting temperature is unlikely because it would require that the remaining 20 wt% of the spinels in this inclusion crystallized from a homogeneous melt, contrary to the Mg isotope data, which indicate that a much larger fraction of the spinels were relict (Fig.7.2). An acceptable T_{max} would also have to take into account the amount of time

that can be maintained at that temperature, and the cooling rate required to preserve Mg isotope heterogeneity in the inclusion. The cooling rates should also be compatible with the textures observed in the inclusions. These constraints will be discussed in a later section.

The plot of $|F_{Mg}|$ in spinel versus the liquidus temperature (T_{Liq}) for the composition of group 1 POIs (Fig.7.2) shows a relation between the amount of spinel (reflected by T_{Liq}) and the range of Mg fractionation. The higher F_{Mg} values observed in the POIs with higher T_{Liq} are likely associated with preservation of more relict spinels. The range of F_{Mg} from 0 to 6 ‰ for the inclusion with a T_{Liq} of 1520°C suggests that a significant portion of the spinels in that inclusion grew from a homogenized melt. Fig.7.2 also shows that the POIs whose T_{Liq} are above 1500°C exhibit isotopically fractionated Mg, while those below that temperature show normal Mg. If these POIs experienced similar thermal events, it is inferred that the T_{max} is approximately 1500°C. Higher melting temperatures would have erased the Mg isotope heterogeneity in most of the POIs. For compositions in which a silicate phase is the first liquidus phase, it is also possible that some silicates were relict. However, neither the phase equilibria data nor the chemical and isotopic compositions provide sufficient evidence to prove the preservation of relict silicates.

7.6.2. Cooling Rates of POIs

The diffusion data from my experiments provided accurate data on the activation

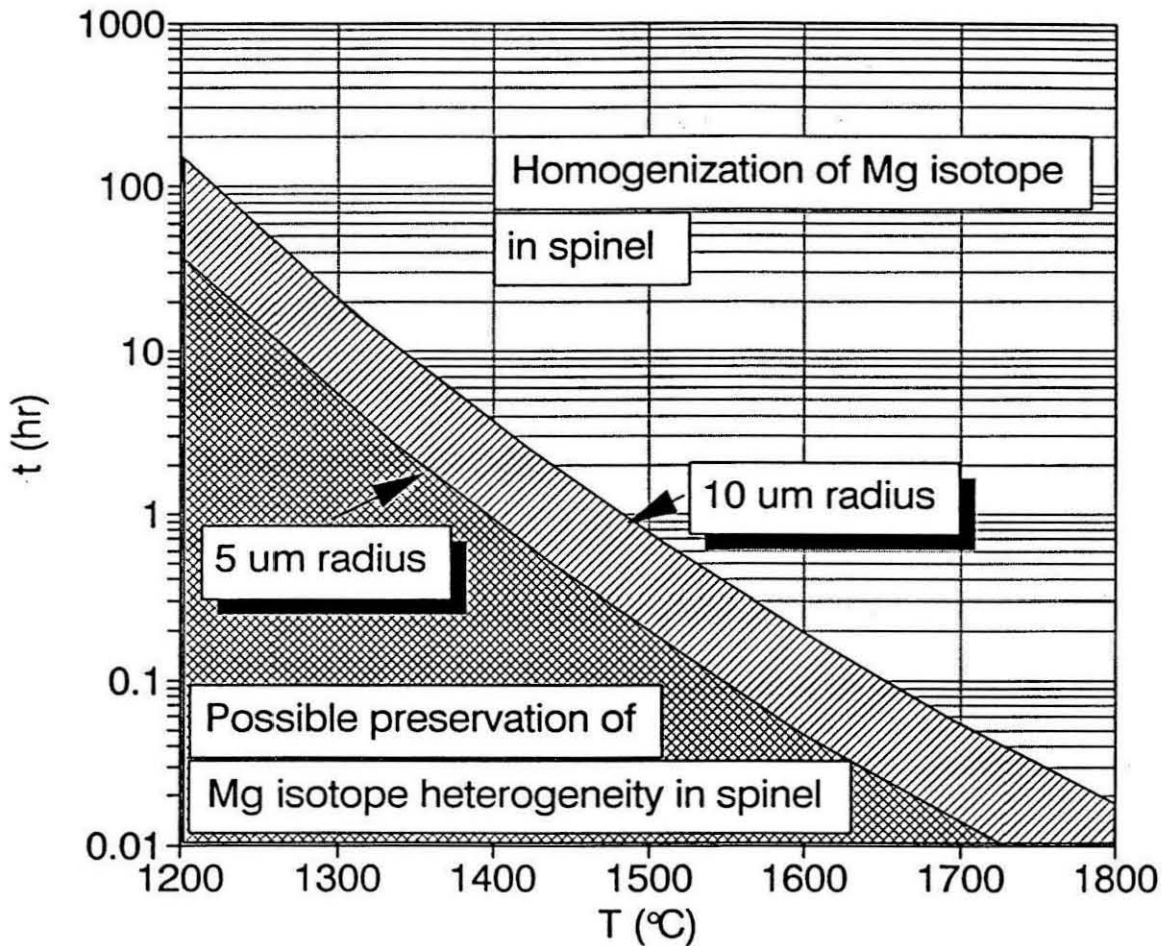


Fig.7.3 For spinel grain with a radius of 5 and 10 μm , the diffusion data from our experiments constrain time that the spinel can be maintained at a certain temperature and still allow preservation of Mg isotope heterogeneity in spinel. This does not account for the time elapsed during heating or cooling of the inclusion and thus represents an upper limit on the duration of the heating event at T_{max} . In order to preserve Mg isotopic heterogeneity at a heating temperature of 1500°C , the maximum amount of time allowed is less than one hour.

energy for diffusion of Mg in spinel and allows us to evaluate the nature of the thermal event(s). The temperature dependent diffusion coefficient of Mg in spinel is used to evaluate the duration, thermal limits, and the nature of the heating process that partially melted the POIs. I also discuss the possible initial cooling rates of these partially melted droplets following a heating event.

If we take spinel of a certain grain size x and plot the estimated homogenization time ($x^2 \approx D_R t$) versus temperature (Fig.7.3), the maximum time that a spinel and melt can be maintained at any specified temperature and still preserve Mg isotope heterogeneity in POIs can be approximated. For example, assuming a spinel with radius of $10 \mu\text{m}$ (the maximum grain size of spinel in POIs), the homogenization time at 1500°C is less than one hour. At an elevated temperature of 1700°C , Mg isotopic homogenization would occur within a few minutes (Fig.7.3). Even if the maximum temperature were only 1350°C , the isotopic heterogeneities in POI spinels would not be expected to survive more than a few hours. Clearly, a short thermal event is implied.

A more realistic scenario for the thermal history reflected in POIs can be obtained by considering the case of instantaneous heating to a maximum temperature followed by cooling. We can define the time integral of the diffusion coefficient

$$\tau(t) \equiv \int_0^t D(\eta) d\eta \quad .$$

If we integrate the above equation over a sufficiently long time so that diffusion effectively ceases, the total time integral $\tau(\infty)$ of the diffusion coefficient from an initial

temperature T_0 to freeze out ($D \rightarrow 0$) is

$$\tau(\infty) \approx D_0 \int_0^{\infty} e^{-E/RT(t)} dt \quad ,$$

where the temperature T is some function of time t . As shown by Kaiser and Wasserburg (1983),

$$\begin{aligned} \tau(\infty) &\approx D_0 \int_0^{\infty} e^{-E/RT(t)} dt \\ &\approx \frac{RT_0 D_0 e^{-E/RT_0}}{\rho E} \\ &\approx \frac{RT_0^2 D(T_0)}{r_0 E} \quad , \end{aligned}$$

where the initial cooling rate r_0 is related to the fractional cooling rate ρ (Goldstein and Ogilvie, 1965) by the relation $r_0 = \rho T_0$. Using the above equation, the characteristic diffusion distance is given by

$$x^2 \approx \tau(\infty) = \frac{RT_0^2 D(T_0)}{r_0 E}$$

Let us regard the penetration distance x as the minimum grain size (radius) of the spinel that will preserve the isotopic heterogeneity. By plotting r_0 versus T_0 , for a given grain size, the initial cooling rate can be determined if the initial or maximum melting temperature (T_0) is known.

The dependence of initial cooling rate (r_0) on T_0 for given x , calculated using this

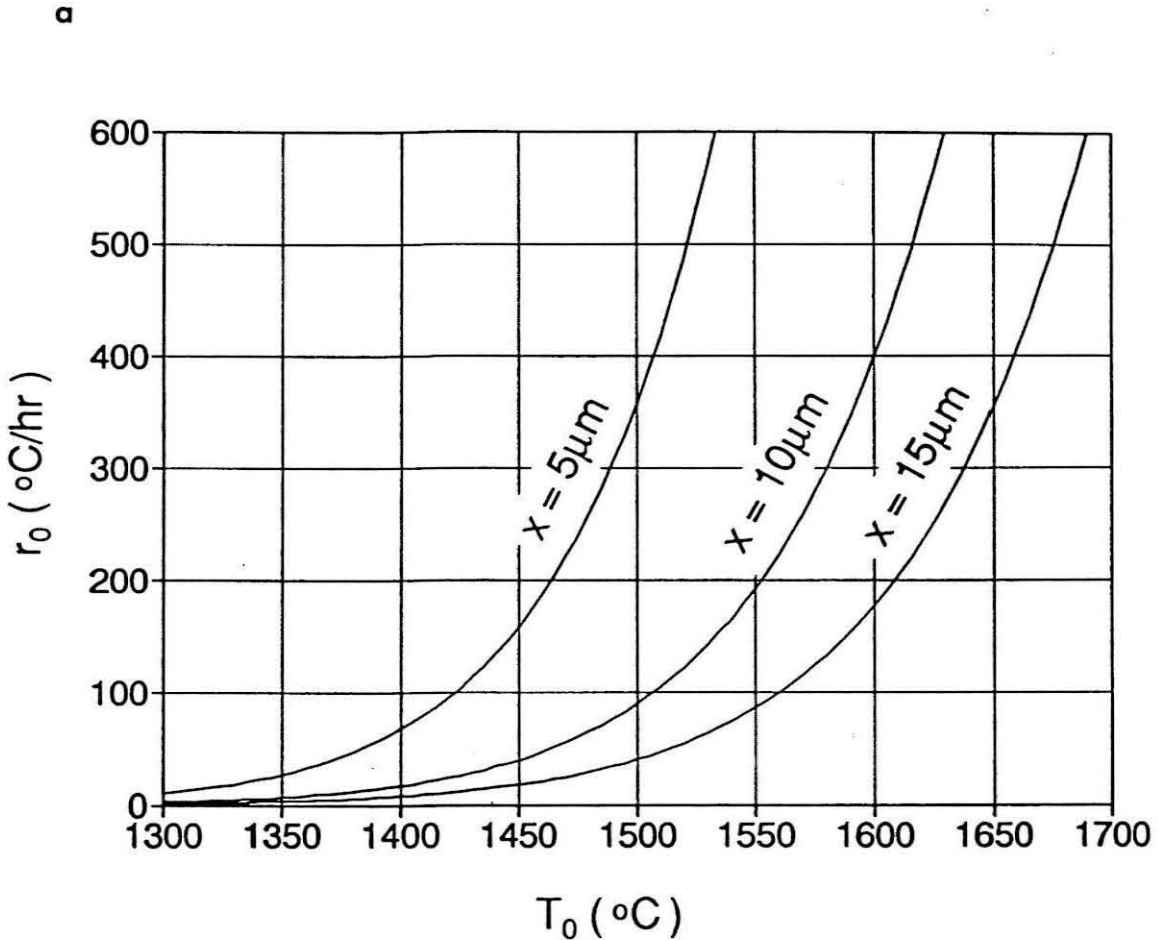
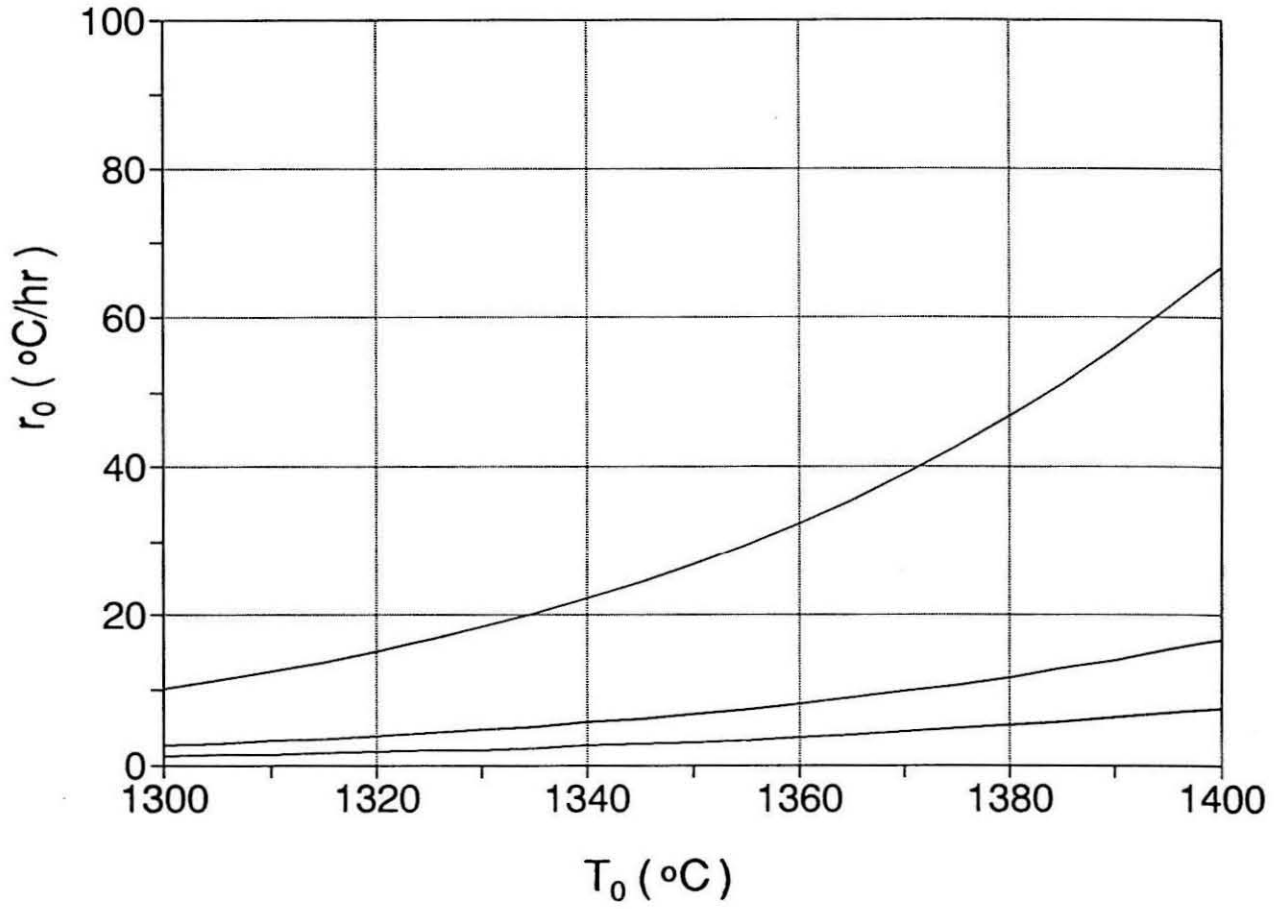


Fig.7.4 a) Calculated curves showing the dependence of initial cooling rate (r_0) upon temperature (T_0) for respective grain with radius of 5, 10, and 15 μm . At a specified temperature, Mg isotope heterogeneity can be preserved in spinel of a given grain size if the initial cooling rate is greater than that defined by the calculated curve for that grain size. Spinel in POIs are generally smaller than 5 μm , thus in order to escape Mg isotope homogenization we would expect initial cooling rates greater than 25°C/hr at suggested melting temperatures of POIs.

b) Details of the cooling curves at lower temperatures.

b



relation is shown in Fig.7.4. The initial rates at $T_0=1500^\circ\text{C}$ for x of 5, 10, and 15 μm are, respectively, 356, 89, and 40°C/hr . For a 10 μm grain size, homogenization would occur if the cooling rate is slower than 89°C/hr , or, for r_0 of 89°C/hr , grain sizes of less than 10 μm would be homogenized. Thus, for any given spinel grain size and T_0 , a lower limit on the r_0 that would allow preservation of initial isotopic compositions can be determined.

Since isotopically fractionated Mg was observed in 5 μm spinel grains, we can consider a lower limit on the initial cooling rate for given T_0 . In order to preserve Mg isotopic heterogeneity, the minimum initial cooling rates for this grain size at $T_0=1350$, 1400, and 1500° are, respectively, 25, 64, and 356°C/hr . These lower limits on the cooling rates are comparable to or up to ten times greater than those inferred from experimental and textural studies of synthetic CAI systems (Wark and Lovering, 1982; MacPherson *et al.*, 1984; Stolper and Paque, 1986). If T_0 were 1600°C or higher, the required cooling rate would be at least several thousand degrees per hour, contradicting the observed textures in these POIs. On the basis of POI textures and observed Mg isotope heterogeneities, it is considered that the possible temperature range to which the POIs were subjected and which caused them to be dominantly melted was about 1350 - 1500°C . It also appears that the igneous textures of POIs are generally compatible with the cooling rates estimated to produce CAI textures, but much faster rates, which would still preserve isotopic heterogeneity, may be inconsistent with petrographic observations. Experimental studies of textures of POI composition melts as a function of cooling rate will be required to address this issue. Faster cooling rates, however, would be

compatible with the glassy and skeletal textures of CACs (Bischoff and Keil, 1984). Thus, if isotopically heterogeneous aggregates were also their precursor, and if the temperature did not exceed their liquidus, isotopic heterogeneity may also be preserved in CACs. The lower limits on cooling rates for POIs are much lower than radiative loss cooling rates of mm-size droplets in a cold nebula (MacPherson *et al.*, 1984). This would therefore require formation of POIs in a relatively hot region or parcel of the nebula.

There are similarities and differences in the melting process inferred for POIs (this study) and CAIs (Stolper and Paque, 1986). The liquidus temperature of an average Type B CAI composition is about 1550°C (Stolper and Paque, 1986), which is within the liquidus temperature range for group 1 POIs. The melting temperatures of Type B CAIs, which they inferred from their experimental studies, is between 1400 to 1500°C, similar to the temperature range inferred for POIs, but the cooling rate they inferred for CAIs appears to be slower. For $T_0 = 1420^\circ\text{C}$ and $r \leq 20^\circ\text{C/hr}$, as suggested for some Type B CAIs from laboratory study of textures as a function of cooling rates (Stolper and Paque, 1986), our calculations show

$$x = \sqrt{\frac{D(1693\text{K}) R 1693^2}{20 E}} = 11 \mu\text{m} \quad .$$

Thus spinels less than 11 μm radius would be isotopically homogenized in Mg. If CAIs initially contained spinel or other similar relict phases of this size with fractionated Mg, they would consequently be reequilibrated at this slower cooling rate. The presence of Mg isotope heterogeneity in POIs and the results of the diffusion experiments provide

one of the most direct means of establishing a constraint on the thermal history of these inclusions. The presence or absence of Mg isotopic heterogeneity could be used as a measure of the T_0 and cooling rate not only of POIs but also of other types of refractory inclusions and chondrules if we assume that these objects had sampled similar material.

7.6.3. Possible Heat Source

The scenario of POIs formed in the solar nebula by melting of pre-existing solids is similar to that generally accepted for processing of CAIs and chondrules. There is, however, no consensus as to the heat source responsible for these thermal processing events. Possible heat sources proposed by various authors include lightning strikes, magnetic flaring, melting at shock fronts, frictional heating, transient heating events associated with the primitive sun, impact melting, and splashing in collision. The pros and cons of these various processes have been reviewed in many studies (e.g., Wasson, 1972; Wood and McSween, 1977; Dodd, 1978; Lux *et al.*, 1981; Taylor *et al.*, 1983; Stolper and Paque, 1986; Grossman, 1988) and will not be discussed here.

Although the data from this study does not provide an unambiguous choice of the heat source for the formation of POIs, a number of criteria have to be satisfied. That the POIs were extensively melted suggest melting temperatures greater than 1350°C. The fact that POIs retained large amounts of relatively volatile elements such as Na indicate that the heating events were quite short. This is further established by the presence of isotopic heterogeneity and the preservation of relict phases which require

very short heating events, of the orders of minutes or less in duration, and cooling rates of a few hundred °C/hr for melting temperatures $\geq 1500^{\circ}\text{C}$, and for temperature of 1350°C , the heating event must be less than 2 hours followed by cooling rates in excess of 25°C/hr (see Figs. 7.3, 7.4). It is assumed that these cooling rates would be compatible with the observed textures. This range of cooling rates also implies that POIs, like CAIs (MacPherson *et al.*, 1984), did not cool by freely radiating into cold space. Rather, cooling must have taken place in an environment that would prevent very rapid dissipation of heat. Some possible scenarios that can be envisioned to produce such environments are: 1) flash heating in a hot parcel or region of the nebula which was sufficiently opaque; 2) impact melting in which the melted or partially melted inclusions were immersed in a hot and sufficiently dense parcel created during the impact. Other scenarios also can be possible as long as the melting and cooling requirements are met.

7.7. CONCLUSIONS

POIs are a group of objects that possess distinct chemical, mineralogical and textural characteristics. POIs are igneous inclusions, as indicated by both their textural characteristics and by the fact that their observed phase assemblages and crystallization sequences are, in general, consistent with that predicted for melts of their respective bulk compositions. The observations also show that although POIs have been melted/partially-melted, some of them contain relict spinel that preserves an earlier isotopic identity. The spinel-bearing precursor material originated from reservoirs containing isotopically

fractionated Mg. The isotopically fractionated material was later mixed with silicates whose average isotopic composition was approximately normal and was then heated such that the silicates melted but some spinel survived, generating the igneous texture but cooling at a rapid rate so that some relict spinels were preserved, maintaining the Mg isotopic heterogeneity. The temperatures of melting of POIs is believed to be in the range of 1350-1500°C, the duration of these heating events was $\ll 1$ hr. The results from the Mg self diffusion experiments in spinel show that for melting in this temperature range, the initial cooling rate was $>25^\circ\text{C/hr}$ and possibly up to several hundred degrees per hour. This appears to be faster than the cooling rate of a few tenths to $\sim 50^\circ\text{C/hr}$ for CAIs.

The formation of POIs suggests a broader connection and wider affinity with CAIs and chondrules. The formation of POIs requires multiple processes, including condensation, dust/gas fractionation, mixing and aggregation of chemically and isotopically heterogeneous materials and partial melting. It appears that these materials reflect an ongoing and repeated sequence of mixing and partial melting, evaporation and re-condensation, affecting the metal oxides. These processes are common to most CAIs and many chondrules. Let us consider a starting material of different parcels of interstellar dust grains each having slightly different isotopic compositions. These parcels were rapidly heated by localized processes of unknown nature producing condensates that then reaggregated. This reprocessing took place in a similar fashion over an extended time scale of several million years. The CAIs are considered to be produced by relatively early melting of refractory condensates or evaporative residues produced by

the above processes. The CAIs were homogenized during melting, but exhibit characteristic isotopic anomalies from sample to sample reflecting their parent material. The POIs are considered to be produced later, based on the $^{26}\text{Mg}^*/\text{Al}$ ratios, by mixing of some earlier processed material incorporating more MgO , SiO_2 as well as less refractory material enriched in Na_2O , Cr_2O_3 and MnO . The degree of isotopic homogeneity of the final POI is mainly a reflection of their individual thermal histories. The major differences between Type B CAIs and the POIs reflect the types of material that were aggregated, the temperatures to which they were heated, and the timing of the last thermal metamorphic event. POIs were heated to a lower temperature or, more likely, cooled more rapidly than most CAIs, preserving some phases that retained their original isotopic identity. The melting occurred after most ^{26}Al had decayed. It is also possible that some CAIs are, in fact, formed (or rather, reformed) at a late time. This would explain the absence of ^{26}Al in some CAIs as distinct from a model requiring that ^{26}Al be distributed very heterogeneously in the solar nebula. It is considered that these processes (both for CAIs and POIs) affected the dust and reprocessed, remelted dust after most of the nebular gases had dissipated. It is also considered that the formation of POIs post dated the extensive (but not understood) oxygen isotopic exchange between solids and gas that were recorded in many CAIs. The melting of POIs is probably by flash heating, such as impact melting, in a hot parcel or region of the nebula, or which was sufficiently opaque to prevent rapid dissipation of heat. The absence of ^{26}Al in most POIs suggests heating occurred a couple of million years after CAI formation. Thus repetitive heating events may have frequently generated or reprocessed refractory

residues which may not have been primary residues but reflect similar heating processes over a prolonged timescale of very early solar system history.

REFERENCES

- Allen J.M., Grossman L., Davis A.M. and Hutcheon I.D. (1978) Mineralogy, texture and mode of formation of a hibonite-bearing Allende inclusion. Proc. Lunar Sci. Conf. 9, 1209-1233.
- Anders E. and Grevesse N. (1989) Abundance of the elements: Meteoritic and solar. Geochim. Cosmochim. Acta **53**, 197-214.
- Andersen C.A. and Hinthorne J.R. (1972) Ion microprobe mass analyzer. Science **175**, 853-860.
- Andersen O. (1915) The system anorthite-forsterite-silica. Am.J.Sci. **39** (Fourth Series), 407-454.
- Armstrong J.T. (1984) Quantitative analysis of silicate and oxide minerals: A reevaluation of ZAF corrections and proposal for new Bence-Albee coefficients. In Microbeam Analysis (eds. A. Romig and J.I. Goldstein), 208-212. San Francisco Press.
- Armstrong J.T., Hutcheon I.D. and Wasserburg G.J. (1984) Fremdlinge in Leoville and Allende CAI: Clues to post-formation cooling and alteration. Meteoritics **19**, 186-187.
- Beckett J.R. (1986) The origin of calcium-, aluminum-rich inclusions from carbonaceous chondrites: An experimental study. Ph.D. Thesis, U. of Chicago.
- Beckett J.R. and Grossman L. (1988) The origin of type C inclusions from carbonaceous chondrites. Earth and Planet. Sci. Lett. **89**, 1-14.
- Beckett J.R. , Spivack A.J. , Hutcheon I.D. , Wasserburg G.J. and Stolper E.M. (1990) Crystal chemical effects on the partitioning at trace elements between mineral and melt: An experimental study of melilite with applications to refractory inclusions from carbonaceous chondrites. Geochim. Cosmochim. Acta **54**, 1755-1774.
- Begemann F. (1980) Isotopic anomalies in meteorites. Rep. Prog. Phys. **43**, 1309-1356.
- Bence A.E. and Albee A.L. (1968) Empirical correction factors for the electron microanalysis of silicates and oxides. J.Geol. **76**, 383-403.
- Berman R.G. (1983) A thermodynamic model for multicomponent melts, with application to the system CaO-MgO-Al₂O₃-SiO₂. Ph.D Thesis, Univ. of British Columbia.
- Bischoff A. and Keil K. (1983) Ca-Al-rich chondrules and inclusions in ordinary chondrites. Nature **303**, 588-592.
- Bischoff A. and Keil K. (1984) Al-rich objects in ordinary chondrites: Related origin of

- carbonaceous and ordinary chondrites and their constituents. Geochim. Cosmochim. Acta **48**, 693-709.
- Bischoff A., Keil K. and Stöffler D.** (1985) Perovskite-hibonite-spinel-bearing inclusions and Al-rich chondrules and fragments in enstatite chondrites. Chem. Erde **44**, 97-106.
- Bischoff A., Palme H. and Spettel B.** (1989) Al-rich chondrules from the Ybbsitz H4-chondrite: evidence for formation by collision and splashing. Earth and Planet. Sci. Lett. **93**, 170-180.
- Blander M. and Fuchs L.H.** (1975) Calcium-aluminum inclusions in the Allende meteorite: evidence for a liquid origin. Geochim. Cosmochim. Acta **39**, 1605-1619.
- Blander M., Planner H.N. and Keil K.** (1976) The origin of chondrules; experimental investigations of metastable liquids in the system $Mg_2SiO_4-SiO_2$. Geochim. Cosmochim. Acta **40**, 889-896.
- Boctor N.Z., Hutcheon I.D. and Wasserburg G.J.** (1988) Petrology of a plagioclase-rich forsterite-bearing Allende inclusion. Lunar Planet. Sci. Conf. XIX, 110-111.
- Boctor N.Z., Hutcheon I.D. and Wasserburg G.J.** (1989) Petrology and opaque mineralogy of an armalcolite-bearing basaltic CAI from the Allende meteorite. Lunar Planet. Sci. Conf. XX, 88-89.
- Bowen N.L.** (1914) The ternary system diopside-forsterite-silica. Am.J.Sci. **38** (Fourth Series), 207-264.
- Boynton W.V.** (1975) Fractionation in the solar nebula, condensation of yttrium and the rare earth elements. Geochim. Cosmochim. Acta **39**, 569-584.
- Boynton W.V.** (1984) Cosmochemistry of the rare earth elements: Meteorite studies. In *Rare Earth Element Geochemistry* (ed. P. Henderson), 63-115. Elsevier.
- Brigham C.A.** (1990) Isotopic heterogeneity in calcium-aluminum rich meteoritic inclusions. Ph.D Thesis, California Institute of Technology.
- Brigham C.A., Hutcheon I.D., Papanastassiou D.A. and Wasserburg G.J.** (1988) Isotopic heterogeneity and correlated isotope fractionation in purple FUN inclusions. Lunar Planet. Sci. Conf. XIX, 132-133.
- Castaing R. and Slodzian G.** (1960) Microanalyse par émission ionique secondaire. Proc. Eur. Reg. Conf. on Electron Microscopy, Delft **1**, 169-172.
- Castaing R. and Slodzian G.** (1962) Microanalyse par émission ionique secondaire. Microscopie **1**, 395-410.
- Catanzaro E.J., Murphy T.J., Garner E.L. and Shields W.R.** (1966) Absolute isotopic

abundance ratios and atomic weight of magnesium. J. Res. Natl. Bur. Stand. **70A**, 453-458.

- Chen J.H. and Tilton G.R.**(1976) Isotopic lead investigation on the Allende carbonaceous chondrite. Geochim. Cosmochim. Acta **40**, 635-643.
- Chou C., Baedeker P.A. and Wasson J.T.** (1975) Allende inclusions: volatile-element distribution and evidence for incomplete volatilization of presolar solids. Geochim. Cosmochim. Acta **39**, 85-94.
- Christophe Michel-Lévy, M.** (1968) Un chondre exceptionnel dans la météorite de Vigarano. Bulletin de la Société Française de Minéralogie et de Cristallographie **91**, 212-214.
- Clark S.P., Jr., Schairer J.F., and de Neufville J.** (1962) Phase relations in the system $\text{CaMgSi}_2\text{O}_6\text{-CaAl}_2\text{SiO}_6\text{-SiO}_2$ at low and high pressure. Carnegie Inst. Wash. Yb. **61**, 59-68.
- Clayton D.D.** (1982) Cosmic chemical memory: A new astronomy. Quar. J. Roy. Astron. Soc. **23**, 174-212.
- Clayton R.N., Grossman L. and Mayeda T.K.** (1973) A component of primitive nuclear composition in carbonaceous meteorites. Science **182**, 485-488.
- Clayton R.N., Mayeda T.K., and Molini-Volsko C.A.** (1985) Isotopic variations in solar system material: evaporation and condensation of silicates. In Protostars and Planets II (eds. D. Black and M.S. Matthews), 755-771. Univ. Arizona Press, Tucson.
- Clayton R.N., Onuma N., Grossman L. and Mayeda T.K.** (1977) Distribution of pre-solar component in Allende and other carbonaceous chondrites. Earth Planet. Sci. Lett. **34**, 209-224.
- Clayton R.N., MacPherson G.J., Hutcheon I.D., Davis A.M., Grossman L., Mayeda T.K., Molini-Velsko C., Allen J.M. and El Goresy A.** (1984) Two forsterite-bearing FUN inclusions in the Allende meteorite. Geochim. Cosmochim. Acta **48**, 535-548.
- Coles J.N. and Long J.V.P.** (1973) An ion-microprobe study of the self-diffusion of Li^+ of lithium fluoride. Philos. Mag. **29**, 457-471.
- Colson R.O., McKay G.A. and Taylor L.A.** (1988) Temperature and composition dependencies of trace element partitioning: Olivine/melt and low-Ca pyroxene/melt. Geochim. Cosmochim. Acta **52**, 539-553.
- Crank J.** (1975) The Mathematics of Diffusion. Clarendon Press, Oxford, 414 p.
- Cygan R.T. and Lasaga A.C.** (1985) Self-diffusion of magnesium in garnet at 750° to 900°C. Amer. J. Sci. **285**, 328-350.

- Deer W.A., Howie R.A. and Zussman J.** (1978) Rock-forming Minerals, Vol.2A, Single-chain Silicates. Halsted Press, 668 p.
- DeVries R.C. and Osborn E.F.** (1957) Phase equilibria in high-alumina part of the system CaO-MgO-Al₂O₃-SiO₂. J. Amer. Ceram. Soc. **40**, 6-15.
- Dodd R.T.** (1978) The composition and origin of large microporphyritic chondrules in the Manych (L-3) chondrite. Earth Planet. Sci. Lett. **39**, 52-66.
- El Goresy A.** (1976) Oxide minerals in lunar rocks. MSA short course notes: Oxide minerals, (ed. D. Rumble), Chap.6.
- El Goresy A., Nagel K. and Ramdohr P.** (1978) Fremdlinge and their noble relatives. Proc. Lunar Sci. Conf. **9**, 1279-1303.
- Esat T.M., Lee T., Papanastassiou D.A. and Wasserburg G.J.** (1978) Search for ²⁶Al effects in the Allende FUN inclusion C1. Geophys. Res. Letters **5**, 807-810.
- Freer R.** (1980) Bibliography: Self-diffusion and impurity diffusion in oxides. J. Material Sci. **15**, 803-824.
- Freer R.** (1981) Diffusion in silicate minerals and glasses: a data digest and guide to the literature. Contrib. Mineral. Petrol. **76**, 440-454.
- Freer R., Carpenter M.A., Long J.V.P. and Reed S.J.B.** (1982) "Null result" diffusion experiments with diopside: implications for pyroxene equilibria. Earth and Planet. Sci. Lett. **58**, 285-292.
- Fuchs L.H.** (1969) Occurrence of cordierite and aluminous orthoenstatite in the Allende meteorite. Amer. Mineral. **54**, 1645-1653.
- Fuchs L.H.** (1971) Occurrence of wollastonite, rhönite, and andradite in the Allende meteorite. Amer. Mineral. **56**, 2053-2068.
- Fuchs L.H. and Blander M.** (1977) Molybdenite in calcium-aluminum-rich inclusions in the Allende meteorite. Geochim. Cosmochim. Acta **41**, 1170-1174.
- Gentile A.L. and Foster W.R.** (1963) Calcium hexaluminate and its stability relations in the system CaO-Al₂O₃-SiO₂. J. Amer. Ceram. Soc. **46**, 74-76.
- Gibb F.G.** (1974) Supercooling and the crystallization of plagioclase from a basaltic magma. Mineralogical Magazine **39**, 641-653.
- Goldschmidt V.M.** (1954) Geochemistry (ed. A. Muir). Oxford: Clarendon Press.
- Goldstein J.I., Newbury D.E., Echlin P., Joy D.C., Fiori C., and Lifshin E.** (1981) Scanning Electron Microscopy and X-ray microanalysis. Plenum Press, 674 p.

- Goldstein J.I. and Ogilvie R.E. (1965) The growth of the Widmanstätten pattern in metallic meteorites. Geochim. Cosmochim. Acta **29**, 893-920.
- Goswami J.N., Srinivasan G. and Ulyanov A.A. (1991) Titanium, calcium and magnesium isotopic compositions in a hibonite-rich inclusion from Efremovka. Meteoritics.
- Gray C.M., Papanastassiou D.A. and Wasserburg G.J. (1973) The Identification of early condensates from the solar nebula. Icarus **20**, 213-239.
- Grossman J.N. (1988) Formation of chondrules. In *Meteorites and the Early Solar System* (eds. J.F. Kerridge and M.S. Matthews) pp. 680-696. Univ. Arizona Press, Tucson.
- Grossman L. (1972) Condensation in the primitive solar nebula. Geochim. Cosmochim. Acta **36**, 597-619.
- Grossman L. (1973) Refractory trace elements in Ca-Al-rich inclusions in the Allende meteorite. Geochim. Cosmochim. Acta **37**, 1119-1140.
- Grossman L. (1975) Petrography and mineral chemistry of Ca-rich inclusions in the Allende meteorite. Geochim. Cosmochim. Acta **39**, 433-454.
- Grossman L. (1980) Refractory inclusions in the Allende meteorite. Ann. Rev. Earth Planet. Sci. **8**, 559-608.
- Grossman L. and Ganapathy R. (1975) Volatile elements in Allende inclusions. Proc. Lunar Sci. Conf. **6**, 1729-1736.
- Gutt W. and Russell A.D. (1977) Studies of the system CaO-SiO₂-Al₂O₃-MgO in relation to the stability of blast furnace slag. J. Material Sci. **12**, 1869-1878.
- Haggerty S.E. (1973) Armalcolite and genetically associated opaque minerals in lunar samples. Proc. Lunar Sci. Conf. **4**, 777-797.
- Haggerty S.E. (1975) The chemistry and genesis of opaque minerals in kimberlites. Phys. Chem. Earth **9**, 295-307.
- Hashimoto A., Kumazawa N. and Onuma N. (1979) Evaporation metamorphism of primitive dust material in the early solar nebula. Earth Planet. Sci. Lett. **43**, 13-21.
- Higgins J.B., Ribbe P.H. and Herd R.K. (1979) Sapphirine I. Crystal chemical contributions. Contrib. Mineral. Petrol. **68**, 349-356.
- Huneke J.C., Armstrong J.T. and Wasserburg G.J. (1983) FUN with PANURGE: High mass resolution ion microprobe measurements of Mg in Allende inclusions. Geochim. Cosmochim. Acta **47**, 1635-1650.
- Hutcheon I.D. (1982) Ion probe magnesium isotopic measurements of Allende inclusions. In

Nuclear and Chemical Dating Techniques: Interpreting the Environmental Record (ed. L.A. Curie), Amer. Chem. Soc. Symposium Series No.176, pp. 95-128.

- Hutcheon I.D., Armstrong J.T. and Wasserburg G.J.** (1987) Isotopic studies of Mg, Fe, Mo, Ru and W in Fremdlinge from Allende refractory inclusions. Geochim. Cosmochim. Acta **51**, 3175-3192.
- Hutcheon I.D., Steele I.M., Smith J.V. and Clayton R.N.** (1978) Ion microprobe, electron microprobe and cathodoluminescence data for Allende inclusions with emphasis on plagioclase chemistry. Proc. Lunar Sci. Conf. **9**, 1345-1368.
- Hayashi T. and Muehlenbachs K.** (1986) Rapid oxygen diffusion in mwlilite and its relevance to meteorites. Geochim. Cosmochim. Acta **50**, 585-591.
- Jost W.** (1960) Diffusion in solids, liquids, gases. Academic Press, 558 p.
- Jurewicz A.J.G. and Watson E.B.** (1988) Cations in olivine, part 1: calcium partitioning and calcium-magnesium distribution between olivines and coexisting melts, with petrologic applications. Contrib. Mineral. Petrol. **99**, 176-185.
- Kaiser T. and Wasserburg G.J.** (1983) The isotopic composition and concentration of Ag in iron meteorites and the origin of exotic silver. Geochim. Cosmochim. Acta **47**, 43-58.
- Keith M.L. and Schairer J.F.** (1952) Stability field of sapphirine in the system MgO-Al₂O₃-SiO₂. J. Geol. **60**, 181-186.
- Kennedy A.K., Hutcheon I.D. and Wasserburg G.J.** (1989) Chemical and isotopic constraints on the formation and evolution of SA-1, a basaltic CAI from Allende. Lunar Planet. Sci. Conf. **XX**, 514-515.
- Kennedy A.K., Hutcheon I.D. and Wasserburg G.J.** (1991) Chemical and isotopic constraints on the formation and differentiation of SA-1, a basaltic inclusion from Allende. In preparation.
- Lange R.A. and Carmichael I.S.E.** (1987) Densities of Na₂O-K₂O-CaO-MgO-FeO-Fe₂O₃-Al₂O₃-TiO₂-SiO₂ liquids: New measurements and derived partial molar properties. Geochim. Cosmochim. Acta **51**, 2931-2946.
- Larimer J.W.** (1967) Chemical fractionations in meteorites - I. Condensation of the elements. Geochim. Cosmochim. Acta **31**, 1215-1238.
- Lee T.** (1979) New isotopic clues to solar system formation. Rev. Geophys. Space Phys. **17**, 1591-1611.
- Lee T. and Papanastassiou D.A.** (1974) Mg isotopic anomalies in the Allende meteorite and correlations with O and Sr effects. Geophys. Res. Lett. **1**, 225-228.

- Lee T., Papanastassiou D.A. and Wasserburg G.J.** (1976) Demonstration of ^{26}Mg excess in Allende and evidence for ^{26}Al . Geophys. Res. Lett. **3**, 109-112.
- Lee T., Papanastassiou D.A. and Wasserburg G.J.** (1977) Aluminum-26 in the early solar system. Fossil or fuel? Astrophys. J. **211**, L107-L110.
- Leeman W.P. and Scheidegger K.F.** (1977) Olivine/liquid distribution coefficients and a test for crystal-liquid equilibrium. Earth and Planet. Sci. Letters **35**, 247-257.
- Lensch G.** (1971) Das Vorkommen von Sapphirin im Peridotitkörper von Finero (Zone von Ivrea, Italienische Westalpen). Contrib. Mineral. Petrol. **31**, 145-152.
- Liebl H.** (1967) Ion microprobe mass analyzer. J. Appl. Phys. **38**, 5277-5283.
- Liebl H. and Herzog R.F.K.** (1963) Sputtering ion source for solids. J. Appl. Phys. **34**, 2893-2896.
- Lindner R. and Åkerström Å.** (1958) Diffusion von Ni-63 in Nickelspinellen. Zeitschrift Phys. Chem. **18**, 303-307.
- Lofgren G.** (1980) Experimental studies on the dynamic crystallization of silicate melts. In Physics of Magmatic Processes (ed. R.B. Hargraves), pp. 487-551, Princeton University Press.
- Lofgren G. and Russell W.J.** (1986) Dynamic crystallization of chondrule melts of porphyritic and radial pyroxene composition. Geochim. Cosmochim. Acta **50**, 1715-1726.
- Longhi J.** (1987) Liquidus equilibria and solid solution in the system $\text{CaAl}_2\text{Si}_2\text{O}_8\text{-Mg}_2\text{SiO}_4\text{-CaSiO}_3\text{-SiO}_2$ at low pressure. Amer. J. Sci. **287**, 265-331.
- Longhi J. and Boudreau A.** (1980) The orthoenstatite liquidus field in the system forsterite-diopside-silica. Amer. Mineral. **64**, 563-573.
- Longhi J. and Pan V.** (1988) A reconnaissance study of phase boundaries in low-alkali basaltic liquids. J. Petrol. **29**, 115-147.
- Lorand J.P. and Cottin J.Y.** (1987) A new natural occurrence of zirconolite ($\text{CaZrTi}_2\text{O}_7$) and baddeleyite (ZrO_2) in basic cumulates: the Laouni layered intrusion (Southern Hoggar, Algeria). Mineral. Mag. **51**, 671-676.
- Lord H.C. III** (1965) Molecular equilibria and condensation in a solar nebula and cool stellar atmospheres. Icarus **4**, 279-288.
- Love G. and Scott V.D.** (1978) Evaluation of a new correction procedure for quantitative electron probe microanalysis. J. Phys. D-11, 1369-1376.
- Lux G., Keil K., and Taylor G.J.** (1981) Chondrules in H3 chondrites: textures, compositions

and origins. Geochim. Cosmochim. Acta **45**, 675-685.

Macdougall J.D. (1979) Refractory element-rich inclusions in CM meteorites. Earth Planet. Sci. Lett. **42**, 1-6.

MacPherson G.J. and Grossman L. (1981) A once-molten, coarse-grained, Ca-rich inclusion in Allende. Earth Planet. Sci. Lett. **52**, 16-24.

MacPherson G.J. and Grossman L. (1984) "Fluffy" Type A Ca-, Al-rich inclusions in the Allende meteorite. Geochim. Cosmochim. Acta **48**, 29-46.

MacPherson G.J., Paque J.M., Stolper E. and Grossman L. (1984) The origin and significance of reverse zoning in melilite from Allende Type B inclusions. J. Geol. **92**, 289-305.

MacPherson G.J., Hashimoto A. and Grossman L. (1985) Accretionary rims on inclusions in the Allende meteorite. Geochim. Cosmochim. Acta **49**, 2267-2279.

MacPherson G.J., Fahey A.J., Lundberg L.L., and Zinner E. (1988) Al-Mg isotopic systematics and metamorphism in five coarse-grained Allende CAIs. Meteoritics **23**, 286-287.

MacPherson G.J., Wark D.A. and Armstrong J.T. (1988) Primitive material surviving in chondrites: refractory inclusions. In Meteorites and the Early Solar System (eds. J.F. Kerridge and M.S. Matthews), Univ. Arizona Press, pp. 746-807.

Martin P.M. and Mason B. (1974) Major and trace elements in the Allende meteorite. Nature **249**, 333-334.

Mason B. and Martin P.M. (1977) Geochemical differences among components of the Allende meteorite. Smithsonian Contributions to the Earth Sciences, No.19, 84-95.

McKeegan K.D. and Ryerson F.J. (1990) Diffusion of oxygen in diopside and spinel: implications for oxygen isotopic anomalies in CAIs. Lunar Planet. Sci. Conf. XXI, 775-776.

McSween H.Y. (1977) Chemical and petrographic constraints on the origin of chondrules and inclusions in carbonaceous chondrites. Geochim. Cosmochim. Acta **41**, 1843-1863.

McSween H.Y. (1979) Are Carbonaceous chondrites primitive or processed? A review. Reviews of Geophy. and Space Physics **17**, 1059-1078.

Meeker G.P., Wasserburg G.J. and Armstrong J.T. (1983) Replacement textures in CAI and implications regarding planetary metamorphism. Geochim. Cosmochim. Acta **47**, 707-721.

Meyer H.O.A. and Boctor N.Z. (1974) Opaque mineralogy: Apollo 17, rock 75035. Proc.

Lunar Sci. Conf. 5, V.1, 706-716.

- Misawa K. and Nakamura N. (1987) Rare earth elements in chondrules from the Felix (CO3) chondrite: Comparison with the Allende (CV3) chondrules. Symp. Ant. Met. **12**, 90-92.
- Nagahara H. and Kushiro I. (1982) Calcium-aluminum-rich chondrules in the unequilibrated ordinary chondrites. Meteoritics **17**, 55-63.
- Niederer F.R. and Papanastassiou D.A. (1984) Ca isotopes in refractory inclusions. Geochim. Cosmochim. Acta **48**, 1279-1294.
- Niederer F.R. and Papanastassiou D.A., and Wasserburg G.J. (1985) Absolute isotopic abundances of Ti in meteorites. Geochim. Cosmochim. Acta **49**, 835-851.
- Osborn E.F. and Gee K.H. (1969) Phase equilibria at liquidus temperatures for a part of the system CaO-MgO-Al₂O₃-TiO₂-SiO₂ and their bearing on the effect of titania on the properties of blast furnace slag. Bull. Earth and Mineral Sci. Experiment Station **85**, 57-80.
- Osborn E.F. and Tait D.B. (1952) The system diopside-forsterite-anorthite. Amer. J. Sci. **239**, 721-763.
- Osborn E.F., DeVries R.C., Gee K.H. and Kraner H.M. (1954) Optimum composition for blast furnace slag as deduced from liquidus data for the quaternary system CaO-MgO-Al₂O₃-SiO₂, J. Metals **6**, 33-45.
- Palme H. and Wlotzka F. (1976) A metal particle from a Ca, Al-rich inclusion from the meteorite Allende, and the condensation at refractory siderophile elements. Earth Planet. Sci. Lett. **33**, 45-60.
- Pan V. and Longhi J. (1989) Low pressure liquidus relations in the system Mg₂SiO₄-Ca₂SiO₄-NaAlSiO₄-SiO₂. Amer. J. Sci. **289**, 1-16.
- Papanastassiou D.A., Lee T. and Wasserburg G.J. (1977) Evidence for ²⁶Al in the solar system. In Comets, Asteroids, Meteorites (ed. A.H. Delsemme), Univ. of Toledo, pp. 343-349.
- Papanastassiou D.A., Brigham C.A. and Wasserburg G.J. (1984) Search for Mg isotopic signatures in Allende. Lunar Planet. Sci. Conf. XV, 629-630.
- Pedersen A.K. (1981) Armalcolite-bearing Fe-Ti Oxide Assemblages in graphite-equilibrated salic volcanic rocks with native iron from Disko, Central West Greenland. Contrib. Mineral. Petrol. **77**, 307-324.
- Planner H.N. and Keil K. (1983) Evidence for the three-stage cooling history of olivine-porphyrific fluid droplet chondrules. Geochim. Cosmochim. Acta **46**, 317-330.

- Podosek F.A.**(1978) Isotopic structures in solar system materials. Ann. Rev. Astron. Astrophys. **16**, 293-334.
- Prince A.T.** (1954) Liquidus relationship on 10% MgO plane of the system lime-magnesia-alumina-silica. J. Amer. Ceram. Soc. **37**, 402-408.
- Rankin G.A. and Merwin H.E.** (1918) The ternary system MgO-Al₂O₃-SiO₂. Amer. J. Sci. fourth series XLV **268**, 301-325.
- Reed D.J. and Wuensch B.J.** (1979) Ion-probe measurement of oxygen self-diffusion in single-crystal Al₂O₃. J. Amer. Cer. Soc. **63**, 88-92.
- Rubin A.E. and Wasson J.T.** (1988) Chondrules and matrix in the Ornans CO3 meteorite: Possible precursor components. Geochim. Cosmochim. Acta **52**, 425-432.
- Schairer J.F. and Yoder H.S., Jr.** (1969) Critical planes and flow sheet for a portion of the system CaO-MgO-Al₂O₃-SiO₂ having petrological applications. Carnegie Inst. Wash. Yb. **68**, 202-214.
- Schramm D.N., Tera F. and Wasserburg G.J.**(1970) The isotopic abundance of ²⁶Mg and limits on ²⁶Al in the early solar system. Earth Planet. Sci. Lett. **10**, 44-59.
- Schreyer W. and Schairer J.F.** (1961) Composition and structural states of anhydrous Mg-cordierites: a re-investigation of the central part of the system MgO-Al₂O₃-SiO₂. J. Petrol. **2**, 324-406.
- Scott V.D. and Love G.**(1983) Quantitative Electron-probe Microanalysis. Halsted press, 345 p.
- Sears D.W.G. and Dodd R.T.**(1988) Overview and classification of meteorites. In Meteorites and the Early Solar System (eds. J. F. Kerridge and M.S. Matthews), pp. 3-31.
- Segnit E.R.** (1957) Sapphirine-bearing rocks from Robertson Land, Antarctica. Mineral.Mag. **31**, 690-697.
- Sheng Y.J., Hutcheon I.D. and Wasserburg G.J.** (1988) Plagioclase-Olivine Inclusions in Allende- a link between CAI and ferro-magnesian chondrules. Lunar Planet.Sci. Conf. XIX, 1075-1076.
- Sheng Y.J., Hutcheon I.D. and Wasserburg G.J.** (1990) Magnesium isotope heterogeneity in Plagioclase Olivine Inclusions. Lunar Planet.Sci. Conf. XXI, 1138-1139.
- Sheng Y.J., Hutcheon I.D. and Wasserburg G.J.** (1991a) Origin of Plagioclase-Olivine Inclusions in carbonaceous chondrites. Geochim. Cosmochim. Acta **55**, 581-599.
- Sheng Y.J., Beckett J.R., Hutcheon I.D. and Wasserburg G.J.** (1991b) Experimental constraints on the origin of plagioclase-olivine inclusions and CA chondrules. Lunar Planet. Sci. Conf. XXII, 1231-1232.

- Sheng Y.J., Hutcheon I.D. and Wasserburg G.J. (1991c) Mg self-diffusion in spinel: constraints on the thermal history of plagioclase-olivine inclusions. Lunar Planet. Sci. Conf. XXII, 1233-1234.
- Shimizu N. and Hart S.R. (1982) Isotope fractionation in secondary ion mass spectrometry. J. Appl. Phys. **53**, 1303-1311.
- Shimizu N., Semet M.P., and Allegrè C.J. (1978) Geochemical Applications of quantitative ion-microprobe analysis. Geochim. Cosmochim. Acta **42**, 1321-1334.
- Slodzian G. (1964) Etude d'une méthode d'analyse locale chimique et isotopique utilisant l'émission ionique secondaire. Ann. Phys. 18 ème série, Tome 9 (Paris: Masson).
- Slodzian G. (1980) Microanalyzers using secondary ion emission. Advances in Electronics and Electron Physics, supplement 13B, ed. A. Septier (New York: Academic Press), 1-32.
- Spear F.S., Rumble III D. and Ferry J.M. (1982) Linear algebraic manipulation of n-dimensional composition space. In Reviews in Mineralogy, V10, Characterization of Metamorphism through Mineral Equilibria (ed. J.M. Ferry). Mineralogical Society of America pp. 53-98.
- Srinivasan G., Ulyanov A. A. and Goswami J. N. (1991) Magnesium isotopic fractionation in refractory inclusions: Indications for a mineralogic control. Meteoritics.
- Stolper E. (1982) Crystallization sequences of Ca-Al-rich inclusions from Allende: An experimental study. Geochim. Cosmochim. Acta **46**, 2159-2180.
- Stolper E. and Paque J.M. (1986) Crystallization sequences of Ca-Al-rich inclusions from Allende: An experimental study. Geochim. Cosmochim. Acta **50**, 1785-1806.
- Suess H.E. and Urey H.C. (1956) Abundances of the elements. Rev. Mod. Phys. **28**, 53-74.
- Sung C., Abu-Eid R.M. and Burns R.G. (1974) Ti^{3+}/Ti^{4+} ratios in lunar pyroxenes: implications to depth of origin of mare basalt magma. Proc. Lunar Sci. Conf. **5**, 717-726.
- Tanaka T. and Masuda A. (1973) Rare-earth elements in matrix, inclusions, and chondrules of the Allende meteorite. Icarus **19**, 523-530.
- Taylor G.J., Scott E.R.D. and Keil K. (1983) Cosmic setting for chondrule formation. In Chondrules and their Origins (ed. E.A. King) pp. 262-278. Lunar and Planetary Science Institute.
- Taylor S.R. and Mason B. (1978) Chemical characteristics of Ca-Al-rich inclusions in the Allende meteorite. Lunar Planet. Sci. **IX**, 1158-1160.
- Tsuchiyama A., Nagahara H. and Kushiro I. (1980) Experimental reproduction of textures of

chondrules. Earth and Planetary Sci. Letters **48**, 155-165.

Urey H.C.(1952) Abundances of the elements. Phys. Rev. **88**, 248-252.

VanSchmus W.R. and Wood J.A.(1967) A chemical-petrologic classification for the chondritic meteorites. Geochim. Cosmochim. Acta **38**, 47-64.

Velde D. (1975) Armalcolite-Ti-phlogopite-diopside-analcite-bearing lamproites from Smoky Butte, Garfield County, Montana. Amer. Mineral. **60**, 566-573.

Wark D.A. (1987) Plagioclase-rich inclusions in carbonaceous meteorites: Liquid condensates? Geochim. Cosmochim. Acta **51**, 221-242.

Wark D.A. and Lovering J.F.(1976) Refractory/platinum metal grains in Allende calcium-aluminum-rich clasts (CARC's): Possible exotic presolar material? Lunar Sci. **VII**, 912-914.

Wark D.A. and Lovering J.F. (1977) Marker events in the early evolution of the solar system: Evidence from rims on CA-Al-rich inclusions in carbonaceous chondrites. Proc. Lunar Sci. Conf. **8**, 95-112.

Wasserburg G.J. (1985) Short-lived nuclei in the early solar system. In Protostars and Planets II (eds. D. Black and M.S. Matthews), 703-754. Univ. Arizona Press, Tucson.

Wasserburg G. J. and Papanastassiou D. A. (1982). Some short-lived nuclides in the early solar-system -- A connection with the placental ISM. In Essays in Nuclear Astrophysics (eds. C.A. Barnes, D.D. Clayton, and D.A. Schraimm) Cambridge: Cambridge Univ. Press, pp. 71-140.

Wasserburg G.J., Papanastassiou D.A. and Lee T. (1980) Isotopic heterogeneities in the solar system. In Early Solar System Processes and the Present Solar System, 144-191. (Bologna: Soc. Italiana di Fisica).

Wasserburg G.J., Lee T. and Papanastassiou D.A. (1977) Correlated O and Mg isotopic anomalies in Allende inclusions: II. Magnesium. Geophys. Res. Lett. **4**, 299-302.

Wasson J.T. (1972) Formation of ordinary chondrites. Rev. Geophys. Space Phys. **10**, 711-759.

Wasson J.T. (1974) Meteorites (Heidelberg: Springer-Verlag) 316 p.

Watson E.B. (1979) Calcium content of forsterite coexisting with silicate liquid in the system Na₂O-CaO-MgO-Al₂O₃-SiO₂. Amer. Mineral. **64**, 824-829.

Watson E.B., Harrison T.M. and Ryerson F.J. (1985) Diffusion of Sm, Sr, and Pb in fluorapatite. Geochim. Cosmochim. Acta **49**, 1813-1823.

Williams P. (1985) Secondary ion mass spectrometry. Ann. Rev. Mater. Sci. **15**, 517-548.

- Williamson J.H.** (1968) Least-squares fitting of a straight line. Canadian J. Phys. **46**, 1845-1847.
- Wood J.A. and McSween H.Y., Jr.** (1977) Chondrules as condensation products. In *Comets, Asteroids, Meteorites: Interrelations, Evolutions, and Origins* (ed. A.H. Delsemme), pp. 365-373. Univ. of Toledo Press, Ohio.
- Yang H., Salmon J.F. and Foster W.R.** (1972) Phase equilibria of the join akermanite-anorthite-forsterite in the system CaO-MgO-Al₂O₃-SiO₂ at atmospheric pressure. Amer. J. Sci. **272**, 161-188.
- Yurimoto H. and Sueno S.** (1984) Anion and cation partitioning between olivine, plagioclase phenocrysts and the host magma: A new application of ion microprobe study. Geochemical Journal **18**, 85-94.
- Yurimoto H., Morioka M. and Nagasawa H.** (1989) Diffusion in single crystals of melilite; I, Oxygen. Geochim. Cosmochim. Acta **53**, 2387-2394.
- Zhang Y., Walker D., and Leshner C. E.** (1989) Diffusive crystal dissolution. Contrib. Mineral. Petrol. **102**, 492-513.
- Zinner E.** (1989) Isotopic measurements with the ion microprobe. U.S.G.S. Bulletin **1890**, 145-162.
- Zinner E. and Crozaz G.** (1986) A method for the quantitative measurement of rare earth elements in the ion microprobe. Int. J. Mass Spec. Ion Proc. **69**, 17-38.

Origin of plagioclase-olivine inclusions in carbonaceous chondrites*

Y. J. SHENG, I. D. HUTCHEON, and G. J. WASSERBURG

The Lunatic Asylum of the Charles Arms Laboratory, Division of Geological and Planetary Sciences,
California Institute of Technology, Pasadena, CA 91125, USA

(Received May 30, 1990; accepted in revised form November 9, 1990)

Abstract—Plagioclase-Olivine Inclusions (POIs) are an abundant group of chondrule-like objects with igneous textures found in carbonaceous chondrites. POIs consist of plagioclase, olivine, pyroxene, and spinel, and cover a wide range of compositions between Type C Ca-Al-rich Inclusions (CAIs) and ferromagnesian chondrules. POIs are distinguished from CAIs by the absence of melilite, lack of refractory siderophile-rich opaque assemblages, more sodic plagioclase, and abundance of olivine and aluminous-enstatite. Rare accessory minerals including armalcolite, zirconolite, rutile, and sapphirine are found in several POIs. The petrographic and chemical properties of POIs indicate that they are not condensates or evaporative residues but formed by melting or partial melting of pre-existing solids. Seven of fourteen POIs contain isotopically fractionated Mg, and despite their textures these POIs are not isotopically homogeneous. Spinel is the major carrier of fractionated Mg in six POIs. The magnitude of Mg isotopic fractionation (F_{Mg}) of spinel ranges from -8 to $+11\%$ amu among the POIs but F_{Mg} is always either positive or negative within an individual POI. Within a single inclusion, F_{Mg} of coexisting spinel is not constant but varies by up to 7% amu. Isotopic fractionation of Mg in silicates is less common and always positive ($F_{Mg} > 0$). Pyroxenes in two POIs and plagioclase in a third contain isotopically heavy Mg. Radiogenic $^{26}Mg^*$ is rare in POIs as only two inclusions show evidence of excess ^{26}Mg with $^{26}Mg^*/^{27}Al \sim 4 \times 10^{-6}$. The preservation of isotopic heterogeneity in objects whose igneous textures suggest crystallization from a homogeneous melt implies that melting was incomplete, allowing survival of relict phases. A comparison of the essential characteristics of POIs and CAIs suggests that the major processes leading to formation of POIs—including condensation, dust/gas fractionation, aggregation of chemically and isotopically disparate materials, and partial melting—are common to most CAIs and chondrules. We present a scenario for the formation of these objects and conclude that the homogeneity of the final assemblage—CAI, POI, or chondrule—is primarily a reflection of the thermal history rather than the nature of precursor materials.

INTRODUCTION

THE ISOTOPIC AND CHEMICAL properties of Ca-Al-rich Inclusions (CAIs) provide important clues to early solar system processes and history. Relative to average chondritic material and to ferromagnesian chondrules, CAIs are enriched in Al, Ca, and Ti and in refractory lithophile and siderophile trace elements. Early workers were impressed by the remarkable similarity of CAI bulk compositions and mineralogy to those of high-temperature condensates predicted to form in a cooling gas of solar composition (LORD, 1965; LARIMER, 1967; GROSSMAN, 1972; BLANDER and FUCHS, 1975). However, more recent studies have demonstrated that CAIs are not simply vapor-to-solid or vapor-to-liquid condensates and underscore the complexity of this diverse group of objects. Texturally, most coarse-grained CAIs appear to have experienced a molten or partially molten origin, but the variety and complexity of the chemical, mineralogical, and isotopic signatures of CAIs attest to multi-stage formation involving a number of processes, including evaporation (CHOU et al., 1975; HASHIMOTO et al., 1979), condensation (MACPHERSON and GROSSMAN, 1984; ALLEN et al., 1978), melting (MACPHERSON and GROSSMAN, 1981; STOLPER, 1982; STOLPER and PAQUE, 1986), and metamorphism (MEEKER et al., 1983; CLAYTON et al., 1977; ARMSTRONG, 1984). Re-

fractory inclusions are often treated as distinct from normal chondrules, but observations of anorthite-rich Type C CAIs (GROSSMAN, 1975; WARK, 1987; BECKETT and GROSSMAN, 1988) and forsterite-rich CAIs (WARK et al., 1987), which are significantly less refractory than melilite-rich Type A CAIs and fassaite-rich Type B CAIs, and of ferromagnesian chondrules enriched in refractory lithophile trace elements (MISAWA and NAKAMURA, 1987; RUBIN and WASSON, 1988) and of CA chondrules (BISCHOFF and KEIL, 1984) suggest the existence of precursor materials common to all these objects. CAIs are widely believed to preserve a record of conditions and processes that prevailed early in the solar nebula. The possibility that remnants of this record are also contained in less refractory objects is a central theme of this work. The identification of the major processes leading to the formation, not only of the relatively rare CAIs but also of objects with much closer affinities to normal chondrules, should provide important information on early nebular and planetary processes and environments.

In this paper we describe a group of inclusions in three CV chondrites and one ungrouped chondrite that are quite different from typical CAIs in their chemistry, mineralogy, and isotopic composition. We refer to these objects as Plagioclase-Olivine Inclusions (POIs) as they consist of plagioclase, olivine, pyroxene, and spinel in various proportions and range from plagioclase-rich to olivine-rich. Rare mineral phases, some of which have not been reported in CAIs, or in

* Division Contribution No. 4680 (639).

meteorites in general, are also found in this group of inclusions. POIs are fairly abundant, occurring approximately one per thin section. The variation in POI mineralogy is reflected in their bulk chemistries which range from Ca-Al-rich objects similar to Type C CAI, to more Mg-, Si-rich objects grading into CA chondrules (CHRISTOPHE MICHEL-LÉVY, 1968; MCSWEEN, 1977; BISCHOFF and KEIL, 1984) and Mg-rich porphyritic chondrules. We use the chemical, mineralogical, and isotopic features displayed by these inclusions to demonstrate that mixing and partial melting processes were superimposed on more ancient, isotopically heterogeneous material. Preliminary work on these inclusions was reported by SHENG et al. (1988, 1990).

ANALYTICAL METHODS

Plagioclase and olivine-bearing inclusions were identified by petrographic observations on doubly polished thin sections using optical microscopy and by backscattered electron imaging on an SEM. The 20 inclusions studied were from 15 thin sections of Allende and one each from the Adelaide, Leoville, and Vigarano carbonaceous chondrites. Quantitative analysis of major and minor elements was performed on a Tracor TN-5500 energy dispersive X-ray analyzer (EDS) attached to a JEOL JSM-35 CF SEM using Bence-Albee (BENCE and ALBEE, 1968) procedures for data reduction and on a JEOL 733 electron microprobe using ZAF correction (LOVE and SCOTT, 1978) as modified by ARMSTRONG (1984). Bulk compositions of the inclusions were obtained by averaging the EDS analyses obtained by rastering the electron beam over several $250 \times 300 \mu\text{m}$ regions of each inclusion.

The Mg isotopic compositions of coexisting phases in 13 POIs were determined with the PANURGE IMS-3F ion microprobe (one POI was analyzed by PAPANASTASSIOU et al. (1984) using the thermal ionization technique). Data were collected in an automated peak-jumping mode under conditions described by HUNEKE et al. (1983) and HUTCHEON et al. (1987). Measured $^{25}\text{Mg}/^{24}\text{Mg}$ ratios may deviate from normal due either to mass-dependent fractionation intrinsic to the sample or to fractionation produced during sputtering and secondary ion formation in the ion probe. Studies have shown that $^{25}\text{Mg}/^{24}\text{Mg}$ ratios measured on the ion probe vary with the mineralogy and chemical composition of the phase analyzed (SLODZIAN, 1980; HUTCHEON, 1982; HUNEKE et al., 1983). To minimize these matrix effects, terrestrial samples of similar compositions to the phases in the inclusions were chosen as standards. They include Miakajima plagioclase (An_{96}), Burma spinel, Ti-pyroxene glass, aluminous enstatite, and forsteritic olivine (Fo_{90}). Since a major objective of this study was the measurement of intrinsic Mg fractionation in the POIs, standards were run daily prior to and after sample analysis to monitor shifts in the $^{25}\text{Mg}/^{24}\text{Mg}$ ratio due to different tuning conditions in the instrument.

Isotopic fractionation of Mg intrinsic to a POI was determined from the difference in the $^{25}\text{Mg}/^{24}\text{Mg}$ ratio of the sample relative to the ratio in a standard of appropriate mineralogy: $F_{\text{Mg}} = \Delta^{25}\text{Mg} - \Delta_{\text{std}}^{25}\text{Mg}$, where $\Delta^{25}\text{Mg}$ expresses the deviation in permil of the $^{25}\text{Mg}/^{24}\text{Mg}$ ratio relative to 0.12663 (CATANZARO et al., 1966). Typical errors in F_{Mg} , based on the reproducibility of analyses of standards, are $\pm 2\%$ for olivine, spinel, and pyroxene, and $\pm 3\%$ for plagioclase. To search for evidence of radiogenic $^{26}\text{Mg}^*$, the Mg isotopic data were also corrected for fractionation by normalizing to $^{25}\text{Mg}/^{24}\text{Mg} = 0.12663$ using a power law and the corrected ratios ($^{26}\text{Mg}/^{24}\text{Mg}$)_c used to calculate $\delta^{26}\text{Mg}$, expressed as

$$\delta^{26}\text{Mg} = \left[\frac{(^{26}\text{Mg}/^{24}\text{Mg})_c}{0.13955} - 1 \right] \times 1000.$$

This represents the permil deviation from the normal reference value, $^{26}\text{Mg}/^{24}\text{Mg} = 0.13955$ (BRIGHAM, 1990), and is used to identify non-linear isotopic shifts in the ^{26}Mg abundance.

RESULTS

Petrography

The mineral assemblages of POIs are dominated by plagioclase and olivine with variable amounts of olivine, spinel, fassaite, enstatite, and diopside. Melilite, a major component in CAIs, is not present. Most POIs are spheroidal, ranging from 0.5 to 5 mm in diameter. The texture is most commonly sub-ophitic to intersertal with plagioclase and olivine phenocrysts in a fine-grained matrix (Fig. 1a,b). Textures similar to those observed in ordinary chondrules, such as barred olivine (Fig. 1c), porphyritic (Fig. 1d), radiating (Fig. 1e), and granular, are also observed.

The occurrence of secondary phases containing Na and Fe such as nepheline, sodalite, and hedenbergite is quite restricted in POIs. These phases compose less than 5% of the mode of all POIs and occur only near the rims of inclusions or along cracks and in interstitial regions within inclusions, and do not appear to be directly associated with plagioclase or the Na-rich mesostases. The unaltered appearance of plagioclase with clearly defined boundaries is in sharp contrast to the embayed and extensively veined plagioclase and melilite frequently observed in Type B CAIs. POIs do not contain grossular or monticellite, two common secondary phases of Type B CAIs. Unlike the pervasive alteration of Type B CAIs, POIs do not appear to have been subjected to extensive post-crystallization open-system alteration.

A common feature of many POIs is the presence of one or more clusters (up to $200 \mu\text{m}$ in diameter) of equigranular olivine crystals located near the periphery of inclusions (Fig. 1f). These olivine clusters resemble granular olivine chondrules. The rim sequences that surround most CAIs (WARK and LOVERING, 1977) are not found in POIs, but sulfide-rich rims similar to those surrounding many ordinary chondrules are common. In some cases, aggregates of fine-grained olivine and pyroxene form accretionary rims on POIs, similar to those described by MACPHERSON et al. (1985).

The petrographic characteristics of POIs are summarized in Table 1. For simplicity of description, we have classified POIs into three groups. These three groups are classified solely on a petrographic basis and are not intended to be a distinction of their origin or REE abundances. The trend from group 1 to group 3 is defined by the monotonic decrease in the modal abundances of spinel and plagioclase compensated by an increase in the abundance of olivine. The chemical compositions of POIs in the three groups change in accordance with the variations in mineralogy and are discussed in the following section.

Group 1 POIs contain abundant spinel (5–30% modal abundance) and plagioclase (20–66%). Inclusions 5ALLB6, BG82DH2, and ALA1-2 are similar in both mineral assemblage and texture. All have sub-ophitic textures with randomly oriented plagioclase laths. Subhedral to anhedral olivine and pyroxene terminate against or surround the plagioclase. Olivines are commonly rimmed by Mg-rich pyroxene. Titanium-rich fassaite is interstitial and is interpreted to be a late crystallizing phase. Spinel occurs as sub-rounded to euhedral crystals poikilitically enclosed in the other silicates. Many of the euhedral spinels appear to be included in the interstitial

fassaites. Small grains (10–50 μm) of Ti-rich oxides, including armalcolite, rutile, ilmenite, and perovskite, are associated with the interstitial fassaites. Several small grains of zirconolite ($\text{CaZrTi}_2\text{O}_7$), about 1 micron in diameter, associated with perovskite were observed in Allende inclusion 5ALLB6. This is only the second meteoritic occurrence of zirconolite. Zirconolite was reported by EL GORESY et al. (1978) but was not documented.

Two other group 1 POIs, USNM 3510 and BG82CLII, although quite different from each other in texture and modal mineralogy, both contain sapphirine ($\text{Mg}_2\text{Al}_4\text{SiO}_{10}$). USNM 3510 consists of a coarse-grained (50–100 μm) mantle and a fine-grained (10 μm) core. Mineral phases in both rim and core are plagioclase, forsterite, spinel, and Al-enstatite. Sub-hedral to anhedral olivine and pyroxene terminate against euhedral plagioclase laths. Spinel is included in all three phases. BG82CLII has the least amount of plagioclase (20%) but the most abundant spinel (30%) among the group 1 POIs. Plagioclase and Al-enstatite occur as laths and prismatic crystals radiating inward from the rim. A central zone of densely populated spinel marks a boundary between the core and the spinel-free mantle of the inclusion. In both of these inclusions sapphirine occurs as randomly oriented euhedral prisms (5 \times 25 μm) embedded in a Na- (15% Na_2O) and Cl-rich (3%), Ca-poor (1.5% CaO) mesostasis (Fig. 2b). In 3510, sapphirine is localized in small pockets, whereas in BG82CLII it is much more abundant and distributed in much larger regions.

Group 2 POIs contain minor spinel (<5%) and abundant plagioclase (30–60%). Allende inclusions SA-1 and BG82DH1A have been described by BOCTOR (1988, 1989) and KENNEDY et al. (1989, 1990). These two inclusions plus BG82CH1, B14D, and ADEL-1 all have sub-ophitic textures. ADEL-1 is an inclusion from the Adelaide chondrite and is the most silica-rich POI. A symplectitic intergrowth of tridymite (or its polymorph) and plagioclase is found in regions interstitial to plagioclase laths in the interior of the inclusion. The few forsteritic olivines are rimmed by enstatite. A few small clusters of spinel are enclosed within plagioclase laths. These spinel grains appear to be strongly resorbed with corroded boundaries (Fig. 2a). BG82CLJa exhibits a radiating texture consisting mainly of plagioclase laths and tabular pyroxene grains. The pyroxenes are Fe-poor pigeonite surrounded by diopside. Spinel is rare and, where present, strongly resorbed. PPX contains granular olivines poikilitically enclosed in plagioclase. Calcium-poor pyroxene grains are interstitial among plagioclase and spinel is rare.

Group 3 POIs have the highest abundance of olivine (>40%) with lesser plagioclase (<25%) and rare spinel. This group is characterized by porphyritic, granular, and barred textures, commonly found in ferromagnesian chondrules. BG82CLJb is the only inclusion in this group that has a modest amount of spinel (5%). A cluster of spinel grains occurs in the center of the inclusion, enclosed by plagioclase. Olivine grains vary greatly in size, ranging from 10 to 200 microns in diameter. Larger grains developed near the rim of the inclusion grade into smaller grains towards the center. Both A-47 and BG82CLI resemble barred olivine chondrules, except that plagioclase and diopside occur as anhedral grains interstitial to the olivine bars. Redeye consists of large olivine

grains with interstitial plagioclase and pyroxene, and is the only POI exhibiting chromium-rich ($\sim 30\%$ Cr_2O_3), rather than aluminous, spinel.

Bulk Chemistry

Bulk compositions of POIs are given in Table 2. The POIs span a wide range in composition, reflected in a four-fold variation in CaO (4–17 wt%), a three-fold variation in MgO (10–34 wt%) and in Al_2O_3 (12–36 wt%), and more than a ten-fold variation in Na_2O (0.6–6.8 wt%) (Table 3). The most Ca- and Al-rich POI, ALA1-2, contains 44.8 wt% CaO + Al_2O_3 , whereas POI Redeye has only 6.2 wt% CaO + Al_2O_3 . Since Redeye is an extreme member among POIs, its composition was excluded from the preceding discussion. Corresponding to the classification outlined in the previous section, the CaO + Al_2O_3 content for the three POI groups are: (1) CaO + Al_2O_3 > 40 wt%; (2) 20% < CaO + Al_2O_3 < 40%; (3) CaO + Al_2O_3 < 20%. The difference in the CaO + Al_2O_3 content for the three groups is mainly a reflection of the modal abundances of spinel + plagioclase versus olivine.

The bulk chemical compositions of POIs are summarized in Table 2 and Fig. 4. Representative analyses of Types B and C coarse-grained CAIs, fine-grained CAIs, and CA chondrules are shown for comparison. It is evident from the data plotted in Fig. 4a and b that with the exception of the olivine-rich POI Redeye, the bulk compositions of POIs are quite distinct from those of Types B and C CAIs and ferromagnesian chondrules. Relative to coarse-grained CAIs, the POIs are enriched in Na, Mg, and Si and depleted in Al and Ca. All POIs have CaO contents <18%, whereas in Types B and C CAIs, CaO is always >18%. The bulk compositions of some POIs fall within the range of compositions exhibited by CA chondrules, but, as a group, POIs are distinguished from CA chondrules by lower contents of Na_2O , SiO_2 , and FeO. POIs are also readily distinguished from CA chondrules by their characteristic mineralogy, as will be discussed below.

Most POIs contain much higher Na_2O than coarse-grained CAIs. The analyses of plagioclase compositions and modal abundances of POIs indicate that a significant portion (10–50%) of the Na_2O can be attributed to the albite component in plagioclase (An_{82} – An_{98}). In POIs with the highest Na_2O contents, a large fraction of the Na is contained in the mesostasis. As will be discussed later, these mesostasis regions are believed to be primary. In contrast to Type B CAIs, only a minor amount of the Na_2O in POIs is present in secondary phases such as nepheline and sodalite.

Mineral Chemistry

Plagioclase

Plagioclase compositions (Table 3) in POIs range from An_{82} to An_{98} , with An_{95} the most frequently observed composition. Plagioclase contains small amounts of MgO (0.25–0.92 wt%) and FeO (0–0.4 wt%) but no K_2O . Both Na_2O and MgO contents of plagioclase in POIs are higher than typically found in plagioclase in Type B CAIs, but the positive linear correlation between Mg and Na contents in plagioclase (Fig. 5) is similar to that found in Type B CAIs (HUTCHEON et al., 1978). No correlation between Fe and either Mg or

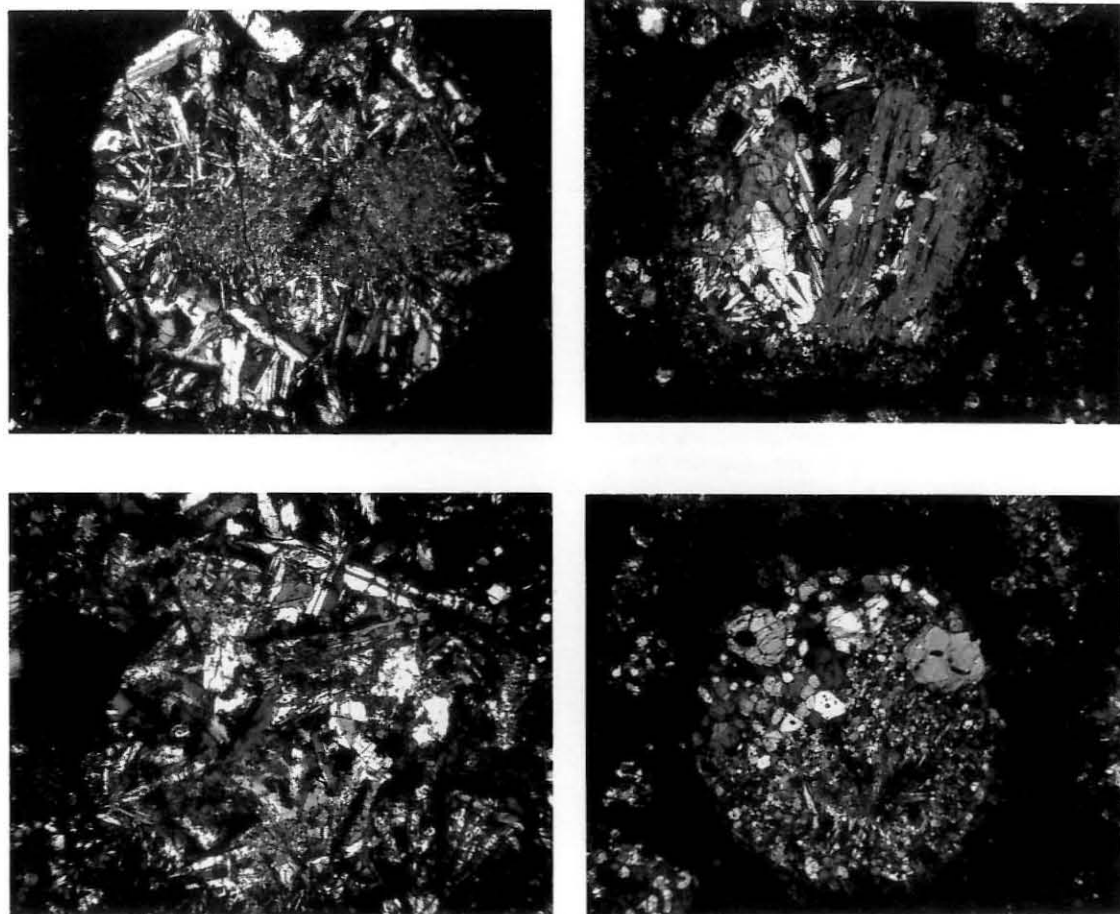


FIG. 1. Transmitted light photomicrographs of POIs: (a) USNM 3510 showing a coarse-grained mantle of plagioclase and olivine surrounding a fine-grained core of plagioclase, olivine, spinel, enstatite, and sapphirine; (b) 5ALLB6 showing coarse plagioclase laths and olivine grains; (c) BG82CLI displaying a texture similar to that of a barred-olivine chondrule with the addition of plagioclase laths distributed between olivine bars; (d) BG82CLJb showing a porphyritic texture with several coarser grained olivines among finer olivines and pyroxenes with plagioclase and spinel distributed near the core of the inclusion; (e) radiating texture in BG82CLJa with pyroxene and plagioclase phenocrysts crystallized inward from the rim transitioning into radiating crystals towards the core—The field of view in the above photomicrographs is 4×3.2 mm; (f) backscattered electron image of POI BG82CLII showing a cluster of granular olivines embayed near the rim of the inclusion. Other phases in this inclusion are Al-enstatite, plagioclase, spinel, and sapphirine. The scale bar is $10 \mu\text{m}$.

Na in POI plagioclase was observed. Within each POI, plagioclase compositions are nearly constant with only a subtle increase of ≤ 1 wt% Na_2O . Alteration of plagioclase crystals by low-temperature phases such as sodalite and nepheline is not observed except near cracks and near the rims of inclusions.

Olivine

Olivine compositions are highly variable among the different POIs, but are generally forsteritic, ranging from Fo_{63} to Fo_{99} (Table 4). Individual grains in the interior of POIs are only slightly zoned, with rims that are marginally higher in Fe content. The difference in FeO content between center

and rim occasionally reaches 5 wt% but is generally less than 1%. The more Fe-rich olivines (Fo_{63} to Fo_{85}) are consistently found in olivine clusters embayed near the exterior margin of many POIs. These spherical clusters of equigranular grains (Fig. 1f) are very similar in appearance and composition to granular olivine chondrules. In contrast to interior olivines, the cluster olivines are strongly zoned in FeO with more Fe-rich rims. The difference in FeO content between center and rim of individual grains typically exceeds 5%. The contrast in composition, in terms of both the maximum FeO content and the magnitude of core-to-rim zonation, between olivine phenocrysts and granular olivines in the clusters is clearly shown in Fig. 6. However, other than their high FeO content, there is no significant difference in their chemistry and Mg

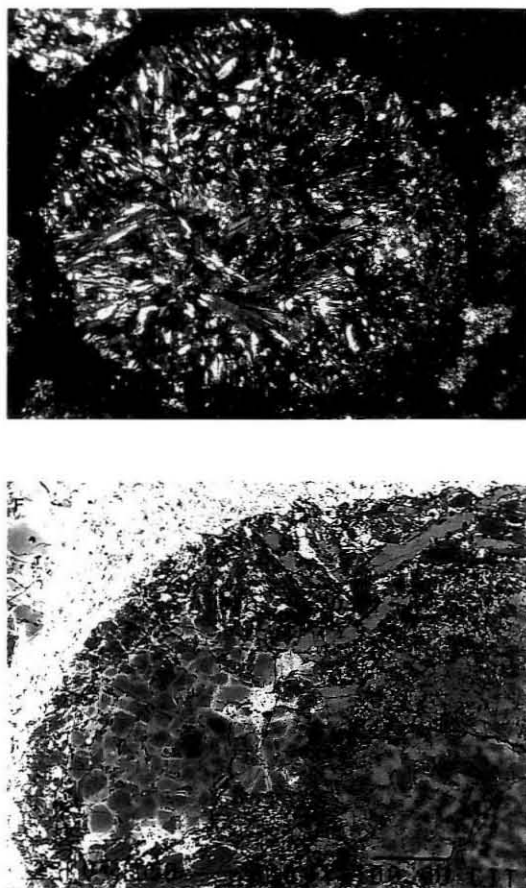


FIG. 1. (Continued)

isotopic composition with respect to the olivine grains in the interior of the POIs.

Spinel

Spinel in POIs are Mg-rich, generally containing less than 4% FeO. Iron contents of spinels within an individual POI can be variable, and individual spinel grains are also zoned in FeO. In most cases the center of the grain contains less than 2% FeO. Within individual spinel the variation of FeO content from core to rim is generally less than 2%, but in rare cases, such as in POI BG82CLII, the difference can be as high as 5%. In contrast to spinels in CAIs, which commonly contain less than 0.2 wt% Cr₂O₃ (WARK, 1983), the spinels in POIs have higher Cr₂O₃ contents, generally over 1% and as high as 5%. Spinel in 5ALLB6 have the widest range of Cr₂O₃ content, ranging from 0.2 to 10%. A distinguishing characteristic of spinel in 5ALLB6 is the presence of 1–2 μm wide Cr-rich (Cr₂O₃ > 5%) mantles or overgrowths on Cr-poor (Cr₂O₃ < 0.5%) cores. A gradation of Cr₂O₃ content between core and mantle is shown in Fig. 7. The low-Cr cores

usually have a corroded appearance, whereas the Cr-rich mantles assume euhedral to subhedral forms (Fig. 2c). Spinel in the unique POI Redeye contains 20–30 wt% Cr₂O₃. The Cr₂O₃ content of all spinels in POIs is unrelated to the amount of FeO. Representative spinel analyses are given in Table 5.

Pyroxene

POIs contain a variety of different pyroxenes, including Al-, Ti-bearing fassaite, diopside, Al-rich enstatite and Fe-poor pigeonite (Table 6). Several different pyroxenes may occur in individual POIs, especially in group 2 and 3 POIs. For example, in BG82CLJa, B14D, and ADEL-1 either enstatite or pigeonite is mantled by diopside. Fassaite is a major phase in four of the six group 1 POIs but is uncommon in groups 2 and 3 POIs. Most fassaites are zoned with respect to Ti and Al and typically exhibit a linear relationship between the Al₂O₃ and TiO₂ contents. The data plotted in Fig. 8 reveal a bimodal distribution of Al₂O₃/TiO₂ ratios among POI fassaites that clearly distinguishes fassaites in POIs from those in Type B1 CAIs. One population, typically found in POIs containing Ti-rich oxide minerals, is composed of fassaites with roughly equal Al₂O₃ and TiO₂ contents. This 1:1 ratio between Al₂O₃ and TiO₂ is not found in fassaites in other types of CAIs but is characteristic of pyroxenes in armalcolite-bearing lunar rocks (SUNG et al., 1974). A second population, generally found in POIs together with Al-rich enstatite, pigeonite, and diopside, is characterized by lower TiO₂ content

Table 1
PETROGRAPHIC FEATURES OF POI*

INCLUSION	DIAMETER (mm)	TEXTURE	MAJOR PHASES	MINOR PHASES [†]
Group 1				
ALAI-2	1.7	sub-ophitic	pl,fas,ol,sp	arm,ilm
V477	2.1	sub-ophitic	pl,fas,sp,ol	
5ALLB6	2.7	sub-ophitic	pl,ol,fas,sp	arm,ru,ilm, zir,pv
BG82DH2	1.5	sub-ophitic	pl,ol,fas,sp,pi	arm,ru,ilm
3510	2.1	sub-ophitic	pl,ol,sp,en	fas,sap
BG82CLII	1.5	porphyritic and radiating	pl,sp,en,mes	sap
Group 2				
BG82DHIA	4.0	sub-ophitic	pl,ol,fas,di,sp	
B14D	2.0	sub-ophitic	pl,ol,pi,di,sp	
LEO1009	0.6	porphyritic	pl,pi,sp	gl
SA-1	2.3	sub-ophitic	pl,di,pi,sp,ol	ilm
ADEL-1	0.5	sub-ophitic	pl,ol,sp,di,en	
BG82CHII	2.2	sub-ophitic	pl,di,ol,en	sp
BG82CLJa	1.8	porphyritic and radiating	pl,en,pi,di,mes	sp
SA-1b	0.8	porphyritic	pl,ol,en	
PPX	0.9	poikilitic	pl,ol,en	sp
Group 3				
A-47	2.1	barred with interstitial ol and di	ol,pl,fas,sp	
BG82CLJb	1.5	porphyritic	ol,pl,sp,pi,fas	
BG82CLJb	1.5	granular	ol,di,pl,pi	
BG82CLJ	1.9	barred with interstitial ol and di	ol,pl,en,di	
REDEYE	4.8	porphyritic	ol,pl,di	en,sp

* arm - armalcolite, di - diopside, en - enstatite, fas - fassaite, gl - glass, il - ilmenite, mes - mesostasis, ol - olivine, pi - pigeonite, pl - plagioclase, pv - perovskite, ru - rutile, sap - sapphirine, sp - spinel, zir - zirconolite.

[†] minor mesostasis is present in all POI.

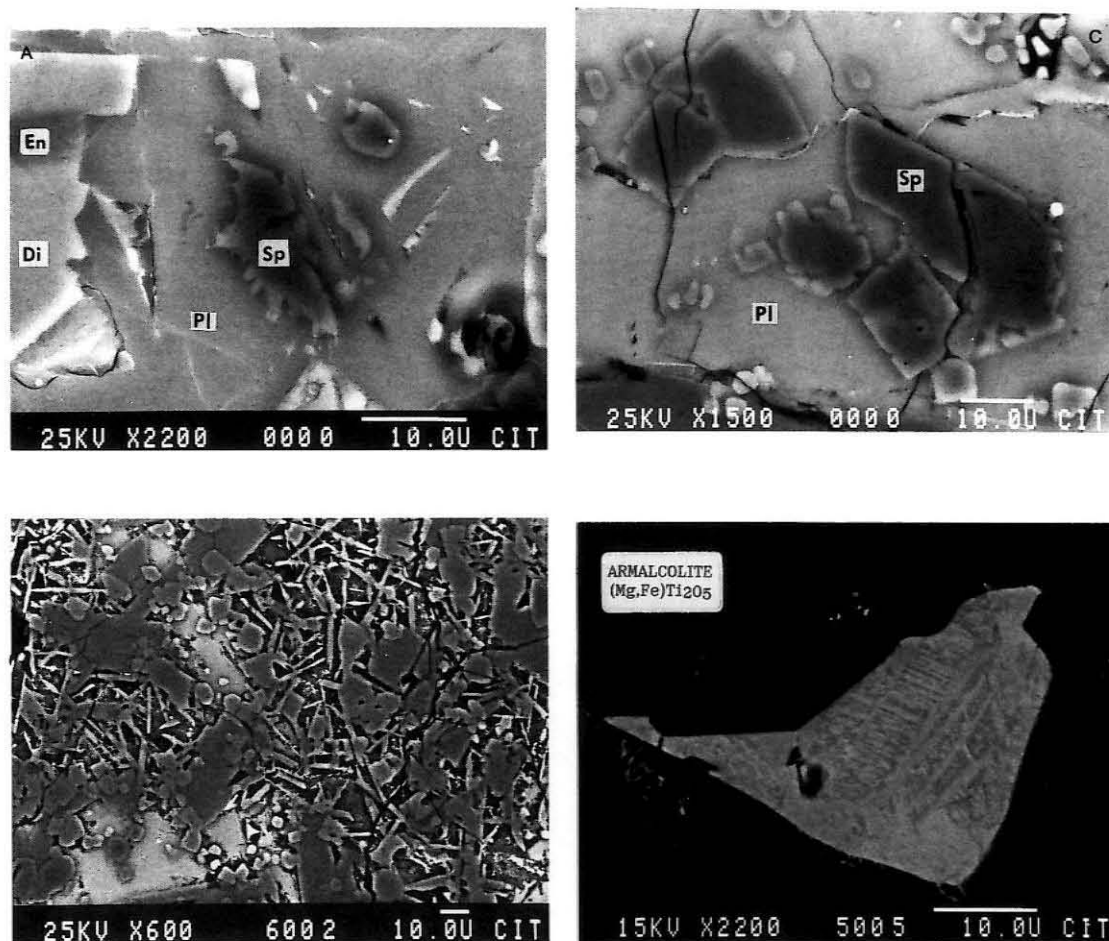


FIG. 2. (a) Backscattered electron (BSE) image of ADEL-1 showing strongly resorbed spinel (Sp) with a serrated boundary included in plagioclase (Pl). (b) BSE image of randomly oriented, prismatic sapphirine crystals ($\sim 2 \times 20 \mu\text{m}$) embedded in a Na-rich mesostasis in BG82CLII. Also shown are sub-rounded spinels, aluminous-enstatite (rectangular laths), and plagioclase (light grey). (c) BSE image of 5ALLB6 showing several resorbed Cr-poor spinels mantled by Cr-rich spinel. Chromium-rich spinel appears as light colored rims on host spinels and as individual, light colored, micron size crystals. Spinels are enclosed in plagioclase. (d) BSE image of an armalcolite crystal in 5ALLB6 displaying the fine lamellae of rutile, ilmenite, and Mg-enriched armalcolite resulting from the subsolidus breakdown of the armalcolite grain. The armalcolite is interstitial to plagioclase and fassaite. The scale bar is $10 \mu\text{m}$ in all micrographs.

and much higher $\text{Al}_2\text{O}_3/\text{TiO}_2$ ratios. The more Al-rich fassaite of this population have compositions that fall within the range of fassaite compositions in Types B2 and C CAIs (WARK, 1987). Fassaite in POIs are also distinguished from those in Types B2 and C CAIs by their high MnO content, which is typically between 0.1 and 0.4%, but may be as high as 1.0%. Fassaite pyroxenes with similar MnO content have been found in Al-rich chondrules (BISCHOFF et al., 1989).

Calculations of Ti^{3+} versus Ti^{4+} in Ti-rich fassaite, made by assuming pyroxene stoichiometry, suggest that 60–80% of the total Ti is trivalent, similar to fassaite in Type B CAIs. Such ratios suggest that POIs formed in a reducing environment ($f_{\text{O}_2} \sim 10^{-17}$ at 1300°C) similar to that inferred for CAIs (STOLPER, 1982; BECKETT, 1986).

Armalcolite

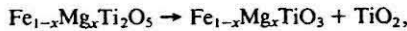
Three group 1 POIs (5ALLB6, BG82DH2, ALA1-2) contain armalcolite, accompanied by the Ti-rich oxides rutile, ilmenite, perovskite, and zirconolite. The composition of armalcolite in POIs differs from the ideal formula ($\text{Mg}_{0.5}\text{Fe}_{0.5}\text{Ti}_2\text{O}_5$) in that the Mg/Fe ratio is much higher, ranging from 1.2 to 4.3 (Table 7). This ratio is also much different from that characteristic of armalcolite in lunar and terrestrial rocks, in which the Mg/Fe ratios range from 0.36 to 0.49 (HAGGERTY, 1973; PEDERSEN, 1981). One group 2 POI (SA-1) also contains armalcolite (BOCTOR et al., 1989), but its composition is quite different from that of the armalcolite in group 1 POIs. Whereas an ilmenite rim sur-

	Na ₂ O	MgO	Al ₂ O ₃	SiO ₂	K ₂ O	CaO	TiO ₂	Cr ₂ O ₃	FeO	SUM
ALA1-2	2.9	10.0	32.0	38.4	0.1	12.8	1.5	0.3	1.5	99.5
V477	1.9	11.1	27.6	39.0	n.d.	16.8	1.8	0.4	1.2	99.8
5ALLB6	1.4	13.7	31.6	38.1	n.d.	12.6	0.9	0.6	0.6	99.5
BG82DH2	1.5	14.9	30.9	38.1	0.1	11.3	0.7	0.3	1.7	99.5
3510	2.0	11.5	29.6	41.6	<0.1	12.4	0.4	0.3	1.5	99.3
BG82CLII	3.8	18.1	36.8	31.6	0.1	4.0	0.7	0.9	2.9	98.9
BG82DH1A	0.7	20.9	24.7	38.9	n.d.	11.4	0.1	n.d.	3.5	100.0
B14D	3.6	13.4	25.7	42.9	0.1	10.1	0.7	0.2	1.6	98.3
LEO1009	1.2	11.6	22.9	47.5	<0.1	9.3	0.9	0.6	4.8	98.8
SA-I	4.1	11.6	18.5	46.2	0.1	14.7	1.2	0.4	1.9	98.7
ADEL-1	0.9	9.6	18.4	50.7	n.d.	13.8	0.7	0.5	4.6	99.2
BG82CH1	3.6	15.0	17.3	45.8	0.2	11.0	0.7	0.5	3.5	97.6
BG82CLJa	6.8	14.3	17.3	45.5	0.2	9.6	1.3	0.5	2.4	97.9
SA-1b	5.8	19.9	18.1	43.1	0.5	5.1	0.7	0.5	5.2	98.9
PPX	2.4	24.1	15.2	43.5	0.1	5.8	0.4	0.5	6.5	98.5
A-47	1.3	33.1	13.7	42.2	n.d.	6.6	0.3	0.3	1.8	99.3
BG82CLJb	1.3	34.0	15.6	38.8	n.d.	4.3	0.3	0.6	4.1	99.0
BG82CLIB	1.2	28.5	12.6	43.5	n.d.	6.2	0.2	0.4	5.2	97.8
BG82CLI	2.0	31.6	12.4	40.9	0.1	5.9	0.4	0.3	4.8	98.4
REDEYE	1.0	44.6	3.9	41.7	0.1	2.3	0.1	0.4	5.6	99.7

* EDS analysis by raster scan of the POI in the thin section.

n.d. - not detected

rounding armalcolite is commonly observed in lunar basalts (EL GORESY, 1976), no rims are found on the armalcolite in POIs. Armalcolite in 5ALLB6 exhibits submicron lamella of armalcolite, rutile, and ilmenite (Fig. 2d), indicating the breakdown of armalcolite by the reaction



where x is between 0 and 1. This reaction is rarely observed in lunar and terrestrial samples and may provide information on the low-temperature subsolidus history of POIs.

Zirconolite

Zirconolite ($\text{CaZrTi}_2\text{O}_7$) occurs as micron-size, irregularly shaped blebs surrounding a small, $3 \mu\text{m}$ perovskite crystal in an interstitial region between plagioclase and olivine in POI 5ALLB6. Electron probe wavelength dispersive analyses of the zirconolite total only to 90 wt%, including 4.38% Y_2O_3 and 0.92% CeO (other REEs were not analyzed). Using a

long counting time with the EDS we have identified the presence of Nd, Gd, Dy, Er, and Yb. If the abundances of these elements are similar to those in lunar zirconolites (HAGGERTY, 1973; MEYER and BOCTOR, 1974), these REEs would comprise the missing components in the electron probe analysis. The major differences in composition between terrestrial, lunar, and POI zirconolites appear to be in their Ca and Fe contents. Terrestrial zirconolites show high CaO (>10%) and FeO (5%) (LORAND and COTTIN, 1987), lunar zirconolites show high FeO (10%) and low CaO (<3%), whereas zirconolite in the POIs has moderate CaO (5%) and very low FeO (0.2%). The low FeO in the Allende zirconolite appears to be related to the very low concentration of Fe in the inclusion.

Oxide wt. %	5ALLB6*	3510*	BG82DH2*	BG82CLII*	A-47*	BG82DH1A*
Na ₂ O	0.26	0.54	0.50	0.75	0.77	0.44
MgO	0.25	0.39	0.44	0.26	0.56	0.59
CaO	19.43	19.15	19.14	18.81	18.27	19.21
FeO	0.11	0.10	0.12	0.36	0.19	0.21
Al ₂ O ₃	35.95	35.85	35.43	33.98	34.94	36.51
SiO ₂	43.34	44.64	44.08	45.33	44.86	43.64
SUM	99.34	100.67	99.71	99.49	99.59	100.60
An	97	94	95	94	91	95

* WDS analysis

* EDS analysis

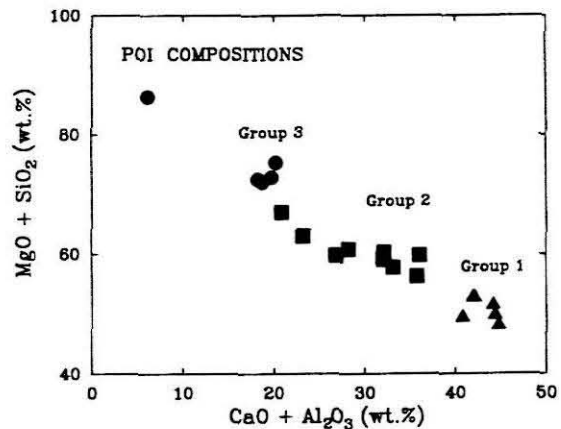


FIG. 3. Difference in the amount of $\text{CaO} + \text{Al}_2\text{O}_3$ versus $\text{MgO} + \text{SiO}_2$ among the three petrographic groups of POIs. The compositional variation from high $\text{CaO} + \text{Al}_2\text{O}_3$ to high $\text{MgO} + \text{SiO}_2$ reflects changes in the modal mineralogy of POIs from spinel-rich group 1 to olivine-rich group 3.

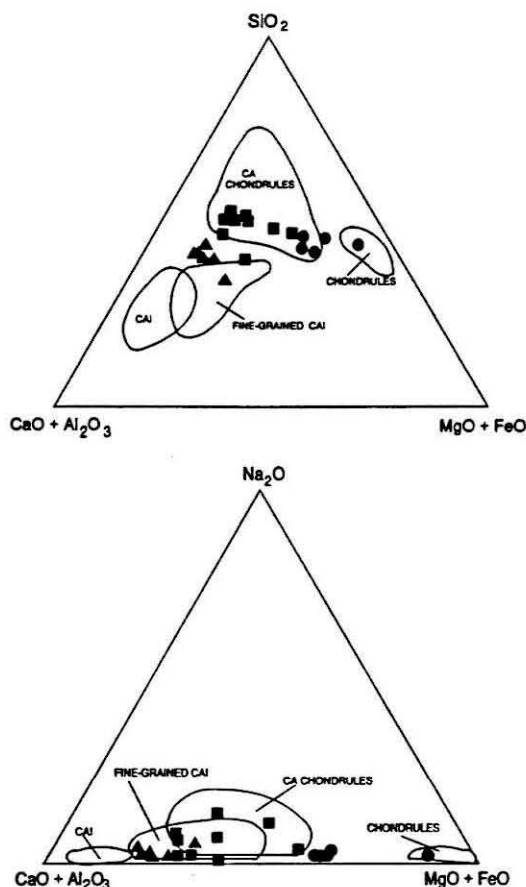


FIG. 4. Two representations of the bulk compositions of POIs (filled symbols) compared with the compositional ranges of CAIs, fine-grained CAIs, ferromagnesian chondrules, and CA chondrules. Filled triangles are group 1 POI, squares are group 2, and circles are group 3. POIs have lower $\text{CaO} + \text{Al}_2\text{O}_3$ content than CAIs but higher SiO_2 (a) and Na_2O (b). Their compositions overlap with fine-grained CAIs and CA chondrules. Only the olivine-rich POI Redeye has a composition within the field of chondrules. Sources of data are: CAIs from MASON and MARTIN (1977) and MCSWEEN (1977); CA chondrules from BISCHOFF and KEIL (1984); fine-grained CAIs from BRIGHAM (1990) and MASON and MARTIN (1977); ferromagnesian chondrules from MCSWEEN (1977).

Sapphirine

Sapphirine was observed in the two Allende POIs BG82CLII and 3510. This is the first reported meteoritic occurrence of sapphirine. The composition of sapphirine, calculated from the average composition from four electron probe analyses (cf. Table 8), is



and deviates from the ideal formula, $\text{Mg}_2\text{Al}_4\text{SiO}_{10}$. Variations in sapphirine compositions attributed to the coupled substitution of Mg and Si for Al have been observed in terrestrial samples, and a number of different formulae have been proposed (DEER et al., 1978). Terrestrial sapphirine closely ap-

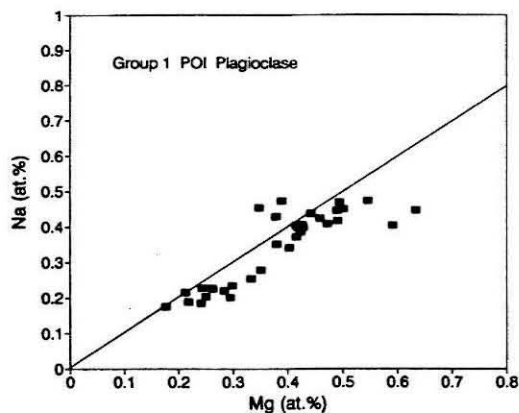


FIG. 5. Electron probe wavelength dispersive (WDS) analyses of Na and Mg contents of plagioclases in POIs 3510, 5ALLB6, and BG82DH2. The data show that the Na and Mg contents in these plagioclases are linearly related; similar behavior has been observed in plagioclase in Type B CAIs (HUTCHEON et al., 1978).

proaches a solid solution series between $\text{Mg}_8\text{Al}_{16}\text{Si}_4\text{O}_{40}$ and $\text{Mg}_7\text{Al}_{18}\text{Si}_3\text{O}_{40}$. However, the composition of sapphirine in the POIs appears to be higher in MgO and SiO_2 than terrestrial sapphirine (Table 8). A significant difference in minor element abundances between Allende and terrestrial sapphirine is also observed. Allende sapphirine has much higher concentrations of TiO_2 and Cr_2O_3 , presumably due to the higher abundance of these elements in the inclusions. Synthetic sapphirine crystallized from a melt whose composition approximates compositions of sapphirine-bearing POIs (SHENG et al., 1991) is also enriched in MgO and SiO_2 relative to the ideal sapphirine composition and has a composition corresponding to $\text{Mg}_{2.12}\text{Ca}_{0.01}\text{Al}_{3.74}\text{Si}_{1.10}\text{Ti}_{0.01}\text{O}_{10}$, very similar to that of natural POI sapphirine.

Glass and mesostasis

Many POIs contain optically isotropic or very fine-grained regions in their interiors. These areas are localized either in

Table 4
REPRESENTATIVE OLIVINE COMPOSITIONS*

Oxide wt. %	5ALLB6*	5ALLB6*	3510*	B14D*	B14D*	BG82CH1*
MgO	56.24	50.02	56.44	55.75	45.27	56.57
CaO	0.38	0.25	0.08	0.17	0.13	0.40
MnO	0.27	0.14	0.05	0.08	0.12	0.07
FeO	1.11	9.97	0.68	2.05	15.70	1.11
NiO	0.01	0.02	n.d.	0.03	0.09	n.a.
Al_2O_3	0.09	0.06	0.13	0.02	n.d.	0.13
Cr_2O_3	0.20	0.03	0.42	0.04	0.03	0.23
SiO_2	42.29	40.79	42.14	42.39	39.89	42.29
TiO_2	0.22	0.05	0.29	0.13	0.07	0.09
SUM	101.31	101.34	100.23	100.66	101.30	100.89
Fo	98	90	99	98	84	98

* WDS analysis
n.a. - not analyzed
* cluster olivine
* interior olivine

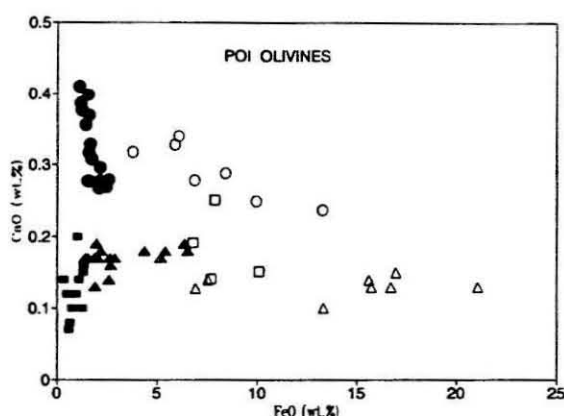


FIG. 6. Representative WDS analyses showing CaO versus FeO contents of olivines in three POIs. Filled symbols are analyses of olivine phenocrysts in the interior of POIs, and open symbols are analyses of granular olivines located in the clusters embayed at the rims of POIs (see Fig. 1f). Circles represent olivines of 5ALLB6, triangles represent B14D, and squares are 3510. Olivines in the interior of POIs are characterized by lower FeO, in contrast to the much higher and variable FeO content of olivines in the clusters. Within an individual POI, CaO contents of both occurrences of olivine are, however, similar.

interstitial regions or as matrix surrounding randomly oriented euhedral silicates. There is no clear evidence of reaction at mesostasis-crystal contacts. These areas contain very high Na_2O (>10%) and in extreme cases can account for 90% of the total Na content in the bulk POI. SiO_2 is also high in the mesostasis, but CaO is depleted relative to the bulk composition of the inclusion. The composition of a residual melt derived by subtracting all the major phases from the bulk composition of the POI is similar to the composition of the mesostasis, suggesting that the mesostasis regions are the product of fractional crystallization rather than low-temperature metamorphism.

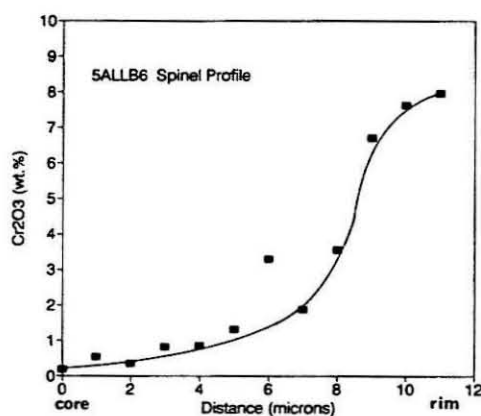


FIG. 7. Variation of Cr content between the Cr-rich rim and the Cr-poor core of a crystal in 5ALLB6 (cf. Fig. 2c). The data indicate the Cr-rich overgrowth is only 1–2 μm wide, with little diffusion of Cr into the interior of the host spinel.

Table 5
REPRESENTATIVE SPINEL COMPOSITIONS

Oxide wt. %	5ALLB6*	5ALLB6*	BG82CLII*	BG82CLII*	BG82DH2*	BG82DH1A*
MgO	27.89	27.01	26.57	21.17	26.01	25.53
CaO	0.06	0.00	0.10	0.13	0.12	0.22
FeO	0.95	1.19	0.70	8.87	2.55	3.29
Al_2O_3	69.65	58.34	69.77	65.41	68.46	69.15
V_2O_5	0.38	0.69	0.09	n.d.	0.43	0.22
Cr_2O_3	0.59	9.76	1.26	1.69	0.83	0.95
SiO_2	0.00	0.00	0.46	0.71	n.d.	0.37
TiO_2	0.43	2.94	0.33	0.72	0.71	0.19
SUM	99.95	99.93	99.28	98.70	99.11	99.92
Number of cations normalized to 6 oxygens						
Mg	0.994	0.999	0.951	0.793	0.942	0.919
Ca	0.002	0	0.003	0.003	0.003	0.006
Fe	0.019	0.025	0.014	0.186	0.052	0.066
Al	1.962	1.706	1.974	1.936	1.960	1.967
V	0.007	0.014	0.002		0.008	0.004
Cr	0.011	0.191	0.024	0.033	0.016	0.018
Si	0	0	0.011	0.018		0.009
Ti	0.008	0.055	0.006	0.014	0.013	0.003
SUM	3.002	2.990	2.983	2.984	2.995	2.993

* EDS analysis

* WDS analysis

Magnesium Isotopic Data

The Mg isotopic data were obtained on several different crystals of the major phases in each of the POIs studied. The purpose was to establish the presence of isotopic effects due to either mass-dependent fractionation, general nonlinear effects, or radiogenic $^{26}\text{Mg}^*$ from ^{26}Al decay. During the course

Table 6
REPRESENTATIVE PYROXENE COMPOSITIONS

Oxide wt. %	5ALLB6*	3510*	B14D*	BG82CLJa*	BG82DH2*	ALA1-2*
MgO	13.13	34.97	31.40	21.75	33.78	14.69
CaO	23.38	0.43	4.47	16.24	1.91	22.41
MnO	n.a.	n.d.	0.10	0.40	0.50	n.a.
FeO	0.19	0.44	0.92	1.16	1.02	0.22
Al_2O_3	10.57	7.82	5.70	3.86	3.64	9.55
V_2O_5	0.33	n.d.	0.30	n.d.	0.10	n.d.
Cr_2O_3	0.71	0.50	0.70	1.10	1.30	0.30
SiO_2	42.75	53.14	53.59	52.00	53.95	44.20
TiO_2	10.75	2.14	1.45	2.93	3.08	8.55
SUM	101.81	99.44	98.63	99.44	99.18	99.92
Number of cations normalized to 6 oxygens						
Mg	0.706	1.768	1.623	1.162	1.737	0.797
Ca	0.903	0.016	0.166	0.624	0.071	0.874
Mn			0.003	0.015	0.013	
Fe	0.006	0.012	0.024	0.020	0.016	0.007
Al	0.449	0.313	0.233	0.163	0.148	0.410
V	0.010		0.008		0.003	
Cr	0.020	0.013	0.019	0.031	0.035	0.009
Si	1.542	1.803	1.859	1.865	1.862	1.610
Ti	0.292	0.055	0.038	0.079	0.080	0.237
SUM	3.928	3.980	3.973	3.959	3.966	3.944
Ti^{3+} %	75					71

* EDS analysis

* WDS analysis

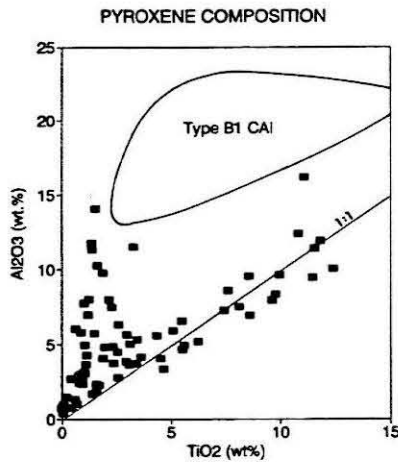


FIG. 8. Plot of Al_2O_3 versus TiO_2 showing the bimodal distribution of pyroxene compositions in POIs. Titanium-rich pyroxenes plot along the 1:1 line. A second group, characteristic of the Ti-poor pyroxenes in POIs, shows much higher $\text{Al}_2\text{O}_3/\text{TiO}_2$ ratios. A comparison with fassaites of Type B1 CAIs (WARK, 1987) shows that fassaitic pyroxenes in POIs are compositionally distinct with much lower Al_2O_3 contents.

of these analyses it became clear that particular attention to the isotopic homogeneity of POIs was required. Measurements on spinel, olivine, pyroxene, and plagioclase are summarized in Tables 9 and 10.

The most striking feature of the isotopic data is the extent of Mg isotopic heterogeneity within and among the POIs. Seven of the fourteen inclusions examined in this study exhibit variations in F_{Mg} among coexisting phases. (POI SA-1,

Oxide wt. %	5ALLB6*	BG82DH2*	ALA1-2*	Lunar*	Disko†
MgO	10.68	16.99	13.75	6.93	8.40
CaO	0.98	2.41	0.69	0.32	0.10
MnO	n.a.	n.a.	n.a.	0.16	0.55
FeO	6.80	6.37	2.49	15.08	13.50
Al_2O_3	1.21	1.57	3.78	1.61	1.25
V_2O_5	1.41	0.60	0.96	n.a.	n.a.
Cr_2O_3	3.68	0.83	0.26	2.44	0.22
SiO_2	0.51	1.10	1.40	0.32	0.10
TiO_2	74.23	70.25	76.67	74.82	75.20
ZrO_2	0.30	n.a.	n.a.	<0.05	0.11
SUM	99.00	100.12	99.60	101.73	99.43
Number of cations normalized to 5 oxygens					
Mg	0.553	0.870	0.685	0.363	0.446
Ca	0.036	0.089	0.025	0.012	0.004
Mn				0.041	0.019
Fe	0.198	0.183	0.070	0.407	0.401
Al	0.050	0.064	0.149	0.067	0.053
V	0.039	0.017	0.026		
Cr	0.101	0.023	0.007	0.068	0.006
Si	0.018	0.038	0.047	0.011	0.004
Ti	1.941	1.815	1.927	1.976	2.017
Zr	0.005			0.001	0.002
SUM	2.941	3.099	2.936	2.946	2.952

* WDS analysis
Data from: † Haggerty (1973); ‡ Pedersen (1981); † This study.

Oxide wt. %	BG82CLII	3510	Finero	Mauson
MgO	23.58	23.13	21.5	19.89
CaO	0.15	0.22	0.52	1.13
MnO	0.12	n.d.	0.04	n.a.
FeO	0.52	0.27	3.90	3.16
Al_2O_3	53.92	53.86	58.0	54.77
V_2O_5	0.06	0.15	n.a.	n.a.
Cr_2O_3	1.89	1.12	n.a.	n.a.
SiO_2	19.49	18.50	16.0	16.71
TiO_2	1.60	2.30	0.01	0.67
SUM	101.33	99.55	98.97	96.33
Number of cations normalized to 10 oxygens				
Mg	2.010	2.003	1.880	1.800
Ca	0.009	0.014	0.033	0.073
Mn	0.006		0.003	
Fe	0.025	0.013	0.190	0.160
Al	3.634	3.688	4.010	3.918
V	0.003	0.007		
Cr	0.085	0.051		
Si	1.115	1.075	0.939	1.014
Ti	0.069	0.101	0.001	0.031
SUM	6.956	6.952	7.055	6.986

* This study; average of 4 WDS analyses;
† EDS analysis; ‡ sapphirine in hornblende-granulitic facies rock from Italian Alps (Lensch, 1971); § sapphirine from Antarctica (Segnit, 1957).

studied by KENNEDY et al., 1991, also contains internal variations in F_{Mg} but is excluded from the present discussion.) The predominant isotopic effect, present in seven POIs, is a

SAMPLE	F_{Mg} † ±2σ mean	$\delta^{26}\text{Mg}$ ‡ ±2σ mean	$^{27}\text{Al}/^{26}\text{Mg}$ ±2σ mean
plagioclase			
5ALLB6 plag1	1.5 ± 3.3	6.0 ± 5.6	173 ± 5
5ALLB6 plag2	0.5 ± 1.8	2.2 ± 2.3	161 ± 5
5ALLB6 plag3	0.9 ± 1.3	4.2 ± 3.1	222 ± 5
5ALLB6 plag4	1.5 ± 1.7	1.2 ± 3.9	130 ± 5
BG82CLII plag1	1.4 ± 1.5	-0.1 ± 2.1	78 ± 5
B14Dplag1	1.0 ± 1.3	2.3 ± 2.2	85 ± 5
B14D plag2	2.2 ± 1.8	1.3 ± 3.0	159 ± 5
3510 plag1	†	4.3 ± 2.3	59 ± 5
3510 An 1*	-3.0 ± 1.8	5.0 ± 3.0	98 ± 5
3510 An 2-1*	0.5 ± 2.4	6.0 ± 4.0	128 ± 5
3510 An 2-2*	-2.1 ± 1.8	7.0 ± 3.0	103 ± 5
3510 An 2-3*	-2.0 ± 2.2	3.0 ± 4.0	86 ± 5
3510 An 5*	-2.2 ± 2.0	2.0 ± 4.0	114 ± 5
BG82DH2 plag1	†	3.3 ± 1.9	62 ± 5
BG82DH2 plag2	1.2 ± 1.3	1.0 ± 2.3	87 ± 5
PPX plag1	8.0 ± 2.4	-2.1 ± 4.9	183 ± 5
PPX plag2	6.3 ± 1.8	0.0 ± 3.2	150 ± 5
V477 plag1	-3.0 ± 1.6	-0.4 ± 3.0	111 ± 5
ADEL-1	-3.0 ± 1.0	-1.1 ± 1.8	29 ± 5
BG82CH1 plag1	4.6 ± 1.4	-0.8 ± 2.4	35 ± 5
BG82CH1 plag2	3.7 ± 1.6	0.3 ± 2.6	40 ± 5
BG82CH1 plag3	4.8 ± 1.4	1.2 ± 2.5	39 ± 5
ALA1-2 plag1	-3.3 ± 1.3	-0.6 ± 4.9	178 ± 5
BG82CLII plag1	1.8 ± 1.5	-0.1 ± 2.1	78 ± 5
REDEYE plag1†	0.5 ± 2.1	1.3 ± 0.9	

* Data from Hutcheon (1982); † Data from Papanastassiou et al. (1984)
† F_{Mg} values not calculated.

Table 10
Mg ISOTOPIC COMPOSITIONS OF
OTHER PHASES

SAMPLE	F_{Mg} ‰ ±2σ mean	$\delta^{26}Mg$ ‰ ±2σ mean
olivine		
5ALLB6 ol1	-1.3 ± 0.8	0.9 ± 1.9
BG82CLJb ol1	-0.8 ± 1.0	0.6 ± 1.9
BG82CLJb ol2	-0.4 ± 1.2	0.1 ± 2.0
3510 ol1	0.3 ± 0.7	-2.1 ± 1.3
3510 ol*	0.4 ± 1.0	2.5 ± 1.2
3510 ol*	-0.8 ± 1.2	-0.8 ± 1.4
BG82DH2 ol1	-1.3 ± 0.8	2.4 ± 1.5
PPX ol1	-1.2 ± 0.8	-1.7 ± 1.5
BG82CLII ol1	-1.5 ± 0.9	0.9 ± 1.5
BG82CLJa ol1	1.0 ± 0.7	0.3 ± 1.2
ADEL-1 ol1	1.0 ± 0.9	-0.5 ± 1.6
REDEYE ol1	2.6 ± 1.1	-1.1 ± 0.2
REDEYE ol2	0.7 ± 1.8	-0.4 ± 0.2
spinel		
5ALLB6 sp1	6.4 ± 0.9	3.1 ± 1.8
5ALLB6 sp2	6.0 ± 1.1	0.0 ± 1.9
5ALLB6 sp3	3.7 ± 1.1	3.6 ± 1.8
5ALLB6 sp4	4.6 ± 1.0	0.1 ± 1.6
5ALLB6 sp5	4.2 ± 1.3	1.8 ± 2.1
5ALLB6 sp6	5.1 ± 1.0	0.5 ± 2.2
5ALLB6 sp7	5.0 ± 1.1	-0.1 ± 2.2
BG82CLJb sp1	5.4 ± 1.2	0.2 ± 2.0
B14D sp1	1.4 ± 0.9	0.9 ± 1.6
B14D sp2	0.3 ± 1.0	0.3 ± 1.7
3510 sp1	1.9 ± 1.3	1.1 ± 2.3
BG82DH2 sp1	4.9 ± 0.9	0.9 ± 1.7
BG82DH2 sp2	4.4 ± 1.2	2.4 ± 2.1
ALA1-2 sp1	-7.0 ± 1.1	1.9 ± 1.9
ALA1-2 sp2	-0.3 ± 1.0	0.1 ± 1.7
ALA1-2 sp3	-4.1 ± 1.0	2.3 ± 1.8
ALA1-2 sp4	-4.0 ± 1.0	0.8 ± 1.7
BG82CLII sp1	11.1 ± 1.1	2.2 ± 2.0
BG82CLII sp2	7.2 ± 1.1	2.4 ± 2.1
BG82CLII sp3	8.6 ± 1.0	0.3 ± 1.9
BG82CLII sp4	8.4 ± 1.2	1.3 ± 2.0
ADEL-1 sp1	-3.3 ± 1.0	2.7 ± 1.8
ADEL-1 sp2	-1.0 ± 0.9	0.6 ± 3.0
LEO1009 sp1	1.7 ± 1.0	0.9 ± 1.7
LEO1009 sp2	2.1 ± 1.0	1.8 ± 1.6
pyroxene		
5ALLB6 px1	1.9 ± 0.9	3.3 ± 1.7
5ALLB6 px2	0.1 ± 1.0	3.0 ± 1.8
5ALLB6 px3	1.4 ± 2.4	-0.2 ± 4.0
5ALLB6 px4	5.2 ± 1.0	-0.3 ± 1.8
5ALLB6 px5	5.5 ± 1.2	-1.0 ± 2.0
5ALLB6 px6	4.0 ± 1.3	2.8 ± 2.1
BG82DH2 px1	2.1 ± 0.7	1.2 ± 1.1
BG82DH2 px2	3.9 ± 0.8	0.0 ± 1.4
ALA1-2 px1	-0.7 ± 0.9	1.5 ± 1.6
ALA1-2 px2	1.3 ± 0.9	-1.4 ± 1.6
BG82CLII px1	0.4 ± 0.9	3.2 ± 1.5
BG82CLII px2	1.8 ± 1.0	0.0 ± 1.7
BG82CLII px3	2.7 ± 0.9	-1.1 ± 1.6

* Data from Hutcheon (1982)

significant difference in F_{Mg} between spinel and coexisting silicates (Fig. 9a). Differences in F_{Mg} between silicate phases are found in three POIs (Fig. 9b), two of which also contain isotopically heterogeneous spinel. In four POIs (BG82CLII, 5ALLB6, BG82DH2, and BG82CLJb) spinel is enriched in the heavier Mg isotopes relative to silicates, whereas in two inclusions (ALA1-2 and ADEL-1) spinel is enriched in the lighter Mg isotopes. The total range in F_{Mg} , -8 to +11‰/

amu, is surprisingly large in view of the igneous textures of nearly all POIs and is much larger than the variation in F_{Mg} found in other (non-FUN) refractory inclusions. Within individual POIs, F_{Mg} in spinel is not constant but may vary by up to 7‰/amu. Spinels containing isotopically fractionated Mg are found in all three petrographic groups of POIs, but, in general, the most pronounced isotopic heterogeneity is found in those inclusions that have abundant spinel. For example, BG82CLII, which contains the most spinel (30%), also has the largest range in fractionation among its constituent phases, $-1 < F_{Mg} < 11$ ‰/amu. No correlation between F_{Mg} and spinel chemistry was observed. The evidence of Mg isotopic heterogeneity in silicate phases within POIs resembles that in spinels but occurs much less frequently. Variations in F_{Mg} among coexisting pyroxenes occur in two POIs, both

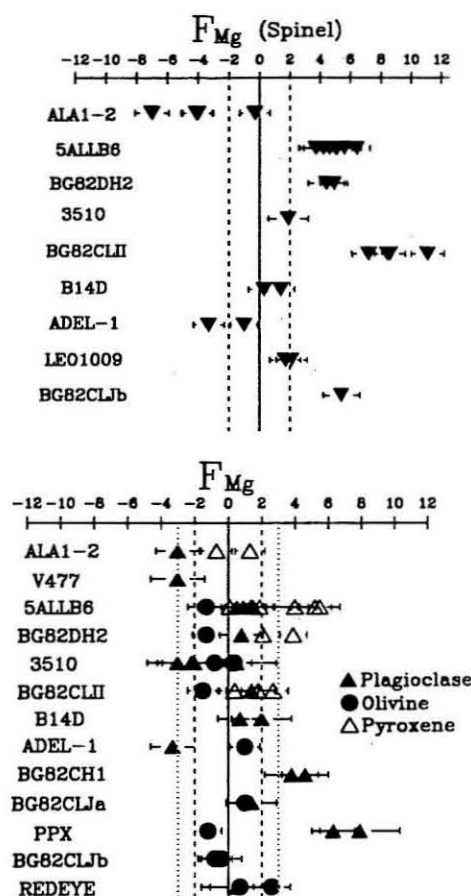


FIG. 9. Magnesium isotopic fractionation, F_{Mg} , plotted in permil per amu for (a) spinel and (b) pyroxene, olivine, and plagioclase from 14 POIs. Seven of the fourteen inclusions are isotopically heterogeneous. Spinel in six POIs exhibits enrichments in both the lighter (ALA1-2 and ADEL-1) and heavier (5ALLB6, BG82DH2, BG82CLII, and BG82CLJb) Mg isotopes, but F_{Mg} is always either positive or negative within an individual POI. Fractionation effects in pyroxene and olivine are comparable in magnitude but occur in only three POIs. Olivine has a normal Mg isotopic composition in all inclusions. The $2\sigma_{\text{mean}}$ error in F_{Mg} , based on the reproducibility of standards, is shown as the vertical dotted lines in (a) (spinel) and (b) (pyroxene), and as a dashed line in (b) (plagioclase).

belonging to petrographic group 1, while only one inclusion (PPX, a group 2 POI) contains plagioclase with a distinct F_{Mg} . Despite the scarcity, the magnitude of the differences in F_{Mg} among silicates is similar to that of differences between spinel and silicates. Fassaite pyroxenes in 5ALLB6 exhibit both the largest Mg fractionation and the greatest range of F_{Mg} among POI pyroxenes; F_{Mg} in fassaite ranges from 0 to 5.5‰/amu compared to a range of 3.7 to 6.4‰/amu in spinel. One feature that distinguishes the isotopic record of pyroxene from that of spinel in both 5ALLB6 and BG82DH2 is the presence of some isotopically normal pyroxenes ($F_{Mg} = 0$) in both POIs. All of the spinels in both inclusions, in contrast, have $F_{Mg} > 0$.

Isotopic fractionation effects in plagioclase are restricted to inclusion PPX. Plagioclase appears to be isotopically homogeneous, with fractionation favoring the heavier Mg isotopes, $F_{Mg} \approx +7\text{‰}/\text{amu}$. Spinel is rare and very small in this inclusion, and we were unable to obtain isotopic measurements of spinel. Olivine in PPX has $F_{Mg} \approx 0$.

In sharp contrast to spinel and pyroxene, olivine in all of the POIs contains isotopically normal Mg. The values of F_{Mg} cluster about zero, ranging from -1.5 to $+1\text{‰}/\text{amu}$. No significant variations in isotopic composition were found for interior olivine phenocrysts or for the more Fe-rich olivines located in the equigranular olivine clusters.

Most POIs do not show evidence for radiogenic $^{26}\text{Mg}^*$. Only two POIs, 3510 and 5ALLB6, show small but significant enrichments in ^{26}Mg . The $^{26}\text{Mg}/^{24}\text{Mg}$ ratios in plagioclases in these two inclusions are correlated with the respective $^{27}\text{Al}/^{24}\text{Mg}$ ratios measured at the same point of analysis. Four of the six plagioclase analyses in 3510 indicate clear ^{26}Mg excesses (Fig. 10). The linear correlation between the $^{26}\text{Mg}/^{24}\text{Mg}$ and $^{27}\text{Al}/^{24}\text{Mg}$ ratios strongly suggests the *in situ* decay of ^{26}Al . The best-fit slope of the isochron for 3510 (Fig. 10) and 5ALLB6 corresponds to $^{26}\text{Mg}^*/^{27}\text{Al} = 6.1 \times 10^{-6}$, and $^{26}\text{Mg}^*/^{27}\text{Al} = 2.6 \times 10^{-6}$, respectively. In all the other POIs this ratio is less than 1×10^{-6} .

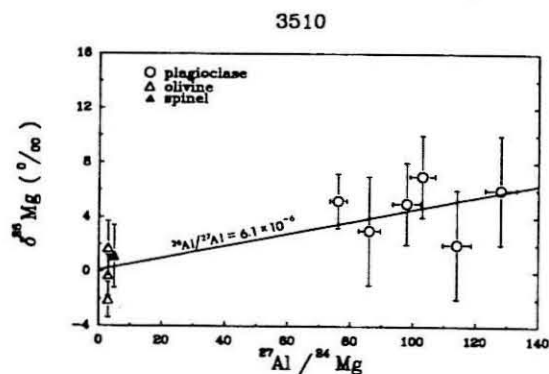


FIG. 10. Correlation of the $^{26}\text{Mg}/^{24}\text{Mg}$ ratio, expressed as $\delta^{26}\text{Mg}$ (permil), with the $^{27}\text{Al}/^{24}\text{Mg}$ ratio for coexisting plagioclase, olivine, and spinel in POI 3510. Plagioclase contains small but clearly resolved ^{26}Mg excesses indicative of the *in situ* decay of ^{26}Al . The best-fit slope of the correlation line, corresponding to $(^{26}\text{Al}/^{27}\text{Al})_0 = 6.1 \times 10^{-6}$, is much less than the value of $\sim 4 \times 10^{-5}$ characteristic of many Type B1 CAIs.

DISCUSSION

Plagioclase-olivine inclusions constitute a distinct group of objects distinguished from both CAIs and chondrules by their mineralogy, chemistry, and isotopic composition. Objects that have the closest resemblance to POIs are the Type C (or I) CAIs (WARK, 1987; GROSSMAN, 1975) and CA chondrules (BISCHOFF and KEIL, 1984). Type C CAIs are anorthite-rich (An_{99-100}) refractory inclusions with substantial amounts of fassaite and spinel, and can have melilite and olivine. CA chondrules are smaller (0.1–0.8 mm) than POIs (0.5–5 mm) and commonly consist of elongated, partly skeletal crystals of fassaite and olivine embedded in a fine-grained Na-rich microcrystalline to glassy matrix. Plagioclase is a minor phase in CA chondrules and, when present, is more sodic (mean An_{80}) than the plagioclase in POIs. Spinel is rare in CA chondrules and contains high FeO (12–20 wt%), in sharp contrast to spinel in POIs. POIs are easily distinguished from both CA chondrules and Type C CAIs on the basis of their petrography and mineralogy, and compose a distinct group unrecognized in previous studies. A comparison of the chemical features between POIs, Type C CAIs, and CA chondrules as well as Type B CAIs is shown in Table 11.

The spheroidal shape and igneous texture of POIs are consistent with crystallization from liquid droplets. However, in the following discussion we will show that there are several features that preclude formation by equilibrium crystallization from an initially homogeneous liquid. A major challenge is the reconciliation of the chemical and mineralogical evidence suggestive of an igneous origin with the isotopic evidence suggesting the presence of relict phases and incomplete melting.

Interpretation of Textural and Chemical Features

The petrographic observations strongly suggest that POIs experienced an igneous history. The subophitic texture common to many POIs, consisting of plagioclase and olivine phenocrysts embedded in a fine-grained matrix, is similar to that found in rocks known to have crystallized from rapidly cooled melts. The porphyritic, barred, and radiating textures also found in several POIs are commonly observed in chondrules, and these textures have been reproduced in experimental studies (LOFGREN, 1980; LOFGREN and RUSSELL, 1986; TSUCHIYAMA et al., 1980). Cooling rates of 20–100°C/min are suggested by these studies.

Experimentally determined phase equilibria in systems appropriate to POI bulk compositions (SHENG et al., 1991) also support the interpretation that POIs crystallized from a homogeneous melt. Both the mineral assemblages and the inferred sequence of crystallization in the natural POIs are consistent with experimental results. In nine POIs spinel is the first phase to crystallize, whereas in seven other POIs olivine is the earliest crystallizing phase, followed by either spinel, pyroxene, or plagioclase. In all 16 of these POIs the observed phase assemblages are compatible with equilibrium or fractional crystallization.

Fractional crystallization of the parental melt is also the most plausible explanation for the overgrowths of enstatite

Table 11 Bulk Compositions of POI, Type B CAI, Type C CAI and CA Chondrules

	POI	Type C CAI*	CA chondrule [†]	Type B CAI*
(wt.%)	range (mean)	range (mean)	range (mean)	range (mean)
Na ₂ O	0.7-6.8 (2.5)	0.05-0.7 (0.2)	0.5-4.6 (4.5)	0.07-0.9 (0.3)
MgO	10-45 (19)	4-13 (7)	4-34 (14)	9-16 (10)
CaO	2-17 (10)	18-26 (22)	4-18 (7)	22-32 (27)
FeO	0.6-6.5 (3)	0.1-0.9 (0.4)	2-14 (6)	0.3-1.7 (1.8)
Al ₂ O ₃	4-37 (22)	26-47 (32)	11-28 (17)	25-34 (31)
Cr ₂ O ₃	0.2-0.9 (0.45)	0.03-0.5 (0.13)	0.1-3.2 (0.5)	0-0.08 (0.05)
SiO ₂	36-50 (41)	21-41 (37)	40-57 (51)	25-35 (29)
TiO ₂	0.4-1.8 (0.7)	0.6-1.6 (1.1)	0.3-1.3 (0.7)	0.9-1.9 (1.5)

* Data from Wark (1987)

† Data from Bischoff and Keil (1984)

* Data from Mason and Martin (1977), McSween (1977)

around olivine and diopside around pigeonite in several inclusions. The cores of these crystals represent an early crystallized phase that was isolated from the liquid. The overgrowth of enstatite around olivine can be attributed to increasing SiO₂ content in the liquid, whereas diopside overgrowths around pigeonite result from increasing CaO in the liquid.

Additional evidence suggestive of equilibrium or fractional crystallization is provided by variations in the chemical composition of plagioclase and olivine. Experimental data of PAN and LONGHI (1989) in the Na₂O-CaO-MgO-Al₂O₃-SiO₂ (NCMAS) system, simulating compositions of alkaline basic lavas, show that for liquid compositions containing 4.2 to 5.3% Na₂O, the corresponding plagioclase compositions range between An₉₅ and An₈₈. Whereas these results agree qualitatively with our observations in POIs, the nepheline-normative composition used by PAN and LONGHI (1989) limits the applicability of the data. YURIMOTO and SUENO (1984) determined the crystal-liquid partition coefficients between olivine and plagioclase and tholeiitic basalt magma. Using their experimental results and measured Na concentrations in POI plagioclase, we calculate that the parent melt for POIs would have contained 0.5 to 2.8% Na₂O. Thus, to the extent that the bulk composition of the POI system can be approximated by tholeiitic to alkalic basalt melts, the experimental data on the distribution of Na between crystal and melt are in good agreement with our data on natural and synthetic POIs, and suggest that substantial Na₂O was present in the POI parent melt during crystallization of the major silicates.

The calcium content in interior olivines in POIs is consistent with the experimentally determined calcium partition coefficient between olivine and liquid in the NCMAS system for basaltic compositions (WATSON, 1979). The CaO content in olivines typically exhibits a progressive decrease from center to rim. An example of this behavior for an olivine from inclusion BG82DH2 is shown in Fig. 11. The predicted CaO content in the coexisting melt, calculated using the distribution coefficient of WATSON (1979), is in excellent agreement with the measured CaO content of the bulk inclusion.

The preceding discussion has focussed on characteristics of POIs that are compatible with an igneous origin. The majority of the chemical and mineralogical properties of 16 of the 20 POIs examined fall into this group. However, in four group 2 POIs the presence of spinel contradicts the experi-

mentally determined phase equilibria. Spinel should not crystallize at equilibrium from melts of the respective bulk compositions of ADEL-1, BG82CH1, SA-1, and BG82CLJa. In ADEL-1, BG82CH1, and BG82CLJa spinel is rare and strongly resorbed, and only occurs included within plagioclase. In SA-1 spinel occurs as rare inclusions in plagioclase, olivine, and pyroxene. The extent of disequilibrium in ADEL-1 is emphasized by the presence of both spinel and tridymite in close proximity. Phase equilibria data (LONGHI, 1987; LONGHI and PAN, 1988) clearly show that these two phases are incompatible, and textures suggest that spinel is a relict phase. The strongly resorbed character of the spinels, with serrated and embayed boundaries (Fig. 2a), can only be explained by reaction with a spinel-undersaturated liquid. The preservation of relict spinels in such a liquid at high temperature is possible only as a result of isolation of the spinels from the liquid by inclusion in early crystallizing plagioclase crystals. Relict spinel that remained in contact with the liquid would rapidly dissolve, explaining the low abundance of spinel in these POIs.

The preservation of relict spinel is also the most plausible explanation for the Cr-rich mantles on Cr-poor spinel in inclusion 5ALLB6. Although spinel can be the earliest phase

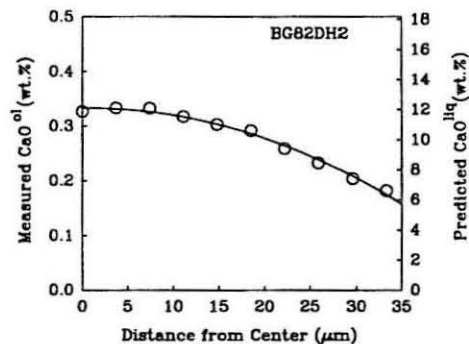


FIG. 11. Electron probe WDS analyses showing the variation of CaO across an olivine phenocryst in BG82DH2 (open circles). The measured CaO contents are compared with the predicted values (solid curve) calculated using the experimentally determined distribution coefficient (WATSON, 1979). The agreement between the measured and predicted values indicates equilibrium crystallization of olivine from the POI melt.

to crystallize in this inclusion, the large difference in Cr_2O_3 contents between core and mantle suggests that the coexisting spinels could not have crystallized from a single homogeneous melt. Since Cr is a compatible element in spinel, spinel crystallized from a Cr-rich liquid should contain substantial Cr, and the early crystallization of spinel will deplete Cr in the liquid. If spinel is zoned, the zonation should be gradational with decreasing Cr from core to rim. In contrast, the spinels in 5ALLB6 have Cr-poor cores and Cr-rich overgrowths (Fig. 2c). Analysis of Cr contents in spinels and coexisting Cr-doped glasses with compositions similar to POIs and CAIs suggests a partition coefficient of Cr between spinel and coexisting liquid of approximately 40 (SHENG et al., 1991). The partition coefficient of Cr between olivine and a basaltic liquid is about 1 (LEEMAN and SCHEIDEGGER, 1977). Since the olivines in 5ALLB6 contain about 0.2% Cr_2O_3 , and the core and mantle of the spinels contain <0.5% and 5–10% Cr_2O_3 , respectively, it is apparent that the Cr-poor spinel core could not have crystallized together with the olivines from a liquid, whereas the Cr-rich spinel rims could. We also note that in a preliminary experiment, we were able to grow a 2 μm wide layer of Cr-rich spinel on a wafer of Mg-rich spinel by placing the Mg-spinel in contact with a Cr-doped spinel-oversaturated melt with composition similar to a POI.

The petrographic and chemical evidence indicates that the Cr-rich rims were late overgrowths on the Mg spinel core. The spinel overgrowths, crystallized from a spinel-oversaturated, Cr-enriched liquid, thus were in equilibrium with the liquid and should contain isotopically normal Mg (see discussion on POI formation). We attempted to verify this prediction by searching for differences in Mg isotopic composition between the core, $F_{\text{Mg}} \sim 6\text{‰}$ /amu, and mantle of a spinel in 5ALLB6. The difficulty we encountered was to measure the 1 micron wide rim with an ion beam about 5 μm in diameter. We attempted to analyze a spinel enclosed in plagioclase by stepping the primary ion beam onto the Cr-rim from the plagioclase side. Ideally, if we positioned the ion beam such that it was tangent to the Cr-rich boundary within the spinel, the bulk of the Mg^+ ion signals would have been derived from the Cr-rich spinel. However, the results show that the maximum Cr/Mg ratio in the spinel from the ion probe analysis is an order of magnitude less than the ratio from WDS analysis. This suggests that there was a significant overlap of the ion beam into the Mg-rich spinel core, inhibiting our ability to decipher the Mg isotope composition of the Cr-rich spinel mantle.

Implications of Igneous Texture versus Mg Isotope Heterogeneity

Our studies show that at least seven POIs are isotopically heterogeneous in Mg. Four of these seven are group 1 inclusions, two are group 2 inclusions—one of which was reported by KENNEDY et al. (1991)—and another is a group 3 POI. The presence of spinel with distinct Mg isotopic compositions suggests that some spinel are relicts and carry the isotopic signature of a different source region. Relict phases can be identified on the basis of differences in isotopic composition (F_{Mg}) or by their occurrence in inclusions whose bulk composition does not allow crystallization of the phase. The

compositions of the group 1 POI are spinel-saturated, and relict spinels cannot be identified petrographically. However, differences in F_{Mg} between coexisting spinel and silicates, and among spinels of up to 11‰/amu, strongly suggest that some spinels are relicts. Four group 2 POIs have spinel-undersaturated compositions, and phase equilibria considerations require spinel to be a relict phase. Spinel is rare and small ($\leq 2 \mu\text{m}$) in this group of inclusions, making isotopic measurements very difficult. In two spinel-undersaturated POIs, the observed differences in F_{Mg} between spinel and silicate support the identification of spinel as a relict phase.

The variation in mineralogy and bulk composition among the POIs implies a range in refractory "character" and melting temperature among the inclusions, and suggests that the abundance of relict phases may vary systematically among the POI groups. Relict spinel would be expected to be most abundant in POIs with the lowest melting temperatures, yet sufficiently refractory to contain some spinel. The spinel-rich group 1 POIs have the most refractory bulk compositions, while calculated melting temperatures, based on the method of BERMAN (1983), show that groups 1 and 3 have roughly equal melting temperatures (1500–1700°C), while group 2 POIs melt at significantly lower temperatures. Four out of six group 1 POIs that we analyzed show isotopic heterogeneities plausibly attributed to the preservation of relict spinel. However, the scarcity of spinels large enough to analyze isotopically in the other groups of POIs makes it difficult to answer unambiguously the question of a correlation between the abundance of relict spinel and POI bulk composition.

As shown in Fig. 9a, the isotopic fractionation of spinels in POIs can favor enrichment in either the lighter Mg isotopes or in the heavier Mg isotopes, but never both in the same inclusion. Fractionation effects in silicates, found in only three POIs, have similar magnitude but always exhibit positive F_{Mg} values. This Mg isotopic signature clearly distinguishes POIs from both refractory inclusions and chondrules. With the exception of crystals in the Wark-Lovering rims of some CAIs, most coarse-grained CAIs and chondrules are isotopically homogeneous in their $^{25}\text{Mg}/^{24}\text{Mg}$ ratios (MACPHERSON et al., 1988). Types A, B, and C CAIs generally exhibit little evidence of Mg isotopic fractionation, and when isotopic fractionation is present F_{Mg} is always positive. Large, positive isotopic fractionation is found in FUN inclusions, but most FUN CAIs are also isotopically homogeneous (WASSERBURG et al., 1977; ESAT et al., 1978; CLAYTON et al., 1984). An important exception are the purple, spinel-rich Allende inclusions, some of which exhibit both large isotopic fractionation and variations in F_{Mg} among coexisting phases (BRIGHAM et al., 1988; BRIGHAM, 1990). Isotope fractionation in these inclusions is always positive, and the isotopic heterogeneity is believed to reflect partial isotopic exchange during alteration. Many fine-grained inclusions, in contrast, are fractionated favoring the lighter Mg isotopes and are usually isotopically heterogeneous within individual inclusions (BRIGHAM, 1990). The POIs are thus distinguished from these types of inclusions as the first group of objects to exhibit both positive and negative Mg isotopic fractionation and the first group of igneous-textured inclusions to exhibit heterogeneity in F_{Mg} with such frequency.

A major challenge posed by the data is to understand the preservation of large Mg isotope heterogeneities and in at least one POI, BG82CLII, the generation of a highly fractionated Group II REE pattern (SHENG et al., 1990), in a class of objects whose textures would otherwise suggest crystallization from a homogeneous melt. Two possible models can be constructed within the constraints imposed by our data. One model suggests that each inclusion is an aggregate of grains from different sources that were not homogenized by subsequent thermal processes. Spinel containing isotopically fractionated Mg was a precursor phase and was not completely melted during POI formation, thus retaining its original isotopic signature. A requirement of this model is incomplete melting of the precursor material during POI formation. An alternative model suggests that the inclusions formed from a single homogeneous source containing isotopically fractionated Mg. Partial isotopic reequilibration with an isotopically normal gas via sub-solidus gas-solid exchange gave rise to the observed heterogeneity. This model requires large differences in Mg diffusion rates between spinel and silicates.

Model for POI Formation

Although neither model can be excluded on the basis of the available data and several crucial measurements, such as the diffusion rate of Mg in spinel, await completion, we believe there are several lines of evidence that strongly favor formation of POIs by aggregation of isotopically dissimilar materials followed by partial melting. In this section we critically examine the essential characteristics of POIs and present a model for their formation.

The data show large Mg isotopic heterogeneity between major Mg-rich silicates and oxides in POIs; spinel and host silicates show variations in F_{Mg} of up to 10‰/amu on a spatial scale of tens of microns. This isotopic heterogeneity on a microscopic scale is similar to observations of oxygen isotope heterogeneity in refractory inclusions (CLAYTON et al., 1977), where spinel and host melilite exhibit strikingly different oxygen isotopic compositions. Most CAIs are generally assumed to have formed from an ^{16}O -rich reservoir and to have acquired their oxygen isotopic heterogeneity through gas-solid diffusive exchange with an ^{16}O -depleted gas. In this model the isotopic heterogeneity arises from large differences in the rates of oxygen diffusion in spinel and melilite. We note that, although this model is widely accepted, recent experimental measurements of oxygen diffusion in spinel and melilite (YURIMOTO et al., 1989; MCKEEGAN and RYERSON, 1990) require a reexamination of the critical assumptions.

If POIs originally formed as homogeneous melts containing isotopically fractionated Mg, the observed variations in F_{Mg} require that Mg diffuse much faster in olivine and pyroxene than in spinel. Since the silicates in POIs are much larger than spinels, the Mg self-diffusion coefficients in olivine and pyroxene must be ~ 100 times larger than that in spinel to produce the observed isotopic heterogeneity. However, the few available data indicate that Mg self-diffusion in spinel is very rapid, with $D = 3.4 \times 10^{-10} \text{ cm}^2/\text{s}$ at 1600°C (LINDNER

and AKERSTROM, 1955), whereas that for forsterite is $2.74 \times 10^{-12} \text{ cm}^2/\text{s}$ at 1600°C (FREER, 1981), contrary to the requirements of this model. If the Mg isotopic heterogeneity was due to partial isotopic reequilibration, we would expect to observe some correlation between the magnitude of isotopic exchange and the severity of alteration. However, no such correlation is observed in the POIs. In contrast to CAIs, most POIs, in fact, show remarkably little evidence of mineralogical alteration. Alteration of plagioclase to nepheline and sodalite or spinel to feldspathoid plus olivine, two common occurrences of secondary metamorphism, is rare in POIs. We also observed no correlation between spinel chemistry and F_{Mg} . The more Fe-rich spinels do not, in general, have lower F_{Mg} , as might be expected if diffusive exchange with a nebular gas at lower temperature were pervasive. Thus, we conclude that it is unlikely that POIs originated as homogeneous melts and obtained their isotopic heterogeneity as the result of diffusive gas-solid exchange.

The formation of POIs from an assemblage of chemically and isotopically heterogeneous materials requires that the inclusions were never completely melted, allowing the most refractory phase (e.g., spinel) to preserve its original isotopic signature. Both our petrographic observations of natural POIs and the results of our experimental phase equilibria studies of melts with compositions similar to the more Ca-Al-rich POIs are consistent with this essential requirement. Five of the seven isotopically heterogeneous POIs have spinel as the liquidus phase. Relict spinels included in a melt of this composition could, therefore, survive if the partial melt of the POI precursor were spinel-saturated, if the maximum temperature to which the POI was heated was below the spinel liquidus, or if the heating event were sufficiently brief to inhibit spinel dissolution and isotopic reequilibration between spinel and the melt. In a spinel-oversaturated melt, corresponding to group 1 POI, it is possible that spinel crystallized from the melt could coexist with isotopically anomalous, relict spinel in the same POI. Partial dissolution of some relict spinel may also occur during partial melting. Spinel crystallized from the melt would have a nearly normal Mg isotopic composition, while partially reacted, relict spinel may experience isotopic exchange with the melt and acquire an isotopic composition intermediate between those of the primary, relict spinel and the melt. The large range in F_{Mg} , observed in several POIs, is a reflection of the presence of these several generations of spinels. The remaining POI containing isotopically heterogeneous spinel, ADEL-1, belongs to petrographic group 2, and spinel does not appear in the crystallization sequence. The highly resorbed appearance of the rare spinel found in this inclusion provides independent evidence that spinel is a relict phase.

Phase equilibria prohibit the presence of relict pyroxenes in group 1 POIs. The variation of F_{Mg} among pyroxenes in two group 1 POIs most plausibly can be attributed to the partial dissolution of relict spinel (with $F_{Mg} > 0$) and incorporation of some isotopically fractionated Mg in late-crystallizing pyroxene. This scenario leads to the prediction that measured values of F_{Mg} in pyroxene must lie between the maximum F_{Mg} of relict spinel and the average F_{Mg} of the silicate precursor. In this case pyroxenes with the highest F_{Mg}

should be the latest to crystallize and should contain large enrichments in the REEs.

The one inclusion containing plagioclase with isotopically fractionated Mg, PPX, is also a group 2 POI and contains almost no spinel. The large difference in F_{Mg} for plagioclase and olivine requires that either plagioclase is a relict phase or that olivine acquired its normal Mg isotopic composition by sub-solidus exchange with the nebular gas. The data do not allow an unambiguous resolution of the alternatives. It is possible that the dissolution of very small amounts of relict spinel in plagioclase could cause this effect. Phase equilibria considerations permit the presence of relict plagioclase, but petrographic observations of plagioclase laths intergrown with olivine phenocrysts suggest that both phases crystallized from the melt. The observation that olivine in all of the POIs contains isotopically normal Mg, irrespective of the abundance of relict spinel with isotopically fractionated Mg, is consistent with the isotopic exchange hypothesis. This model requires that the rate of Mg isotope exchange via gas-solid diffusion is much faster in olivine than in the other silicates in POIs or in spinel. Most POIs also show very little petrographic evidence of extensive reaction with a nebular gas.

Our preferred scenario for the origin of POIs consists of

the following events (illustrated in Fig. 12): (1) Formation of spinel containing isotopically fractionated Mg; spinel may contain isotopically fractionated Mg with $F_{Mg} > 0$ or $F_{Mg} < 0$, or may contain normal Mg. Some silicates may also be present. (2) Formation of a separate silicate precursor material representing a wide range of bulk compositions but containing significant Na and Cr, and low refractory siderophiles. Some of these silicates must be produced by gas/solid fractionation during condensation/evaporation to produce Group II REE abundances (SHENG et al., 1990). The silicate precursor material may have contained components with isotopically fractionated Mg, but the average composition of most silicates was near $F_{Mg} = 0$. The observation of plagioclase and pyroxene containing isotopically fractionated Mg in one POI attests to the presence of silicate precursors with $F_{Mg} > 0$. (3) Mixing of spinel and separate silicate precursor components. (4) A heating episode which melted the silicates but only partially reacted or melted spinel. The Fe-rich olivine clusters embedded at the rims of many POIs are believed to be materials accreted from another source during the final solidification of the POIs. (5) Relatively rapid cooling and little subsequent alteration to preserve isotopic heterogeneity. In some cases mesostasis is preserved as a quench product of the melting event. This model underscores a major difference in the way in which POIs and CAIs obtained their respective Mg and oxygen isotopic heterogeneity. The Mg isotopic heterogeneity of POIs reflects the inherited Mg isotopic variability of relict spinel, whereas the O isotopic heterogeneity in CAIs is most plausibly produced during post-crystallization exchange between silicates and the nebular gas.

The similarities in major element composition and in the extent of Mg isotopic heterogeneity between the POIs and fine-grained Ca-, Al-rich inclusions suggests that the POI precursor material may be related to fine-grained inclusions. The observation of a Group II REE pattern in one POI, BG82CLII (SHENG et al., 1990), also provides support for this argument. However, this POI contains spinel with large positive F_{Mg} , whereas most fine-grained inclusions are enriched in the lighter Mg isotopes. In fact, all but two of the fractionated POIs are enriched in the heavier Mg isotopes. This behavior shows that even though POIs and fine-grained CAIs share many common chemical characteristics, there still exist essential differences inhibiting a simple and direct relationship.

CONCLUSIONS

We have described POIs as a group of objects that possess distinct chemical, mineralogical, and textural characteristics. Our observations show that although POIs have been partially melted, some of them contain relict spinel that preserves an earlier isotopic identity. The spinel-bearing precursor material originated from reservoirs containing isotopically fractionated Mg. The isotopically fractionated material was later mixed with silicates whose average isotopic composition was approximately normal and was then heated such that the silicates melted but some spinel survived, generating the igneous texture yet preserving some relict spinels and creating the Mg isotopic heterogeneity. The observation of Mg isotopic heterogeneity in POIs has apparent similarities with the observations of oxygen isotope heterogeneity in CAIs. In both

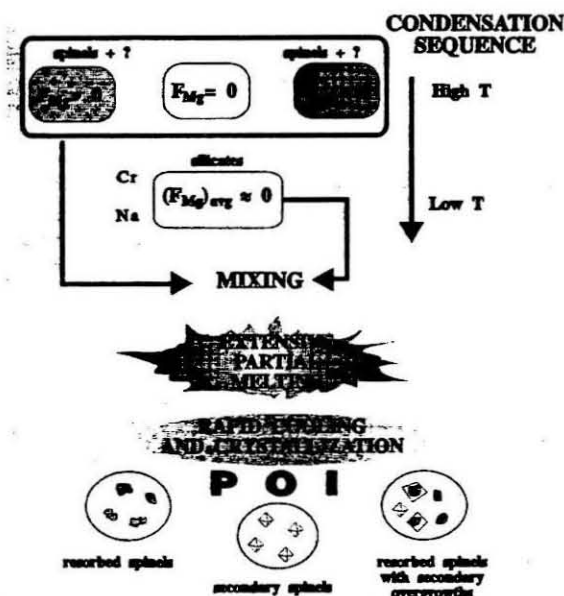


FIG. 12. Cartoon illustrating the proposed model for the formation of POI. Spinel from several reservoirs containing distinctly different F_{Mg} were mixed with silicate components from another reservoir containing isotopically normal Mg (or with average $F_{Mg} = 0$) and enriched in volatile species (e.g., Na, Cr). The silicate material may have been isotopically heterogeneous on a microscopic scale. A brief heating episode melted the silicates but only partially reacted spinel. The observed isotopic heterogeneity was created by rapid cooling and crystallization which preserved some relict spinels with their original isotopic signature and created second generation spinels as separate crystals or as overgrowths on partially resorbed relicts. Some late-crystallizing silicates acquired isotopically fractionated Mg due to partial dissolution of spinel.

classes of inclusions, spinel is the major host of the isotopic anomaly, whereas silicate phases have a more nearly normal isotopic composition. However, the two classes of inclusions are clearly distinguished by major differences in the nature of the precursor components and by the processes by which the isotopic heterogeneity was established and preserved.

The formation of POIs suggests a broader connection and wider affinity with CAIs and chondrules. The formation of POIs requires multiple processes, including condensation, dust/gas fractionation, mixing and aggregation of chemically and isotopically heterogeneous materials, and partial melting. It appears that these materials reflect an ongoing and repeated sequence of mixing and partial melting, evaporation and recondensation, affecting the metal oxides. These processes are common to most CAIs and many chondrules. We consider a starting material of different parcels of interstellar dust grains each having slightly different isotopic compositions. These parcels were rapidly heated by localized processes of unknown nature producing condensates that then reaggregated. This reprocessing took place in a similar fashion over an extended time scale of several million years. We consider CAIs to be produced by relatively early melting of refractory condensates or evaporative residues produced by the above processes. The CAIs were homogenized during melting, but exhibit characteristic isotopic anomalies from sample to sample, reflecting their parent material. The POIs are considered to be produced later, based on the $^{26}\text{Mg}^*/^{27}\text{Al}$ ratios, by mixing of some earlier-processed material, incorporating more MgO , SiO_2 , as well as less-refractory material enriched in Na_2O , Cr_2O_3 , and MnO . The degree of homogeneity of the final POIs is mainly a reflection of their thermal history. The major differences between Type B CAIs and the POIs reflect the types of material that were aggregated, the temperatures to which they were heated, and the timing of the last thermal metamorphic event. POIs were heated to a lower temperature or cooled more rapidly than most CAIs, preserving some phases that retained their original isotopic identity. The melting occurred after most ^{26}Al had decayed. It is also possible that some CAIs are, in fact, formed (or rather, reformed) late. This could explain the absence of ^{26}Al in some CAIs as distinct from a model requiring that ^{26}Al be distributed very heterogeneously in the solar nebula. We consider these processes (both for CAIs and POIs) to affect the dust and reprocessed, remelted dust after most of the nebular gases have dissipated.

Acknowledgments—The senior author appreciates generous help on optical and instrumental techniques and interpretations by J. T. Armstrong, N. Z. Boctor, and A. K. Kennedy. J. R. Beckett and E. M. Stolper provided valuable comments. We thank L. M. Hedges for sample preparation and G. J. MacPherson, H. Y. McSween, and an anonymous reviewer for their careful reviews of the manuscript. The section containing USNM 3510 was provided by the United States National Museum. This work was supported by NASA, under grant NAG 9-43.

Editorial handling: J. D. Macdougall

REFERENCES

- ALLEN J. M., GROSSMAN L., DAVIS A. M., and HUTCHEON I. D. (1978) Mineralogy, texture and mode of formation of a hibonite-bearing Allende inclusion. *Proc. Lunar Sci. Conf.* 9, 1209–1233.
- ARMSTRONG J. T. (1984) Quantitative analysis of silicate and oxide minerals: A reevaluation of ZAF corrections and proposal for new Bence-Albee coefficients. In *Microbeam Analysis—1984* (eds. A. ROMIG and J. I. GOLDSTEIN), pp. 208–212. San Francisco Press.
- ARMSTRONG J. T., HUTCHEON I. D., and WASSERBURG G. J. (1984) Fremdlinge in Leoville and Allende CAI: Clues to post-formation cooling and alteration. *Meteoritics* 19, 186–187.
- BECKETT J. R. (1986) The origin of calcium-, aluminum-rich inclusions from carbonaceous chondrites: An experimental study. Ph.D. thesis, Univ. Chicago.
- BECKETT J. R. and GROSSMAN L. (1988) The origin of type C inclusions from carbonaceous chondrites. *Earth Planet. Sci. Lett.* 89, 1–14.
- BENCE A. E. and ALBEE A. L. (1968) Empirical correction factors for the electron microanalysis of silicates and oxides. *J. Geol.* 76, 383–403.
- BERMAN R. G. (1983) A thermodynamic model for multicomponent melts, with application to the system $\text{CaO-MgO-Al}_2\text{O}_3\text{-SiO}_2$. Ph.D. thesis, Univ. British Columbia.
- BISCHOFF A. and KEIL K. (1984) Al-rich objects in ordinary chondrites: Related origin of carbonaceous and ordinary chondrites and their constituents. *Geochim. Cosmochim. Acta* 48, 693–709.
- BISCHOFF A., PALME H., and SPETTEL B. (1989) Al-rich chondrules from the Ybbsitz H4-chondrite: evidence for formation by collision and splashing. *Earth Planet. Sci. Lett.* 93, 170–180.
- BLANDER M. and FUCHS L. H. (1975) Calcium-aluminum inclusions in the Allende meteorite: evidence for a liquid origin. *Geochim. Cosmochim. Acta* 39, 1605–1619.
- BOCTOR N. Z., HUTCHEON I. D., and WASSERBURG G. J. (1988) Petrology of a plagioclase-rich forsterite-bearing Allende inclusion. *Lunar Planet. Sci. Conf. XIX*, 110–111.
- BOCTOR N. Z., HUTCHEON I. D., and WASSERBURG G. J. (1989) Petrology and opaque mineralogy of an armalcolite-bearing basaltic CAI from the Allende meteorite. *Lunar Planet. Sci. Conf. XX*, 88–89.
- BRIGHAM C. A. (1990) Isotopic heterogeneity in calcium-aluminum rich meteoritic inclusions. Ph.D. thesis, California Institute of Technology.
- BRIGHAM C. A., HUTCHEON I. D., PAPANASTASSIOU D. A., and WASSERBURG G. J. (1988) Isotopic heterogeneity and correlated isotope fractionation in purple FUN inclusions. *Lunar Planet. Sci. Conf. XIX*, 132–133.
- CATANZARO E. J., MURPHY T. J., GARNER E. L., and SHIELDS W. R. (1966) Absolute isotopic abundance ratios and atomic weight of magnesium. *J. Res. Natl. Bur. Stand.* 70A, 453–458.
- CHOU C., BAEDECKER P. A., and WASSON J. T. (1975) Allende inclusions: volatile-element distribution and evidence for incomplete volatilization of presolar solids. *Geochim. Cosmochim. Acta* 40, 85–94.
- CHRISTOPHE MICHEL-LÉVY, M. (1968) Un chondre exceptionnel dans la météorite de Vigarano. *Bull. Soc. Française Minéral. Cristallogr.* 91, 212–214.
- CLAYTON R. N., GROSSMAN L., and MAYEDA T. K. (1973) A component of primitive nuclear composition in carbonaceous meteorites. *Science* 182, 485–488.
- CLAYTON R. N., ONUMA N., GROSSMAN L., and MAYEDA T. K. (1977) Distribution of pre-solar component in Allende and other carbonaceous chondrites. *Earth Planet. Sci. Lett.* 34, 209–224.
- CLAYTON R. N., MACPHERSON G. J., HUTCHEON I. D., DAVIS A. M., GROSSMAN L., MAYEDA T. K., MOLINI-VELSKO C., ALLEN J. M., and EL GORESY A. (1984) Two forsterite-bearing FUN inclusions in the Allende meteorite. *Geochim. Cosmochim. Acta* 48, 535–548.
- DEER W. A., HOWIE R. A., and ZUSSMAN J. (1978) *Rock-forming minerals: Single-chain silicates*, Vol. 2A, 2nd edn. Halsted Press.
- EL GORESY A. (1976) Oxide minerals in lunar rocks. In *MSA Short Course Notes: Oxide minerals* (ed. D. RUMBLE), Chap. 6, pp. EG-1–EG-46. Mineralogical Society of America.
- EL GORESY A., NAGEL K., and RAMDOHR P. (1978) Fremdlinge and their noble relatives. *Proc. 9th Lunar Sci. Conf.*, 1279–1303.
- ESAT T. M., LEE T., PAPANASTASSIOU D. A., and WASSERBURG

- G. J. (1978) Search for ^{26}Al effects in the Allende FUN inclusion C1. *Geophys. Res. Lett.* **5**, 807–810.
- FREER R. (1981) Diffusion in silicate minerals and glasses: a data digest and guide to the literature. *Contrib. Mineral. Petrol.* **76**, 440–454.
- GROSSMAN L. (1972) Condensation in the primitive solar nebula. *Geochim. Cosmochim. Acta* **36**, 597–619.
- GROSSMAN L. (1975) Petrography and mineral chemistry of Ca-rich inclusions in the Allende meteorite. *Geochim. Cosmochim. Acta* **39**, 433–454.
- HAGGERTY S. E. (1973) Armalcolite and genetically associated opaque minerals in lunar samples. *Proc. 4th Lunar Sci. Conf.* **777–797**.
- HAGGERTY S. E. (1975) The chemistry and genesis of opaque minerals in kimberlites. *Phys. Chem. Earth* **9**, 295–307.
- HASHIMOTO A., KUMAZAWA N., and ONUMA N. (1979) Evaporation metamorphism of primitive dust material in the early solar nebula. *Earth Planet. Sci. Lett.* **43**, 13–21.
- HUNEKE J. C., ARMSTRONG J. T., and WASSERBURG G. J. (1983) FUN with PANURGE: High mass resolution ion microprobe measurements of Mg in Allende inclusions. *Geochim. Cosmochim. Acta* **47**, 1635–1650.
- HUTCHEON I. D. (1982) Ion probe magnesium isotopic measurements of Allende inclusions. In *Nuclear and Chemical Dating Techniques: Interpreting the Environmental Record* (ed. L. A. CURIE); *Amer. Chem. Soc. Symp. Ser.* **176**, pp. 95–128.
- HUTCHEON I. D., STEELE I. M., SMITH J. V., and CLAYTON R. N. (1978) Ion microprobe, electron microprobe and cathodoluminescence data for Allende inclusions with emphasis on plagioclase chemistry. *Proc. 9th Lunar Sci. Conf.* **1345–1368**.
- HUTCHEON I. D., ARMSTRONG J. T., and WASSERBURG G. J. (1987) Isotopic studies of Mg, Fe, Mo, Ru and W in Fremdlinge from Allende refractory inclusions. *Geochim. Cosmochim. Acta* **51**, 3175–3192.
- KENNEDY A., HUTCHEON I. D., and WASSERBURG G. J. (1989) Chemical and isotopic constraints on the formation and evolution of SA-1, a basaltic CAI from Allende. *Lunar Planet. Sci. Conf. XX*, 514–515.
- KENNEDY A., HUTCHEON I. D., and WASSERBURG G. J. (1991) Chemical and isotopic constraints on the formation and differentiation of SA-1, a basaltic inclusion from Allende (in prep.).
- LARIMER J. W. (1967) Chemical fractionations in meteorites—I. Condensation of the elements. *Geochim. Cosmochim. Acta* **31**, 1215–1238.
- LEEMAN W. P. and SCHEIDEGGER K. F. (1977) Olivine/liquid distribution coefficients and a test for crystal-liquid equilibrium. *Earth Planet. Sci. Letters* **35**, 247–257.
- LENSCH G. (1971) Das Vorkommen von Sapphirin in Peridotitkörper von Finero (Zone von Ivrea, Italienische Westalpen). *Contrib. Mineral. Petrol.* **31**, 145–152.
- LINDNER R. and AKERSTROM A. (1958) Diffusion von Ni-63 in Nickelspinellen. *Zeitschrift für Physikalische Chemie Neue Folge* **18**, 303–307.
- LOFGREN G. (1980) Experimental studies on the dynamic crystallization of silicate melts. In *Physics of Magmatic Processes* (ed. R. B. HARGRAVES), pp. 487–551. Princeton Univ. Press.
- LOFGREN G. and RUSSELL W. J. (1986) Dynamic crystallization of chondrule melts of porphyritic and radial pyroxene composition. *Geochim. Cosmochim. Acta* **50**, 1715–1726.
- LONGHI J. (1987) Liquidus equilibria and solid solution in the system $\text{CaAl}_2\text{Si}_2\text{O}_8\text{-Mg}_2\text{SiO}_4\text{-CaSiO}_3\text{-SiO}_2$ at low pressure. *Amer. J. Sci.* **287**, 265–331.
- LONGHI J. and PAN V. (1988) A reconnaissance study of phase boundaries in low-alkali basaltic liquids. *J. Petrol.* **29**, 115–147.
- LORAND J. P. and COTTIN J. Y. (1987) A new natural occurrence of zirconolite ($\text{CaZrTi}_2\text{O}_7$) and baddeleyite (ZrO_2) in basic cumulates: the Laouni layered intrusion (Southern Hoggar, Algeria). *Mineral. Mag.* **51**, 671–676.
- LORD H. C., III (1965) Molecular equilibria and condensation in a solar nebula and cool stellar atmospheres. *Icarus* **4**, 279–288.
- LOVE G. and SCOTT V. D. (1978) Evaluation of a new correction procedure for quantitative electron probe microanalysis. *J. Phys.* **D-11**, 1369–1376.
- MACPHERSON G. J. and GROSSMAN L. (1981) A once-molten, coarse-grained, Ca-rich inclusion in Allende. *Earth Planet. Sci. Lett.* **52**, 16–24.
- MACPHERSON G. J. and GROSSMAN L. (1984) "Fluffy" Type A Ca-, Al-rich inclusions in the Allende meteorite. *Geochim. Cosmochim. Acta* **48**, 29–46.
- MACPHERSON G. J., HASHIMOTO A., and GROSSMAN L. (1985) Accretionary rims on inclusions in the Allende meteorite. *Geochim. Cosmochim. Acta* **49**, 2267–2279.
- MACPHERSON G. J., FAHEY A. J., LUNDBERG L. L., and ZINNER E. (1988) Al-Mg isotopic systematics and metamorphism in five coarse-grained Allende CAIs. *Meteoritics* **23**, 286–287.
- MASON B. and MARTIN P. M. (1977) Geochemical differences among components of the Allende meteorite. *Smithsonian Contrib. Earth Sci.* **19**, 84–95.
- MCKEEGAN K. D. and RYERSON F. J. (1990) Diffusion of oxygen in diopside and spinel: implications for oxygen isotopic anomalies in CAIs. *Lunar Planet. Sci. Conf. XXI*, 775–776.
- MCSWEEN H. Y. (1977) Chemical and petrographic constraints on the origin of chondrules and inclusions in carbonaceous chondrites. *Geochim. Cosmochim. Acta* **41**, 1843–1863.
- MEEKER G. P., WASSERBURG G. J., and ARMSTRONG J. T. (1983) Replacement textures in CAI and implications regarding planetary metamorphism. *Geochim. Cosmochim. Acta* **47**, 707–721.
- MEYER H. O. A. and BOCTOR N. Z. (1974) Opaque mineralogy: Apollo 17, rock 75035. *Proc. 5th Lunar Sci. Conf.* **1**, 706–716.
- MISAWA K. and NAKAMURA N. (1987) Rare earth elements in chondrules from the Felix (CO3) chondrite: Comparison with the Allende (CV3) chondrules. *Symp. Antarctic Met.* **12**, 90–92.
- ONUMA N., CLAYTON R. N., and MAYEDA T. K. (1972) Oxygen isotope cosmo thermometer. *Geochim. Cosmochim. Acta* **36**, 169–188.
- PAN V. and LONGHI J. (1989) Low pressure liquidus relations in the system $\text{Mg}_2\text{SiO}_4\text{-Ca}_2\text{SiO}_4\text{-NaAlSi}_3\text{O}_8\text{-SiO}_2$. *Amer. J. Sci.* **289**, 1–16.
- PAPANASTASSIOU D. A., BRIGHAM C. A., and WASSERBURG G. J. (1984) Search for Mg isotopic signatures in Allende. *Lunar Planet. Sci. Conf. XV*, 629–630.
- PEDERSEN A. K. (1981) Armalcolite-bearing Fe-Ti Oxide Assemblages in graphite-equilibrated salic volcanic rocks with native iron from Disko, Central West Greenland. *Contrib. Mineral. Petrol.* **77**, 307–324.
- RUBIN A. E. and WASSON J. T. (1988) Chondrules and matrix in the Ormans CO3 meteorite: Possible precursor components. *Geochim. Cosmochim. Acta* **52**, 425–432.
- SEGNIT E. R. (1957) Sapphirine-bearing rocks from Robertson Land, Antarctica. *Mineral. Mag.* **31**, 690–697.
- SHENG Y. J., HUTCHEON I. D., and WASSERBURG G. J. (1988) Plagioclase-Olivine Inclusions in Allende—a link between CAI and ferro-magnesian chondrules. *Lunar Planet. Sci. Conf. XIX*, 1075–1076.
- SHENG Y. J., HUTCHEON I. D., and WASSERBURG G. J. (1990) Magnesium isotope heterogeneity in Plagioclase Olivine Inclusions. *Lunar Planet. Sci. Conf. XXI*, 1138–1139.
- SHENG Y. J., BECKETT J. R., HUTCHEON I. D., WASSERBURG G. J., and STOLPER E. M. (1991) Experimental constraints on the origin of Plagioclase Olivine Inclusions (in prep.).
- SLODZIAN G. (1980) Microanalyzers using secondary ion emission. In *Advances in Electronics and Electron Physics* (ed. A. SEPTIER), Suppl. **13B**, pp. 1–32. New York: Academic Press.
- STOLPER E. (1982) Crystallization sequences of Ca-Al-rich inclusions from Allende: An experimental study. *Geochim. Cosmochim. Acta* **46**, 2159–2180.
- STOLPER E. and PAQUE J. M. (1986) Crystallization sequences of Ca-Al-rich inclusions from Allende: The effects of cooling rate and maximum temperature. *Geochim. Cosmochim. Acta* **50**, 0001–0022.
- SUNG C., ABU-EID R. M., and BURNS R. G. (1974) $\text{Ti}^{3+}/\text{Ti}^{4+}$ ratios in lunar pyroxenes: implications to depth of origin of mare basalt magma. *Proc. 5th Lunar Sci. Conf.* **717–726**.

- TSUCHIYAMA A., NAGAHARA H., and KUSHIRO I. (1980) Experimental reproduction of textures of chondrules. *Earth Planetary Sci. Letters* **48**, 155-165.
- VELDE D. (1975) Armalcolite-Ti-Phlogopite-Diopside-Analcite-bearing lamproites from Smoky Butte, Garfield County, Montana. *Amer. Mineral.* **60**, 566-573.
- WARK D. A. (1983) The Allende meteorite: information from Ca-Al-rich inclusions on the formation and early evolution of the solar system. Ph.D thesis, Melbourne University.
- WARK D. A. (1987) Plagioclase-rich inclusions in carbonaceous meteorites: Liquid condensates? *Geochim. Cosmochim. Acta* **51**, 221-242.
- WARK D. A. and LOVERING J. F. (1977) Marker events in the early evolution of the solar system: Evidence from rims on Ca-Al-rich inclusions in carbonaceous chondrites. *Proc. 8th Lunar Sci. Conf.*, 95-112.
- WASSERBURG G. J., LEE T., and PAPANASTASSIOU D. A. (1977) Correlated O and Mg isotopic anomalies in Allende inclusions: II. Magnesium. *Geophys. Res. Lett.* **4**, 299-302.
- WASSERBURG G. J., PAPANASTASSIOU D. A., and LEE T. (1980) Isotopic heterogeneities in the solar system. In *Early Solar System Processes and the Present Solar System*, pp. 144-191. Soc. Italiana di Fisica, Bologna.
- WATSON E. B. (1979) Calcium content of forsterite coexisting with silicate liquid in the system $\text{Na}_2\text{O-CaO-MgO-Al}_2\text{O}_3\text{-SiO}_2$. *Amer. Mineral.* **64**, 824-829.
- YURIMOTO H. and SUENO S. (1984) Anion and cation partitioning between olivine, plagioclase phenocrysts and the host magma: A new application of ion microprobe study. *Geochem. J.* **18**, 85-94.
- YURIMOTO H., MORIOKA M., and NAGASAWA H. (1989) Diffusion in single crystals of melilite; I. Oxygen. *Geochim. Cosmochim. Acta* **53**, 2387-2394.

PLAGIOCLASE-OLIVINE INCLUSIONS IN ALLENDE - A LINK BETWEEN CAI AND FERRO-MAGNESIAN CHONDRULES. Y.J. Sheng, I.D. Hutcheon & G.J. Wasserburg. The Lunatic Asylum, Div. Geol. & Planet. Sci., Caltech, Pasadena, CA 91125.

The unique isotopic and chemical properties of CAI provide important clues regarding early solar system history. However, the relationship between CAI and much more abundant ferromagnesian chondrules in ordinary chondrites is still not clear. We identified a group of 18 Allende inclusions that differ from typical coarse-grained CAI in both mineralogy and chemistry and appear to be intermediate between CAI and ferromagnesian chondrules. These inclusions (POI) comprise mainly plagioclase and olivine and range in composition from type C CAI to porphyritic olivine chondrules (Red Eye) [1]. POI contain several rare accessory phases. Sapphirine and zirconolite, which have not been reported in CAI or in meteorites, appear unique to POI, while armalcolite, common in lunar basalts but reported in only 1 CAI [2], is found in several POI. 4 POI contain armalcolite; 5 have enstatite instead of fassaite, 2 of which are associated with sapphirine. Mineralogically, POI are characterized by the absence of melilite, the abundance of olivine, a distinctive pyroxene composition and more sodic plagioclase ($An_{85}-An_{95}$). POI do not contain Fremdlinge, rarely contain metal and lack the Wark-Lovering rims characteristic of coarse-grained CAI. Most POI have a sulfide rim. POI are usually spherical and 2 to 5 mm in diameter. They differ from type B CAI in their lower CaO (2-20%), and higher SiO_2 (30-50%) contents. In contrast to other anorthite-rich CAI, types B3 and C, POI cannot be related to any single compositional type, as they show a continuous variation in bulk chemistry from high Al to high Mg, projecting outside the An-Fo join in the gehlenite-anorthite-forsterite-spinel phase diagram (Fig. 1a) [3]. By taking into account the Na content of these inclusions (0.5-5% Na_2O) and using a projection from spinel and nepheline onto the Ge- An_{90} -Fo plane, with exception of POI containing Fe-rich pyroxene or enstatite, POI plot along the An_{90} -Fo join (Fig. 1b).

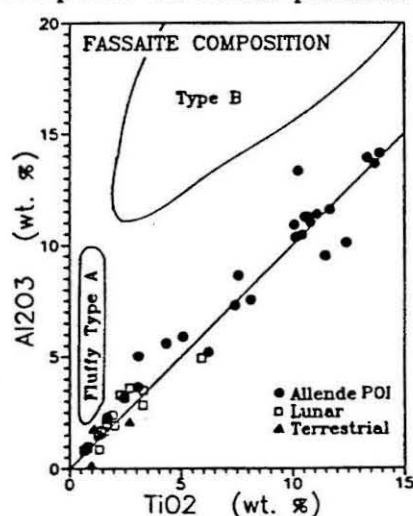
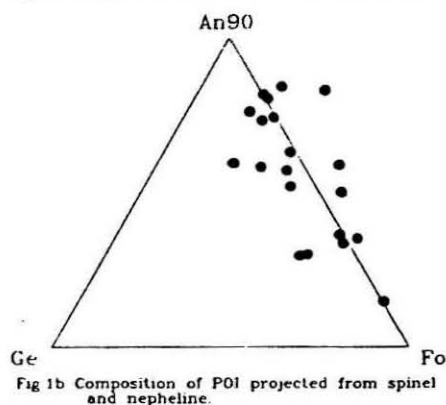
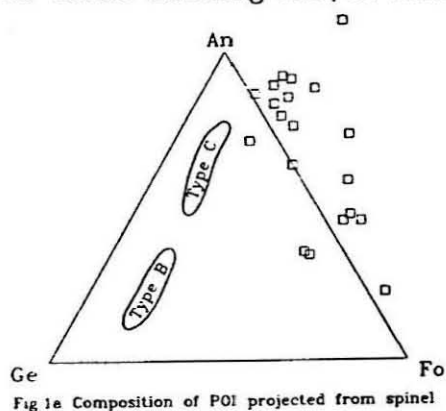
Sapphirine-bearing inclusions. POI 3510 and BG82CLII have similar mineralogy but have different proportions of plagioclase, spinel, Al-enstatite, olivine and sapphirine. Sapphirine ($Mg_2Al_4SiO_{10}$) occurs as randomly oriented clusters of prismatic, euhedral crystals in a Na-rich 'glassy' matrix. Both POI have coarser-grained exteriors grading into a fine-grained core, implying rapid cooling following initial crystallization from the rim. Sapphirine appears in mutual contact with spinel or enstatite; the sharp contact gives no indication of any reaction. The bulk compositions of the sapphirine-bearing POI and of the sapphirine regions within the POI show that if anorthite and enstatite or olivine are fractionated from the residual melt, a liquid similar to that from which sapphirine crystallizes is formed. The predicted order of crystallization, Sp-An-Ol-En-Sap, agrees with our observations, strongly suggesting that sapphirine is primary. The high Na content in the residual liquid may have expanded the sapphirine field and stabilized sapphirine at much lower temperature than suggested by the CMAS phase diagram [4].

Armalcolite-bearing inclusions. Armalcolite-bearing POI consist of plagioclase (~70%), olivine (~20%) with minor spinel and fassaite. Armalcolite $[(Fe,Mg)Ti_{205}]$ is found in association with rutile, perovskite and ilmenite. Zirconolite $[(Ca,Y)ZrTi_2O_7]$, a new phase in meteorites, was identified in one POI. The pyroxenes in these POI are characterized by a TiO_2/Al_2O_3 ratio of ~1. Such a high ratio is unique to pyroxenes in armalcolite-bearing rocks, including lunar and terrestrial rocks, and contrasts sharply with the much lower ratio in fassaites of typical CAI (Fig. 2). Armalcolite and pyroxene in POI appear interstitial to plagioclase and olivine. In contrast, petrographic and

Sheng, Y.J., Hutcheon, I.D. & Wasserburg, G.J.

experimental studies of lunar basalts [5] indicate that armalcolite, followed by clinopyroxene, is the earliest phase to crystallize. A possible explanation is that the bulk Ti/Al ratio in POI is much lower than that reported for lunar rocks. Anorthite crystallizing from the melt would deplete the residual melt in Al, thus increasing the Ti/Al ratio. The late-crystallizing pyroxene and associated Ti-rich oxides would then have a high Ti/Al ratio. Unlike lunar armalcolite, armalcolite in POI is not mantled by ilmenite, but armalcolite in 1 POI shows fine lamella of rutile-ilmenite intergrowth, which we interpret as a breakdown of armalcolite. The stability of armalcolite is very sensitive to f_{O_2} [6,7]. At 1200°C, armalcolite is stable between f_{O_2} of $10^{-9.5}$ - $10^{-10.5}$ and breaks down to ilmenite plus a reduced Mg-armalcolite at lower f_{O_2} . Further studies of the stability of Mg-armalcolite are needed to investigate whether composition of armalcolite is an indicator of f_{O_2} during POI crystallization.

The discovery of this distinct group of inclusions establishes an important connection between CAI and ferromagnesian chondrules. POI are associated with CAI by their high Al content and abundant plagioclase; the more refractory POI merge with type C CAI. Contrary to Wark [8], POI do not have a sharply defined composition and grade into olivine chondrules at the low-Ca end. The existence of the diverse types of POI confuses the definition of "refractory" inclusion and suggests that chondrules and CAI formed by similar processes. Based on the bulk composition of POI, we can exclude the possibility of formation as (1) liquid or solid condensates from a solar gas, (2) evaporative residues, or (3) fractional crystallization of a type B CAI. The origin of the parent liquid of the POI remains problematical. However, the similarity of the armalcolite-bearing POI to lunar basalts suggests that planetary magmatic processes must be considered. The presence of small excesses of radiogenic $^{26}Mg^*$ in two POI, USNM 3510 and Red Eye [1,9], gives added significance to a planetary origin since the inferred abundance of ^{26}Al is sufficient to cause melting and/or metamorphism on small planetary bodies. (#605)



Refs.: [1] Papanastassiou et al., LPSC XV (1984) 629; [2] Haggerty, Nature 276 (1978) 221; 221; [3] Stolper, GCA 46 (1982) 2159; [4] Humphries, Prog. Exp. Petrol. (1972) 140; [5] Akimoto et al., LSC 1st (1970) 129; [6] Friel & Harker, GCA 41 (1977) 403; [7] Stanin & Taylor, LPSC XI (1980) 117; [8] Wark, GCA 51 (1987); [9] Hutcheon, ACS Symp. #176 (1982) 95.

Mg ISOTOPE HETEROGENEITY IN PLAGIOCLASE OLIVINE INCLUSIONS; Y.J. Sheng, I.D. Hutcheon, & G.J. Wasserburg. The Lunatic Asylum, Division of Geological and Planetary Sciences, Caltech, Pasadena, CA 91125.

Plagioclase Olivine Inclusions (POI) [1] are abundant in C3V carbonaceous chondrites. We have studied 21 POI in the Allende (19), Leoville (1) and Adelaide (1) chondrites, contained in 18 thin sections. POI are characterized by an igneous texture, and a mineralogy composed of varying proportions of plagioclase (Pg) (5-60 vol.%), olivine (Ol) (10-70%), pyroxene (Px) (5-25%) and spinel (Sp) (5-20%), that distinguishes POI from both from CAI and ordinary chondrules. The bulk chemistry of POI spans a wide range of compositions, from Ca-Al-rich objects similar to Type C CAI [2] to more Mg-, Si-rich POI grading to CA and ferromagnesian chondrules [3,4]. POI contain significant Na_2O (1-6%), 15-60% contributed by plagioclase (An85-95), but low FeO and resemble fine-grained CAI in bulk composition. Spinel occurs in 18 of 21 POI and phase equilibria studies show that 9 of these inclusions have Sp as the liquidus phase, while 7 others have Ol as the first phase followed by Sp or Px. In all but 2 POI, the observed phase assemblages are compatible with equilibrium or fractional crystallization from melts of POI composition. In these 2 POI, spinel is present but is not a liquidus phase. The similarity in bulk composition suggested a relationship between fine-grained CAI and POI and led us to initiate a study of Mg isotopes and REE abundances to examine the possibility that fine-grained CAI were a major precursor component of POI.

The abundances of Mg isotopes and rare earth abundances (REE) were measured with the PANURGE ion probe [5]. Mass-dependent isotopic fractionation is expressed as F_{Mg} , the permil deviation of $^{25}\text{Mg}/^{24}\text{Mg}$ in POI minerals relative to the values in the respective standards. REE data were collected using an energy filtering technique [6]. Ca-normalized abundances for each phase are calculated relative to abundances in natural and synthetic standards.

In contrast to most CAI and chondrules, POI are not isotopically homogeneous in Mg (Fig. 1). Within individual POI, F_{Mg} in spinel is not constant but varies by up to $8^\circ/\text{‰}/\text{amu}$; Ol and Px, in contrast, have $F_{\text{Mg}}=0$. The observed range in F_{Mg} is -8 to $+11^\circ/\text{‰}/\text{amu}$ but F_{Mg} contrasts strongly with data from CAI, which show $F_{\text{Mg}} < 0$ in fine-grained CAI and $F_{\text{Mg}} > 0$ in coarse-grained CAI. Radiogenic $^{26}\text{Mg}^*$ is rare in POI. Plagioclase in 2 POI exhibits small enrichments in ^{26}Mg corresponding to $^{26}\text{Mg}^*/^{27}\text{Al}$ of 2 and 6×10^{-6} , respectively. The REE data for 4 POI are shown in Fig. 2. Whole inclusion REE abundances were calculated using modal mineralogy and SIMS data on individual phases. Two POI have relatively flat (Group I) patterns with 2-10 \times C1 levels of REE. Plagioclase (LREE-enriched and clinopyroxene exhibit complementary REE patterns consistent with equilibrium partitioning of REE during closed-system crystallization. The positive Eu anomaly in 5ALLB6 and PPX may reflect an overestimate of the modal abundance of Pg but the shape of the REE pattern is very similar to that found in Group I CAI (cf. [7]). The LREE-depleted pattern of 818-B reflects the absence of Pg in the mode for this POI. Inclusion BG82CLII, in contrast, exhibits much higher LREE abundances (up to 70 \times C1) and an HREE-depleted Group II REE pattern. In this POI, a Na- and Cl-rich mesostasis with abundant sapphirine, rather than Px, is the major REE host. No correlation between major element chemistry, REE levels or Mg isotopic composition was observed for any POI.

A major challenge posed by the data is to understand the preservation of large Mg isotope heterogeneities and, in at least one POI, the generation of a highly fractionated REE pattern in a class of objects whose textures would otherwise suggest crystallization from a homogeneous melt. The heterogeneous

distribution of F_{Mg} for spinel in POI contrasts with a much more uniform distribution in coarse-grained CAI and suggests significant differences in the nature of the precursor material and in the subsequent thermal history between POI and CAI. The observation of Mg isotope heterogeneity in POI has apparent similarities with the observation of oxygen isotope heterogeneity in CAI. In both classes of inclusions, spinel is the major host of the isotope anomaly, while silicate phases have a more nearly normal isotopic composition. However, the two classes of inclusions are clearly distinguished by major differences in the nature of the precursor components and in the process by which the isotopic heterogeneity was established and then preserved.

The variation in F_{Mg} for spinel within individual POI requires that either (1) solid spinel was a precursor phase and was not completely melted during POI formation, thus retaining its original Mg isotope signature, or (2) POI crystallized from an isotopically homogeneous melt and acquired isotopic heterogeneity through post-crystallization gas-solid exchange reactions. Since (1) POI appear to have suffered much less low temperature, post-crystallization alteration than most CAI and (2) phase equilibria data indicate that spinel is a relic phase in at least two POI, we favor the first scenario given above and suggest that the formation of POI included the following events.

(1) Condensation of spinel containing isotopically fractionated Mg; spinel has both $F_{Mg} > 0$ and $F_{Mg} < 0$ but the two types remain unmixed. Some silicates might be present. (2) Formation of a silicate precursor material representing a wide range of bulk compositions but containing significant Na_2O and low refractory siderophiles. Some of the silicates must be produced by gas/solid fractionation during condensation/evaporation to produce Group II REE abundances. (3) Mixing of spinel and silicate precursor components followed by heating to melt silicates but not spinel. (4) Relatively rapid cooling and little subsequent alteration to preserve isotopic heterogeneity. This model underscores a major difference in the way in which POI and CAI obtained their isotopic heterogeneity. The isotopic heterogeneity of POI reflects the inherited Mg isotopic variability of spinel while isotopic heterogeneity in CAI is produced by post-crystallization exchange of silicates. (#698) Ref.: [1] Sheng et al., LPSC XIX (1988) 1075. [2] Wark D.A. (1987) GCA 51, 221. [3] McSween H.Y. (1977) GCA 41, 1843. [4] Bischoff A. and Keil K. (1984) GCA 48, 693. [5] Hutcheon et al. (1987) GCA 51, 3175. [6] Zinner and Crozaz (1986) IJMS 69, 17. [7] Boynton W.V. (1983) in Rare Earth Elementary Geochemistry, 63-114.

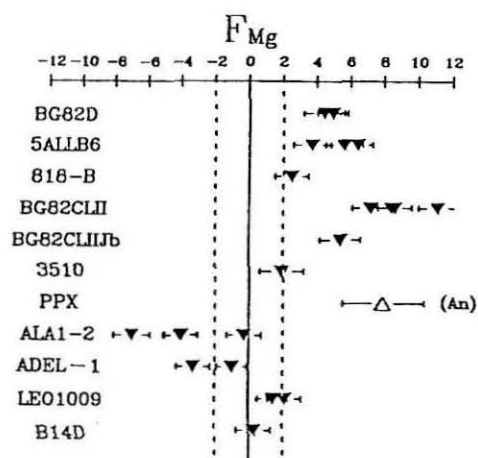


Fig.1 Mg isotopic fractionation in POIs in permil/annu. Px, Ol and An data plot between the dashed lines.

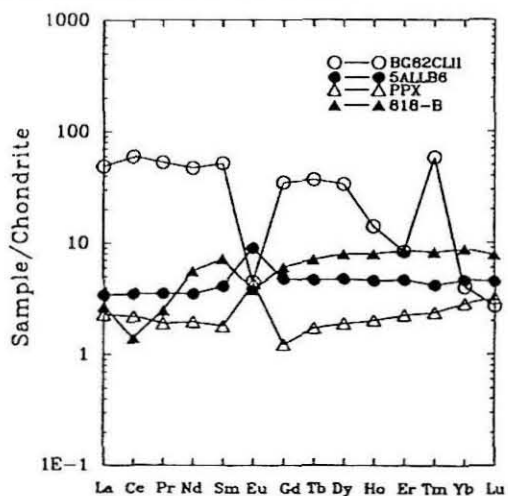


Fig.2 REE pattern of 4 POIs. The chondrite normalized abundance is recalculated using modal mineralogy and SIMS data on individual phases.

EXPERIMENTAL CONSTRAINTS ON THE ORIGIN OF PLAGIOCLASE-OLIVINE INCLUSIONS AND CA CHONDRULES ^{1,2}Y.J. Sheng, ²J.R. Beckett, ^{1,2}I.D. Hutcheon, and ^{1,2}G.J. Wasserburg. ¹The Lunatic Asylum, ²Division of Geological and Planetary Sciences, Caltech, Pasadena, CA 91125.

Plagioclase-Olivine Inclusions (POIs) are a distinct group of objects in carbonaceous chondrites consisting of plagioclase (Plag; An₆₂₋₉₈), olivine (Fo₆₂₋₉₉), enstatite (En), clinopyroxene (Cpx), and spinel (Sp) in various proportions [1]. CA chondrules (CACs) in ordinary [2,3] and enstatite [4] chondrites are similar to POIs but Plag is rare to absent while glass or Ca-rich mesostasis (Mes) is common. POIs and CACs cover a wide range of bulk compositions intermediate between those of ferromagnesian chondrules (FMCs) and Ca-, Al-rich inclusions (CAIs). Although there have been experimental efforts to characterize phase relations and dynamic crystallization behavior of CAIs [5,6] and FMCs [7,8], intermediate compositions relevant to POIs and CACs have not been studied systematically. We conducted equilibrium crystallization experiments on representative POI compositions at 1 atm total pressure in order to develop a framework to assist our interpretation of petrographic and isotopic data on POIs and to investigate possible differences in crystallization sequences between POI and CAI melts. For many POIs and CACs, concentrations of Na₂O and FeO are sufficiently low so the system CaO-MgO-Al₂O₃-SiO₂ is an excellent approximation to their bulk compositions and we can use projections to describe the crystallization behavior.

Homogeneous glasses corresponding in composition (Table 1) to representative POI were synthesized from oxide mixes. Experiments were conducted at constant temperature in air using techniques of [5] and run products were analyzed using optical microscope, SEM and electron probe techniques. Experimentally determined crystallization sequences are given in Table 1. Figs. 1-3 are multiply saturated liquidus phase diagrams constructed using data from this study and literature sources together with projected compositions of POIs and CACs. In Fig. 1, melt compositions are projected from MgAl₂O₄ Sp onto a plane defined by the compositions of CaAl₂Si₂O₈ anorthite (An), Mg₂SiO₄ forsterite (Fo), and tridymite (Tr). Liquid (L) compositions on the Sp-saturated surface are contoured in wt. % Sp above the An-Fo-Tr plane. Sp + cordierite (Cd) is stable as indicated in Fig. 1. However, in short runs (< ~35 hrs) aluminous En often coexists with Sp. The key feature of this phase diagram is the thermal boundary represented by the Sp-Plag-Fo plane, the exact position of which for CACs and POIs will depend on the Plag composition. During fractional crystallization, liquids on the Tr-poor side of this plane will evolve towards the Cpx + Sp + L field (shown in [5]) and crystallize Cpx. Liquids on the Tr-rich side of the thermal divide will evolve toward the invariant point Sp + An + Fo + Cd + L. However, Sp is in a reaction relationship with the melt at this invariant point, along the Sp + An + Fo + L boundary curve and in the shaded region, so such liquids may leave the Sp saturation surface and crystallize En. This can be seen in Fig. 2, a projection from Fo of olivine saturated melt compositions onto the plane defined by Sp-Tr-diopside (Di). The plane Fo + Plag + Sp is a thermal boundary for compositions in the Sp + L field. Sp-saturated L on the Tr-poor side of this plane will crystallize Cpx, but in many cases won't crystallize Opx. Fig. 3 is the projection of An-saturated melt compositions from An onto the plane Sp + Tr + Di. Fo and Pr are both in reaction with L at the invariant point An + Fo + ortho-enstatite (Oe) + proto-enstatite (Pr) + L.

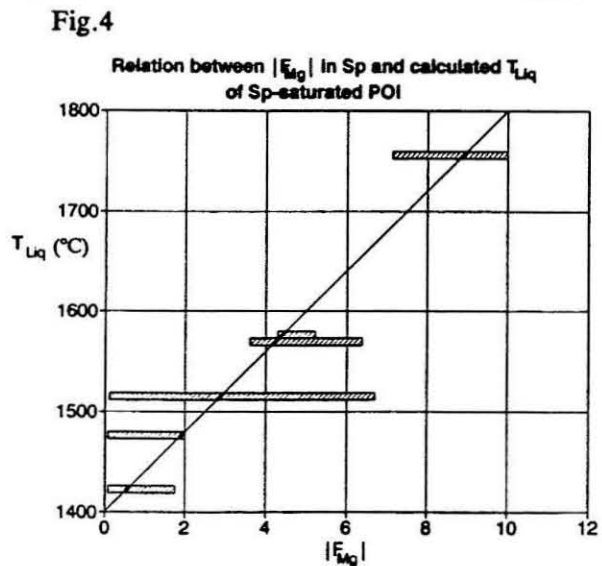
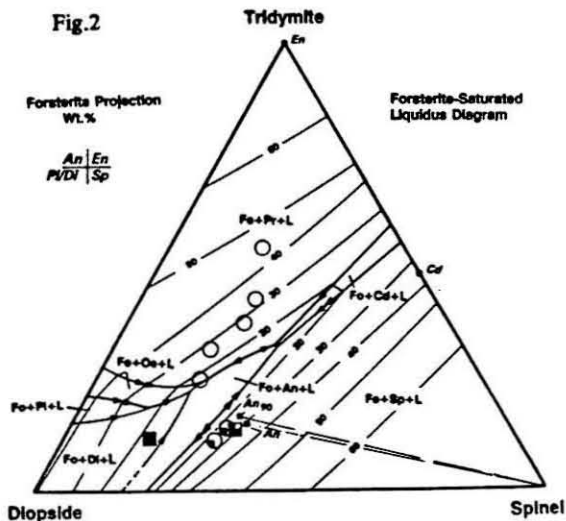
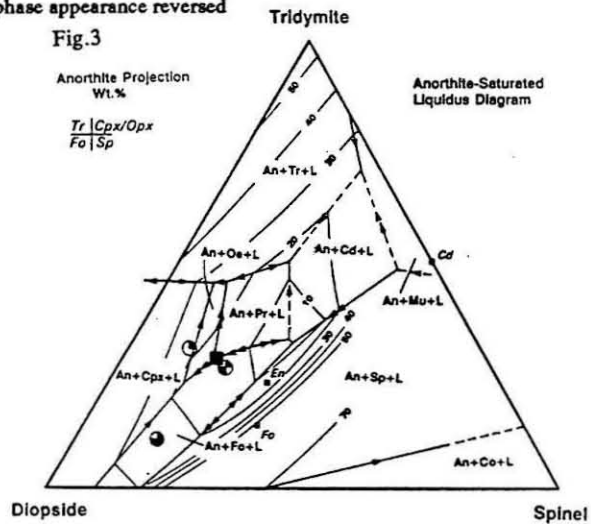
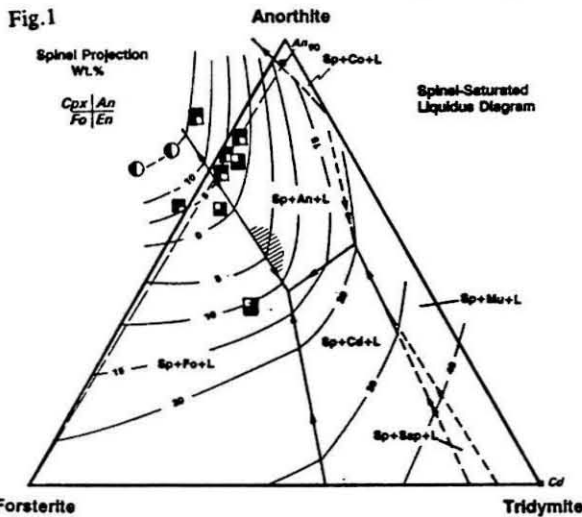
Figs. 1-3 provide a framework for the interpretation of mineral assemblages observed in many POIs and CACs. Phase assemblages predicted on the basis of phase equilibria are generally consistent with those observed in the meteoritic inclusions. Inconsistencies are either associated with the unexpected presence of Sp or, for CACs, the absence of Plag (+presence of glass or Mes). The latter may reflect faster cooling rates in CACs relative to POIs and the well known difficulty of Plag nucleation [9]. Sp in POIs that appear anomalous based on phase relations also have anomalous Mg isotopes versus other phases and are often strongly resorbed [1]. Hence these grains are relicts that pre-date the melting event. Isotopically anomalous Sp are also found in POIs with Sp on the liquidus. Fig. 4 shows liquidus temperatures (T_{Liq}) for these POIs calculated using the model of [10] and ranges in Mg isotopic fractionation (F_{Mg}) in Sp of [1]. Isotopic anomalies in Sp are common in POIs but bulk inclusions are typically normal. Hence Sp that crystallized from or re-equilibrated with the melt will have $F_{Mg} \sim$ bulk; anomalous Sp are earlier. Sp in POIs with $T_{Liq} < 1500^\circ\text{C}$ have $F_{Mg} \sim$ bulk while for $T_{Liq} > 1500^\circ\text{C}$ F_{Mg} is variable. There are no systematic variations in grain size with T_{Liq} so the maximum temperature of the melting event (T_{max}) for POIs was probably $\sim 1500^\circ\text{C}$. A $T_{max} = 1500^\circ\text{C}$ is also consistent with the observation that $|F_{Mg}|$ tends to increase with T_{Liq} . The proportion of Sp in a POI that crystallized from the melt below T_{max} with $F_{Mg} \sim$ bulk decreases with increasing T_{Liq} . Hence the higher T_{Liq} is, the more relict Sp will be present in the final assemblage. From Mg self-diffusion data in spinel [11], POIs were melted at $\geq 1500^\circ\text{C}$ for less than an hour. Otherwise, all of the isotopically anomalous Sp would have completely reequilibrated.

References: [1] Sheng Y. *et al.* (1991) GCA 55, in press; [2] Nagahara H. and Kushiro I. (1982) Meteoritics 17, 55; [3] Bischoff A. and Keil K. (1983) Nature 303, 588; [4] Bischoff A. *et al.* (1985) Chem. Erde 44, 97; [5] Stolper E. (1982) GCA 46, 2159; [6] Stolper E. and Paque J. (1986) GCA 50, 1785; [7] Blander M. *et al.* (1976) GCA 40, 889; [8] Lofgren (1989) GCA 53, 461; [9] Gibb F. (1974) Min. Mag. 39, 641. [10] Berman R. (1983) Ph.D. Thesis, Univ. B.C.; [11] Sheng *et al.* (1991) LPSC XXII. **Captions:** Figs.1-3. Multiply saturated liquidus phase diagrams. Squares represent POIs, circles CACs. The 4 quadrants in the symbol denote the presence (filled) or absence (empty) of corresponding phases. Small squares are mineral compositions. Fig.1. Projection from Sp. Co-corundum, Mu-mullite, Sap-sapphirine. Fig.2. Projection from Fo. Pigeonite. Data of [4] are plotted as empty circles since phase assemblages weren't given. Fig.3. Projection from An. Fig.4 Correlation of T_{Liq} ($^{\circ}C$) with range in $|F_{Mg}|$ of Sp in POIs.

Table 1 Composition of starting material and experimental results*

	Na ₂ O	MgO	Al ₂ O ₃	SiO ₂	CaO	TiO ₂	SUM	Crystallization sequences
POI-1	0	15.50	34.76	40.18	9.12	0.51	100.07	Sp(1605-13 $^{\circ}C$) \rightarrow An(1332-43 $^{\circ}C$) [#] \rightarrow Fo(1271-81 $^{\circ}C$) [#] \rightarrow Cd(-1260 $^{\circ}C$)
POI-2	0	12.88	32.53	41.14	12.61	1.01	100.17	Sp(1546-52 $^{\circ}C$) \rightarrow An(1381-91 $^{\circ}C$) \rightarrow Fo(1271-81 $^{\circ}C$) [#]
POI-3	0	22.52	21.11	51.41	4.96	1.05	101.05	Sp-Fo(1351-1451 $^{\circ}C$) \rightarrow Cd(1285-1301 $^{\circ}C$) \rightarrow An(1261-69 $^{\circ}C$)
POI-2Na2	2.17	12.71	32.06	39.47	12.45	1.14	100.00	Sp(1550-1613 $^{\circ}C$) \rightarrow Plag(1300-11 $^{\circ}C$) \rightarrow Fo(1281-88 $^{\circ}C$)
POI-2Na5	5.03	12.43	31.27	38.14	11.92	1.21	100.00	Sp(1550-1613 $^{\circ}C$) \rightarrow Fo(1237-50 $^{\circ}C$)

* WDS analysis on starting glass composition. # phase appearance reversed



Mg SELF-DIFFUSION IN SPINEL: CONSTRAINTS ON THE THERMAL HISTORY OF PLAGIOCLASE-OLIVINE INCLUSIONS. Y.J. Sheng, G.J. Wasserburg, and I.D. Hutcheon. The Lunatic Asylum, Division of Geological and Planetary Sciences, Caltech, Pasadena, CA 91125.

A prominent feature of Plagioclase-Olivine Inclusions (POIs), which distinguishes them from most coarse-grained CAIs and chondrules, is the Mg isotope heterogeneity both between coexisting spinel and silicates and among spinels. Sheng *et al.* [1] characterized POIs and proposed that the variation in Mg isotope fractionation among coexisting phases within POIs is the result of incomplete melting of silicate-rich precursors containing relict spinel with isotopically fractionated Mg. The preservation of isotopic heterogeneity indicates that the thermal event which partially melted the precursor and produced an igneous texture either had too low a temperature or was too brief to allow complete Mg isotope homogenization. Differences in thermal history are proposed to be the major factor leading to differences in isotopic composition and textures between POIs and CAIs. The temperature history required to homogenize Mg isotopes depends on the diffusion rate of Mg in spinels. In order to establish this critical rate we designed experiments to determine the self-diffusion coefficients of Mg in spinel at temperatures reflecting possible melting conditions of POIs.

We investigated Mg self-diffusion in $MgAl_2O_4$ spinel (Sp) by an isotope tracer method. Experiments were made on single crystal gem quality Sp. Polished Sp wafers were annealed for 24 hrs. at $1500^\circ C$. The diffusion couple consists of a piece of the annealed polished Sp wafer placed together with ^{25}Mg -doped $CaO-MgO-Al_2O_3-SiO_2$ (CMAS) glass and held at the run temperature at 1 atm in air for different times. The wetting of the melt yielded a boundary of Sp to glass that was a sharp welded contact. The glass was produced by adding ^{25}MgO to CMAS mixture and melted at $1550^\circ C$ for 24 hours. The glass was verified to be both chemically and isotopically homogeneous. Initial ratios of the starting glasses were $^{25}Mg/^{24}Mg = 1.2$ to 1.6 and $^{26}Mg/^{24}Mg \sim 0.140$. The glasses contained 13.6-14.7 wt. % MgO. The bulk compositions of starting glasses were chosen so that they are spinel-saturated at the run temperature of a given experiment. Deviations from the saturation composition would be compensated by nucleation of Sp from the melt or dissolution of the Sp wafer. Since in our experiments, the starting glasses were chosen to be close to Sp-saturated compositions and that the Sp/melt volume ratio is relatively large ($\sim 1:5$), slight deviations from Sp-saturated condition in the melt will be compensated with negligible effects to the Sp-melt diffusion couple. Variations in Mg isotopes in Sp and glass were measured with the PANURGE ion microprobe using methods described by [2,3]. Analyses were made across a traverse perpendicular to the diffusion interface. Diameter of the primary ion beam was approximately $3 \mu m$. The 2σ error for measured $^{25}Mg/^{24}Mg$ ratios is $\pm 3\%$ and $^{26}Mg/^{24}Mg$ is $\pm 2\%$.

The results are shown in Figs. 1 and 2. Fig. 1 shows the variation of $^{25}Mg/^{24}Mg$ across a traverse in the Sp wafer from one experiment. The fitted curve is the calculated diffusion profile. The self-diffusion of Mg in Sp is modeled as diffusion in an infinite composite medium. The Sp-melt diffusion couple is in chemical equilibrium but with Mg isotopic exchange. The solution to the diffusion equations was taken to account for the complementary diffusion of ^{24}Mg , ^{25}Mg and ^{26}Mg in both phases with the total concentration of Mg in each phase to be constant. This approach implies that the Sp-glass boundary has constant Mg isotopic composition. A diffusion coefficient (D) for each run is extracted by using a least square best fit to the measured data. The temperature dependence of D for Mg self diffusion in Sp is obtained from the Arrhenius relation $D = D_0 \exp(-Q/RT)$ (Fig. 2). The activation energy (Q) and pre-exponential factor D_0 derived by a linear regression of the experimental diffusion data are, respectively, 356 ± 26 kJ and 7.77 ± 1.17 cm^2/s .

The results from this study indicate that Mg isotopic reequilibrium can be achieved in a relatively short time at melting temperatures of POIs determined from the phase diagrams [4]. As suggested by [4], maximum melting temperature (T_{max}) for POIs is $\sim 1500^\circ C$. Assuming a spinel grain size (x) in POIs of about $10 \mu m$ (typically $< 5 \mu m$), the homogenization time of Mg isotopes in a Sp-saturated silicate melt at temperatures above $1500^\circ C$, using the approximation $x^2 \approx Dt$, is < 1 hr. For temperatures between $1500-1400^\circ C$ the homogenization time (t) is 1-4 hrs, and at $1400-1300^\circ C$ $t \sim 4-20$ hrs. Thus for the range of expected melting temperatures of POIs, the Mg diffusion data provides limits on the maximum time the POI melt could have remained at a specific temperature. The dependence of cooling rate (r) with T_{max} for given x calculated using the relation $x = D(T)tRT^2/rQ$ [5] is shown in Fig. 3. The initial rates at $T = 1500^\circ C$ for x of 5, 10, and $15 \mu m$ are, respectively, 305, 76, and $34^\circ C/hr$ (Fig. 3). The nature of the heating process is thus required by our data to be short, such as flash heating or impact melting.

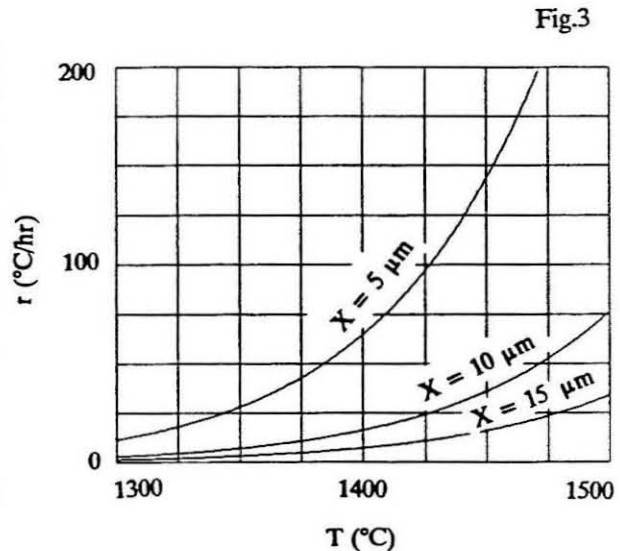
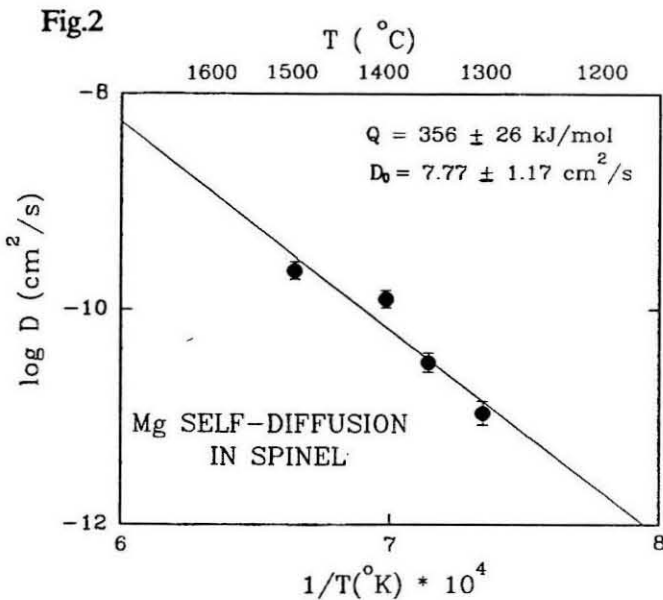
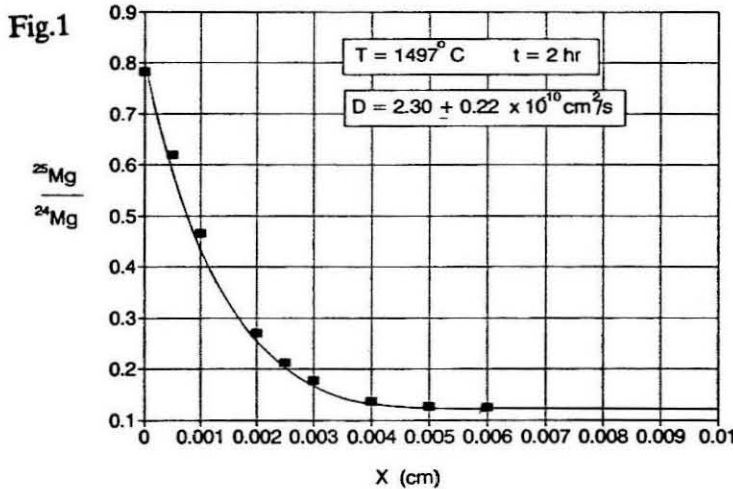
These grain-size dependent bounds on cooling rates are comparable to or up to $10 \times$ greater than those inferred from experimental and textural studies of synthetic systems [6,7]. It appears that the igneous textures of

POIs are compatible with the cooling rates determined in this experiment, but much faster rates, which would preserve isotopic heterogeneity, are probably inconsistent with petrographic observations. The cooling rates for POIs are much lower than radiative loss cooling rates of mm-size droplets, requiring formation of POIs in a hot region of the nebula. For $T_{\max} = 1420^{\circ}\text{C}$ and $r \leq 20^{\circ}\text{C}$, as suggested for some Type B CAIs [7], our data suggests that Sp with $x \leq 10 \mu\text{m}$ would be isotopically homogenized in Mg. If CAIs initially contained Sp with fractionated Mg or other similar relict phases, they would be consequently reequilibrated at this slower cooling rate. The presence of Mg isotope heterogeneity in POIs and the results of our diffusion experiments provide one of the most direct means of establishing a constraint on the thermal history of these inclusions. The presence or absence of Mg isotopic heterogeneity could be used as a measure of the T_{\max} and cooling rate not only of POIs but also of other types of refractory inclusions and chondrules if we assume that these objects had sampled similar material.

Acknowledgement. We thank D. Burnett for generously allowing use of his lab, M. Johnson and T. LaTourette for their kind support.

References. [1] Sheng Y. *et al.* (1991) GCA 55, in press; [2] Huneke J. *et al.* (1983) GCA 47, 1635; [3] Hutcheon I. *et al.* (1987) GCA 51, 3175; [4] Sheng Y. *et al.* (1991) LPSC XXII; [5] Kaiser T. and Wasserburg G. (1983) GCA 47, 43; [6] Wark D. and Lovering J. (1982) GCA 46, 2651; [7] Stolper E. and Paque J. (1986) GCA 50, 1785.

Captions. Fig.1. Variation of $^{25}\text{Mg}/^{24}\text{Mg}$ across a traverse in Sp from Sp-glass interface. The fitted curve is the calculated diffusion profile. Fig.2. Arrhenius plot showing the least square best fit of the experimental data. Fig.3. Dependence of cooling rate (r) upon temperature (T) for Sp grain sizes of 5, 10, and 15 μm .



AN EXPERIMENTAL STUDY OF Mg SELF-DIFFUSION IN SPINEL. Y.J. Sheng, I.D. Hutcheon, and G.J. Wasserburg. The Lunatic Asylum, Div. of Geol. and Planet. Sci., Caltech, Pasadena 91125.

Mg isotope heterogeneity, both between coexisting spinel and silicates and among spinels, is a prominent feature of Plagioclase-Olivine Inclusions (POIs) [1]. The preservation of isotopic heterogeneity and relict spinel (Sp) in inclusions with igneous textures indicates that the thermal event which partially melted the precursor material either had too low a temperature or was too brief to allow Mg isotope homogenization between Sp and the melt. Since the temperature history required to homogenize Mg isotopes depends on the diffusion rate of Mg in Sp, we designed experiments using an isotope tracer method to determine this critical rate [2]. The diffusion couple consists of a gem quality $MgAl_2O_4$ Sp wafer and ^{25}Mg -doped glass of POI composition. The bulk compositions of starting glasses were chosen from phase equilibria data [3] to be Sp-saturated at the run temperature of a given experiment. The presence of chemical equilibrium between glass and Sp for each run ensures that Mg diffuses only in response to the isotopic disequilibrium. Glasses were verified to be chemically and isotopically homogeneous and were then equilibrated at a temperature slightly below the spinel saturation temperature of the melt to ensure chemical equilibrium. Polished Sp wafers were pre-annealed for 24 hrs. at $1500^\circ C$. The polished surfaces of the Sp wafer and glass were placed together and held at temperatures between 1260 and $1550^\circ C$ for 20 to 0.5 hr. Mg isotope profiles in Sp and glass were measured with the PANURGE ion microprobe [4,5] across a traverse perpendicular to the diffusion interface. Measured $^{25}Mg/^{24}Mg$ ratios were corrected for differences in isotopic fractionation between Sp and glass by normalizing to $^{26}Mg/^{24}Mg=0.13955$. The diffusion coefficients (D) were calculated from the measured isotope profiles using a model that includes the complimentary diffusion of ^{24}Mg , ^{25}Mg and ^{26}Mg in both phases with the constraint that the Mg content of each phase is constant. Diffusion profiles measured in Sp and glass for the experimental run at $1553^\circ C$ are shown in Fig.1,2. The temperature dependence of D for Mg self diffusion in Sp is obtained from an Arrhenius relation. The activation energy and pre-exponential factor are, respectively, 397 ± 21 kJ and 199.4 ± 1.2 cm^2/s . This is somewhat different to the numbers previously reported [2] due to the inclusion of new data. For a maximum melting temperature for POIs of $\sim 1500^\circ C$ [3] these results show that a $10 \mu m$ diameter Sp would equilibrate isotopically with a melt within 60 min. To preserve isotopic heterogeneity, the POIs must have initially cooled faster than 50 to $250^\circ C/hr$. **References.** [1] Sheng Y. *et al.* (1991) GCA 55, 581; [2] Sheng Y. *et al.* (1991) LPSC XXII, 1233; [3] Sheng Y. *et al.* (1991) LPSC XXII, 1231; [4] Huneke J. *et al.* (1983) GCA 47, 1635; [5] Hutcheon I. *et al.* (1987) GCA 51, 3175; **Captions.** Variation of $^{25}Mg/\Sigma Mg$ across a traverse in glass (Fig.1) and Sp (Fig.2) for the experimental run at $1553^\circ C$. The fitted curve is the calculated diffusion profile.

Fig.1

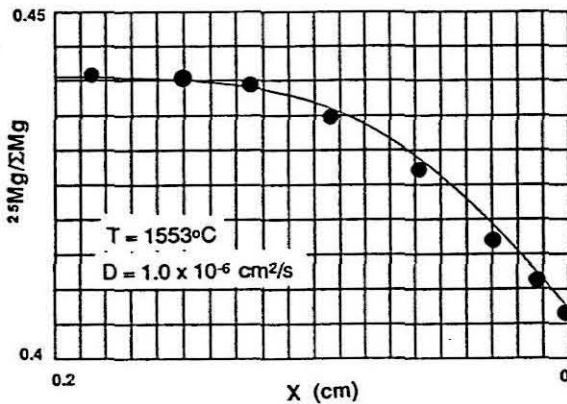


Fig.2

